

Density gradients in spherical tokamak plasmas

Density gradients in spherical tokamak plasmas

PROEFSCHRIFT

ter verkrijging van de graad van doctor aan de
Technische Universiteit Eindhoven, op gezag van de
Rector Magnificus, prof.dr. R.A. van Santen, voor een
commissie aangewezen door het College voor
Promoties in het openbaar te verdedigen op
donderdag 10 april 2003 om 16.00 uur

door

ERIC RONALD ARENDS

geboren te Hillegom

Dit proefschrift is goedgekeurd door de promotoren:

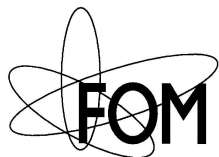
prof.dr. N.J. Lopes Cardozo

en

prof.dr. F.C. Schüller

Copromotor:

dr. M.J. Walsh



The work described in this dissertation is a part of a research program of the 'Stichting voor Fundamenteel Onderzoek der Materie' (FOM) with financial support from the 'Nederlandse Organisatie voor Wetenschappelijk Onderzoek' (NWO), the 'United Kingdom Atomic Energy Authority' (UKAEA) and Euratom. The work was carried out at the 'UKAEA Fusion' laboratory in Culham in Oxfordshire in the United Kingdom.

A je to!
Buurman & Buurman

ik draag dit proefschrift op aan mijn ouders

Samenvatting

Het onderzoek dat in dit proefschrift is beschreven is onderdeel van het wereldwijde ontwikkelingsprogramma van kernfusie als energiebron. Kernfusie - het proces waarin twee lichte atoomkernen samensmelten, waarbij zeer veel energie vrijkomt - heeft buitengewoon aantrekkelijke eigenschappen als energiebron: het proces is schoon en veilig, en veroorzaakt geen uitstoot van het broeikasgas CO₂. De brandstof is onuitputtelijk en overal voorhanden. Vijftig jaar onderzoek hebben de wetenschappelijke haalbaarheid van beheerste kernfusie aangetoond. In wereldwijde samenwerking zal nu de eerste fusiereactor worden gebouwd, ITER, waarvan het geproduceerde vermogen circa tien keer groter is dan het opgenomen vermogen.

ITER is een 'tokamak', een reactor waarin de brandstof is opgesloten in een torusvormig vat. De brandstof is waterstofgas, dat op een temperatuur van 150 miljoen graden moet worden gebracht. Het gas ioniseert dan en wordt een plasma. Het plasma wordt op zijn plaats gehouden met behulp van magneetvelden.

Het plasma in ITER - en andere zogenaamde conventionele tokamaks - heeft een vorm die vergelijkbaar is met de binnenband van een auto. Het is echter ook mogelijk een tokamak zo te ontwerpen dat het plasma de vorm heeft van een uitgeboorde appel. Deze 'sferische tokamak' kan leiden tot een compactere constructie van de fusiereactor. Het concept is echter nog jong en moet zorgvuldig worden vergeleken met de conventionele tokamak.

De eerste sferische tokamak waarin plasmatemperaturen van miljoenen graden werden bereikt was START (in Culham, Engeland). De veelbelovende resultaten van dit experiment waren aanleiding voor de bouw van de Mega-Ampere Spherical Tokamak MAST (ook in Culham). In deze machine, die in december 1999 in bedrijf kwam, worden plasma's gemaakt met een plasmastroom van 1.35 mega-ampere gedurende 0.7 seconde.

ITER volgt het 'standaardscenario' dat uit het fusie-onderzoek naar voren is gekomen. Dat wil zeggen dat gekozen is voor het zogenaamde 'H-mode' (high-confinement) regime, een toestand waarin het plasma doelmatig kan worden verhit. Net als conventionele tokamaks kan MAST in de H-mode worden bedreven.

Dit proefschrift is een studie van diverse aspecten van de H-mode in MAST, en maakt de vergelijking met de conventionele tokamak. In vergelijking met de L - (low-confinement) mode kan - bij gelijk verhittingsvermogen - in de H-mode een veel hogere plasmadruk worden bereikt. Dit is te danken aan het ontstaan van een 'transportbarrière' aan de rand van het plasma. Kenmerkend voor de H-mode is ook het optreden van randinstabiliteiten, zogenaamde ELM's (Edge Localised Modes). Deze instabiliteiten zorgen voor een plotseling, en kortdurend, verlies van warmte en deeltjes uit het plasma. Deze uitstoot wordt in korte tijd op de wand van de reactor gedeponerd, hetgeen kan leiden tot ongewenste erosie van de reactorwand. ELM's treden op in alle tokamaks, sferische zowel als conventionele. De vraag is of de energie-uitstoot door een ELM in de compacte sferische tokamak tot problemen zou kunnen leiden.

De centrale vraag van dit proefschrift is: hoe vergelijkt de H-mode in MAST - als voorbeeld van een sferische tokamak - zich met die in conventionele tokamaks. Daarbij krijgen twee aspecten speciale aandacht. Ten eerste: de ontwikkeling van de gradiënten van dichtheid en temperatuur aan de rand van het plasma, en ten tweede: de uitstoot van deeltjes tijdens ELM's.

Om deze vragen aan te kunnen pakken werden twee meetsystemen ontwikkeld. Het eerste maakt gebruik van de verstrooiing van een laserbundel (Thomsonverstrooiing) om een nauwkeurige meting van de gradiënten van dichtheid en temperatuur te doen. Deze meting kan eenmaal per plasma-ontlading worden uitgevoerd. Dit systeem werd aanvankelijk gebouwd met een ruimtelijk oplossend vermogen van 30-40 meetpunten verdeeld over de diameter van het plasma. Later werd dit aantal verhoogd tot bijna 300 meetpunten, om nog meer detail te kunnen zien. Dit resulteerde in een aaneengesloten meting van de dichtheids- en temperatuurprofielen van de binnen- tot de buitenzijde in het middenvlak van het plasma. Dit is uitzonderlijk en MAST bevindt zich daarom in een unieke positie voor het bestuderen van deze grootheden in de H-mode. Het tweede meetsysteem maakt gebruik van het licht dat neutraal waterstof, dat in de rand van het plasma voorkomt, uitzendt. Ook dit systeem levert een meting van de gradiënt van de dichtheid in de rand van het plasma, maar in tegenstelling tot de eenmalige meting met laserverstrooiing, geeft deze methode een tijdsafhankelijk signaal met een repetitiefrequentie van 1 kHz of meer. Dit systeem heeft de eenmalige laserverstrooiingsmeting wel nodig als ijking en meet de gradiënt alleen aan de buitenzijde. Met behulp van deze meetapparatuur werden de volgende resultaten bereikt.

De H-mode in MAST blijkt veel overeenkomsten te vertonen met die in een conventionele tokamak. Zeer belangrijk is dat de energie-opsluittijd - een maat voor de doelmatigheid van de magnetische opsluiting van het plasma - voldoet aan dezelfde schalingswetten, zodat MAST in dit opzicht volledig vergelijkbaar is met conventionele tokamaks. Er zijn echter ook belangrijke verschillen:

- In MAST vormt zich gedurende H-mode een zeer geprononceerde dichtheidsgradiënt - er kunnen zelfs 'dichtheids-oren' ontstaan - maar de sprong in de temperatuur is veel kleiner dan bij conventionele tokamaks.
- De plasmadruk - hetgeen een product van dichtheid en temperatuur is - is zeer laag aan de rand van het plasma in MAST. Nochtans, de energie-opsluiting - welke voortvloeit uit de totale plasmadruk - schaal als in conventionele tokamaks.

Het ontstaan van de dichtheids-oren kan goed worden begrepen als een gevolg van een zeer traag deeltjestransport, een beeld dat ook wordt gehanteerd in conventionele tokamaks voor het ontstaan van gradiënten. De andere observaties, wijzen er echter op dat de uitwisseling van deeltjes tussen het plasma en het gebied daarbuiten in MAST anders is dan in conventionele tokamaks. Dit zal waarschijnlijk komen doordat het plasma in MAST is omringd door een groot volume met neutraal waterstof, dat als een continue bron van laag-energetische neutralen kan fungeren. In een conventionele tokamak is deze omhullende, neutrale laag heel dun en speelt de wand een veel belangrijkere rol. De vraag blijft echter open in hoeverre het verschil in plasma-vorm in dezen een belangrijke rol speelt.

Ook aangaande de uitstoot van plasma tijdens een ELM werden interessante conclusies bereikt. De belangrijkste is dat deze uitstoot sterk is geconcentreerd aan de buitenzijde van de plasma-bol. Met andere woorden, de kolom die door het smalle gat in het centrum van het plasma loopt en potentieel schade zou kunnen oplopen tijdens de ELM, krijgt slechts een zeer klein deel van de totale uitstoot te verwerken.

De sterke concentratie van de uitstoot aan de buitenzijde van het plasma is een positief resultaat voor ontwikkeling van reactorconcepten volgens het principe van de sferische tokamak. De betekenis van de resultaten betreffende de randgradiënten en de neutralen is in dit kader nog niet geheel duidelijk.

Summary

The work described in this dissertation is part of the worldwide program that has the aim to develop nuclear fusion as energy source. Fusion - the process in which two light nuclei fuse, releasing vast amounts of energy - is very attractive as a source of energy: it is a clean and safe process, and it does not produce the greenhouse gas CO₂. The fuel resources are inexhaustible and widely available. Fifty years of research has proven the scientific feasibility of controlled nuclear fusion. The first fusion reactor, ITER, in which the produced power will be approximately ten times bigger than the power input, will be built in a worldwide collaboration.

ITER is a 'tokamak', a reactor in which the fuel is contained in a torus-shaped tank. The fuel is hydrogenic gas, which must be heated to 150 million degrees Celsius. Thus the gas ionises and becomes a plasma. The plasma is kept in place by means of magnetic fields.

The ITER plasma - and that of other so-called conventional tokamaks - has a shape that can be compared to the inner tube of a car tire. However, it is also possible to design the tokamak in such a way that the plasma has the shape of a cored apple. This 'spherical tokamak' can result in a more compact construction of the fusion reactor. This is a rather recent concept and needs to be compared thoroughly with the conventional tokamak.

The first spherical tokamak in which plasmas of millions of degrees were produced was START (in Culham, England). The promising results obtained on this experiment, have led to the development of the Mega-Ampere Spherical Tokamak MAST (also in Culham). This machine achieved its first plasma in December 1999 and has since demonstrated plasma currents of 1.35 mega-ampere during 0.7 seconds.

ITER follows the 'standard scenario' that has resulted from fusion research. This means that it will operate in the so-called 'H-mode' (high-confinement) regime, a state in which the plasma can be efficiently heated. Just like conventional tokamaks, MAST can also operate in H-mode.

This dissertation is the result of a study of several aspects of H-mode in MAST, and makes a comparison with the conventional tokamak. In comparison to the L - ('low-confinement') mode, the H-mode can achieve much higher plasma pressure using equal heating power. This is the result of the formation of a 'transport barrier' at the edge of the plasma. Associated with H-mode is the occurrence of edge instabilities, so-called ELMs (Edge Localised Modes). These instabilities produce pulsed outflows of heat and particles. These outflows are deposited in a short time on the wall of the reactor, which could lead to increased material wear. ELMs occur in all tokamaks, spherical as well as conventional. It is to be verified whether the power exhaust during an ELM will cause problems in the compact spherical tokamak.

The key question of this dissertation is: how does H-mode in MAST - as representative of spherical tokamaks - compare with that on conventional tokamaks. In this, two aspects are especially considered. First, the development of density and temperature gradients at the edge of the plasma, and secondly: the exhaust of particles during ELMs.

In order to be able to answer these questions two diagnostics have been developed. The first uses the scattering of a laser beam (Thomson scattering) to perform an accurate measurement

of the density and temperature gradients. This measurement can be taken once per plasma discharge. This system was originally built with a resolution of 30-40 data points distributed over the diameter of the plasma. At a later stage, the system was upgraded to close to 300 data points in order to provide better resolution. This has resulted in a measurement of the density and temperature profile from the inside to the outside along the central midplane of the plasma. With this unique measuring capability, MAST is in a good position to study these quantities in H-mode. The second system uses the light that is emitted by neutral hydrogen at the edge of the plasma. This system, too, produces a measurement of the density gradient at the edge of the plasma, but in contrast to the scattering system which produces a single measurement, this system produces a time resolved measurement with a frequency of 1 kHz or higher. However, for calibration purposes this system requires the single measurement of the laser scattering diagnostic and only a measurement of the outside gradient is produced. The following results have been obtained using these diagnostics.

It has turned out that H-mode in MAST resembles that in a conventional tokamak to great extent. Of great importance is that the energy confinement time - a measure of the efficiency of the magnetic confinement of the plasma - follows the same scaling laws, making MAST, in this respect, very comparable to conventional tokamaks. However, there are also substantial differences:

- During H-mode in MAST a very pronounced density gradient is formed - potentially leading to the formation of the edge density 'ear' - but the increase in temperature is much smaller than that in conventional tokamaks.
- The plasma pressure - which is the product of density and temperature - at the edge of the plasma in MAST is small. Nonetheless, the energy confinement - being the result of the total plasma pressure - scales as in conventional tokamaks.

The development of the density ears can be well understood as the result of very low particle transport, which image is generally expected to explain the formation of gradients in a conventional tokamak. The other observations, however, indicate that the exchange of particles and heat between the plasma and its surroundings in MAST differs from that in conventional tokamaks. This is likely due to the fact that the MAST plasma is surrounded by a large volume of neutral hydrogen, which can act as a continuous source of low-energetic neutrals. In a conventional tokamak this surrounding, neutral layer is much narrower and the role of the wall in the recycling process much more pronounced. However, the question remains to what degree the difference in plasma shape plays an important role in this.

Also concerning the outflow of plasma during ELMs interesting results were obtained. Of these the most significant is that the outflow is strongly biased to the outside of the plasma sphere. In other words, the column that cuts through the centre of the plasma and that could potentially be damaged by the effect of ELMs, only receives a very small portion of the total exhaust.

The fact that the power exhaust is strongly concentrated on the outside of the plasma is a positive result for the development of reactor concepts based on the spherical tokamak design. In this framework, the impact of the results concerning the edge gradients and neutrals is not yet entirely clear.

Contents

1	Introduction	1
1.1	Fusion energy research	1
1.2	The high-confinement regime	4
1.3	This dissertation	5
1.4	Publications	6
	Bibliography	9
2	Spherical tokamak	11
2.1	Introduction	11
2.2	The role of the ST in confinement scaling	12
2.3	Results of ST experiments	13
2.4	Conclusions	14
	Bibliography	15
3	MAST machine & diagnostics	17
3.1	Introduction	17
3.2	MAST machine	17
3.3	Auxiliary heating & fuelling	19
3.4	Diagnostics	19
	Bibliography	22
4	Thomson scattering theory	25
4.1	Introduction	25
4.2	Scattering from a single electron	25
4.3	Scattering from a group of electrons	28
	Bibliography	29
5	Measurement and modelling of ‘ears’	31
5.1	Introduction	31
5.2	Thomson scattering diagnostic	33
5.3	Results	36
5.4	Transport analysis	39
5.5	Modelling results	44
5.6	Summary and discussion	49
	Bibliography	50
5.A	Numerics	52
5.B	Simplified analytical solution	56

6	High-resolution Thomson scattering	57
6.1	Introduction	57
6.2	Instrumental setup	58
6.2.1	Hardware	58
6.2.2	Triggering system	63
6.2.3	Operation	64
6.3	Calibration	65
6.4	Data processing	70
6.5	Error estimates	74
6.6	Normalised-flux resolution	79
6.7	Known issues	82
6.8	Profile examples	85
6.9	Summary	87
	Bibliography	89
6.A	Setup of test CCD image	90
7	Edge density gradient measurements	91
7.1	Introduction	91
7.2	... from Thomson scattering	92
7.2.1	Comparison of inboard and outboard density gradient measurements	92
7.2.2	Fitting edge gradient and pedestal	94
7.3	... from linear D_α camera	98
7.4	Summary and discussion	103
	Bibliography	104
8	High confinement in MAST	107
8.1	Introduction	107
8.2	Characteristics of H-mode in MAST	108
8.3	H-mode access in MAST	112
8.4	H-mode profiles	115
8.5	Asymmetric power exhaust during ELMs	118
8.6	Addition of aspect ratio to pedestal scaling law	127
8.7	Conclusions	132
	Bibliography	133
8.A	Determination of the global energy confinement	135
9	Evaluation and discussion	139
9.1	Summary of diagnostics development	139
9.2	Results of H-mode studies	140
9.3	In conclusion	142
	List of abbreviations	143
	List of symbols and constants	145
	Acknowledgements	147
	Curriculum vitae	149

Chapter 1

Introduction

1.1 Fusion energy research

Fusion research

World energy demands are growing due to the improving living standards in Western and developing countries. At the same time, the use of fossil fuels has a major impact on the environment, with CO₂ concentration levels increasing in the atmosphere and world wide pollution becoming critical. Furthermore, the future of fossil fuels looks precarious and the prospect of depending on oil-producing countries is not attractive. It is therefore necessary to find alternative energy sources that have less or no impact on the environment and have a more sustainable future.

There are currently some environment-friendly energy sources in development and already in use, such as solar and wind energy; however, their contribution to the world energy pool is at less than 0.5% of the primary energy supply [1], less than the growth in demand. It is therefore imperative to find new ways of producing energy for the future; one of those is nuclear fusion. This highly efficient process is how the Sun has been able to sustain itself and produce energy ever since its birth 5 billion years ago. In fact, it is this very process in the Sun that has made all the current terrestrial forms of energy production possible.

During the fusion process two light nuclei are fused to form a new set of elements. The total mass of the reaction products is lower than the total initial mass, which, according to Einstein's $E = mc^2$, results in a release of energy. The application of this phenomenon could be a potentially limitless source of energy for the world's use and benefit. As yet, however, it is not available as an energy source for industrial or domestic use.

For over 50 years scientists have investigated the possibility of nuclear fusion as an energy source on earth. During these years much progress has been made, which has resulted in a record fusion power production of 16 MW on JET (Joint European Torus) in 1997 [2]. Part of the reason why the development has taken taking so long is that the fuel is hard to handle and difficult to control. A temperature of ~ 100 million degrees Celsius is required to give the particles enough energy to overcome the repelling Coulomb force caused by their positive charge. At those temperatures the fuel is fully ionised; in that state, it is referred to as plasma. Several techniques have been developed to confine the plasma at these very high temperatures. These techniques will be described in the next section. The energy producing process must be efficient: in current fusion reactors the ratio Q of energy output over input in the reactor is close to unity, while a factor of 10 or more is required for an efficient reactor. This requires large reactors with a considerable price tag attached to them. It is this required investment budget rather than technological issues which considerably slows down fusion development.

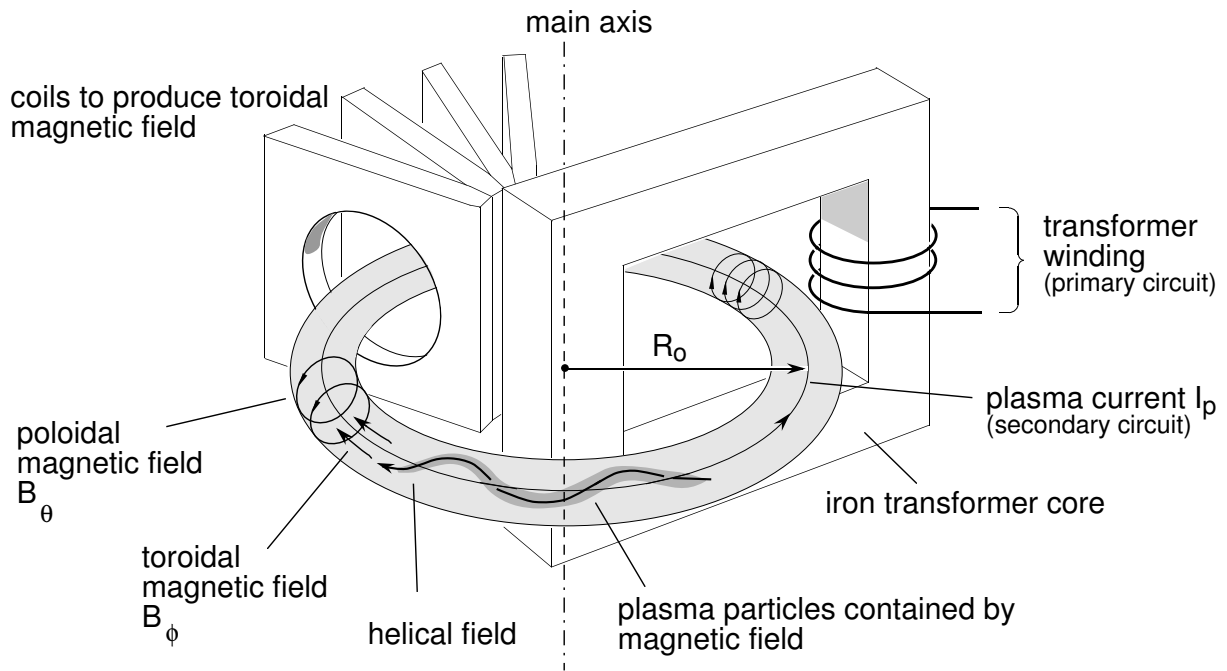


Figure 1.1: Schematic of a tokamak, its magnetic fields and some of its subsystems. The major radius is indicated by R_0 .

Plasma confinement

Two serious methods of controlling the plasma, in order to achieve nuclear fusion, are currently being explored worldwide; magnetic confinement and inertial confinement. In the latter, many powerful lasers are required to compress the plasma in order to reach the required conditions. Magnetic confinement is currently looking more promising, with the recent designing of a device called ITER, that should demonstrate $Q > 10$, currently awaiting the go-ahead for construction. The new machine is of the ‘tokamak’ class, a machine type first designed in Russia in the 1960s, the name being an acronym for toroidal chamber and magnetic coil.¹

In a tokamak, the charged particles in the plasma are confined by means of magnetic fields as illustrated in figure 1.1. The plasma acts as the secondary winding of the transformer; the thus induced toroidal current generates the poloidal magnetic field (B_θ). The toroidal magnetic field (B_ϕ) is generated by coils surrounding the torus. The two fields together produce helical field lines. The torus has a minor radius a and major radius R_0 . The vertical and horizontal position of the plasma is controlled by the additional radial and vertical magnetic fields, respectively. Often the solenoid forming the primary circuit is wound around the main axis of the machine and together with the toroidal field coils forms the centre column.

The magnetic field lines can be labelled with the magnetic winding number q , the number of turns the helical magnetic field lines make around the major circumference for each turn round the minor circumference. If q has a rational value $q = m/n$, where m and n are integers, the magnetic field lines close onto themselves after m toroidal and n poloidal turns. Especially for low values of m and n , this can give rise to resonances, which decrease the stability of the plasma. For this reason, q is known as the ‘safety factor’.

The plasma current is the primary heat source in the plasma; due to the finite resistivity

¹In Russian: тороидальная камера и магнитная катушка

of the plasma the heat is deposited according to Ohm's law. The temperature of the plasma can be further increased by additional heating, usually provided either by fast neutral particles or electromagnetic waves. The fast neutrals that are injected into the plasma are ionised, and transfer their energy to the plasma ions and electrons by means of collisions, thereby heating the plasma. This method can also be used to drive an additional current. The electro-magnetic waves launched into the plasma are resonant with the cyclotron motion of the ions or electrons in the magnetic field at a particular value of the magnetic field, the energy can thus be transferred to the ions or electrons in the plasma.

The heat loss from the plasma is expressed by the energy confinement time (τ_E). The energy confinement time is a crucial element in the design of a tokamak reactor. Confinement times are predicted for new machines with scaling laws based on existing machines, which take into account parameters such as machine size, magnetic field, density, heating power and operating regime.

The most accessible and promising reaction for a fusion reactor is the one which occurs between two hydrogen isotopes, deuterium (D) and tritium (T):



in which helium and an energetic neutron are formed. The deuterium can be extracted from seawater and is therefore a virtually inexhaustible fuel. Tritium can be gained from ${}^6\text{Li}$, which can be mined and is also present in sea water. The fuel supplies will be available for longer than the Sun will burn. The energy of the formed α particle (3.5 MeV) remains in the system. The energy of the fast neutron (14.1 MeV) is used to heat water and the hot water will generate electricity in a process similar to that of a steam engine. Neutrons interact with the lithium containing wall of the reactor and form tritium which is used for refuelling. The tritium is radioactive, but will be burned in the fusion process. The neutrons bombard the wall, causing it to slowly become radio-active. The activated wall material, however, has no military applications. The radio-activity decays in about 50 years to a low background level and therefore causes no significant waste disposal issues. Because the nuclear fusion reactor is inherently safe, has little or no impact on the environment and utilises a virtually inexhaustible fuel supply it holds the promise of a very attractive alternative energy source.

Concept improvement

The ITER project, that is designed to demonstrate net power multiplication ($Q > 10$), is based on the conventional tokamak (CT) design. Most progress in fusion research has, so far, been achieved using this conventional type. However, in parallel, concept improvement studies are carried out. These have led, *e.g.* to the construction of the spherical tokamak (ST). In comparison with the 'doughnut'-shaped plasma in conventional tokamaks, an ST plasma has a more cored-apple shape plasma as illustrated in figure 1.2, hence the name. Quantitatively the compactness of the torus is expressed by means of the aspect ratio (A), which is the ratio of the major radius and the minor radius ($A = R_0/a$). In the first hot plasma ($T_e > 100$ eV) ST experiments in START (Small Tight Aspect Ratio Tokamak) it was verified that this machine type combines some desirable features of other magnetically confined plasma devices, the spheromak and the Reversed Field Pinch, while still having the advantage of tokamak-like confinement and stability. Other advantages include a naturally high vertical elongation of the plasma and the absence of major current-terminating 'disruptions', an event to which the total plasma energy is lost in < 1 ms, causing high stress on the machine structure. The energy confinement times of

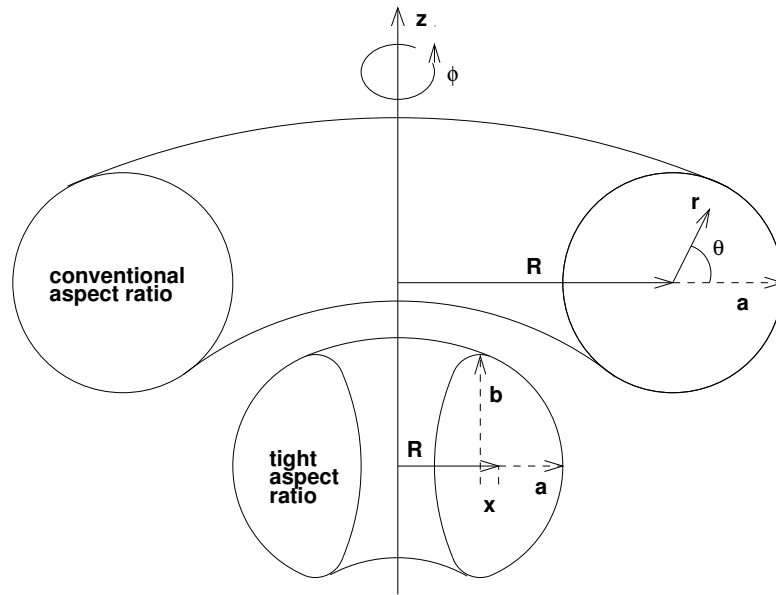


Figure 1.2: Tokamak coordinate system showing conventional (CT) and tight aspect ratio (ST) geometries.

STs are comparable to those of CTs of similar cross-section and obey the same scaling laws. Thus, the ST research contributes to the mainstream tokamak programme. The ST programme worldwide is making impressive advances, with a few machines in operation or near operation; MAST (UK), NSTX (USA), ETE (Brazil), Globus-M (Russia) and TST (Japan). The growth of the ST database leads to better understanding of plasma confinement and machine behaviour of a tight aspect ratio tokamak, and thus provides a wealth of information on the potential of the spherical tokamak as a safe, environment-friendly source of energy for the future.

1.2 The high-confinement regime

During experimental investigations a regime of improved confinement in tokamaks was established in 1982 [3]. The confinement time typically rises by factor ~ 2 in this regime. This high-confinement regime is indicated as H-mode, as opposed to the low confinement regime (L-mode). However, H-mode does not occur in all discharges in a tokamak. Access to H-mode is limited to specific plasma configurations and requires a heating power above a certain threshold. During H-mode, a steepening of the edge electron density (n_e) gradient is observed. This is generally explained as being the result of locally reduced transport, a so-called transport barrier. When this barrier appears it produces an increase in the average density on the time scale of confinement time, with some further improvement of confinement in the bulk plasma. The leading hypothesis to date for the appearance of H-mode is the reduction of turbulent transport by the shear in $\vec{E} \times \vec{B}$ flow [4].

The improvement in confinement in H-mode has certain negative aspects. Firstly, the increase in density is uncontrolled, and can lead to a transition back to L-mode. Secondly, H-mode is associated with an enhancement of impurity confinement. Both of these effects are remedied by the presence of so-called edge localised modes (ELMs). ELMs, however, are associated with a loss of confinement and pulsed heat loads. These pulsed heat loads could potentially cause problems at low aspect ratio, because of the relatively small target areas on the centre column.

The ultimate usefulness of H-mode depends on whether the benefits of improved confinement can be achieved under controlled conditions without the damaging effects of increased impurity level and buildup of α -particles in a reacting plasma.

H-mode on the spherical tokamak is a relatively unexplored regime due to the small number of ST experiments. The first H-mode on an ST was reported on START [5], where a clear improvement of confinement has been achieved. However, it fell short of scaling law predictions; furthermore, it was only found for the highest plasma currents. Modelling shows that this was associated with the relatively high neutral density in the vessel. For MAST this is predicted to be typically ~ 50 times lower than for similar plasma densities. MAST is therefore predicted to achieve longer H-mode periods of better confinement. Since the effect of the low aspect ratio on the confinement is relatively unknown, the ST will play an important role in clearing these uncertainties.

1.3 This dissertation

The connecting thread of the work discussed in this dissertation is the comparison of the high-confinement regime in the relatively unexplored spherical tokamak to that on the well known conventional tokamak. Related to this theme, a number of questions will be raised. Possibly the most obvious question and relevant question for the progress of fusion research that can be addressed concerns the performance in energy confinement of the ST in H-mode in comparison to scaling laws based on data from CTs. But before this question can be answered H-mode will need to be accessed and identified on the ST. This raises questions about the reproducibility and characteristics of the H-mode on STs, *e.g.* by what means can H-mode be accessed and can the following observations be made on STs: steepening of the edge n_e gradient, increase in density and confinement, appearance of ELMs? When observed, then more specific questions can be addressed: are pedestals formed on the T_e and n_e profiles, how do the pedestals compare to those on CTs when quantified by the stored energy in the pedestal, what is the effect of ELMs on the pedestals, edge gradients and pulsed heat loads from the plasma in ST configuration?

In order to be able to provide answers to these questions, experiments have been carried out on the Mega-Ampere Spherical Tokamak (MAST) at the UKAEA Fusion Culham laboratory in Oxfordshire, United Kingdom. Answers to many of these questions require detailed measurements of the density and temperature profiles in the plasma. For this and other reasons a Thomson scattering system has been developed on MAST. In the initial setup this system was an adjustment to the system used on START. The first measurements during H-mode revealed very steep n_e profiles but only small T_e pedestals. To study these characteristics, and other phenomena, in more detail the TS system has been upgraded to produce high-resolution measurements. This has put MAST in the unique position to study the full plasma profiles during H-mode in high resolution. The system has, amongst others, been used to study ELM phenomena. In addition a diagnostic based on Balmer- α emission from the plasma edge has been developed to study the temporal behaviour of the edge n_e gradient during ELMy H-mode.

This dissertation consists of nine chapters, of which this introduction is the first. Chapter 2 gives a description of the spherical tokamak and compares it with the conventional tokamak. This is followed by an outline of the MAST machine and its diagnostics, from which the data that will be used throughout this dissertation originates, in Chapter 3, and by a description of the theory of Thomson scattering in Chapter 4. Chapter 5 presents the initial measurements of the electron density profiles using a Thomson scattering system, which did not yet have the

full resolution, during ELM-free H-mode and presents a transport model used to describe the behaviour of the measured density profiles. This system was upgraded to a high-resolution system which is presented in Chapter 6. This system provides one measurement of the electron density per plasma discharge. Time resolved measurements of the outboard density gradient were provided by a linear D_α camera system, of which the calibration using measurements of high-resolution TS system is presented in Chapter 7. Chapter 8 describes H-mode in MAST and goes into the details of H-mode access, H-mode density and temperature profiles, power exhaust during ELMs and pedestal energy scaling. An evaluation and discussion of the work presented in this dissertation are given in Chapter 9.

1.4 Publications

The work on the original and high-resolution Thomson scattering diagnostics has yielded many results. In this dissertation, the work dealing with the development of the diagnostics and the study on profiles and gradients during H-mode are described; many other results using the diagnostic have been published elsewhere. Below a list of related publications is given in which the author of this dissertation appears as first author or as co-author. The list contains many publications related to the results taken from the TS diagnostics on MAST, but also contains related work. For clearness the list is divided into journal contributions and conference contributions. The publication marked with ► is included as Chapter 5 in this dissertation.

Journal contributions

- ► ‘Measurement and modelling of H-mode density profiles with edge density ‘ears’ on the MAST spherical tokamak’,
E.R. Arends, M.J. Walsh and M.R. Tournianski, for publication in *Plasma Physics and Controlled Fusion*, March 2003.
- ‘Electron density gradients from linear D_α camera’,
M.R. Tournianski, P.G. Carolan, N.J. Conway, E.R. Arends and M.J. Walsh, *Review of Scientific Instruments*, **74** (3), March 2003.
- ‘Combined visible and infrared Thomson scattering on the MAST experiment’,
M.J. Walsh *et al.* among whom E.R. Arends. *Review of Scientific Instruments*, **74** (3), March 2003.
- ‘Confinement and exhaust in the Mega Ampère Spherical Tokamak’,
G.F. Counsell *et al.*, among whom E.R. Arends, *Plasma Physics and Controlled Fusion*, **44** (12B), December 2002, 23-37.
- ‘H-mode access and performance in the Mega-Amp Spherical Tokamak’,
R. Akers *et al.* among whom E.R. Arends, *Physics of Plasmas*, **9**, (9), September 2002, 3919-3929.
- ‘A review of plasma boundary phenomena in the Mega Ampere Spherical Tokamak’,
G.F. Counsell *et al.* among whom E.R. Arends, accepted for publication in *Journal of Nuclear Materials*.

- ‘Results from the MAST spherical tokamak’,
A. Sykes *et al.* among whom E.R. Arends, accepted for publication in *Fusion Engineering & Design*.
- ‘First physics results from the MAST Mega-Amp Spherical Tokamak’
A. Sykes *et al.* among whom E.R. Arends. *Physics of Plasmas* **8**, 2101 (2001).
- ‘H-mode plasmas in the MAST spherical tokamak’,
A.R. Field *et al.* among whom E.R. Arends, *Plasma Physics and Controlled Fusion*, **44**, (5A), May 2002, A113-A121.
- ‘L-H transition in the Mega-Amp Spherical Tokamak’,
R. Akers *et al.* among whom E.R. Arends, *Physical Review Letters*, **88** (3), 2002, 035002-1-035002-4.
- ‘First results from MAST’,
A. Sykes *et al.* among whom E.R. Arends, *Nuclear Fusion* **41** (10), 2001, 1423-1433.
- ‘Filamentation in the RTP tokamak plasma’,
M.N.A. Beurskens, N.J. Lopes Cardozo, E.R. Arends, C.J. Barth and H.J. van der Meiden, *Plasma Physics and Controlled Fusion*, **43**, (1), January 2001, 13-38 .

Conference contributions

- ‘Edge n_e gradients from the linear D_α camera’,
M.R. Tournianski *et al.* among whom E.R. Arends, Annual Spherical Tokamak Workshop, Princeton, USA, November 2002.
- ‘Overview of Recent Experimental Results on MAST’,
B. Lloyd *et al.* among whom E.R. Arends, *Proceedings of the 19th IAEA Fusion Energy Conference*, Lyon, France, 14-19 October 2002.
- ‘H-mode access physics in MAST’,
P.G. Carolan *et al.* among whom E.R. Arends, *Proceedings of the 19th IAEA Fusion Energy Conference*, Lyon, France, 14-19 October 2002.
- ‘Stability at high performance in the MAST spherical tokamak’,
R.J. Buttery *et al.* among whom E.R. Arends, *Proceedings of the 19th IAEA Fusion Energy Conference*, Lyon, France, 14-19 October 2002.
- ‘Improved H-mode access with inboard gas puffing’,
A.R. Field *et al.* among whom E.R. Arends, *Proceedings of 29th EPS Conference on Controlled Fusion and Plasma Physics*, Montreaux, June 2002, ECA Vol. **26B**.
- ‘Energy confinement in ELMy H-mode on MAST’,
M. Valovič *et al.* among whom E.R. Arends, *Proceedings of 29th EPS Conference on Controlled Fusion and Plasma Physics*, Montreaux, June 2002, ECA Vol. **26B**.
- ‘The effect of magnetic configurations on H-mode in MAST’,
H. Meyer *et al.* among whom E.R. Arends, *Proceedings of 29th EPS Conference on Controlled Fusion and Plasma Physics*, Montreaux, June 2002, ECA Vol. **26B**.

- ‘Electron temperature and density profiles from 300 point Thomson scattering in MAST plasmas’,
S.K. Nielsen *et al.* among whom E.R. Arends, IOP Conference on Plasma Physics, Belfast, UK, March 2002.
- ‘Electron transport in the MAST spherical tokamak’,
E.R. Arends *et al.*, CPS Conference on Plasma Physics and Radiation Technology, Lunteren, the Netherlands, March 2002.
- ‘Confinement in L and H-Mode MAST Plasmas’,
R. Akers *et al.* among whom E.R. Arends, *Proceedings of the 28th EPS Conference on Controlled Fusion and Plasma Physics*, 18-22 June 2001, Funchal, Portugal, **28A**, 581-584.
- ‘Impurity radiation & transport in the MAST tokamak’,
I. Lehane *et al.* among whom E.R. Arends, 43rd Annual Meeting of the Division of Plasma Physics of the APS, Long Beach, California, USA, October-November 2001, abstract in *Bulletin of The American Physical Society* 46, 251 (2001).
- ‘Neoclassical tearing mode physics in the spherical tokamak’,
R.J. Buttery *et al.* among whom E.R. Arends, 43rd Annual Meeting of the Division of Plasma Physics of the APS, Long Beach, California, USA, October-November 2001.
- ‘Initial results from the MAST pellet injector’,
C. Ribeiro *et al.* among whom E.R. Arends, ST Workshop, Inpe, Brazil, July 2001.
- ‘Electron transport during H-mode on MAST’,
E.R. Arends, M.J. Walsh, N.J. Lopes Cardozo and the MAST and NBI teams, *Proceedings of the 28th European Physical Society Conference on Controlled Fusion and Plasma Physics*, 18-22 June 2001, Funchal, Portugal, **25A**, 589-592.
- ‘Electron transport during H-mode on MAST’,
E.R. Arends, M.J. Walsh, P.G. Carolan, N.J. Lopes Cardozo and A. Sykes, 28th IOP Conference, UMIST, Manchester, UK, April 2001.
- ‘On the neutral beam heating of spherical tokamak plasmas’,
R. Akers *et al.* among whom E.R. Arends, *Proceedings of the 18th IAEA Fusion Energy Conference*, Sorrento, Italy, 4-10 October 2000.
- ‘Development of Thomson scattering systems for the MAST tokamak’,
M.J. Walsh *et al.* among whom E.R. Arends, 27th Annual IOP Plasma Physics Conference, Brighton, UK, March 2000.
- ‘Measurement of the effective ion charge in the MAST spherical tokamak’,
E.R. Arends *et al.*, 27th Annual IOP Plasma Physics Conference, Brighton, UK, March 2000.
- ‘Overview of first results from MAST’,
M. Gryaznevich for MAST team, among whom E.R. Arends, *Proceedings of the 27th EPS Conference on Controlled Fusion and Plasma Physics*, Budapest, Hungary, June 2000.

- ‘Small scale structures in the RTP T_e profiles’,
E.R. Arends *et al.*, *Proceedings of the 26th EPS Conference on Controlled Fusion and Plasma Physics*, June 1999, Maastricht, the Netherlands, **23J**, 629-632.
- ‘Small scale structures in the RTP tokamak’,
E.R. Arends *et al.*, CPS conference on Plasma Physics & Radiation Technology, Lunteren, the Netherlands, 2001.
- ‘Electron transport studies in the Rijnhuizen Tokamak RTP’,
N.J. Lopes Cardozo *et al.* among whom E.R. Arends, IAEA-F1-CN-69/EX7/4.

Bibliography

- [1] International Energy Agency. Key World Energy Statistics from the IEA. Paris, 2002.
- [2] M. Keilhacker *et al.* High fusion performance from deuterium-tritium plasmas in JET. *Nuclear Fusion*, 39(2).
- [3] F. Wagner *et al.* Regime of improved confinement and high beta in neutral beam heated divertor discharges of the ASDEX tokamak. *Physical Review Letters*, 49, 1982.
- [4] H. Biglari, P.H. Diamond, and P.W. Terry. Influence of sheared poloidal rotation on edge turbulence. *Physics of Fluids B*, 2:1, 1990.
- [5] A. Sykes *et al.* H-Mode operation in the START spherical tokamak. *Physical Review Letters*, 84(3):495–498, January 2000.

Chapter 2

Spherical tokamak

The spherical tokamak provides the extension of tokamak scaling laws to more extreme geometries. The first hot-plasma spherical tokamak START has confirmed numerous theoretical advantages of the more compact design. The promising concept of the ST is extended to a larger scale with the MAST and NSTX device. This chapter provides an overview of spherical tokamak physics.

2.1 Introduction

The spherical tokamak (ST) is an extension of the conventional tokamak design to a more compact geometry. This extension allows the production of more compact plasmas. The numerous theoretical advantages of the concept of ‘spherical tori’ were outlined by Peng and Strickler in 1986 [1]. Because of the similar values of the safety factor q it was suggested by Robinson [2] that the ST would exhibit confinement and MHD¹ stability typical for tokamaks. Moreover, the ST would also possess various favourable characteristics inherent in spheromaks and reversed field pinch devices. Among these predicted advantages are a natural elongation of the plasma in vertical direction ($\kappa \sim 2$), high efficiency expressed by the toroidal beta (β) and so-called ‘isodynamic’ regions providing improved confinement. These predictions have been confirmed experimentally, initially in the START (Small Tight Aspect Ratio Tokamak), the first spherical tokamak to produce a high temperature (> 100 eV) plasma. These promising results have stimulated the development and construction of the next generation of spherical tokamaks, including GLOBUS-M, MAST, NSTX, ETE and TST.

The new geometry posed new problems and also served as an important test of magnetic confinement theory. Theoretical studies stimulated by the experimental results indicate that spherical tokamaks may have additional advantages in terms of stability and plasma confinement. The next generation of large spherical tokamaks is now operational with important specific aims: firstly, to provide experimental data on confinement in new and overlapping parameter regimes to test models and scaling laws; and secondly to improve the understanding of the physics of toroidal plasma confinement systems due to the inclusion of a more extreme plasma geometry. In addition, the spherical tokamak has potential in itself to indicate the way to achieving high beta compact fusion facilities having various applications such as material testing and power production. References [2–4] also give overviews of spherical tokamak physics and issues, some of which are highlighted here.

¹Magnetohydrodynamics (MHD) is a mathematical description of the plasma and magnetic field, which treats the plasma as an electrically conducting fluid. It is often used to describe relatively large-scale properties of the plasma.

2.2 The role of the ST in confinement scaling

The role of the aspect ratio in the scaling of the global confinement is largely undetermined from the present international database, and can be important in determining the benefits of even modest changes in aspect ratio. Addition of ST confinement data to the databases increases the inverse aspect ratio ($\epsilon = a/R$) operation range: the international database features the range $0.2 < \epsilon < 0.37$, while MAST typically operates at $\epsilon \approx 0.7$. This increase of the ϵ range could help the choice of scaling parameters and could lead to a more compact design of a reactor like ITER. Confinement data from STs could also reduce the uncertainty in performance: the statistical confidence in the prediction, and in the exponent of the aspect ratio in the power-law scaling, increases as the spread of the database increases.

H-mode operation has been established in MAST [5, 6]. First analysis [6] shows that in contrast to START, H-mode discharges in MAST exhibit a clear increase in confinement even at low currents. Figure 2.1 shows a comparison of START and MAST confinement data with the IPB98(y,2) scaling law [7] developed for ITER based on the results of devices with conventional aspect ratios. The data is close to the prediction of the scaling law and thus MAST confinement data scales to a first order approximation as confinement data of conventional tokamaks.

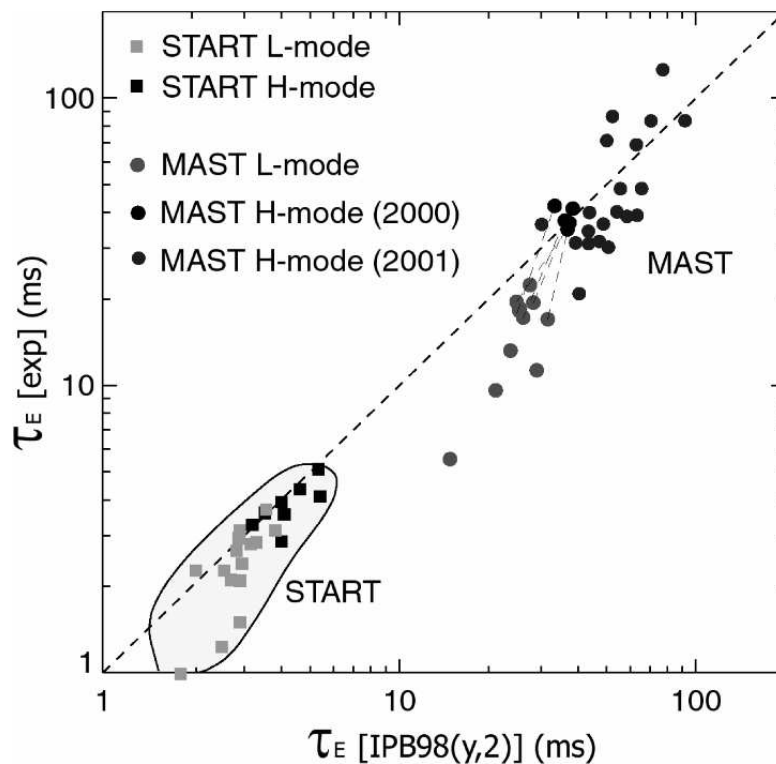


Figure 2.1: Energy confinement time in MAST compared with the prediction of the IPB98(y,2) scaling [8]. Results from the START tokamak are shown for comparison.

2.3 Results of ST experiments

Aspect ratio

A fundamental difference to the conventional design is the low aspect ratio $A = 1/\epsilon$ of the spherical tokamak, being close to unity. The difference in aspect ratio between the two types of tokamak is illustrated in figure 1.2. The low aspect ratio has the advantage of reducing the toroidal field at the plasma centre required to stabilise a given plasma current by usually a factor of 10 compared to conventional tokamaks. While the magnetic surfaces in the plasma centre are similar, at the plasma edge the field lines are mainly concentrated in the inner regions of high magnetic field, which leads to a substantial increase in safety factor q .

Efficiency β

A characteristic of the efficiency of a fusion device is the ratio β of the plasma thermal energy over the magnetic energy. The value of β is limited to $\beta < \beta_N I_N$, where β_N is the so-called Troyon factor [9] and $I_N = I_p/aB_\phi$ the normalised plasma current. Because of the high safety factor q , the normalised current I_N can reach high levels before q falls below 2. This implies that high values of β may be achieved. The β limit implies that β is also improved at high elongation ($\kappa = b/a$) and triangularity ($\delta = x/a$), all of which are automatically improved in the ST with respect to the conventional tokamak design. Furthermore, at high β values, the associated diamagnetic effect compensates for the paramagnetic effect produced by the high normalised current, so that a magnetic well may appear on the $|B|$ profile. This improves plasma stability and also, by modifying the trajectories, reduces the fraction of trapped particles and consequently enhances the bootstrap current generation efficiency - potentially up to 100% of the total plasma current required for fusion [10]. On START $\beta = 40\%$ was obtained during neutral beam heated plasmas. This is more than three times the highest value obtained in a conventional tokamak. The ratio β_N exceeded the conventional Troyon limit ($\beta_N = 3.5$) and it was demonstrated that these high beta values ($\beta > 30\%$ and $\beta_N > 4$) can be sustained over times several times longer than the energy confinement time. Research on larger tokamaks with hotter, less collisional plasmas will determine whether these high beta regimes can be sustained.

Disruptions and halo currents

One of the problems associated with the conventional tokamak is the possibility of the occurrence of the ‘major disruption’, an event to which the total plasma energy is lost within 1 ms. Major disruptions can cause significant problems in a fusion power plant. STs appear resilient to the major disruptions observed on conventional tokamaks. But the range of operating parameters in START in high density low- q regime was usually limited by an effect known as internal reconnection of magnetic field lines, or an internal reconnection event (IRE). This effect appears to be caused by low- m MHD (magnetohydrodynamics) modes, but is also related to other causes. A consequence of the IRE is a flattening of the current profile. This significantly increases the vertical elongation of the low aspect ratio plasma (thus increasing q), but without bringing the plasma into strong contact with material surfaces. Moreover, the reduction in the plasma inductance leads to an appreciable increase in plasma current, which counteracts any decrease in major radius and thereby prevents intensified interaction between the plasma and the inner cylinder of the chamber, therefore avoiding a major disruption. This resilience against major disruptions would be a major advantage in future large facilities with high plasma

currents and is another important property that needs to be studied in the next generation of spherical tokamaks.

If the feedback system of a tokamak does not operate during the termination of the discharge, vertical displacement of the plasma and current dumping can induce halo currents flowing through the plasma and its surrounding conductors. The toroidal asymmetry of the halo currents generates lateral tilting forces which act on the vessel with possible consequences. Results obtained from conventional tokamaks indicate that the total halo current may reach 40% of the plasma current with appreciable toroidal asymmetry. Results on spherical tokamaks show that the halo currents in the central column are very small, have small asymmetry, and thus should not present problems for the next generation of tokamaks.

Power handling

Due to the limited size of the centre column of the ST problems could be expected concerning the power exhaust of fusion plasmas. However, the spherical tokamak features a significant inboard/outboard power exhaust asymmetry. This arises due to the outer plasma surface being greater (~ 4 times) than the inner area, and the large difference in the poloidal magnetic field across the plasma radius, which results in a large power gradient and flux to the outboard surface. Together these considerably reduce the power loading on the inner surface components, including the central column, thereby helping to reduce material wear and thus increase machine lifetime.

Potential problems

Potential problems with the spherical tokamak design arise from the compact geometry and subsequent constraints placed on the central column. Due to the limited space available at the centre of the machine, the solenoid used to drive the toroidal current is necessarily small, giving only a limited flux swing with which to maintain current induction; therefore, alternative, non-inductive current drive mechanisms need to be exploited to achieve long lived discharges. These could be provided by using neutral beam or wave injection, or by the pressure driven 'bootstrap current', a diffusion driven current carried by trapped particles [11]. An additional problem associated with the central column is the high neutron flux that it will be exposed to under burning plasma conditions; this puts significant constraints on the material design and the operational lifetime of this component. Methods for full operation without use of any central solenoid are now under investigation.

2.4 Conclusions

Although research is still at an early stage for spherical tokamaks, the first ST, the START experiment at Culham, was able to demonstrate or indicate many of the above advantages over the large aspect ratio design. This machine greatly exceeded expectations and, as such, has prompted the development of a large range of new ST's, including two large sized machine: MAST (Mega-Ampere Spherical Tokamak) and NSTX (National Spherical Tokamak Experiment). Combined, these will allow a detailed study of the many aspects of spherical plasma physics - looking at the effects of lower aspect ratio, high magnetic fields, longer pulses, increased heating power and larger plasmas. These could help to establish the significance of the spherical tokamak design to the realisation of an economically viable fusion reactor.

Bibliography

- [1] Y-K.M. Peng and D.J. Strickler. Features of spherical torus plasmas. *Nuclear Fusion*, 26(6), 1986.
- [2] D.C. Robinson. *Fusion Energy and Plasma Physics*, page 601, 1987.
- [3] A. Sykes. Physics of spherical tokamaks. *Technical Physics*, 44(9):1047–1053, September 1999.
- [4] A.W. Morris et al. The role of the spherical tokamak in clarifying tokamak physics. *Plasma Physics and Controlled Fusion*, 41:B191–B207, 1999.
- [5] M.P. Gryaznevich. First results from MAST. *Proceedings of the 27th EPS Conference on Controlled Fusion and Plasma Physics*, 2000.
- [6] A. Sykes et al. First results from MAST. *Nuclear Fusion*, 41(10):1423–1433, October 2001.
- [7] ITER Physics Expert Groups on Confinement and Transport and Confinement Modelling and Database, ITER Physics Basis Editors, ITER EDA, and Naka Joint Work Site. Plasma confinement and transport. *Nuclear Fusion*, 39(12):2175–2249, 1999.
- [8] R. Akers et al. L-H transition in the Mega-Amp Spherical Tokamak. *Physical Review Letters*, 88(3):035002–1–035002–4, 21 January 2002.
- [9] F. Troyon et al. *Plasma Physics and Controlled Fusion*, 26:209, 1984.
- [10] W.A. Houlberg et al. *Physics of Plasmas*, 4:3220, 1997.
- [11] J. Wesson. *Tokamaks*. Clarendon Press, Oxford, 1987.

Chapter 3

MAST machine & diagnostics

The MAST machine is a spherical tokamak device that became operational in December 1999. Additional heating is provided by two neutral beam injectors and a radio-frequency heating system. An extensive range of internal and external diagnostics have been installed to provide good plasma monitoring. This chapter provides an overview of the MAST machine and its diagnostics.

3.1 Introduction

The MAST (Mega-Ampere Spherical Tokamak) device [1] is designed to test the promising results obtained from the pioneering START (Small Tight Aspect Ratio Tokamak) experiment [2] operational at Culham from 1991 to 1998. MAST provides a test of the spherical tokamak (ST) concept in a large modern tokamak. The plasma cross-sections are comparable in size to those of medium sized tokamaks with conventional aspect ratio like ASDEX-U and DIII-D. Key parameters of MAST are given in table 3.1.

MAST achieved first plasma in December 1999. Since that time the central solenoid has been rewound with improved insulation, a fully instrumented centre column has been fitted and two beamlines have been installed and operation at up to 2.9 MW has been demonstrated. Extensive internal diagnostics have been installed to provide accurate magnetic reconstruction, to measure halo currents and divertor target heat loads, etc. The wide range of external diagnostics are shown in figure 3.2, of which the ones most important for this dissertation are described here.

3.2 MAST machine

The MAST vessel consists of a stainless steel vacuum tank of cylindrical shape with a diameter of 4.0 m and height of 4.4 m (see figure 3.1). The vacuum tank contains the poloidal field coil set. The toroidal field coil limbs are external to the vacuum vessel. The centre column contains the toroidal field centre column with the central solenoid wound on it. In order to achieve low aspect ratio plasmas the centre column has the limited dimension of 0.4 m diameter. The toroidal field on axis is usually in the range $0.35 \text{ T} < B_\phi < 0.55 \text{ T}$ but, due to the low aspect ratio, the toroidal field varies between around 2 T at the inboard mid-plane to 0.25 T at the outboard, the strong variation across the plasma being a distinct feature of the spherical tokamak.

The plasma can be induced in the manner usually employed in tokamaks, by the use of flux from the central solenoid. This method is known at MAST as ‘direct induction’. More usually,

	Designed	Achieved
Minor radius a (m)	0.65	0.65
Major radius R (m)	0.85	0.85
Aspect ratio R/a	≥ 1.3	1.3
Elongation κ	≤ 3	5
Plasma current (MA)	2	1.35
Toroidal rod current (MA)	2.2	2.2
Toroidal field at R (T)	0.52	0.52
Auxiliary heating		
P_{NBI} (MW)	5	2.9
P_{ECRH} (MW)	1.5	0.6
Pulse length (s)	1-5	0.7
Bake-out temperature ($^{\circ}\text{C}$)	200	150
Plasma volume (m^3)	10	10

Table 3.1: Typical MAST parameters.

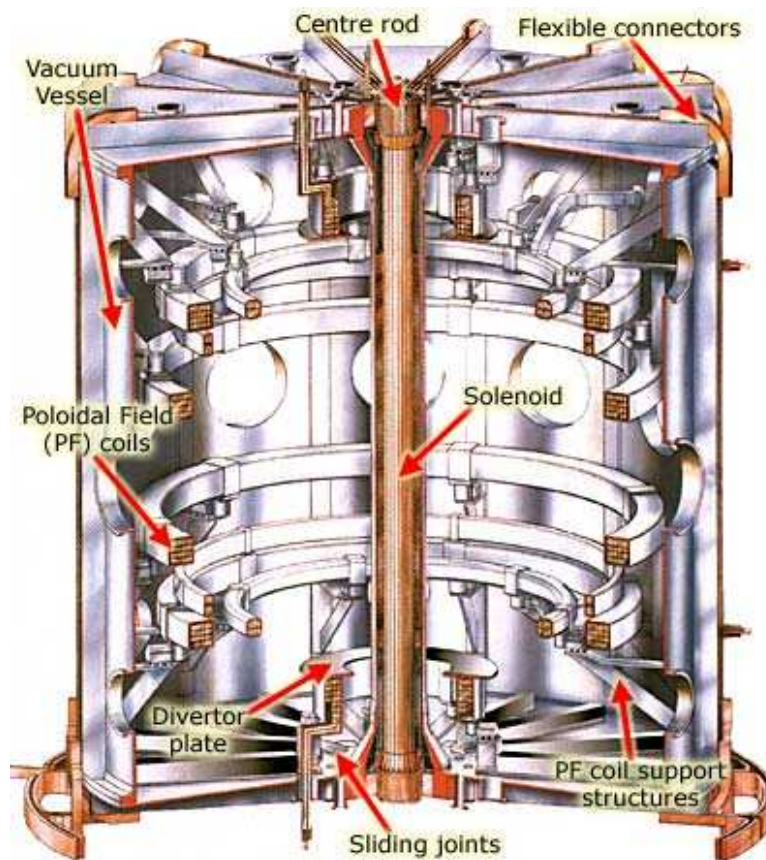


Figure 3.1: Overview of the toroidal and poloidal field coils inside the MAST vessel.

the plasma in MAST is formed by a novel technique called ‘merging-compressing’, pioneered on START, whereby the plasmas can be produced without the need of the flux from the central solenoid. This technique utilises a special feature of the MAST design, namely that the poloidal field coils are inside the vacuum vessel, as shown in figure 3.1. The process involves the use of flux from a pair of the large radius poloidal field coils to initiate the plasma.

3.3 Auxiliary heating & fuelling

NBI

The MAST neutral beam injector (NBI) system consists of two beamlines on loan from Oak Ridge National Laboratory (ORNL) allowing co-injection of fast hydrogen and deuterium neutrals at a tangency radius close to the plasma centre. To date, the beams have operated up to 2.9 MW using 40 keV hydrogen and deuterium injection. They are designed to deliver 5 MW of 70 keV deuterium injection. The pulse length of both beams is currently ~ 300 ms, but this will be extended to ~ 400 ms in the near future.

ECRH

MAST is equipped with a 60 GHz electron cyclotron resonance heating (ECRH) system. Seven ECRH lines, each producing 200 kW, are connected for pre-ionisation and heating studies. A new quasi-optical launcher has been developed and installed on MAST (September 2002) for initial studies of plasma heating with the use of electron Bernstein waves (EBW). The new launcher consists of an array of mirrors which are independently steerable in poloidal ($\pm 15^\circ$) and toroidal ($\pm 25^\circ$) directions. The steering ability allows for the employment of the O-X-B mode conversion mechanism for EBW excitation in overdense plasmas, which is possible only within the narrow angular window around the optimal launch direction.

Pellet injector

The pneumatic 8 pellet gas gun injector (built at Risø) [3] used in MAST has previously been operated in the former RTP device [4]. The injector has been modified to increase the pellet size (necessary because of the larger MAST plasma volume relative to RTP). A variety of cylindrical pellet sizes are available, *i.e.* two small ($\phi_{pel} = l_{pel} = 1.08$ mm), three medium ($\phi_{pel} = l_{pel} = 1.36$ mm), and two big ($\phi_{pel} = l_{pel} = 1.71$ mm) pellets (ϕ_{pel} is the diameter and l_{pel} the length) with inventory N_p 0.5, 1, 2×10^{20} atoms of deuterium, respectively. The pellets are injected slightly non-radial (to avoid pellets hitting the graphite tiles which cover the central column) from the low field side (LFS). Several pellet dedicated diagnostics have already been commissioned [5]. Top launch and impurities doped pellet ($D^+ \sim 2 - 4\%$ Ar/Ne/N₂ etc.) are planned for 2003.

3.4 Diagnostics

Magnetics

Approximately 650 individual coils and loops have been installed in the vacuum vessel in order to measure halo currents, magnetic field fluctuations and vertical magnetic flux and to provide information for plasma equilibrium reconstruction and real time plasma control.

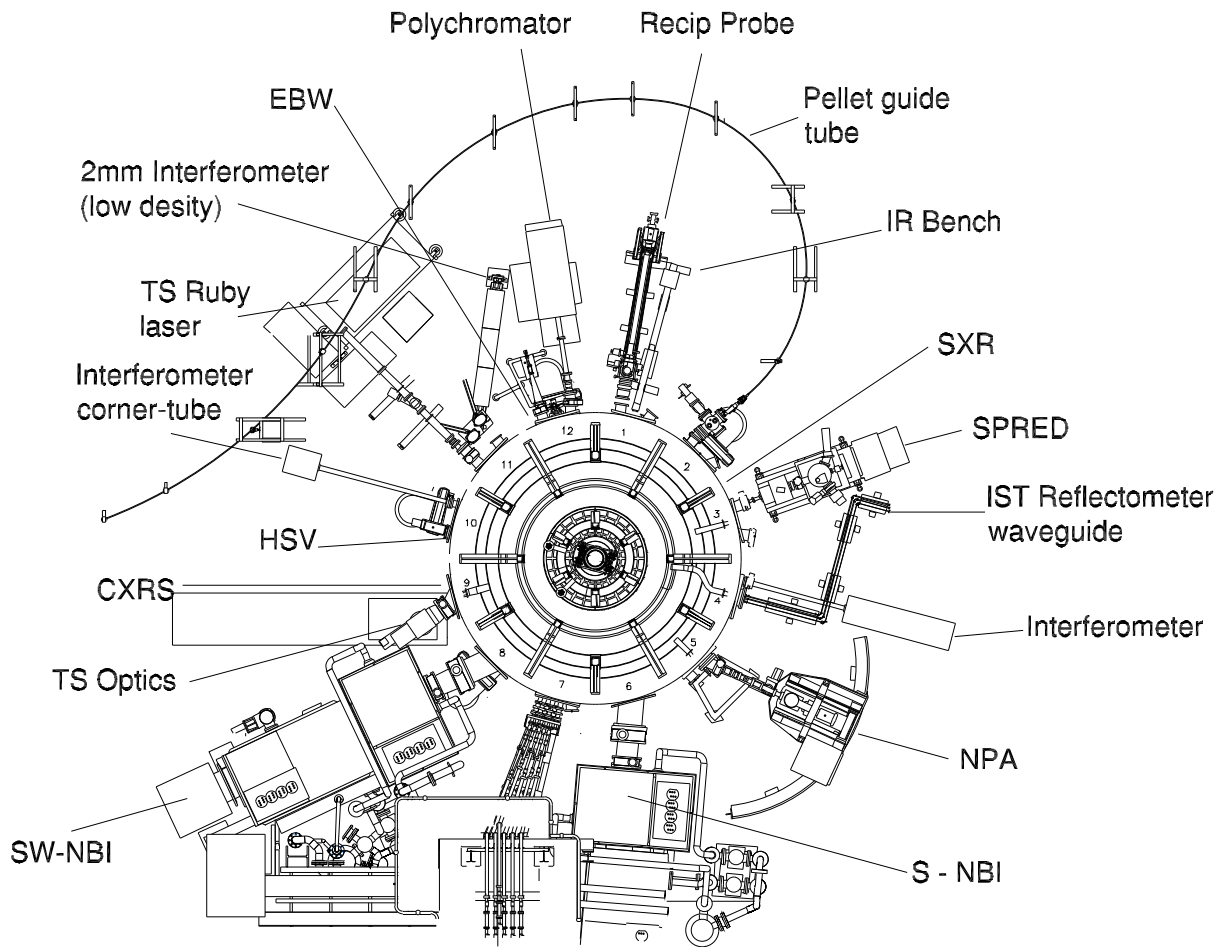


Figure 3.2: Overview of the MAST machine and diagnostics.

EFIT

The equilibrium reconstruction code EFIT [6] (Equilibrium Fitting) uses the magnetic data to determine plasma position, geometry and currents, plasma β and stored energy. The Grad-Shafranov equilibrium equation, which describes the force balance in a plasma, is solved using the available measurements as constraints on the toroidal current density. Since the current also depends on the solution of the equation, the poloidal flux function, this is a nonlinear optimisation problem. The equilibrium constraint allows the two-dimensional current density to be represented by two one-dimensional stream functions (functions only of flux), which significantly reduces the complexity of the problem.

Soft X-ray camera

The horizontal soft X-ray camera (SXR) installed on MAST comprises two multi-channel photodiode detectors which view the plasma through two $3 \text{ mm} \times 1 \text{ mm}$ pinholes. $12.5 \mu\text{m}$ Beryllium foils are mounted behind each pinhole to act as both vacuum windows between the vessel and the camera and filters to prevent low energy line radiation from entering the camera. There are 32 active channels with an additional four passive channels used for noise offset and correction purposes. The three central channels from each array overlap.

CO₂ interferometry

The system comprises two interferometers. One (CO₂) operates at 10.6 μm and is sensitive both to the plasma electron density and to vibration. The other (HeNe) operates at 633 nm and is only sensitive to vibrations. Subtracting the two signals yields the electron density, integrated along the line of sight. The line of sight passes twice through the vessel, passing close to the centre column, at a tangency radius of 240 mm, and thus the total path length is a little over 8 times the minor radius of the plasma. The time resolution is 1 μs , but the signal is usually digitised at 20 μs intervals. The error on the line-integrated density is typically $0.2 \times 10^{19} \text{ m}^{-2}$. The CO₂ interferometer is also used for absolute calibration of the electron density profiles as measured by Thomson scattering.

D _{α} chords

The D _{α} diagnostic consists of a series of horizontal and vertical lines of sight. The system uses H _{α} filtered photomultiplier tubes. Lenses and optical fibres are used to ‘pipe’ the H _{α} /D _{α} light from the plasma to the photomultiplier tubes. Unless otherwise stated, the D _{α} emission from the upper X-point region, which is generally the brightest region, will be shown throughout this dissertation.¹

Linear D _{α} camera

The linear D _{α} camera diagnostic [7] consists of two linear photo diode arrays covering the inboard and the outboard of the plasma. The inboard camera contains 1024 pixels and covers the inner plasma region and the centre column. The outer camera contains 256 pixels and covers the major radial distance from 1.0 m to 1.5 m. The inboard camera has a time resolution of 0.5 μs , the outboard camera 1.0 μs . For both cameras the signal is generally integrated over 1.02 ms, giving a sampling rate of ~ 1 kHz. Data from the linear D _{α} camera is *e.g.* used to derive edge electron density gradient (see Chapter 7).

Thomson scattering

Two Thomson scattering systems are currently operational on MAST [8]. The first measures the electron temperature and density profile at ~ 300 spatial points at high resolution ($\sim 1\%$ of the minor radius) at one time point in the discharge using a high energy (~ 10 J) ruby laser and a TV system detection system (see Chapter 6). The second system uses four 50 Hz Nd:Yag lasers and a range of polychromators and provides 200 Hz profile measurements at 19 spatial positions. Both systems measure the full plasma diameter along a horizontal chord at the midplane of the vessel. The beam paths are quasi-coaxial, share much of the same input and collection optics and both systems avail of a common laser dump. This dissertation focusses on the use of the high-resolution system and data.

Neutral particle analyser

The basic function of the single chord $\vec{E} \parallel \vec{B}$ neutral particle analyser (NPA) is to measure the flux of neutrals originating from charge-exchange reactions within the plasma [9]. Using electromagnetic focusing fields, these fluxes can be resolved according to particle mass and

¹The position of the upper X-point is indicated in figure 8.4

energy, thus allowing the determination of ion velocity distribution functions for the different hydrogen isotopes within the plasma. The energy spectra are often dominated by the fast, non-thermal, ions. Under certain circumstances the fluxes can also be used to determine core ion temperatures.

Charge-exchange recombination spectroscopy

A dual multi-chord Doppler spectrometer system measures the charge-exchange recombination (CXR) spectra produced by excited carbon impurities upon interaction with injected beam neutrals [10]. The diagnostic consists of two viewing fans, of twenty lines of sight each, that collect data across opposite sides of the plasma. This provides a good measurement of the background emission and the active emission due to the neutral particle beams. The collection optics consist of bundles of four 400 μm optical fibres per line of sight. These are connected to their respective 1 m Czerny-Turner spectrometer with a holographic grating coupled to a single CCD camera. The C^{5+} carbon line ($\lambda = 529.05 \text{ nm}$, $n = 8 \rightarrow 7$) is selected for study, because the surrounding wavelength region is relatively free of additional, interfering emission lines. Also, because the electron-impact ionisation rate is reduced for high- n transitions, CXR is the dominant emission process, further simplifying analyses. Although CXR dominates in the core, the background emission can be much greater in the vicinity of the edge, thus masking the radiation originating from the core.

Langmuir probes at the strike points

MAST is equipped with high spatial resolution, flush-mounted Langmuir probe arrays (576 probes in total) covering all four strike point regions on the divertor target plates [11]. The probe arrays are upper and lower symmetrically arranged. The inboard strike points fall on the centre column, which is protected by graphite tiles, while outboard strike points fall on a series of radial divertor ribs. In normal mode, which has an average time resolution of 1 ms, the full length of the plasma is covered. A second probe operation mode, the so-called ‘ultra-fast mode’, is developed in order to catch very fast plasma events such as ELMs for short time periods. The temporal resolution of probe data in this mode increases up to 65 μs , which is fast enough to produce ~ 10 data points during an ELM event.

Bibliography

- [1] A.C. Darke et al. MAST: A Mega Amp Spherical Tokamak. *Fusion Technology*, pages 799–802, 1994.
- [2] A. Sykes, NBI the START, and Theory teams. *Nuclear Fusion*, 39:1271, 1999.
- [3] H. Sørensen, B. Sass, K-V. Wieseberg, A.A.M. Oomens, G. van Dijk, and A.J.H. Tielemans. A multishot pellet injector for RTP. In *Proceedings of the Seventeenth Symposium on Fusion Technology, Rome, Italy*, volume 1, pages 647–650, 1992.
- [4] J. de Kloe, E. Noordermeer, N.J. Lopes Cardozo, and A.A.M. Oomens. Fast backward drift of pellet ablatant in tokamak plasmas. *Physical Review Letters*, pages 2685–2688, 1999.

- [5] C. Ribeiro et al. Pellet injection on START and MAST. *Fusion Engineering and Design*, 58-59:319–324, 2001.
- [6] L.L. Lao, H. St. John, R.D. Stambaugh, A.G. Kellman, and W.W. Pfeiffer. *Nuclear Fusion*, 25:1611, 1985.
- [7] M.R. Tournianski, P.G. Carolan, N.J. Conway, E.R. Arends, and M.J. Walsh. Use of 1D D_{α} camera to measure edge electron density gradients. *Review of Scientific Instruments*, 73(3), March 2003.
- [8] M.J. Walsh et al. Combined visible and infrared Thomson scattering on the MAST experiment. *Review of Scientific Instruments*, 74(3), March 2003.
- [9] C. Byrom. *Thermal & Fast Ion Behaviour in the MAST Experiment*. PhD thesis, Department of Physics, University of Manchester Institute of Science and Technology, Manchester, 2002.
- [10] M. McGrath. *Charge-exchange spectroscopy on the MAST tokamak*. PhD thesis, National University of Ireland, University College, Dublin, March 2003.
- [11] J-w. Ahn. *Investigations of the Boundary Plasma in the MAST tokamak*. PhD thesis, Imperial College of Science, Technology and Medicine, United Kingdom, 2002.

Chapter 4

Thomson scattering theory

This chapter presents a summary of the derivation of the incoherent Thomson scattering spectrum as result of the scattering of electromagnetic waves by free electrons.

4.1 Introduction

Thomson scattering (TS) is one of the available methods to measure the electron temperature (T_e) and density (n_e) in hot plasmas. It is based on a measurement of the spectrum of photons that are scattered by the free electrons in the plasma. It offers excellent accuracy and spatial resolution, but it is characterised by poor time resolution. It has the potential of being absolutely calibrated and being independent of any other measurement.

MAST is equipped with a high-resolution TS diagnostic that is designed for plasmas with a core temperature of $T_e > 1$ keV. Therefore, relativistic effects have to be taken into account in the determination of the scattering spectrum.

In this chapter only incoherent Thomson scattering is considered. Correlated scattering of light on the electrons in the plasma can only take place with wavelengths above a certain scale length, the Debye length λ_D . The wavelength of the light source used in the TS diagnostic on MAST is 694.3 nm and is therefore well below $\lambda_D \approx 3 \times 10^{-5}$ m in the plasma, so that the scattering process is to be considered as incoherent [1].

This chapter presents the derivation of an analytical expression for the power distribution of the relativistic incoherent scattering spectrum which is obtained from Nielsen [2]. For the derivation an isotropic electron velocity distribution is assumed. In principle this distribution need not be isotropic in a tokamak plasma because of the magnetic fields. However, deviations of the scattering spectrum due to the electron cyclotron motion cannot be resolved in such plasma in the case of incoherent Thomson scattering at the ruby laser wavelength (694.3 nm) [3]. For this reason the velocity distribution is assumed to be isotropic in the plane perpendicular to the magnetic field.

4.2 Scattering from a single electron

The scattering process of electromagnetic waves by free electrons has first been described by J.J. Thomson in 1903 [4]. Since then the scattering process has been analysed in much detail [2], including the description of collective and relativistic effects. In order to understand the scattering by a bulk of electrons, the scattering from a single electron is first described.

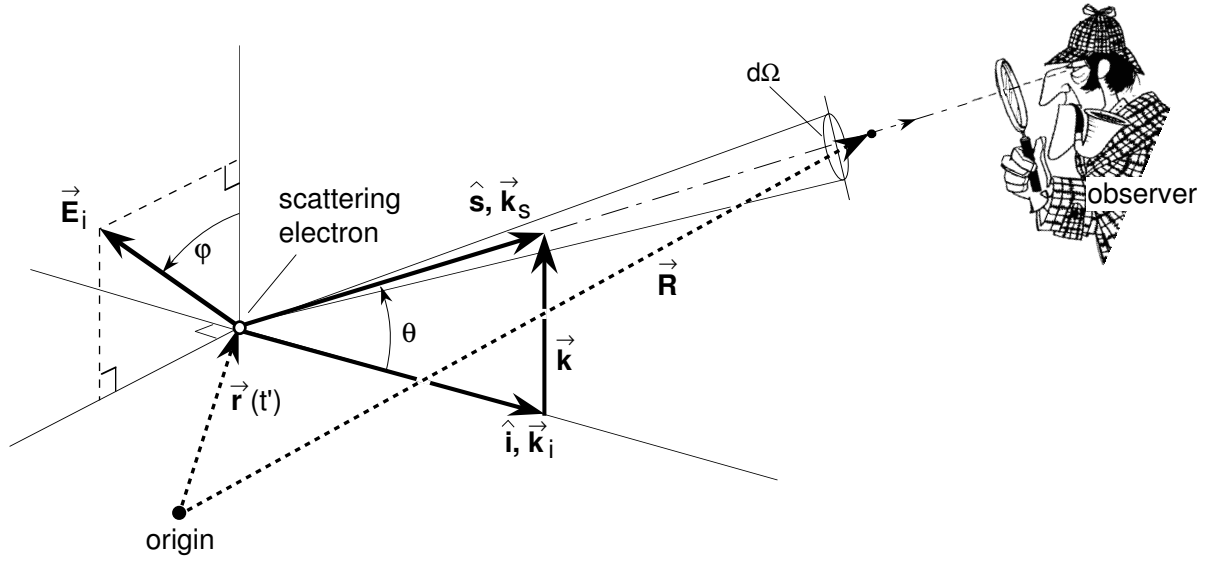


Figure 4.1: Scattering geometry and definition of parameters.

Consider a single electron of mass m , position \vec{r} and velocity \vec{v} in the Cartesian coordinate system of figure 4.1. Incident on the electron is a monochromatic electromagnetic wave, whose electric field is given by:

$$\vec{E}_i(\vec{r}, t) = \vec{E}_{i,0} \cos(\vec{k}_i \cdot \vec{r} - \omega_i t) \quad (4.1)$$

Here \vec{k}_i and ω_i are the incident wave frequency and wavelength respectively. The electron is accelerated by the oscillating field of the radiation and in accelerating it radiates its own electromagnetic waves. The acceleration can be derived from the equation of motion and is given by:

$$\vec{\beta}(\vec{r}, t') = -\frac{e}{m_0} (1 - \beta^2)^{1/2} \left[\vec{E}_i + \vec{\beta} \times (\hat{i} \times \vec{E}_i) - \vec{\beta} (\vec{\beta} \cdot \vec{E}_i) \right] \quad (4.2)$$

where $\vec{\beta} = \vec{v}/c$, c the speed of light in vacuum, m_0 is the rest mass of the electron and \hat{i} is the unit vector in the direction of \vec{k}_i . At the point of observation the field from the charge at time t is related to the behaviour of the charge at a previous time t' , the retarded time:

$$t' = t - \frac{|\vec{R} - \vec{r}(t')|}{c} \approx t - \frac{R - \hat{s} \cdot \vec{r}(t')}{c} = t - \frac{R - \hat{s} \cdot (\vec{r}(0) + \vec{v}t')}{c} \quad (4.3)$$

In the approximation the fact is used that the scattering volumes are small compared to the distance of observation, *i.e.* $|\vec{r}| \ll |\vec{R}|$. The expression for the retarded time equates to:

$$t' = \frac{t - \frac{R - \hat{s} \cdot \vec{r}(0)}{c}}{1 - \hat{s} \cdot \vec{\beta}} \quad (4.4)$$

Using the retarded time the phase of the electromagnetic wave in (4.1) becomes:

$$\begin{aligned} \vec{k}_i \cdot \vec{r}(t') - \omega_i t' &= \vec{k}_i \cdot \vec{r}(0) - (1 - \vec{\beta} \cdot \hat{i}) \omega_i t' \\ &= (\vec{k}_i - \vec{k}_s) \cdot \vec{r}(0) - \omega_s t + |\vec{k}_s| R \end{aligned} \quad (4.5)$$

The scattered electromagnetic wave is Doppler-shifted to the frequency:

$$\omega_s = \frac{1 - \vec{\beta} \cdot \hat{i}}{1 - \vec{\beta} \cdot \hat{s}} \omega_i \quad (4.6)$$

and $\vec{k}_s = \omega_s/c \cdot \hat{s}$.

At the observation point the scattered power per unit solid angle detected is:

$$\frac{dP_s}{d\Omega} = R^2 \vec{S}_s \cdot \hat{s} \quad (4.7)$$

where the Poynting vector \vec{S}_s is defined as:

$$\vec{S}_s = \frac{1}{\mu_0} \vec{E}_s \times \vec{B}_s \quad (4.8)$$

where \vec{E}_s and \vec{B}_s are the scattered electric and magnetic field respectively. The field scattered by the electron is given by the formula obtained from the Lienard-Wiechert potentials in the far field region:

$$\vec{E}_s(\vec{R}, t) = -\frac{e}{4\pi\epsilon_0 c R} \left[\frac{\hat{s} \times (\hat{s} - \vec{\beta}) \times \dot{\vec{\beta}}}{(1 - \hat{s} \cdot \vec{\beta})^3} \right]_{t'} \quad (4.9)$$

The magnetic field is $\vec{B}_s = \hat{s} \times \vec{E}_s/c$. Equation (4.7) can be evaluated to give:

$$\frac{dP_s}{d\Omega} = \frac{1}{2} \epsilon_0 c R^2 E_s^2 \quad (4.10)$$

This is compared to the incident power flux $S_i = \frac{1}{2} \epsilon_0 c E_i^2$ to give the differential power scattering cross section per unit solid angle:

$$\frac{d\sigma}{d\Omega} = \frac{\frac{dP_s}{d\Omega}}{S_i} = R^2 \frac{E_s^2}{E_i^2} \quad (4.11)$$

In a laboratory plasma the electrons cross the scattering volume and scatter the incident wave in a time shorter than the duration of the laser pulse, but much longer than the wave period. This gives rise to an additional correction compared to the case where the electron remains in the scattering volume during the laser pulse length. Taking this 'finite transit time effect' for small scattering volumes [5] into account and evaluating (4.11) for high temperatures ($\beta < 1$) yields the differential scattering cross section:

$$\frac{d\sigma}{d\Omega}(\omega_s) = \sigma_0 \frac{\omega_s^2}{\omega_i^2} \frac{1 - \beta^2}{1 - \beta_s} \quad (4.12)$$

with σ_0 the scattering cross section at the incident wavelength λ_i :

$$\sigma_0 = r_0^2 \quad (4.13)$$

where r_0 is the classical electron radius:

$$r_0 = \frac{e^2}{4\pi\epsilon_0 m_0 c^2} \quad (4.14)$$

4.3 Scattering from a group of electrons

Equation (4.12) is valid for one particular electron velocity v . When the electromagnetic waves scatter from a bulk of electrons the total scattered power scattered is the sum of the scattered power of all the particles in the scattering volume (incoherent Thomson scattering is assumed here). In the case of a relativistic isotropic plasma with temperature T_e the distribution function becomes:

$$f(\beta) = \frac{2\beta_{th}^{-2}}{4\pi K_2(2\beta_{th}^{-2})} \frac{1}{(1-\beta)^{5/2}} \exp\left[-2\beta_{th}^{-2}(1-\beta^2)^{-1/2}\right] \quad (4.15)$$

where K_2 is the modified Bessel function of the second kind of the second order, and β_{th} is the electron thermal velocity normalised to c :

$$\beta_{th} = \sqrt{\frac{2k_b T_e}{m_0 c^2}} \quad (4.16)$$

For the scattering angle θ the scattering cross section per unit solid angle and unit frequency interval is:

$$\frac{d^2\sigma_s}{d\omega_s d\Omega}(\omega_s, \theta) = \iiint f(\beta) \frac{d\sigma}{d\Omega}(\omega_s) \delta(\omega - \omega_s(\beta)) d^3\vec{\beta} \quad (4.17)$$

Nielsen [2] has performed this integration for the most common application of a plane polarised wave with the scattering plane perpendicular to the incident electric field \vec{E}_i ($\varphi = 90^\circ$ in figure 4.1). As a function of scattering wavelength λ_s and for $T_e \leq 25$ keV, which well accommodates the temperature range of MAST plasmas, the scattering cross section is given by:

$$\frac{d^2\sigma_s}{d\lambda_s d\Omega}(\lambda_s, \theta) = \frac{\sigma_0}{\lambda_i} \frac{C(\beta_{th})}{A(\varepsilon, \theta)} \exp\left[-2\beta_{th}^{-2} B(\varepsilon, \theta)\right] \quad (4.18)$$

with:

$$\varepsilon = \frac{\Delta\lambda}{\lambda_i} = \frac{\lambda_s}{\lambda_i} - 1 \quad (4.19)$$

$$A(\varepsilon, \theta) = (1 + \varepsilon)^3 \sqrt{2(1 - \cos\theta)(1 + \varepsilon) + \varepsilon^2} \quad (4.20)$$

$$B(\varepsilon, \theta) = \sqrt{1 + \frac{\varepsilon^2}{2(1 - \cos\theta)(1 + \varepsilon)}} - 1 \quad (4.21)$$

$$C(\beta_{th}) = \sqrt{\frac{1}{\pi\beta_{th}^2}} \left(1 - \frac{15}{16}\beta_{th}^2 + \frac{345}{512}\beta_{th}^4\right) \quad (4.22)$$

Examples of relativistic spectra for incoherent Thomson scattering at the ruby wavelength $\lambda_0 = 694.3$ nm, according to (4.18) are given in figure 4.2. The scattered spectra show a blue shift which increases with temperature. This shift is due to the fact that the electrons radiate preferentially in the forward direction, which corresponds to an asymmetric dipole radiation pattern.

Equation (4.18) now gives the total power P_s per unit wavelength scattered from a plasma of density n_e in a volume ΔV and detected at a point of observation \vec{R} over scattering angle $\Delta\Omega$:

$$\frac{dP_s}{d\lambda_s}(\vec{R}, \lambda_s) = n_e S_i \Delta V \Delta\Omega \frac{d^2\sigma_s}{d\lambda_s d\Omega}(\lambda_s, \theta) \quad (4.23)$$

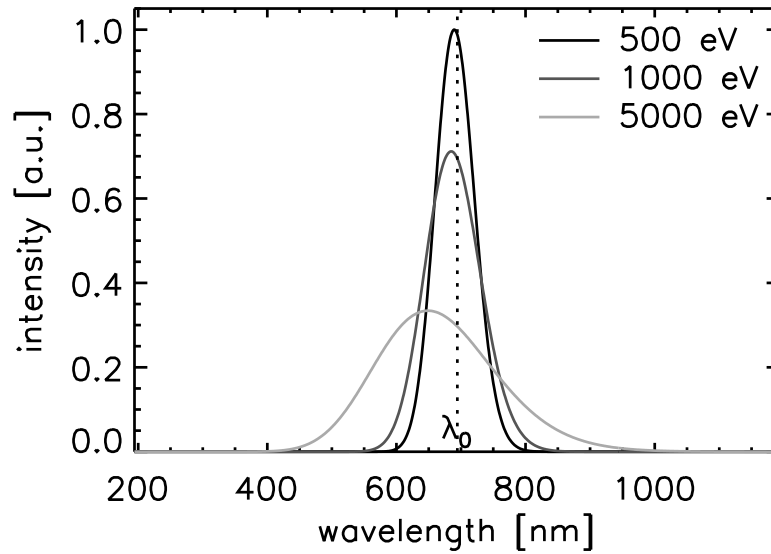


Figure 4.2: Examples of relativistic spectra for incoherent Thomson scattering for Maxwellian velocity distributions at different temperatures.

By substituting $P_i \Delta L = S_i \Delta V$, with ΔL the length of the scattering volume and P_i the incident laser power, this becomes:

$$\frac{dP_s}{d\lambda_s}(\vec{R}, \lambda_s) = n_e P_i \Delta L \Delta \Omega \frac{d^2 \sigma_s}{d\lambda_s d\Omega}(\lambda_s, \theta) \quad (4.24)$$

This equation is fitted to the scattered spectra recorded with a Thomson scattering diagnostic in order to obtain values for T_e and n_e .

In the classical case (4.24) is reduced to:

$$P_s = n_e P_i \Delta L \Delta \Omega r_0^2 \quad (4.25)$$

For a standard experimental Thomson scattering setup, the ratio between scattered and incident power is $P_s/P_i = 10^{-15} - 10^{-14}$. This gives an indication of the required high laser power and required high sensitivity of the detection system.

In approximation (4.24) can be reduced to a Gaussian of the form:

$$\frac{dP_s}{d\lambda_s}(\vec{R}, \lambda_s) \sim \exp\left(-\frac{1}{2} \left(\frac{\lambda_s - \lambda_i}{\sigma_\lambda}\right)^2\right) \quad (4.26)$$

where $\sigma_\lambda = \sqrt{2} \lambda_i \sin(\theta/2) \beta_{th}$ gives the width of the scattered spectrum. This equation is still valid for low temperatures $T_e < 1$ keV.

Bibliography

- [1] C.J. Barth. Laser-aided plasma diagnostics. In *Carolus Magnus Summerschool*, volume 37, pages 344–351. American Nuclear Society, March 2000.
- [2] P. Nielsen. Thomson scattering in high temperature devices. In *Diagnostics for fusion reactor conditions*, volume 1, pages 225–259, Varenna, Italy, September 1982. Commission of the European communities.

- [3] J. Sheffield. *Plasma scattering of electromagnetic radiation*. Academic press, 1975.
- [4] J.J. Thomson. Conduction of Electricity through Gases. pages 268–273, 1903.
- [5] R.E. Pechacek and A.W. Trivelpiece. *Physics of Fluids*, 10:1688, 1967.

Chapter 5

Measurement and modelling of H-mode density profiles with edge density ‘ears’

E.R. Arends, M.J. Walsh¹ and M.R. Tournianski²

Electron density profile measurements using the multi-point Thomson scattering system on the Mega-Ampere Spherical Tokamak show a dramatic increase of the edge density, rising above the central density, and the development of steep edge gradients during ELM-free periods of H-mode. A one-dimensional phenomenological transport model has been set up to simulate these so-called edge density ‘ears’. The measurements can be reproduced by a reduction of the edge diffusion coefficient at the L-H transition from 5.5 ms^{-1} to 0.44 ms^{-1} .

5.1 Introduction

The spherical tokamak (ST) is an extension of the conventional tokamak design to a more compact geometry. Thanks to the low aspect ratio, the ST provides experimental data in new and overlapping parameter regimes, used to test physics models and scaling laws for future generation tokamaks. The future generation tokamaks are designed to operate in the high-confinement regime (H-mode), and exploration of this regime in the ST is therefore beneficial.

This paper presents data taken during the first campaign of MAST [1–3] (Mega-Ampere Spherical Tokamak), January-June 2000. During this campaign H-mode has frequently been accessed in both Ohmic and neutral beam heated (NBI) discharges [4]. A clear increase of the energy confinement time is observed at the H-mode transition. Most H-mode periods were accompanied by Edge Localised Modes (ELMs), but also long ELM-free periods, up to two confinement times, have been observed.

The line-integrated electron density ($\bar{n}_e \ell$) as measured by the CO₂ interferometer, shows an immediate rise after the L-H transition. For long ELM-free periods the density even doubles. The electron density (n_e) profile is measured using the high spatial resolution, multi-point Thomson scattering (TS) diagnostic. These measurements during the ELM-free periods show a dramatic increase of the edge density and the development of steep edge gradients while the cen-

¹Walsh Scientific Ltd., Culham Science Centre, Abingdon, Oxfordshire, OX14 3EB, United Kingdom

²UKAEA Fusion, Culham Science Centre, Abingdon, Oxfordshire, OX14 3DB, United Kingdom

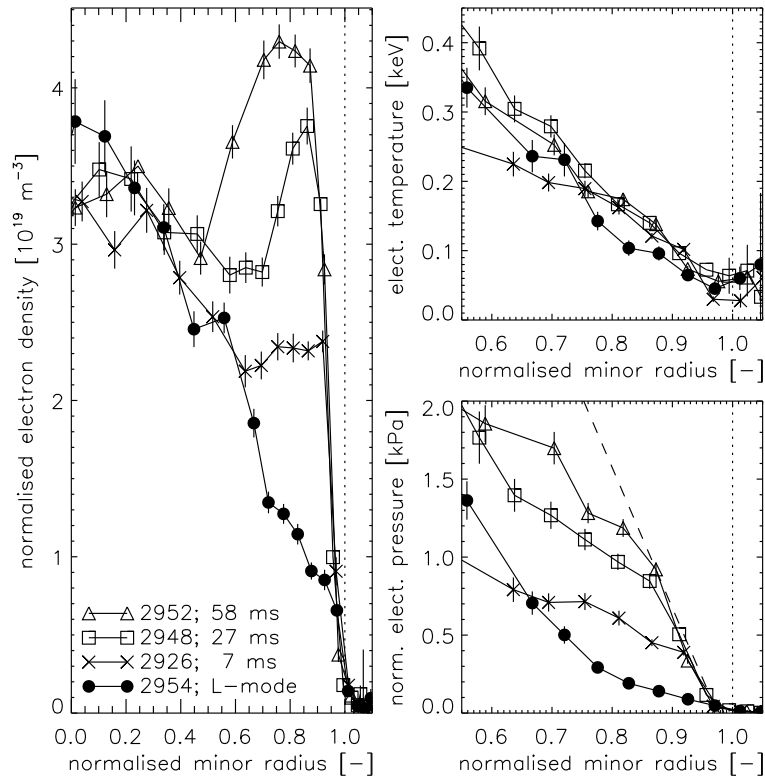


Figure 5.1: Development of the EDE in ELM-free H-mode and corresponding edge temperature (T_e) and pressure (p_e) profiles. Comparable discharges have been used to produce the graphs. Each n_e profile is normalised for \bar{n}_e at the L-H transition to the value of the L-mode discharge. T_e does not change significantly from L- to H-mode. The pressure profile seems to be limited to a pressure gradient. The legend presents the times after the L-H transitions.

tral density remains constant, as shown in figure 5.1. The addition to the normally ‘parabolic’ profile shape resembles an ‘ear’. This phenomenon has, therefore, been named an Edge Density ‘Ear’ (EDE).

EDEs have previously been observed on START [5] and have also been reported on NSTX [6]. DIII-D [7] also has similar observations and EDEs are therefore not a feature of the ST design. An EDE is different from a density pedestal that lifts the overall profile, as first observed during H-mode on ASDEX [8], in that only the density at the edge of the plasma rises. Simulations for ITER [9] also show EDEs together with rising central density due to an enhanced fuelling efficiency at the plasma edge. Stationary EDEs have been recorded on the reversed field pinch RFX [10], where they are explained by an ‘anti-pinch’ velocity. The EDEs in MAST show a unique behaviour, in that they are transient and not associated with a rise in the central density, and their behaviour calls for an explanation.

In order to get a physical understanding of the transient behaviour of the EDE in MAST a simple one-dimensional (1-D) phenomenological transport model has been developed specifically for this purpose. The model is used to test the hypothesis that a reduced edge diffusion coefficient during the ELM-free H-mode is sufficient to explain the development of the EDE. This paper describes the model in section 5.4, and the modelling result in section 5.5. Before that, a description of the high resolution, multi-point Thomson scattering diagnostic that measures the EDEs is given in section 5.2 along with a brief outline of H-mode in MAST in section 5.3.

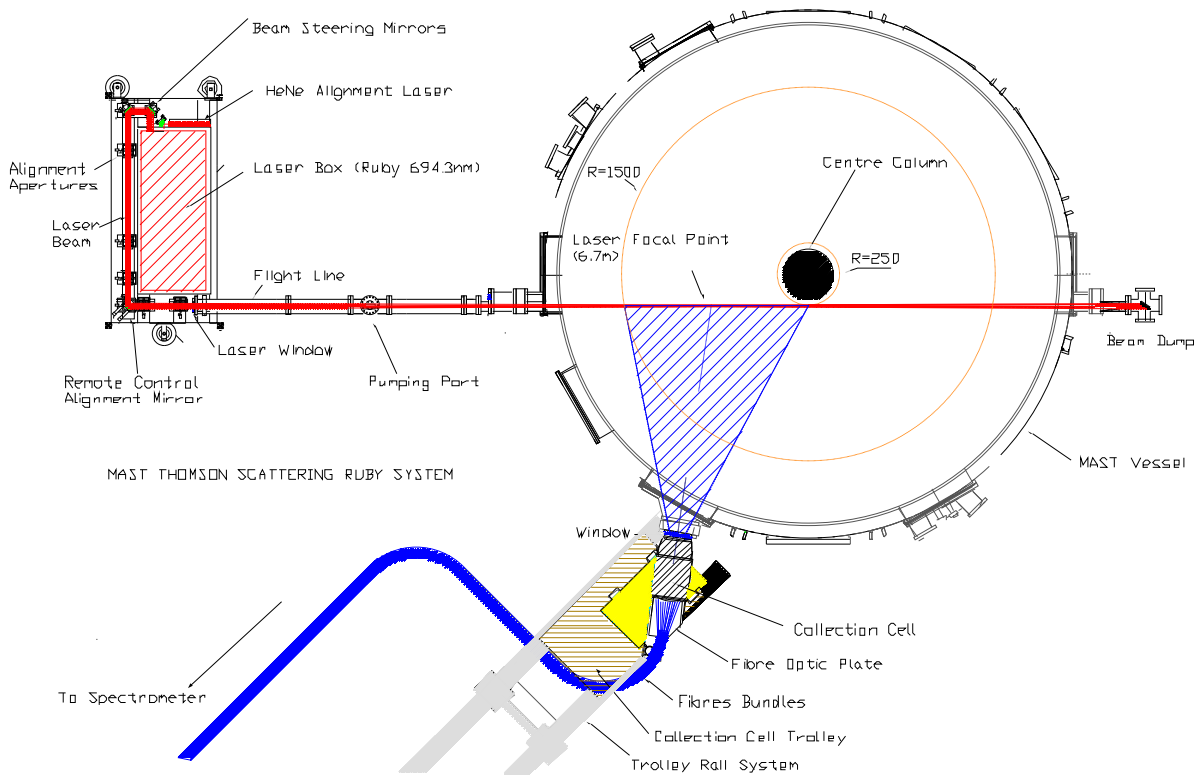


Figure 5.2: Overview of the ruby laser beam path and the light-collection optics on MAST.

5.2 Thomson scattering diagnostic

Figure 5.2 shows a top view of the MAST vessel and the Thomson scattering system.³ The experimental setup is similar to that used on the START tokamak [12]. The light source is a Q-switched ruby ($\lambda_0 = 694.3 \text{ nm}$) oscillator/amplifier system which produces one laser pulse per MAST discharge. The laser beam has an energy of $\sim 10 \text{ J}$, a pulse width of 30 ns and a beam divergence of 0.5 mrad . The laser beam crosses the vessel at the midplane and passes the central column at close distance ($\sim 45 \text{ mm}$) to obtain a good scattering geometry. The Thomson-scattered light, in 40 small elements in the plasma volume ($\sim 30 \text{ mm}$ long, $3\text{-}4 \text{ mm}$ diameter), is collected by a lens ($f/12$) and focussed onto 40 individual fibre-bundles ($f/1.75$). Initially 10 of those fibre-bundles were used to record the background light, but these channels were added to the active array once the background light turned out to be sufficiently low not to disturb the scattered light spectrum significantly. The profiles in this paper therefore show either 30 or 40 spatial positions. The fibre-bundles lead to a grating spectrometer and detector system where the scattered spectra are recorded for analysis.

Spectrometer and detector

The grating spectrometer and detector system are shown in figure 5.3. This system is designed to achieve optimised light transmission and high dynamic range. The scattered light enters the spectrometer through the fibre-bundles that are stacked in a column. Here the fibre-bundles

³This paper gives a description of the status of the Thomson scattering diagnostic at the time when the measurement of the data used in this paper were measured. Ever since, the diagnostic has been upgraded to provide near 300 spatial points [11].

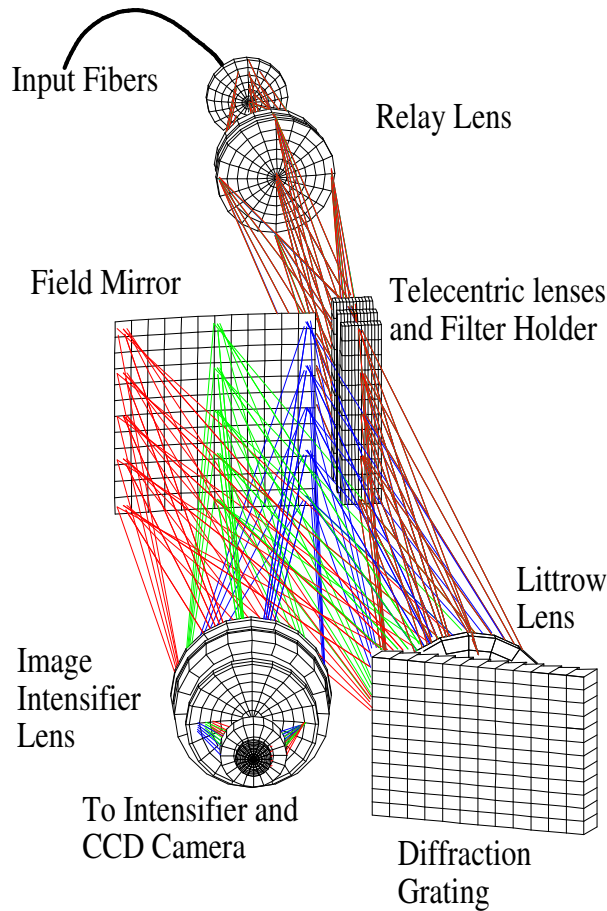


Figure 5.3: Grating spectrometer system in the Littrow setup.

are alternately rotated by 0° and 180° so that any misalignment of the collection end of the fibre-bundle array with respect to the laser beam is easily detected [13]. A relay lens focusses the light onto a slit. The width of this slit determines the wavelength resolution of the system. At this stage a high-pass wavelength filter is positioned to suppress the potential interference of stray light coming from reflections in the vessel and D_α light from the plasma and hence only the red wing of the spectrum is observed. The light then passes through a Littrow lens and falls onto a 1200 lines/mm grating giving a detectable wavelength region of 680 – 830 nm. The first-order reflected light again passes through the Littrow lens and is focussed onto a field mirror which transfers the image to the detector.

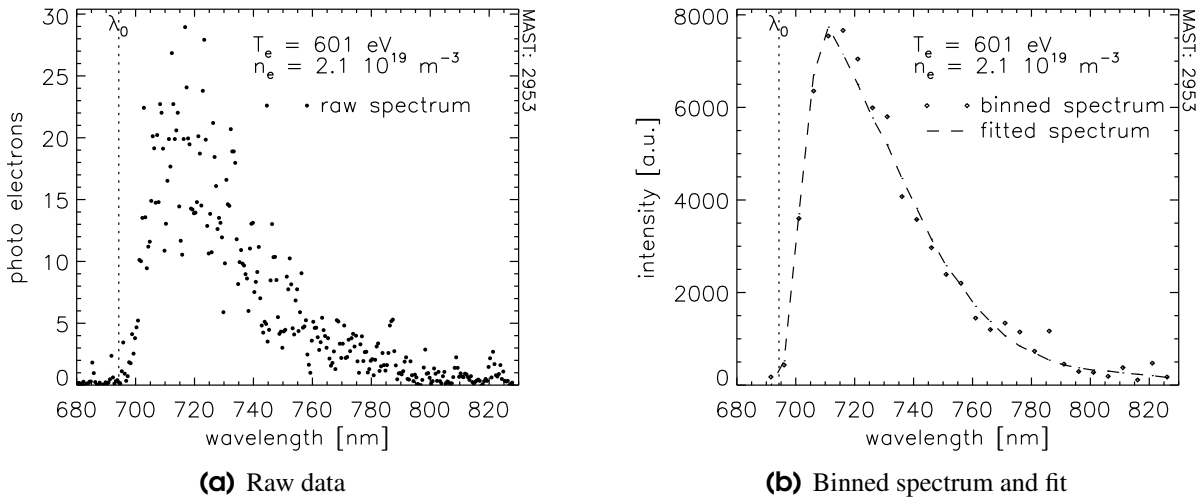
The detector system consists of an image intensifier, CCD camera and a coupling lens. A lens focusses the image from the field mirror onto the image intensifier. This intensifier acts as a fast gate (30 ns) to minimise the collection of plasma light. A lens is used to couple the intensifier onto the CCD camera where the images of the spectra are recorded. The camera image is then transferred to a computer system for analysis. Transmission and detection values of the system are given in table 5.1.

Data analysis

Figure 5.4(a) shows a typical spectrum of a central plasma channel ($T_e = 601 \pm 65$ eV, $n_e = 2.1 \pm 0.1 \times 10^{19} \text{ m}^{-3}$). The spectrum shows the number of ‘effective’ photo-electrons at the input to the micro channel plate (MCP) in the image intensifier. In the analysis the spectrum is

Table 5.1: Transmission parameters.

parameter	symbol	value
transmission collection part	τ_{cp}	0.74
transmission fibre-bundle	τ_{fb}	0.59
transmission spectrometer	τ_{sp}	0.14
total transmission	τ_{tot}	0.06

**Figure 5.4:** Typical recorded spectrum and fit for a central channel.

binned over 10 pixels in the wavelength direction to increase the number of counts in each bin before a least χ^2 fit is performed.

Before the fit, the theoretical curve for the scattered light [14–16] depending on T_e and n_e is convolved with the instrument function in wavelength direction and corrected for a relative spectral calibration. A uniform offset is added to this spectrum to account for the plasma light. The measured spectrum is therefore fitted using 3 parameters. The offset is generally small compared to the scattered light and therefore a uniform offset is justified. An example of a fit to the data is given in figure 5.4(b).

Calibration

A relative spectral calibration is obtained by illuminating white paper that is calibrated against an opal plaque in the line of sight of the collection lens with a calibrated Tungsten lamp. A relative spatial calibration is carried out using Rayleigh scattering on N_2 . The electron density measurement is calibrated for each shot using the line-integrated density measurement of the CO_2 interferometer.

Normalised-flux resolution

The profiles are normally plotted versus R , the distance between the centre of the sample volume and the major axis of the tokamak. Where the laser approaches the centre column at close range (~ 45 mm) this R only changes minimally from one spatial point to the next. A very high spatial resolution is therefore achieved on the inboard side edge. The resolution in flux coordinates (the normalised-flux resolution $\Delta\Psi_N = \Delta R \partial\Psi_N / \partial R$) is further enhanced by the fact that the

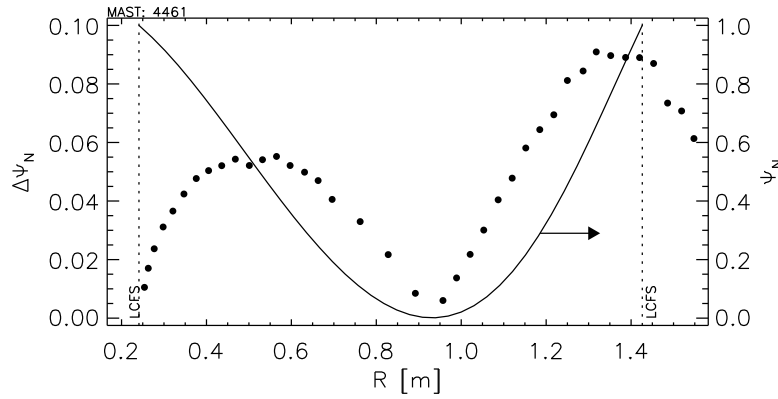


Figure 5.5: Normalised-flux resolution of TS system and Ψ_N from EFIT, where $\Delta\Psi_N = \Delta R \partial\Psi_N / \partial R$. The position (R) and width (ΔR) of the scattering volume in the radial direction are obtained by back-illuminating the fibre-bundles and marking the positions of the fibre-bundle images on a sheet positioned in the laser beam path.

Table 5.2: Typical MAST parameters during the first two campaigns (2000-2001).

parameter	symbol	value
plasma current	I_p	0.8 MA
major radius	R	0.8 m
minor radius	a	0.65 m
aspect ratio R/a	A	1.3
toroidal field at R	B_T	0.5 T
pulse length	Δt	0.4 s

flux surfaces are more widely spaced on the inboard side due to the large Shafranov shift in a spherical tokamak (see figure 5.5). This TS system is therefore a powerful tool in edge gradient studies. A high normalised-flux resolution, $\Delta\Psi_N$, in the plasma centre is naturally achieved due to the low variation of Ψ in this region (see figure 5.5).

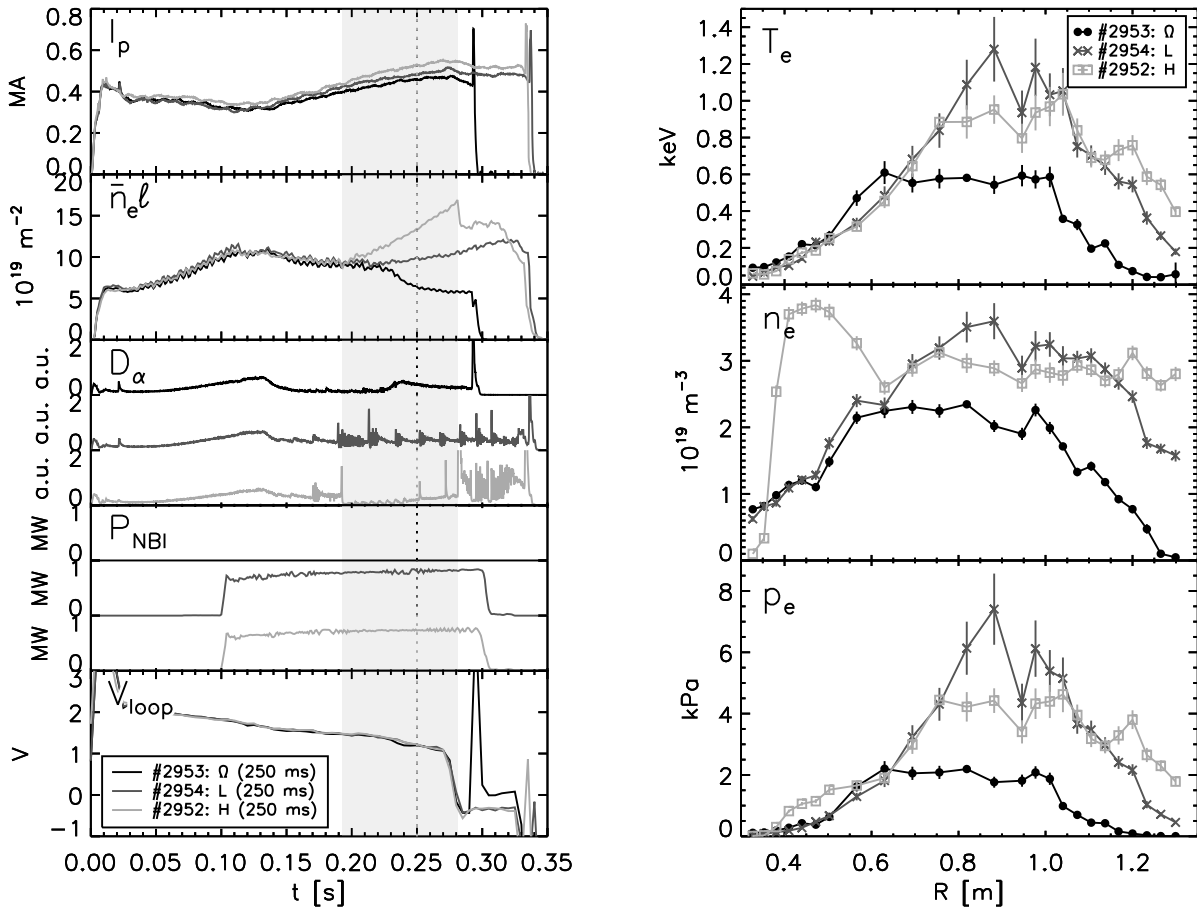
5.3 Results

Operational results from the first MAST campaign, January-June 2000, were reported [2, 3]. Table 5.2 gives an overview of the typical plasma parameters. Good vacuum conditions and operational conditions provided a plasma current of over 1 MA with central temperatures (Ohmic) of $T_e \sim 1$ keV. H-mode was achieved with Ohmic heating or with modest additional NBI power.

The Thomson scattering diagnostic became operational almost at the start of the first MAST campaign, and has been delivering T_e and n_e profiles consistently for practically all MAST discharges.

H-mode in MAST

To give an overview of the ‘typical’ results, three common types of MAST discharges are distinguished: Ohmic, L-mode, and H-mode, where the latter two are NBI heated with $P_{NBI} = 0.8$ MW. Figure 5.6(a) shows these three types compared. All of the selected discharges had $I_p \sim 500$ kA, $B_T \sim 0.40$ T and are similar up to ~ 200 ms in the discharge. The ones in which



(a) Time traces of plasma current, density, D_α emission, NBI power and loop voltage. The three discharges are identical until NBI switch on for #2954 and #2952. The latter enters H-mode at 0.19 s. The vertical lines indicate the TS time, which is also indicated in the legend.

(b) TS profiles showing the heating effect of the NBI. An EDE is measured in the H-mode discharge, #2952. Shot #2954 is taken just before a sawtooth crash and therefore exhibits a very peaked T_e profile.

Figure 5.6: Ohmic (#2953), L-mode (#2954) and H-mode (#2952) discharges, the latter two having NBI applied.

NBI was applied show a somewhat higher plasma current and last longer, but show similar densities to the Ohmic discharge up to L-H transition. Both NBI discharges attempt several L-H transitions [4] at the crash of a sawtooth (not shown in the graph), but only #2952 remains in H-mode. The confinement time of the H-mode discharge reached ~ 32 ms which compares well with the IPB98(y,2) [17, 18] scaling. Figure 5.6(b) shows profiles measured with TS for each of these three discharges.

ELM-free H-mode

The L- and H-mode discharges of figure 5.6(a) are very similar up to the time of the L-H transition for discharge #2952 at 193 ms. A more detailed view of the ELM-free H-mode period is shown in figure 5.7, where the L-mode discharge is also shown for comparison. The density starts rising immediately after the L-H transition and continues doing so until the H-L transition at 281 ms. The rise in \bar{n}_{el} , as measured by the CO_2 interferometer, is mostly independent of

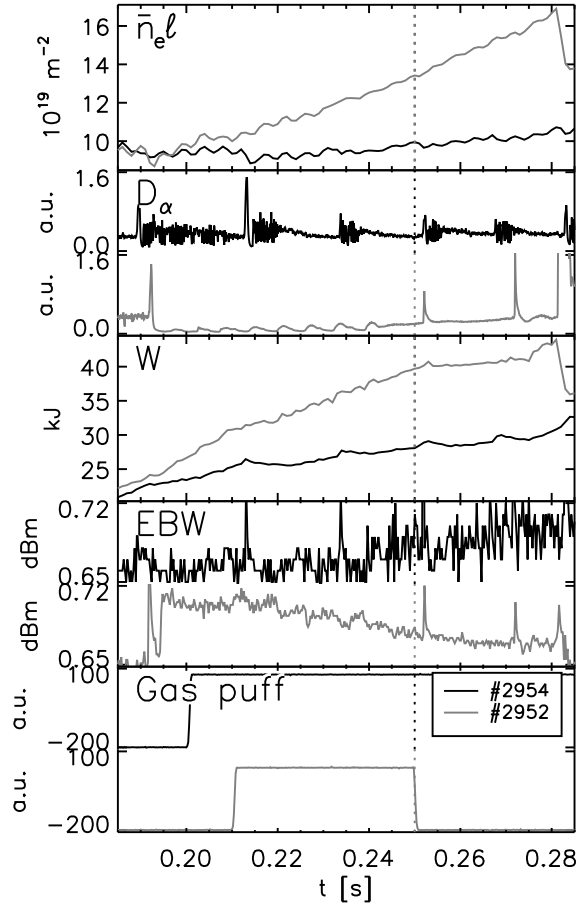


Figure 5.7: Detail of the H-mode period of figure 5.6(a) showing $\bar{n}_e l$, D_α emission, stored energy (W), 31.74 GHz signal from the EBW radiometer and gas puff signal. The L-mode discharge (#2954) is shown for comparison. The vertical lines indicate the TS time.

the applied gas fueling, although the latter is likely to contribute somewhat as a small rise is observed in the L-mode discharge. The ELMs at 252 ms and 272 ms hardly affect the line-integrated density. The stored energy (W), as computed by the equilibrium reconstruction code EFIT [19], rises $\sim 90\%$ over the duration of the ELM-free period - this in comparison with the 41% rise over the same period for the L-mode discharge. The figure also shows the 31.74 GHz signal from the electron Bernstein wave (EBW) radiometer [20]. The signal corresponds to $3\omega_e$ emission at n_e around the O-mode cut-off ($1.25 \times 10^{19} \text{ m}^{-3}$) and reflects the steepness of the edge n_e gradient. From this signal it can be seen that the edge n_e rises immediately after the L-H transition.

EDE measurement

The steep n_e gradient and EDE are clearly observed on the TS profile taken at 58 ms in H-mode (see figure 5.6(b)). In this example the plasma extends beyond the region of observation of the TS diagnostic on the outboard side, but other discharges also show the EDE on the outboard side. Figure 5.1 shows n_e profiles taken at different times in the ELM-free period of comparable discharges showing the development of the EDE. It can be seen that the central density ($n_e(0)$) remains constant, while the EDE grows above $n_e(0)$ for long ELM-free periods ($> \tau_E$). Also the gradient immediately inside the last closed flux surface (LCFS) remains constant. Clearly

the rise in \bar{n}_e is concentrated at the plasma edge.

The change in the gradient on the inside of the EDE to the core plasma might be related to the presence of the $q = 2$ surface at that location. On conventional tokamaks surfaces of rational q have been associated with changes in the diffusive transport, which *e.g.* give rise to magnetic island and internal transport barrier formation [21]. The position of the $q = 2$ in the discussed discharges on MAST is estimated using the presence of an $m = 2$ tearing mode (TM). The flattening in n_e around $r/a = 0.65$ for discharge #2948 in figure 5.1 can be related to such a TM and therefore indicates the position of the $q = 2$ surface. This position coincides well with the change in gradient on the inside of the EDE.

ELMs

H-mode discharges often show long ELM-free periods alternated by ELMs which are detected as spikes on the D_α signal. Small ELMs (D_α scale < 1) have little effect on the density, as can be seen at 252 ms in figure 5.7 and big ELMs (D_α scale > 1) tend to decrease the density as can be seen at 294 ms in figure 5.8(a). Figure 5.8(b) shows the n_e profile measured 4 ms after an ELM. Since the integral of the n_e profile along the chord of the CO₂ interferometer⁴ equals $4\bar{n}_e\ell$, a linear change in $\bar{n}_e\ell$ can be indicated as an areal change in the n_e profile. In this way, the rise in $\bar{n}_e\ell$ between the time of the ELM and the TS measurement can be marked by the shaded area on the n_e profile, such that the profile just after the ELM is reconstructed. The contribution of the outboard side of the profile is taken into account by assuming that n_e is preserved on flux surfaces. In a similar way the profile just before the ELM can be reconstructed from the loss in $\bar{n}_e\ell$ during the ELM, this is indicated by the dashed line; a big EDE is reconstructed. The edge gradient of the reconstructed EDE can be extrapolated from the edge gradient of the measured profile, so can the gradient of the reconstructed EDE facing the magnetic axis. It thus appears that the ELM only affects the edge of the plasma, whereas the centre of the plasma remains unaffected.

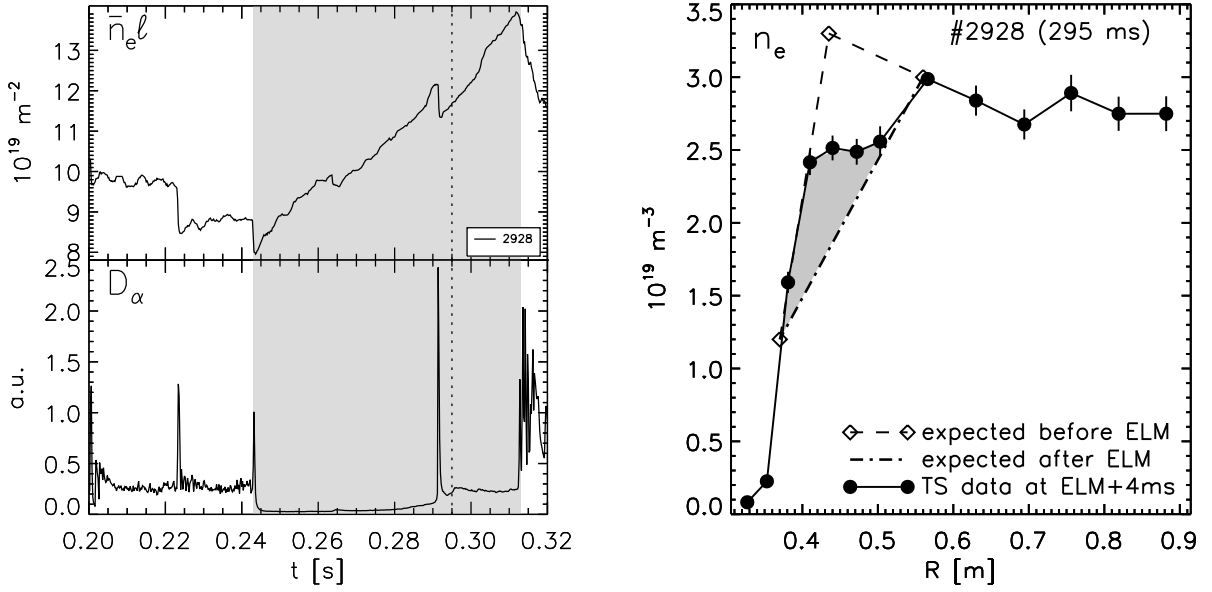
5.4 Transport analysis

A steepening of the edge n_e gradient during H-mode is generally explained as the result of a local reduction of the diffusion coefficient; the so-called edge transport barrier (ETB). The phenomenon could be explained by the following hypotheses:

1. A change of the edge transport on a time scale much shorter than τ_E from the start of the L-H transition could explain the immediate increase of \bar{n}_e .
2. The formation of the n_e gradient on the inside of the EDE could subsequently be the result of slow inward diffusion and/or an increase of the edge electron source as a result of an increased ionisation rate at the edge.

To test these hypotheses a 1-D phenomenological model for the electron transport during H-mode in MAST has been developed. A simple model was preferred above existing codes in order to be able to focus solely on these hypotheses and to provide a semi-analytical solution.

⁴The CO₂ interferometer laser crosses the plasma diameter four times.



(a) Time traces of \bar{n}_e and D_α emission showing the effect of a single ELM on the density. The TS measurement is taken within 4 ms after the start of the ELM as indicated by the vertical dashed line. The L-H transition is triggered by a sawtooth crash.

(b) Expected and measured inboard n_e profiles before and after an ELM. The area marked by the dashed lines corresponds to the density lost due to the ELM as measured by the CO_2 interferometer and shows the expected profile before the ELM. The shaded area corresponds to the density built up between the ELM and the time of the TS measurement. The contribution of the outboard side of the profile has been taken into account by flux mapping.

Figure 5.8: Depletion of the electron density by a single ELM.

Transport model

The transport model is 1-D and uses a cylindrical coordinate system for the minor radius (r) and neglects the toroidal character of the plasma. MAST plasmas in general are D-shaped and have a high elongation ($\kappa \sim 1.8$). The outer half of the plasma can be approximated by half of an ellipse. To accommodate the MAST plasma in the cylindrical coordinate system the minor radius (a) is scaled for elongation: $\sqrt{\kappa}a \rightarrow a$. This scaled a is used from now on throughout the paper.

The transport model is based on the equation of particle conservation for the electrons:

$$\frac{\partial n_e}{\partial t} + \vec{\nabla} \cdot \vec{\Gamma}_e = S \quad (5.1)$$

where S represents the sum of all processes by which electrons come into existence or disappear, also referred to as the particle ‘sources’ and ‘sinks’. The particle flux ($\vec{\Gamma}_e$) is built up of a diffusive term with diffusion coefficient $D(r)$ and a convective term with pinch velocity $\vec{V}(r)$:

$$\vec{\Gamma}_e = -D\vec{\nabla}n_e + \vec{V}n_e \quad (5.2)$$

In steady state, in the core of the plasma, the particle sources can be neglected and $\vec{\Gamma}_e = 0$. A convective term is needed to fuel the core and to cancel the diffusive term. From the density

profile, the ratio of $D(r)$ and $|\vec{V}(r)|$ can be determined. It is proportional to the density gradient length, $L_n(r)$:

$$\frac{D}{|\vec{V}|} = \frac{n_e}{|\vec{\nabla}n_e|} \equiv L_n \quad (5.3)$$

It has been reported for several tokamaks that the n_e profile shape is remarkably insensitive to variations of the plasma parameters, *i.e.* $L_n(r)$ is fixed [17]. Equation (5.3) has the solution:

$$n_e(r) = n_e(0) \exp\left(\int L_n^{-1} dr\right) \quad (5.4)$$

This simple result provides a key connection between any choice of $\vec{V}(r)$ and one of its important physical consequences, namely, the radial distribution of the electrons in equilibrium. The often used form [22]:

$$\vec{V} = -\frac{2D}{a^2} \vec{r} \quad (5.5)$$

yields a Gaussian equilibrium profile. This expression sets $|\vec{V}| = 0$ in the plasma centre and therefore meets a necessary boundary condition. Here the n_e gradient disappears and hence $\vec{\Gamma}_e$ becomes zero. Also, in order to set the pinch term to zero at the LCFS, while keeping the linear dependence of r in the centre, the following expression for $\vec{V}(r)$ is used:

$$\vec{V} = -\frac{2D_c}{a^2} \vec{r} \left(1 - \left(\frac{r}{a}\right)^\lambda\right) \quad (5.6)$$

where λ is a shaping parameter and D_c is a control parameter for the diffusion coefficient - in the simulation $D(r)$ in the plasma centre will be close to D_c . For high λ the profile is linear with the radius for a large part of the plasma. Common physical explanations for the pinch are the Ware effect due to trapped particles in banana orbits and thermo-diffusion in which a T_e gradient causes a particle flux towards the hot region. Several other pinch effects have also been suggested [23], however, it is not the objective of this paper to study the physical origin of the pinch effect.

In the plasma the source for electrons arises from ionisation of the neutrals. Impurities are not included in the model; $Z_{eff} = 1$. In the temperature range ($T_e < 10^3$ eV) of the discharges studied here the ionisation by the electrons dominates that by the ions (see figure 5.9). The neutrals penetrate from the edge of the plasma, are injected by the neutral beam or are a result of charge-exchange processes with ions in the plasma. Charge-exchange itself does not contribute to the total electron source, but it alters the distribution of the neutral population and therefore changes the source function. Through this process a small fraction of the edge neutral population can penetrate into the plasma centre. Simulations using the DOUBLE code for MAST discharges [24, 25] show that for Ohmic discharges the central neutral density ($n_n(0)$) is typically a factor of $\sim 10^4$ lower than the edge neutral density ($n_n(a)$). The DOUBLE code solves the 1-D Boltzmann equation describing the neutral particle distribution $f(\vec{x}, \vec{v})$ in an axisymmetrical, toroidal, steady state plasma. In the model presented in the paper a simple but adequate approximation for the effect of the charge-exchange process on the neutral density profile is made in order to avoid lengthy Monte-Carlo simulations.

The fast neutrals of the neutral beam penetrate directly into the centre of the plasma. However, it can be seen from figure 5.6(a) that the particle source due to the NBI is only small, this assuming that the gas-puffing is the same for the discharges with and without NBI. The beam neutral contribution is therefore not taken into account in the transport model.

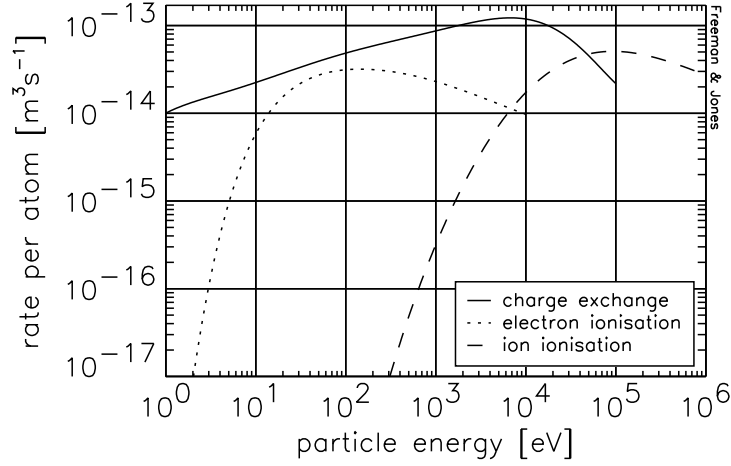


Figure 5.9: Reaction rates ($\langle\sigma v\rangle$) for ionisation and charge-exchange processes affecting hydrogenic atoms in an electron-proton plasma [26].

Particle sinks are the various processes in which free electrons are captured in atoms. The most important of these is the recombination of hydrogen ions and electrons into neutral hydrogen. However, in the plasmas under consideration, the sink due to recombination [27] is much smaller than the source due to electron ionisation at the edge of the plasma; the recombination effect can therefore be neglected.

The source due to electron ionisation is thus expressed by:

$$S = \langle\sigma_{ion}v_e\rangle n_n n_e \quad (5.7)$$

where $\langle\sigma_{ion}v_e\rangle$ is the electron impact ionisation cross-section [26, 28] which is only a function of temperature (see figure 5.9). Since T_e does not significantly change from L-mode to H-mode or during the H-mode period, the cross-section profile is kept constant.

The neutral density profile can be derived in a similar way to the electron density profile from the equations for particle conservation and particle flux:

$$\frac{\partial n_n}{\partial t} + \vec{\nabla} \cdot \vec{\Gamma}_n = -S \quad (5.8)$$

$$\vec{\Gamma}_n = \vec{V}_n n_n \quad (5.9)$$

where $\vec{\Gamma}_n$ is the neutral particle flux and \vec{V}_n is the constant and uniform neutral inward flux velocity. The minus sign in front of the source term is introduced because the neutrals are lost in the ionisation process while the same expression for S is used (and $-S$ thus becomes a sink). The diffusive term is considered to be sufficiently smaller than the convective term to be neglected.

In order to accommodate the effect of the charge-exchange processes on the neutral density profile the neutral density is divided into two terms; one for the direct ionisation of the edge neutrals ($n_{n,ion}$) and one for the ionisation of charge-exchanged neutrals ($n_{n,cx}$):

$$n_n = n_{n,ion} + n_{n,cx} \quad (5.10)$$

The first term will dominate the edge, the second the centre of the plasma. Estimates of the two profiles are taken from a Monte-Carlo simulation using the DOUBLE code [24, 25]. These simulations show that the central n_n profile drops slightly from L-mode to H-mode because of the increase in \bar{n}_e . Due to the EDE the neutrals penetrate less deep into the plasma and therefore n_n drops more rapidly in H-mode than in L-mode.

Steady state L-mode solution

During the L-mode phase the plasma is assumed to be in a steady state. Therefore, an expression for n_n can be derived by solving the differential equation following from (5.7), (5.8) and (5.9):

$$\vec{\nabla} \cdot (\vec{V}_n n_n) + \langle \sigma_{ion} \nu_e \rangle n_e n_n = 0 \quad (5.11)$$

In a cylindrical coordinate system the solution to this equation is given by:

$$n_n(r) = n_n(a) \frac{a}{r} \exp \left(- \int_r^a \frac{\langle \sigma_{ion} \nu_e \rangle n_e(r') dr'}{|\vec{V}_n|} \right) \quad (5.12)$$

where $n_n(a)$ is the value at the LCFS. Since (5.11) only takes electron-impact ionisation and not charge-exchange recombination into account, (5.12) describes $n_{n,ion}$. This solution will be fitted to the results of the DOUBLE simulation of n_n at the edge in order to obtain \vec{V}_n . Since the n_n profile given by DOUBLE also includes the effect of charge-exchange recombination and (5.12) does not, the difference of the two solutions produces $n_{n,cx}$.

Since the MAST vessel is significantly bigger than the plasma volume ($6 - 8 \text{ m}^3$ vs. 55 m^3), n_n is expected to be constant in time outside the LCFS. Recycling mainly takes place at the outboard divertor target plates. These are located sufficiently far from the plasma, such that the assumption can be made that the recycled neutral particles are uniformly distributed along the LCFS. The same is assumed for the neutrals introduced into the vessel by the active gas-puff system.

The transport model does not describe the plasma outside the LCFS. Since the temperature of the plasma directly outside the LCFS is approximately 30 eV, it is assumed that all D_2 molecules have dissociated into atoms at the LCFS. The usual assumption is that the atomic molecular products of molecular dissociation have Franck-Condon energies around 2 eV [29]. However, in several fusion experiments [30] output energies as low as 0.2 eV have been observed.

An estimate of $n_n(a)$ is obtained from the particle confinement time τ_p defined as the ratio of the total number of electrons in plasma volume V over the total electron efflux from the plasma through the LCFS A :

$$\tau_p = \frac{\int_V n_e dV}{|\int_A \vec{\Gamma}_e \cdot d\vec{A}|} = \frac{\int_V n_e dV}{|\int_A \vec{\Gamma}_n \cdot d\vec{A}|} = \frac{\int_0^a r n_e dr}{a |\vec{\Gamma}_n(a)|} = \frac{\int_0^a r n_e dr}{a |\vec{V}_n| n_n(a)} \quad (5.13)$$

Here the fact is used that the electron efflux from the plasma is equal to the neutral flux into the plasma in steady state. An expression for $n_n(a)$ depending on τ_p is therefore found:

$$n_n(a) = \frac{\int_0^a r n_e dr}{a |\vec{V}_n| \tau_p} \quad (5.14)$$

In general the lower limit for τ_p is set by τ_E , the energy confinement time. In this simulation it is assumed that $\tau_p = \tau_E$, where τ_E is obtained from the kinetic measurements of the TS diagnostic using the steady state definition:

$$\tau_E = \frac{W}{P} \quad (5.15)$$

where W is the kinetic energy:

$$W = \frac{3}{2} \int_V (p_e + p_i) dV \quad (5.16)$$

The power (P) is a sum of Ohmic (P_Ω) and NBI power (P_{NBI}). The ion pressure profile (p_i) is assumed to have the same shape as the electron pressure (p_e) measured by TS. The central value $p_i(0)$ is obtained from measurements of the ion temperature (T_i) by the neutral particle analyser [24] and assuming quasi-neutrality in the plasma: $p_i/p_i(0) = p_e/p_e(0)$. Z_{eff} is estimated to be of order of 1.8, which corresponds to a dilution factor of 0.93. The fast ions are excluded from the calculation. The pressure is assumed to be constant on a flux surface, so that the total energy content, W , is an integration over the plasma volume (V) which has an elongation κ .

The n_e and n_n profiles are now obtained in steady state and thus the source S can be calculated. Equation (5.2) then yields the electron flux $\vec{\Gamma}_e$. With the equation for \vec{V} , (5.6), the diffusion profile, $D_L(r)$, can be derived in L-mode after setting D_c at a sensibly chosen value based on results of other transport studies.

Transient H-mode phase

H-mode is a transient phase. $D(r)$ during this phase will be related to the outcome of the steady state phase. During H-mode $D(r)$ at the edge ($r \geq r_{ETB}$) will be reduced according to:

$$D_H(r) = \begin{cases} D_L(r) & : r < r_{ETB} \\ D_L(r_{ETB}) & : r_{ETB} \leq r \leq a \end{cases} \quad (5.17)$$

in order to simulate the ETB. The pinch velocity term is kept constant ($\vec{V}_H(r) = \vec{V}_L(r)$). With these settings the time evolution of n_e is calculated during H-mode.

The neutral density is calculated through (5.10). Solving (5.8) and (5.9) produces $n_{n,ion}$. Results from the DOUBLE code show that the central neutral density, which is governed by charge-exchange processes, decreases for increasing n_e . Therefore, an estimate of $n_{n,cx}$ is obtained by scaling the stationary solution for the increasing electron density using \bar{n}_e .

Numerics

The simulations take place on a two-dimensional grid of space and time. The appendices describe the transport equations on this grid, the solutions to these equations, the boundary conditions that are set and an analytical solution to a simplification of the problem, which among other things can be used to test the numerics of the model.

5.5 Modelling results

The transport model described above has been used to analyse the profiles from figure 5.1. The L-mode profile is used as the steady state profile; the profile measured 58 ms in H-mode is the profile used to match the outcome of the transport simulation to. A comparison of the predictions to the other two profiles will be made later on. The results of this modelling are shown in figure 5.10.

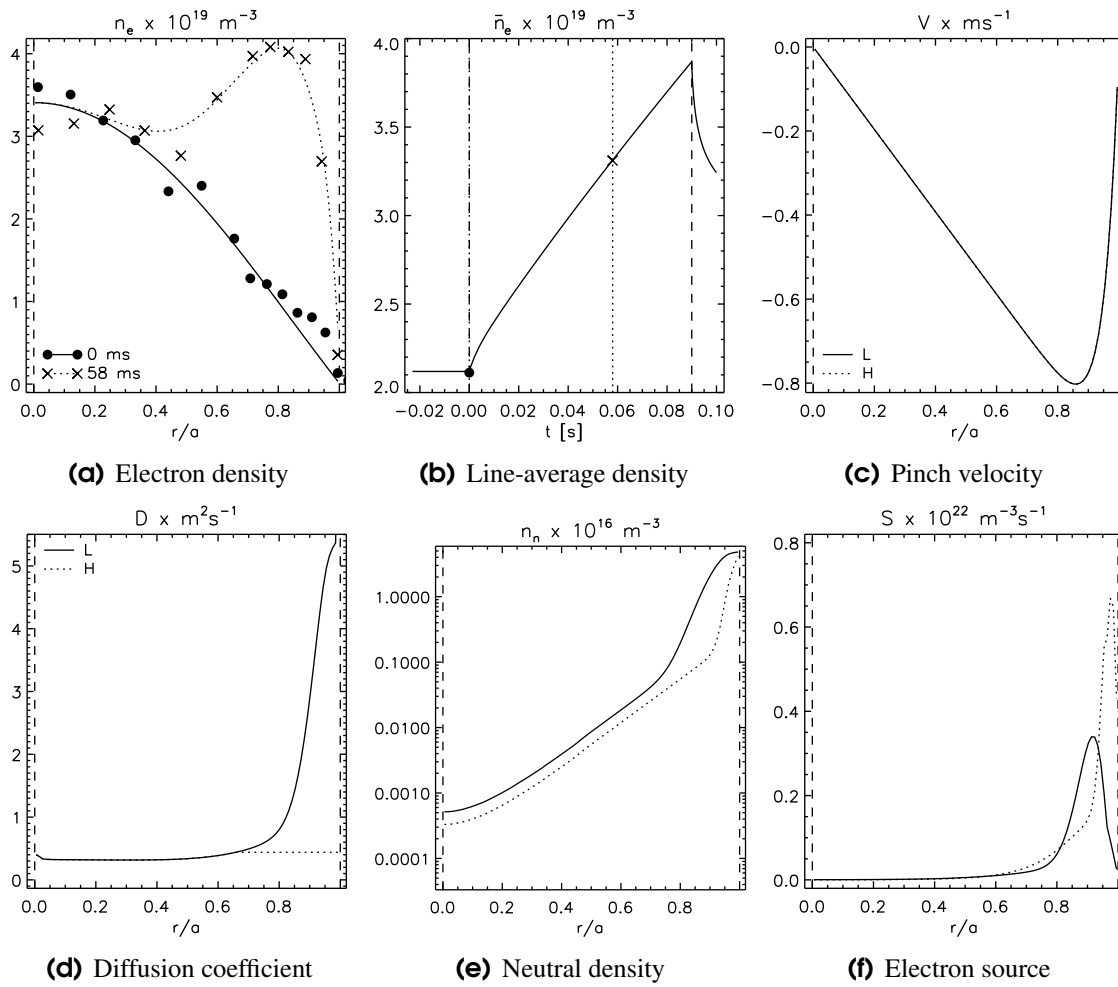


Figure 5.10: Results obtained from the 1-D phenomenological transport model.

Steady state L-mode solution

The focus is on the L-mode discharge first. For this discharge it is found (using (5.15)) that $\tau_E = 19$ ms. The plasma current and line-average density vary less than 5% within $2\tau_E$ around the time of the TS profile measurement (see figure 5.6(a)). The n_e profile is therefore assumed to be measured in a steady state plasma.

This discharge shows a pedestal density of $0.5 \times 10^{19} \text{ m}^{-3}$. The pedestal built up during the attempts to enter H-mode prior to the profile measurement of this discharge, hence the small increase in $\bar{n}_e \ell$ during L-mode shown in figure 5.7. In order to leave out these contributions to the profile, the pedestal has been left out at the start of the simulation.

Using $\tau_p = \tau_E$ and (5.14) yields $n_n(a) = 4.4 \times 10^{16} \text{ m}^{-3}$. Equation (5.14) is based on $n_{n,ion}$ only, but in calculating $n_n(a)$ the contribution of the charge-exchange term $n_{n,cx}$ has also been taken into account, thereby preventing an overestimation of $n_n(a)$. The obtained value for $n_n(a)$ is a factor of two lower than recent estimates of the neutral density, which used D_α emission measurements, for an average discharge. However, such measurements were not available at the time of the discharges used here. Increasing $n_n(a)$ will lead to unrealistically low values of τ_p , (5.14), with τ_p dropping below τ_E .

In order for the neutral density profile of (5.12) to match the DOUBLE simulations at the edge of the plasma, an inward flux velocity of $|\vec{V}_n| = 5.8 \text{ km s}^{-1}$ is used, this corresponds to a

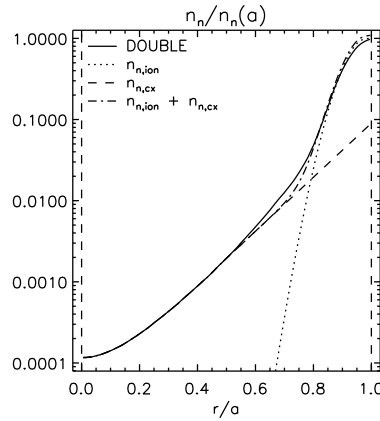


Figure 5.11: Comparison of the neutral density profiles of (5.12) with the DOUBLE solution for the L-mode discharge.

particle energy of $E_n = 0.33$ eV. Similar values have been obtained on other fusion devices [30]. Figure 5.11 compares this solution with the results using the DOUBLE code. Since (5.11) does not take the charge-exchange contributions into account, (5.12) only describes $n_{n,ion}$. The $n_{n,cx}$ profile is added to $n_{n,ion}$ to match the DOUBLE result.

The diffusion coefficient control factor has been set to $D_c = 0.4$ m²s⁻¹ and the $\vec{V}(r)$ shaping factor set to $\lambda = 20$ to produce a \vec{V} profile that is linear with r for most of the plasma. This results in a peak value of $|\vec{V}| = 0.8$ ms⁻¹ at $r/a = 0.86$ (see figure 5.10(c)). This peak increases linearly with D_c . $D_L(r)$ varies around 0.32 m²s⁻¹ for most of the inner plasma and climbs towards ~ 5.5 m²s⁻¹ at the LCFS (see figure 5.10(d)). The λ factor only has a small effect on the diffusion coefficient profile, and mainly affects the middle range around $r/a = 0.5$. D_c mainly affects $D(r)$ in the inner regions of the plasma, while $D(r)$ at the outside remains unchanged for a wide range of values of D_c (0 – 10 m²s⁻¹). $D(r)$ towards the edge is determined in this model by the source profile, and therefore by n_e and n_n .

Transient H-mode phase

During H-mode, $D_H(r)$ is set according to (5.17) and the n_e and n_n profiles are iterated from the L-mode profiles. A good match to the experimental profile data measured at 58 ms in H-mode is obtained in both space and time (see figure 5.10(a)). This match is obtained using $r_{ETB}/a = 0.66$ so that the edge diffusivity becomes $D_{ETB} = 0.44$ m²s⁻¹ (see figure 5.10(d)). The $D(r)$ profile in H-mode is now almost uniform. The EDE can thus be formed by a reduction of the edge diffusion coefficient.

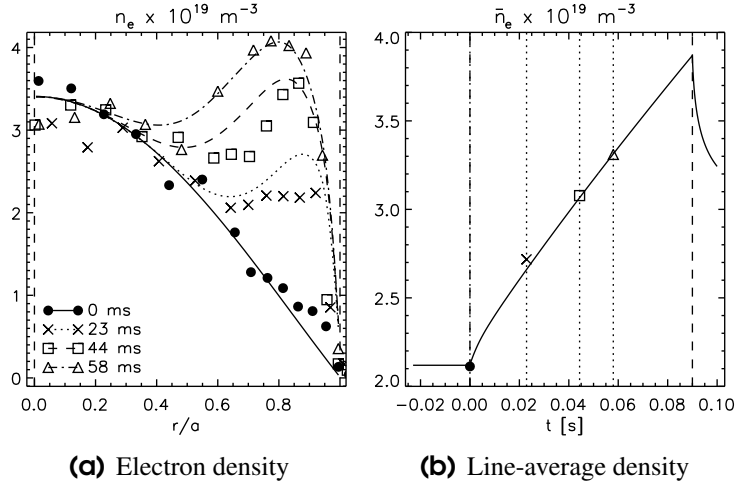
The pinch term $\vec{V}(r)$, as set during the stationary phase, plays a role in the formation of the EDE. The pinch term is required to bring the EDE further into the plasma. A too high pinch term, on the other hand, causes the central density to rise, which is not observed in the experimental data.

As a result of the increased edge n_e , n_n drops more rapidly (see figure 5.10(e)) and the source function narrows and increases in height (see figure 5.10(f)). Similar observations are made for the D_α emission profile given by $\sim \langle \sigma_{ion} v_e \rangle n_e n_n$ [28]. The narrowing and peaking of this profile is in accordance with observations of a newly installed D_α camera on MAST [28].

The particle confinement time τ_p , as given by (5.13), rises in the simulation from $\tau_p = 20$ ms at the L-H transition to $\tau_p = 39$ ms at 58 ms into H-mode. This increase is larger than the

Table 5.3: Parameters of the H-mode discharges.

discharge	Δt_H ms	Δt_{ELM} ms	$d\bar{n}_e/dt$ $10^{19} \text{ m}^{-3} \text{ s}^{-1}$	Δt_H^* ms
#2926	7	6	34.3	23
#2948	27	0	31.9	44
#2926	58	0	19.4	58

**Figure 5.12:** Results from the 1-D phenomenological transport model using the corrected ELM-free times of table 5.3.

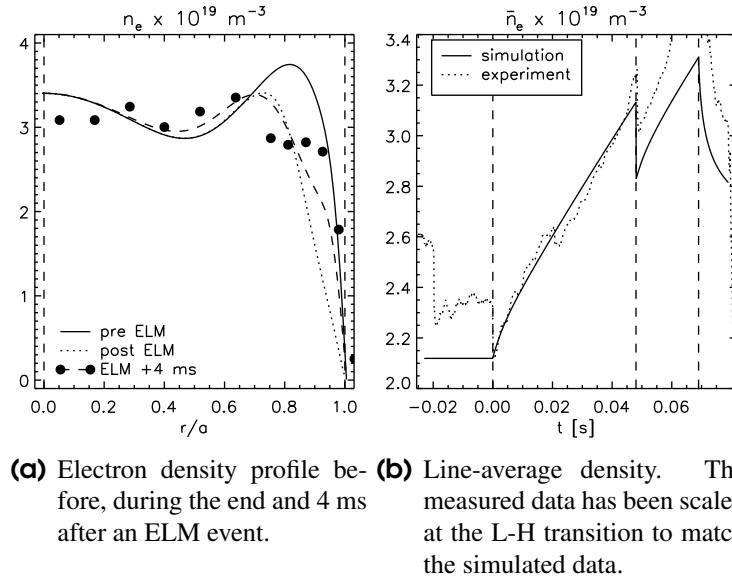
experimentally obtained value of the increase in τ_E (20 eV - 32 eV). Following the earlier made assumption $\tau_p = \tau_E$ this would mean a slight underestimation of the electron losses in this simplified transport model.

Figure 5.10(b) shows the line-average electron density as a function of time as calculated in the simulation. The behaviour is very similar to that observed in the experiments (see figure 5.7). The slope is almost linear, but has a slowly decreasing gradient. The L-mode and 58 ms H-mode profiles match the trace. The other two measurements at 7 ms and 27 ms will show densities higher than the simulation predicts. This can be accounted for by the fact that the CO₂ interferometer measurements show a higher density growth rate ($d\bar{n}_e/dt$) for these discharges.

Table 5.3 gives an overview of H-mode parameters of all H-mode discharges. The profile for discharge #2926 is measured 7 ms after the last ELM event, but the H-mode period begins with an ELMy period of $\Delta t_{ELM} = 6$ ms. The electron density is not affected by these small ELMs and thus the growth time for the density is 13 ms.

Correction of Δt_H for $d\bar{n}_e/dt$ and Δt_{ELM} yields the effective ELM-free time Δt_H^* given in table 5.3. The simulated data at these times now match the measured data (see figure 5.12). A good match to the experimental data of the two discharges without using the $d\bar{n}_e/dt$, but with the Δt_{ELM} correction is also found by widening the ETB to $r_{ETB}/a = 0.6$ and therefore reducing the diffusion coefficient to $D_{ETB} = 0.39 \text{ m}^2 \text{ s}^{-1}$.

In the simulation H-mode is ended after $\Delta t_H = 90$ ms from which time onwards $D(r)$ is set to $D_L(r)$. As a result, a fast drop in \bar{n}_e is observed, similar to the drop measured during the H-L transition (see figure 5.8(a)). The simulation eventually reaches L-mode equilibrium used as starting point, while the plasma can reach a new equilibrium depending on the plasma parameters at that stage of the discharge.



(a) Electron density profile before, during the end and 4 ms after an ELM event. (b) Line-average density. The measured data has been scaled at the L-H transition to match the simulated data.

Figure 5.13: Simulation of an ELM. The ELM is simulated by temporarily (for 0.1 ms) setting the $D(r)$ profile to the L-mode values. The ELM only affects the edge of the plasma: compare to figure 5.8.

The ELM at 294 ms shown at in figure 5.8 has been simulated in a way similar to the simulation of the H-L transition: by increasing $D(r)$ temporarily (for $\Delta t_{ELM} = 0.1$ ms) over an edge region according to:

$$D_{ELM}(r) = \begin{cases} D_L(r) & : r < r_{ELM} \\ 20 \times D_L(r) & : r_{ELM} \leq r \leq a \end{cases} \quad (5.18)$$

In this equation, $r_{ELM}/a = 0.6$ is taken from figure 5.8(b) and the factor 20 is used to match the line-integrated density measurement. To get a match to the experimental data the product of Δt_{ELM} and $D_{ELM}(r_{ELM} \leq r \leq a)$ is important, not the individual values. As a result, \bar{n}_e drops instantaneously during the ELM period and increases afterwards (see figure 5.13(b)) as observed in the measurement shown in figure 5.8(a). Figure 5.13(a) shows the simulated profiles before, during and after the ELM event compared to the measurement after the ELM. The simulated profiles are only affected in the region $r > r_{ELM}$. While the generic behaviour of the ELM is well represented, the complexity of ELM behaviour means that the exact profile is not matched perfectly.

The transport model is used to simulate the development of the n_e profile for long ELM-free periods (see figure 5.14). Initially the central density remains constant, but it increases from 60 ms onwards. A new equilibrium is reached after ~ 900 ms, at which stage the EDE has disappeared and the profile resembles a Gaussian with a pedestal, similar to the profiles observed during H-modes on other tokamaks. To date, there are no MAST data to confirm this observation, but it is likely that an MHD instability or density limit will put a hold to the rise in density, however such limits are not included in the transport model.

Another scenario which can account for the increase in edge n_e is a sudden increase of the edge neutral density during the L-H transition by means of gas-puffing. This would give rise to an increased source at the edge. A small EDE can be formed by increasing $n_n(a)$ by a factor of 10 for the duration of H-mode. This, however, increases the level of D_α radiation contrary to what is observed in the experimental data. This scenario can therefore be rejected. An increase of $n_n(a)$, during the H-mode scenario where reduced edge diffusion is introduced, increases the

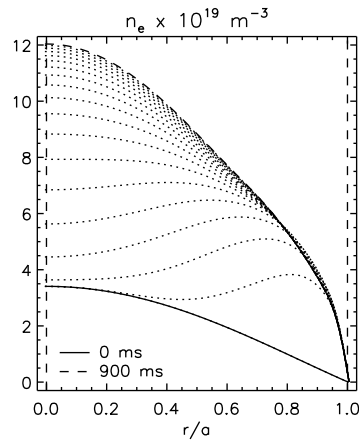


Figure 5.14: Simulation of n_e for long ELM-free periods. The time increment between the profiles is 50 ms.

height of the EDE, while the central density remains constant.

Gregoratto *et al.* [10] explain the stationary EDE in the RFX experiment using an anti-pinch term. The most obvious difference in the observation on MAST is the transient behaviour of the EDE. For that reason a comparison between the two observations cannot be made. In MAST an anti-pinch term can be ruled out because an inward pinch term is required to fuel the core of the plasma.

5.6 Summary and discussion

MAST has been equipped with a Thomson scattering system that measures T_e and n_e at 30-40 spatial points along a horizontal chord tangential to the central column once per discharge. Due to the orientation of the laser beam path, the achieved spatial resolution improves significantly for low R . The normalised-flux resolution is further enhanced by the flux surface expansion on the inboard side. The MAST TS system is therefore a powerful tool in edge gradient studies.

Transient edge density ‘ears’ (EDEs) have been observed during ELM-free periods in H-mode. A 1-D phenomenological transport model has been set up to simulate the formation of the EDEs by testing two hypotheses stated in section 5.4. This model is based on conservation of electrons and makes an heuristic approach for the description of the neutrals using simple analytic methods and results obtained from the transport code DOUBLE. The electron source arises from direct ionisation of edge neutrals and of edge neutrals that have been relocated after charge-exchange processes. The electron flux consists of a diffusive term and a convective term whose coefficients $D(r)$ and $V(r)$ are mutually dependent. The model confirms that the EDE can be formed by reducing $D(r)$ at the edge from $D = 5.5 \text{ m}^2\text{s}^{-1}$ to $D = 0.44 \text{ m}^2\text{s}^{-1}$ in H-mode to produce an almost uniform profile. As a result of the formation of the EDE, n_n drops more rapidly at the edge of the plasma. Consequently the modelled electron source sharpens. Furthermore, the D_α emissivity profile peaks as a result of the change in profiles. This is in accordance with observations of a newly installed D_α camera on MAST. An inward pinch term is required to bring the particles into the plasma and thus to shape the EDE.

Despite the simplicity of the model a good match of the simulated data to the measured data is obtained, both in space and time. A reduction of $D(r)$ at the edge is sufficient to account for the formation of the EDE during H-mode. A slightly different $D(r)$ profile can be assumed or

additional physical processes can be included to improve the match, but that will not change the basic principle behind the formation of the EDE. The results obtained from using this model provide a simple physical understanding of the formation of the EDEs and these results can form the basis for more advanced codes describing the low aspect ratio plasmas in MAST.

While the core density remains constant during H-mode in MAST for ELM-free periods shorter than $2-3\tau_p$, other machines [8] show formation of an n_e pedestal and an increase of the core density rather than an EDE. This pedestal is formed in the simulations of ELM-free periods longer than $\sim 3\tau_p$. For even longer periods the simulation shows that the EDE disappears and the profile resembles a Gaussian with a pedestal, similar to that measured on other tokamaks. A pedestal can also be simulated by increasing the inward pinch velocity. This will reduce n_e at the edge and hence remove the EDE.

The loss in \bar{n}_e due to an ELM can be modelled successfully by increasing $D(r)$ substantially (by a factor of ~ 20) at the edge of the plasma for the duration of the ELM (here 0.1 ms). By doing this, the ELM only affects the edge of the plasma, as is observed in the measured data.

Acknowledgements

Acknowledgements are addressed to P.G. Carolan, N.J. Lopes Cardozo and M. O'Mullane for the fruitful discussions, to A. Thyagaraja for the valuable input in the numerical aspect of the model, to M.R. Dunstan and M.J. Forrest for their valuable contributions in the design and development of the Thomson scattering diagnostic and to the MAST and NBI teams for providing the necessary data.

This work is jointly funded by the UK Department of Trade and Industry and the Foundation FOM with financial support of The Netherlands research organisation NWO and Euratom. The content of this publication is the sole responsibility of its publisher(s) and it does not necessarily represent the views of the Commission or its services.

Bibliography

- [1] A. Sykes et al. First physics results from the MAST Mega-Amp Spherical Tokamak. 8(5):2101–2106, May 2001.
- [2] A. Sykes et al. First results from MAST. *Nuclear Fusion*, 41(10):1423–1433, October 2001.
- [3] M.P. Gryaznevich. First results from MAST. *Proceedings of the 27th EPS Conference on Controlled Fusion and Plasma Physics*, 2000.
- [4] R. Akers et al. L-H transition in the Mega-Amp Spherical Tokamak. *Physical Review Letters*, 88(3):035002–1–035002–4, 21 January 2002.
- [5] A. Sykes et al. H-Mode operation in the START spherical tokamak. *Physical Review Letters*, 84(3):495–498, January 2000.
- [6] R.E. Bell et al. Kinetic profile in NSTX plasmas. In *Proceedings of the 28th EPS Conference on Controlled Fusion and Plasma Physics*, volume 25A, pages 1021–1024, 2001.

- [7] E.A. Lazarus et al. The role of shaping in achieving high performance in DIII-D. In *Proceedings of the 15th International Conference on Plasma Physics and Controlled Nuclear Fusion Research*, volume 1, page 609, 1995. IAEA-CN-60/A5-1.
- [8] F. Wagner et al. Regime of improved confinement and high beta in neutral beam heated divertor discharges of the ASDEX tokamak. *Physical Review Letters*, 49, 1982.
- [9] G.W. Pacher et al. H-mode operation in ITER: determination of trajectories in edge operation space. In *Proceedings of the 28th EPS Conference on Controlled Fusion and Plasma Physics*, volume 25A, pages 625–628, 2001.
- [10] D. Gregoratto, L. Garzotti, P. Innocente, S. Martini, and A. Canton. Behaviour of electron density profiles and particle transport analysis in the RFX reversed field pinch. *Nuclear Fusion*, 38(8):1199–1213, 1998.
- [11] M.J. Walsh et al. Combined visible and infrared Thomson scattering on the MAST experiment. *Review of Scientific Instruments*, 74(3), March 2003.
- [12] M.J. Walsh et al. Interactive Optical Design and Realisation of an Optimised CCD Thomson Scattering System for the Spherical Tokamak START. *Review of Scientific Instruments*, 70(1):742–746, January 1999.
- [13] D. Johnson, D. Dimock, B. Grek, R. Palladino, and E. Tolnas. Alignment of TFTR Thomson scattering system. *Review of Scientific Instruments*, 63(10):4954–4956, October 1992.
- [14] M. Mattioli. Incoherent light scattering from high temperature plasmas. *EUR-CEA-FC-752*, 1974.
- [15] A.C. Selden. Simple analytic form of the relativistic Thomson scattering spectrum. *Physics Letters*, 79A(5,6), October 1980.
- [16] P. Nielsen. Thomson scattering in high temperature devices. In *Diagnostics for fusion reactor conditions*, volume 1, pages 225–259, Varenna, Italy, September 1982. Commission of the European communities.
- [17] ITER Physics Expert Groups on Confinement and Transport and Confinement Modelling and Database, ITER Physics Basis Editors, ITER EDA, and Naka Joint Work Site. Plasma confinement and transport. *Nuclear Fusion*, 39(12):2175–2249, 1999.
- [18] R.J. Akers et al. Confinement in L and H-Mode MAST plasmas. In *Proceedings of the 28th EPS Conference on Controlled Fusion and Plasma Physics*, volume 25A, pages 581–584, 18-22 June 2001.
- [19] L.L. Lao, H. St. John, R.D. Stambaugh, A.G. Kellman, and W.W. Pfeiffer. *Nuclear Fusion*, 25:1611, 1985.
- [20] V. Shevchenko et al. EBW observations on COMPASS-D and MAST. In *Proceedings of the 28th EPS Conference on Controlled Fusion and Plasma Physics*, volume 25A, pages 1285–1288, June 2001.
- [21] N.J. Lopes Cardozo et al. Electron thermal transport in rtp; filaments, barriers and bifurcations. *Plasma Physics and Controlled Fusion*, 39:B303–B316, 1997.

- [22] K. Behringer et al. *Bulletin of the American Physical Society*, 26:887, 1981.
- [23] K.A. Karelse. *Particle convection in thermonuclear plasmas*. PhD thesis, Technische Universiteit Eindhoven, 2001.
- [24] C. Byrom. *Thermal & Fast Ion Behaviour in the MAST Experiment*. PhD thesis, Department of Physics, University of Manchester Institute of Science and Technology, Manchester, 2002.
- [25] Yu.N. Dnestrovskij et al. *Nuclear Fusion*, 19:293, 1979.
- [26] R.L. Freeman and E.M. Jones. Atomic collision processes in plasma physics experiments. (CLM-R 137), May 1974.
- [27] D.E. Post et al. Steady-state radiative cooling rates for low-density high-temperature plasmas. *Atomic data and nuclear data tables*, 20:397–439, 1977.
- [28] M.R. Tournianski, P.G. Carolan, N.J. Conway, E.R. Arends, and M.J. Walsh. Use of 1D D_α camera to measure edge electron density gradients. *Review of Scientific Instruments*, 73(3), March 2003.
- [29] E.U. Condon. *Physical Review*, 32:858–872, 1928.
- [30] Ph. Mertens et al. Hydrogen release from plasma-facing components into fusion plasmas - recent results from a spectroscopic approach. *Plasma Physics and Controlled Fusion*, 43:A349–A373, 2001.
- [31] E. Isaacson and H. Bishop Keller. *Analysis of numerical methods*. John Wiley & Sons, Inc, New York — London — Sydney.
- [32] F. Bowman. *Introduction to Bessel Functions*. Dover Publications Inc., New York, 1958.

5.A Numerics

These are the differential equations for the electrons and the neutrals following from (5.1) and (5.8) to solve:

$$\frac{\partial n_e}{\partial t} = \frac{1}{r} \frac{\partial}{\partial r} \left(rD \frac{\partial n_e}{\partial r} - rVn_e \right) + \langle \sigma_{ion} v_e \rangle n_n n_e \quad (5.19)$$

$$\frac{\partial n_n}{\partial t} = \frac{1}{r} \frac{\partial}{\partial r} (-rVn_n) - \langle \sigma_{ion} v_e \rangle n_n n_e \quad (5.20)$$

The equations are solved on a two-dimensional grid where the first dimension is space and the second dimension is time. The space dimension gets index i , the time dimension index j . The electron density at grid point $[i, j]$ ($n_{e,i,j}$) will be calculated from the n_e in the neighbouring space points $[i-1, j]$ and $[i+1, j]$ and time point $[i, j-1]$ as indicated in figure 5.15. The plasma centre ($r=0$) is located in between space grid points 0 and 1. The LCFS ($r=a$) is

located in between space grid points $N_i - 2$ and $N_i - 1$. The differential equations on the grid for $1 < i < N_i - 2$ now become:

$$\begin{aligned} & \frac{n_{e,i,j} - n_{e,i,j-1}}{\Delta t} = \\ & \frac{1}{r_i \Delta r} \left(r_{i+\frac{1}{2}} D_{i+\frac{1}{2}} \left(\frac{n_{e,i+1,j} - n_{e,i,j}}{\Delta r} \right) - r_{i-\frac{1}{2}} D_{i-\frac{1}{2}} \left(\frac{n_{e,i,j} - n_{e,i-1,j}}{\Delta r} \right) \right) + \\ & - \frac{1}{r_i \Delta r} \left(r_{i+\frac{1}{2}} V_{i+\frac{1}{2}} n_{e,i+1,j} - r_{i-\frac{1}{2}} V_{i-\frac{1}{2}} n_{e,i,j} \right) + \\ & \langle \sigma_{ion} \mathbf{v}_e \rangle_i n_{n,i,j-1} n_{e,i,j-1} \end{aligned} \quad (5.21)$$

$$\begin{aligned} & \frac{n_{n,i,j} - n_{n,i,j-1}}{\Delta t} = \\ & - \frac{1}{r_i \Delta r} \left(r_{i+\frac{1}{2}} V_{n,i+\frac{1}{2}} n_{n,i+1,j} - r_{i-\frac{1}{2}} V_{n,i-\frac{1}{2}} n_{n,i,j} \right) + \\ & - \langle \sigma_{ion} \mathbf{v}_e \rangle_i n_{n,i,j} n_{e,i,j} \end{aligned} \quad (5.22)$$

Where:

$$r_{i\pm\frac{1}{2}} = \frac{r_i + r_{i\pm 1}}{2} \quad (5.23)$$

$$D_{i\pm\frac{1}{2}} = \frac{D_i + D_{i\pm 1}}{2} \quad (5.24)$$

$$V_{i\pm\frac{1}{2}} = \frac{V_i + V_{i\pm 1}}{2} \quad (5.25)$$

After sorting terms this becomes:

$$\begin{aligned} & \left(1 + \frac{\Delta t}{r_i \Delta r^2} \left(D_{i+\frac{1}{2}} r_{i+\frac{1}{2}} + D_{i-\frac{1}{2}} r_{i-\frac{1}{2}} \right) - \frac{\Delta t}{r_i \Delta r} r_{i-\frac{1}{2}} V_{i-\frac{1}{2}} \right) n_{e,i,j} = \\ & + \left(\frac{\Delta t}{r_i \Delta r^2} D_{i+\frac{1}{2}} r_{i+\frac{1}{2}} - \frac{\Delta t}{r_i \Delta r} r_{i+\frac{1}{2}} V_{i+\frac{1}{2}} \right) n_{e,i+1,j} + \\ & + \left(\frac{\Delta t}{r_i \Delta r^2} D_{i-\frac{1}{2}} r_{i-\frac{1}{2}} \right) n_{e,i-1,j} + \\ & + \left(1 + \Delta t \langle \sigma_{ion} \mathbf{v}_e \rangle_i n_{n,i,j-1} \right) n_{e,i,j-1} \end{aligned} \quad (5.26)$$

$$\begin{aligned} & \left(1 - \frac{\Delta t}{r_i \Delta r} r_{i-\frac{1}{2}} V_{n,i-\frac{1}{2}} + \Delta t \langle \sigma_{ion} \mathbf{v}_e \rangle_i n_{e,i,j} \right) n_{n,i,j} = \\ & - \frac{\Delta t}{r_i \Delta r} r_{i+\frac{1}{2}} V_{n,i+\frac{1}{2}} n_{n,i+1,j} + \\ & + n_{n,i,j-1} \end{aligned} \quad (5.27)$$

This can be rewritten into:

$$n_{e,i,j} = A_i^+ n_{e,i+1,j} + A_i^- n_{e,i-1,j} + S_{e,i} \quad (5.28)$$

$$n_{n,i,j} = B_i^+ n_{n,i+1,j} + S_{n,i} \quad (5.29)$$

Where:

$$A_i^+ = \frac{\frac{r_{i+\frac{1}{2}}}{r_i} \left(\frac{\Delta t}{\Delta r^2} D_{i+\frac{1}{2}} - \frac{\Delta t}{\Delta r} V_{i+\frac{1}{2}} \right)}{1 + \frac{\Delta t}{\Delta r^2} \left(D_{i+\frac{1}{2}} \frac{r_{i+\frac{1}{2}}}{r_i} + D_{i-\frac{1}{2}} \frac{r_{i-\frac{1}{2}}}{r_i} \right) - \frac{r_{i-\frac{1}{2}}}{r_i} \frac{\Delta t}{\Delta r} V_{i-\frac{1}{2}}} \quad (5.30)$$

$$A_i^- = \frac{\frac{r_{i-\frac{1}{2}}}{r_i} \frac{\Delta t}{\Delta r^2} D_{i-\frac{1}{2}}}{1 + \frac{\Delta t}{\Delta r^2} \left(D_{i+\frac{1}{2}} \frac{r_{i+\frac{1}{2}}}{r_i} + D_{i-\frac{1}{2}} \frac{r_{i-\frac{1}{2}}}{r_i} \right) - \frac{r_{i-\frac{1}{2}}}{r_i} \frac{\Delta t}{\Delta r} V_{i-\frac{1}{2}}} \quad (5.31)$$

$$S_{e,i} = \frac{(1 + \Delta t \langle \sigma_{ion} \nu_e \rangle) n_{n,i,j-1}}{1 + \frac{\Delta t}{\Delta r^2} \left(D_{i+\frac{1}{2}} \frac{r_{i+\frac{1}{2}}}{r_i} + D_{i-\frac{1}{2}} \frac{r_{i-\frac{1}{2}}}{r_i} \right) - \frac{r_{i-\frac{1}{2}}}{r_i} \frac{\Delta t}{\Delta r} V_{i-\frac{1}{2}}} n_{e,i,j-1} \quad (5.32)$$

$$B_i^+ = \frac{-\frac{r_{i+\frac{1}{2}}}{r_i} \frac{\Delta t}{\Delta r} V_{n,i+\frac{1}{2}}}{1 - \frac{r_{i-\frac{1}{2}}}{r_i} \frac{\Delta t}{\Delta r} V_{n,i-\frac{1}{2}} + \Delta t \langle \sigma_{ion} \nu_e \rangle n_{e,i,j}} \quad (5.33)$$

$$S_{n,i} = \frac{n_{n,i,j-1}}{1 - \frac{r_{i-\frac{1}{2}}}{r_i} \frac{\Delta t}{\Delta r} V_{n,i-\frac{1}{2}} + \Delta t \langle \sigma_{ion} \nu_e \rangle n_{e,i,j}} \quad (5.34)$$

It is important to note that coefficients A_i^+ , A_i^- and B_i^+ are always positive and less than 1. These are requirements to guarantee stability in the solution. The equation for $n_{e,i}$ can now be written into a tridiagonal or Jacobi matrix (the index j has been dropped for simplicity):

$$\begin{bmatrix} 1 & -A_0^+ & 0 & \dots & 0 \\ -A_1^- & 1 & \ddots & & \\ 0 & \ddots & \ddots & -A_{i-1}^+ & \\ & & -A_i^- & 1 & -A_i^+ \\ \vdots & & & -A_{i+1}^- & \ddots & \ddots & 0 \\ & & & \ddots & 1 & -A_{N_i-2}^+ \\ 0 & \dots & 0 & -A_{N_i-1}^- & 1 \end{bmatrix} \cdot \begin{bmatrix} n_{e,0} \\ \dots \\ n_{e,i-1} \\ n_{e,i} \\ n_{e,i+1} \\ \dots \\ n_{e,N_i-1} \end{bmatrix} = \begin{bmatrix} S_{e,0} \\ \dots \\ S_{e,i-1} \\ S_{e,i} \\ S_{e,i+1} \\ \dots \\ S_{e,N_i-1} \end{bmatrix} \quad (5.35)$$

This matrix equation can be solved using standard procedures [31]. The boundary conditions are set through elements A_0^+ , $A_{N_i-1}^-$, $S_{e,0}$ and S_{e,N_i-1} :

$$n_{e,0} = n_{e,1} \Leftrightarrow A_0^+ = 1 \wedge S_{e,0} = 0 \quad (5.36)$$

$$n_{e,N_i-1} = 1 \times 10^{17} \text{m}^{-3} \Leftrightarrow A_{N_i-1}^- = 0 \wedge S_{e,N_i-1} = n_{e,N_i-1} \quad (5.37)$$

The equation for $n_{n,i}$ can be equated directly from the higher neighbour. The boundary condition set here is the edge neutral density:

$$n_{n,N_i-1} = n_n(a) \quad (5.38)$$

Steady state L-mode solution

In the steady state L-mode $n_{e,i,0}$ and $V_{i,0}$ are known, therefore, the following equations are solved for $n_{n,i,0}$ and $D_{i,0}$:

$$0 = \frac{1}{r_i \Delta r} \left(D_{i+\frac{1}{2}} r_{i+\frac{1}{2}} \left(\frac{n_{e,i+1,0} - n_{e,i,0}}{\Delta r} \right) - D_{i-\frac{1}{2}} r_{i-\frac{1}{2}} \left(\frac{n_{e,i,0} - n_{e,i-1,0}}{\Delta r} \right) \right) + \\ - \frac{1}{r_i \Delta r} \left(r_{i+\frac{1}{2}} V_{i+\frac{1}{2}} n_{e,i+1,0} - r_{i-\frac{1}{2}} V_{i-\frac{1}{2}} n_{e,i,0} \right) + \\ \langle \sigma_{ion} \nu_e \rangle n_{n,i,0} n_{e,i,0} \quad (5.39)$$

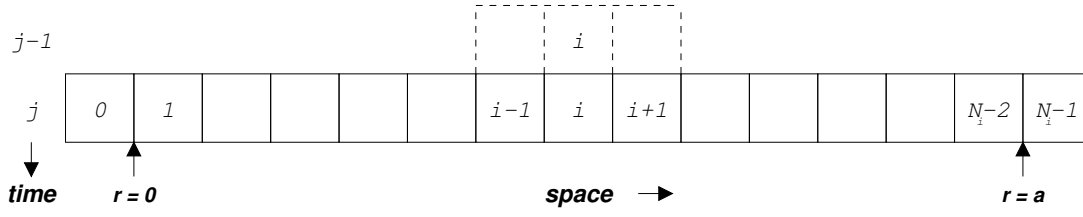


Figure 5.15: Space-time grid used for the transport simulations. Index i corresponds to space, index j to time.

$$0 = -\frac{1}{r_i \Delta r} \left(r_{i+\frac{1}{2}} V_{n,i+\frac{1}{2}} n_{n,i+1,0} - r_{i-\frac{1}{2}} V_{n,i-\frac{1}{2}} n_{n,i,0} \right) + \quad (5.40)$$

$$-\langle \sigma_{ion} v_e \rangle_i n_{n,i,0} n_{e,i,0}$$

Firstly, for $n_{n,i,0}$ is found:

$$n_{n,i,0} = \frac{r_{i+\frac{1}{2}} V_{n,i+\frac{1}{2}}}{r_{i-\frac{1}{2}} V_{n,i-\frac{1}{2}} - r_i \Delta r \langle \sigma_{ion} v_e \rangle_i n_{e,i,0}} n_{n,i+1,0} \quad (5.41)$$

$$n_{n,N_i-1,0} = n_n(a) \quad (5.42)$$

$$n_{n,0,0} = n_{n,1,0} \quad (5.43)$$

Then for $D_{i,0}$ is found:

$$D_{i+\frac{1}{2}} = D_{i-\frac{1}{2}} \frac{\frac{r_{i-\frac{1}{2}}}{\Delta r} (n_{e,i,0} - n_{e,i-1,0}) + \gamma \frac{r_{i-\frac{1}{2}}^2}{a^2} n_{e,i,0}}{\frac{r_{i+\frac{1}{2}}}{\Delta r} (n_{e,i+1,0} - n_{e,i,0}) + \gamma \frac{r_{i+\frac{1}{2}}^2}{a^2} n_{e,i+1,0}} + \quad (5.44)$$

$$-\frac{r_i \Delta r \langle \sigma_{ion} v_e \rangle_i n_{n,i,0} n_{e,i,0}}{r_{i+\frac{1}{2}}^2 (n_{e,i+1,0} - n_{e,i,0}) + \gamma \frac{r_{i+\frac{1}{2}}^2}{a^2} n_{e,i+1,0}}$$

$$D_{\frac{3}{2}} = D_{\frac{1}{2}} = D_c \quad (5.45)$$

$$D_i = 2D_{i-\frac{1}{2}} - D_{i-1} \quad (5.46)$$

$D_{\frac{3}{2}}$ is set as a boundary condition rather than $D_{\frac{1}{2}}$ since the former is independent of the latter according to (5.44) ($r_{\frac{1}{2}} = 0$).

Transient H-mode phase

During the transient H-mode phase the following sequence of calculations is carried out for each time step:

1. (5.28) is solved to give n_e
2. (5.29) is solved to give $n_{n,ion}$
3. $n_{n,cx}$ is scaled for \bar{n}_e
4. n_n is calculated using (5.10)

For the first time step the steady state L-mode solution is used as an input. Boundary conditions are applied as described above.

5.B Simplified analytical solution

To test the numerics of the transport model an analytical solution of the equations for particle conservation is found. The following simplifications are made to achieve this:

- $n_n(a) = 0$ so that $S(r) = 0$
- uniform D : $D(r) = D(0)$
- no convection: $V = 0$

In this way (5.19) reduces to:

$$\frac{\partial n_e}{\partial t} = \frac{1}{r} \frac{\partial}{\partial r} \left(rD \frac{\partial n_e}{\partial r} \right) \quad (5.47)$$

The general solution to this equation, using initial condition:

$$n_e(r, 0) = \phi(r), (0 < r < a) \quad (5.48)$$

and boundary condition:

$$n_e(a, t) = 0, (t > 0) \quad (5.49)$$

can be found using the separation of variables technique to be [32]:

$$n_e(r, t) = \sum_{m=1}^{\infty} A_m e^{-\frac{\gamma_m^2 D}{a^2} t} J_0 \left(\frac{\gamma_m r}{a} \right) \quad (5.50)$$

where the sum extends over all positive roots, γ , of the equation $J_0(x) = 0$ and:

$$A_m = \frac{2}{J_1^2(\gamma)} \int_0^1 x \phi(ax) J_0(\gamma x) dx \quad (5.51)$$

This solution is a set of eigenfunctions with time and radial dependence. In a simple test case the initial condition reduces to:

$$\phi(r) = A_1 J_0 \left(\frac{\gamma_1 r}{a} \right) \quad (5.52)$$

using $A_m = 0$ ($m \geq 2$) and $A_1 = n_e(0, 0)$. The solution of this becomes:

$$n_e(r, t) = e^{-\frac{\gamma_1^2 D}{a^2} t} \phi(r) \quad (5.53)$$

which is a simple exponential decay that can easily be verified numerically in order to check the numerics of the model.

Chapter 6

High-resolution Thomson scattering in MAST

A single-pulse high-resolution Thomson scattering system has been installed on MAST. It measures the electron temperature and density profiles at ~ 300 spatial points along a horizontal chord in the midplane of the plasma. It upgrades the previously installed lower resolution system. The new system uses a ~ 10 J Q-switch ruby laser with a divergence of 0.5 mrad. The scattered light is relayed by means of fibre-optics to a grating spectrometer and detection system. The system is fully automatic for every MAST plasma discharge and requires little adjustment. The measurement accuracy is typically $< 5\%$ of T_e and $< 4\%$ of n_e in the range 40 eV - 2 keV for a density of $n_e \sim 4 \times 10^{19} \text{ m}^{-3}$. Due to the orientation of the laser beam path and of the collection optics, good scattering geometry and high normalised-flux resolution are achieved, especially at the inboard edge and in the magnetic centre.

6.1 Introduction

The regime which is of most interest in operating the tokamak is the high-confinement regime (H-mode), in which confinement is improved due to the reduced radial energy transport out of the plasma. The reduction is mainly concentrated at the edge of the plasma, the so-called edge transport barrier (ETB). Therefore, steep gradients in electron temperature (T_e) and electron density (n_e) can be observed in those regions (see Chapter 5). In improved confinement scenarios on other machines it has been shown that transport coefficients can also be reduced at localised positions deeper into the plasma, the internal transport barriers (ITBs).

On the basis of measurements of density fluctuations in many tokamaks (see *e.g.* [1]) as well as theoretical analyses of magnetic islands (see *e.g.* [2]), it can be expected that microscopic structures in T_e and n_e with a size as small as the ion Larmor radius (ρ_i) could be present in tokamak plasmas. Because of the low magnetic field in MAST ($B_\phi \sim 1.8$ T high field side to $B_\phi \sim 0.4$ T low field side), the ion Larmor radius is expected to vary from $\gtrsim 1$ mm at the plasma edge to $\gtrsim 1$ cm at the plasma centre. The size of a magnetic island in MAST is predicted to be ~ 40 mm [3]. The steep gradients that develop during H-mode are expected to be affected, on a fine scale, by so-called edge localised modes (ELMs). In order to detect structure on these scales, high demands are placed on the spatial resolution of a profile diagnostic such as Thomson scattering (TS).

In order to study these localised phenomena a multi-position Thomson scattering system has been installed on MAST. The system combines high resolution with good measurement accuracy. Figure 6.1(a) shows an example of a TS measurement of T_e and n_e in MAST. The mea-

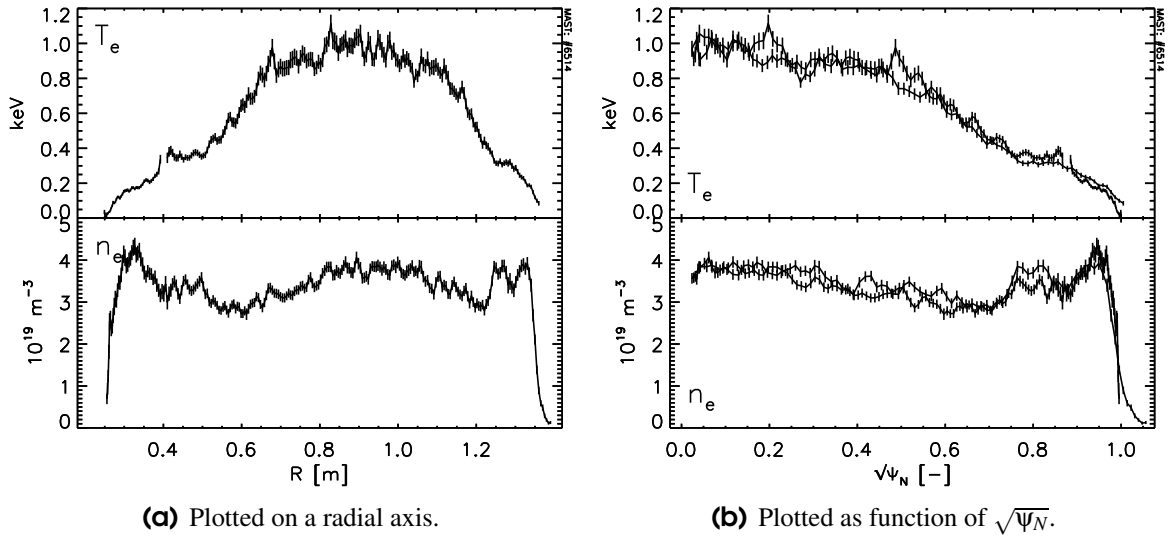


Figure 6.1: Example profiles of T_e and n_e during the high-confinement mode in MAST. The T_e profile shows a ~ 180 eV pedestal, $m = 2$ magnetic island and asymmetric structures in the plasma centre. The n_e profile shows steep edge gradients, EDEs and the $m = 2$ island.

surement is taken during the ELM-free phase of an H-mode plasma heated by neutral particle beam injection (NBI). The apparent asymmetry in the profiles is caused by the large Shafranov shift, a feature of the spherical tokamak design. However, the profiles are highly symmetric, up to small detail, when plotted as function of flux coordinate as shown in figure 6.1(b). Here the profile is plotted as function of the square root of the normalised flux ($\sqrt{\psi_N}$), which causes the axis to be approximately linear with the minor radius. The normalised flux is defined as $\psi_N = (\psi_0 - \psi) / (\psi_0 - \psi_a)$, where ψ is the magnetic flux and ψ_0 and ψ_a are the magnetic flux at the magnetic axis and at the last closed flux surface respectively. The T_e profile shows a ~ 180 eV pedestal, a flattening at $\sqrt{\psi_N} = 0.8$, as well as smaller asymmetric structures in the plasma centre, *e.g.* at $\sqrt{\psi_N} = 0.2$ and at $\sqrt{\psi_N} = 0.5$. The flattening is identified by the magnetics data as a magnetic island of $m = 2$ characteristic. The n_e profile shows the steep edge gradients and a phenomenon called the edge density ‘ear’ (EDE) [4] (see Chapter 5), which are typical features of ELM-free H-mode. The $m = 2$ island can also be identified on the n_e profile, where an increase of density is observed inside the island. These features are revealed thanks to the high spatial resolution of the TS system.

This chapter gives a detailed description of the diagnostic, discussing the hardware, calibrations, data processing and error analysis. This is followed by a discussion of the resolution of the system and the highlighting of some issues worth considering when examining the profiles. Finally, some examples of profile measurements in MAST are presented.

6.2 Instrumental setup

6.2.1 Hardware

The Thomson scattering system used on MAST is similar to that used on the START tokamak [5]. During the first 2 campaigns on MAST, from January 2000 to September 2001, the system ran on a lower resolution with up to 40 spatial points [4] (see Chapter 5). The current system, which became operational in October 2001, is an upgrade of that system giving a higher

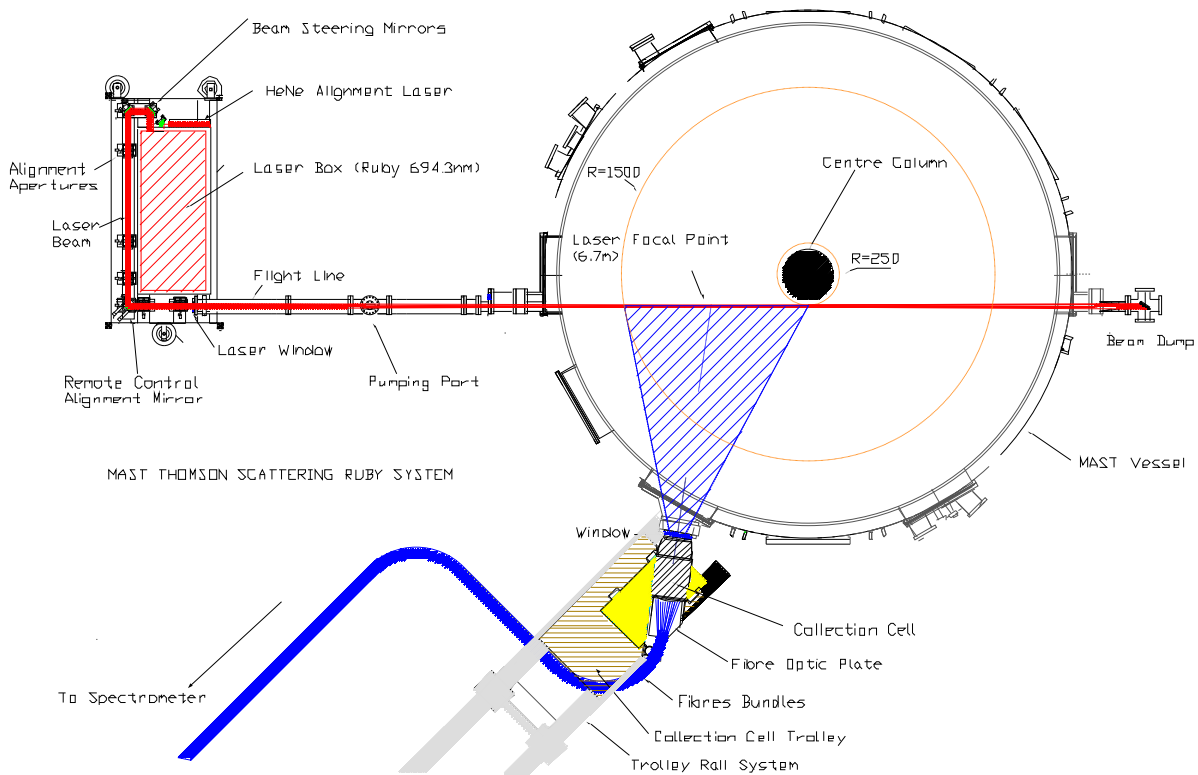


Figure 6.2: Overview of the ruby laser beam path and the light collection optics on MAST.

resolution, up to 300 spatial points, and full plasma coverage.

Figure 6.2 shows a top view of the MAST vessel and the Thomson scattering system. A laser pulse crosses the plasma just below the midplane of the vessel and is absorbed by a beam dump. The Thomson scattered light is collected by a lens and relayed to a spectrometer by means of fibre-optics. The dispersed light is recorded simultaneously for all spatial channels by a detection unit and transferred to a computer system for analysis.

Ruby laser

The light source is a Q-switched ruby ($\lambda_0 = 694.3 \text{ nm}$) oscillator/amplifier system (see figure 6.3) which produces one laser pulse per MAST plasma discharge. The laser pulse has an energy of $\sim 10 \text{ J}$, a pulse width of 30 ns and a beam divergence of 0.5 mrad. The alignment is maintained using HeNe lasers arranged to be co-axial with the ruby laser and drop-in targets that act as reference markers.

Flight line

The laser beam passes a flight line that is mounted on the MAST vessel. The prime function of the flight line is to reduce the amount of stray light entering the vessel by collimating the beam. The entrance window is made of silica glass and positioned at the Brewster angle with respect to the laser beam to minimise reflections off the window surface. The window is facing downwards to avoid accumulation of dust on the surface. The window allows the beam to be transmitted very efficiently without the need for special coatings whilst simultaneously reducing the risk of damaging the laser window thanks to the angle-increased surface area. A number of

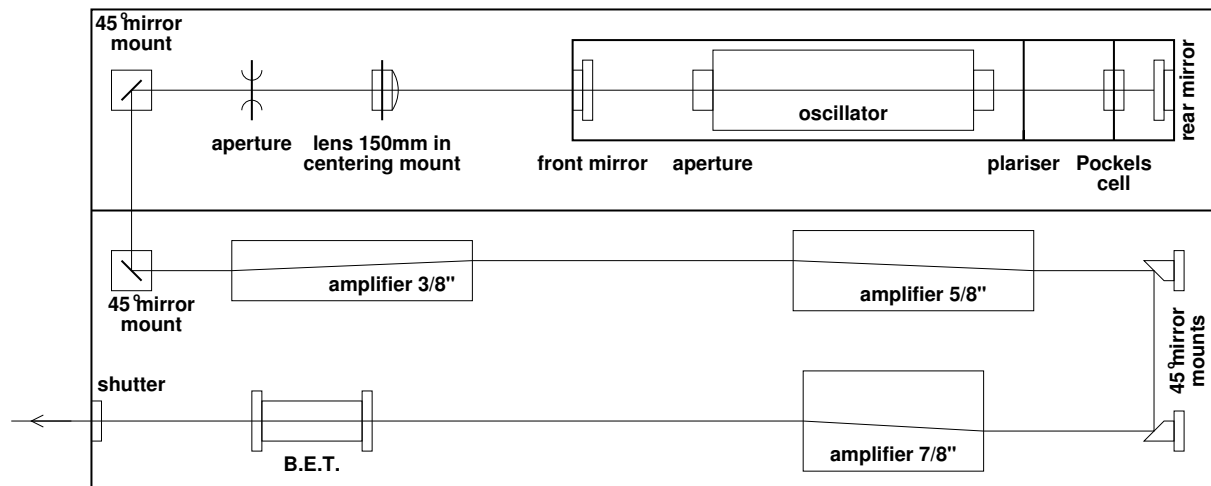


Figure 6.3: Layout of Q-switched ruby oscillator/amplifier laser system.

apertures in the flight line block any stray light that might be produced. The flight line is fitted with viewing ports at the positions of the apertures, thus giving the opportunity to monitor the passing of the beam through the apertures. A vacuum pump keeps the flight line at a pressure equivalent to the vessel pressure.

Inside the vessel, the laser beam crosses the plasma 14.5 mm below the midplane, this distance is small compared to a typical plasma vertical extend of over 2 m. The beam is focussed towards the plasma centre using a 4 m plano-convex lens and passes the central column at close distance (~ 45 mm) to obtain a good scattering geometry.

Beam dump

The beam is finally absorbed by a laser dump that is located close to the machine vessel wall. A graphite laser dump appeared to be sufficient to tolerate the high-power densities placed upon it due to the close proximity of the laser focus to the dump. The graphite dump can also be used for a second TS system installed on MAST that uses Nd:YAG lasers which are coaxial with the ruby system [6]. The beam dump can be retracted to allow HeNe alignment checks.

Light collection

Thomson scattered light from scattering angles in the range $74.6^\circ - 117.6^\circ$ is collected by the collection lens ($f/14.9$). A polariser sheet is placed in front of the lens in order to reduce the non-polarised background light by almost 50% while having a minimal affect affect in the scattered light. The lens focuses the light onto the fibre-bundles. The collection lens is mounted on a moveable trolley and can be pulled back to allow easy access during calibration procedures. The collection lens can be repositioned without any detectable change in the signal.

Fibre-bundles

The fibre-bundles are held in place by a fibre-bundle plate mounted on the collection lens. The fibre-bundles have an $f/2.23$ acceptance angle that is matched by the collection lens. In total, there are 26 fibre-bundles that cover a distance of 1.50 m in the vessel, enough to secure full coverage of the plasma in normal operation. Each fibre-bundle consists of 36 fibres across and

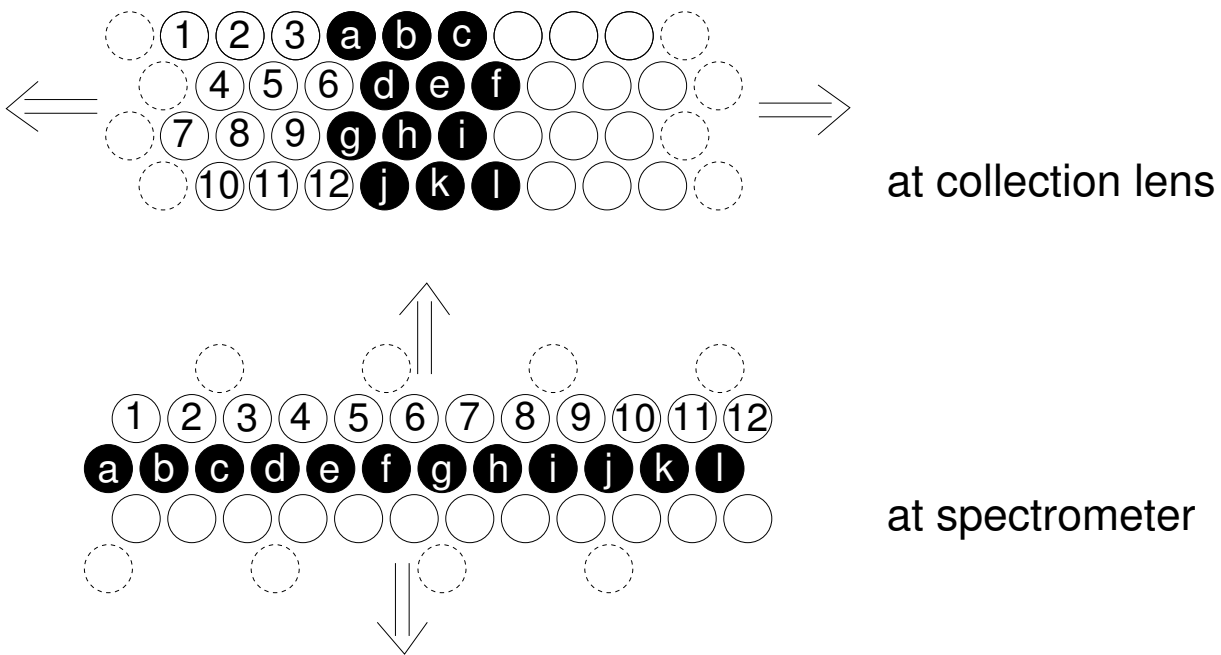


Figure 6.4: Detail of one fibre-bundle showing the mapping of the fibres: a section of 3×4 fibres at the collection lens is mapped to a section of 1×12 at the spectrometer. The arrows indicate the directions of the extensions of the fibre-bundles. Each fibre-bundle consists of 12 such sections.

4 down packed in hexagonal format. Each fibre is $210/230 \mu\text{m}$ in diameter. The fibre-bundles relay the scattered light to the spectrometer.

At the spectrometer input the fibre-bundles are mapped to be packed in a 12×12 configuration. This means that each fibre-bundle can be thought of as consisting of 12 smaller sections of 3×4 fibres at the collection lens and 1×12 fibres at the spectrometer as illustrated in figure 6.4. This mapping allows for achieving the high resolution and the high number of spatial points.

Spectrometer

The spectrometer is based on the Littrow design (see figure 6.5). This facilitates correction of aberrations introduced by the use of very high input slits. The light path in the spectrometer has two intermediate images before being finally imaged at $f/0.75$ onto the detection unit.

The object plane, containing 26 fibre-bundles each $2.23 \times 2.65 \text{ mm}^2$ in size, is oriented to provide a straight image on the detector in both wavelength and space. The 1 m spectrometer slit with $f/6$ input thus necessitates a slit height of 180 mm high allowing for distortion (see figure 6.6).

The grating used has 600 l/mm and is blazed at 656.3 nm at an angle of 11.21° . This has a 62% average efficiency when presented with randomly polarised light. The diffracted light on the return path through the Littrow lens is imaged onto an intermediate image plane - effectively the output slit. The resulting image has an unfavourable curvature for correction by the lens system. To overcome this, a concave mirror is used to act as a field mirror and a correcting element. The intermediate plane is used to mask out the ruby laser wavelength and the D_α line from the plasma using black spray-painted metal strips that follow the curvature of the mirror. The signal measured at the location of the strip is reduced by a factor of ~ 80 . The actual reduction of the signal by the strips is larger than that, but the factor is reduced due to smoothing in the image intensifier, which will be explained in more detail in section 6.6.

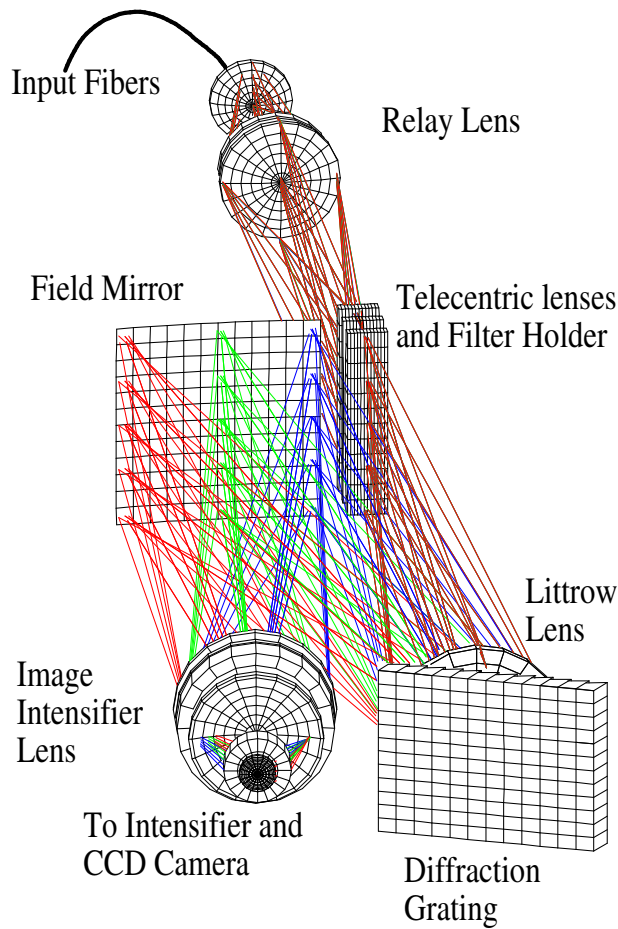


Figure 6.5: Spectrometer system.

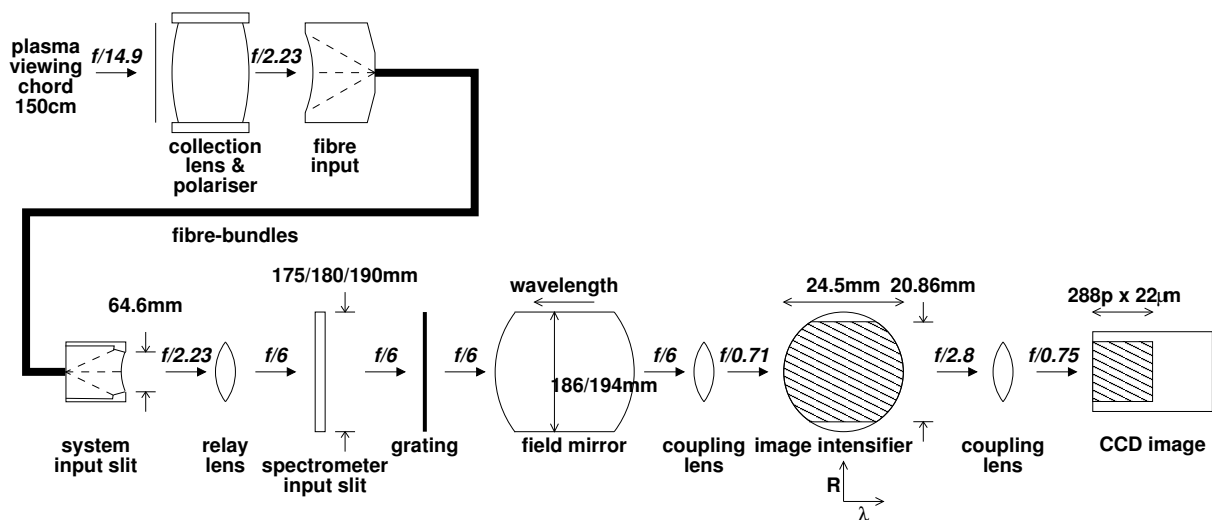


Figure 6.6: Overview of the optical components in collection branch, spectrometer and detection system of the TS diagnostic.

The spectrometer and detection unit are mounted on a granite table in a light-tight room with blackened walls. The granite table has the advantage that it is non-conducting, has a relatively low thermal expansion and is mechanically stable. Individual optical components in their mounts are mounted directly by means of tapped inserts, thus avoiding the use of long optical benches with their inherent expansion problems. This method gave greater flexibility in the layout of the instrument.

Detection unit

The key elements of the detection unit are the image intensifier and the CCD camera. The diffracted light is imaged onto the image intensifier photocathode using a Petzval lens configuration. The final element of this lens is optically connected to the faceplate of the image intensifier with an index matching fluid.

The image intensifier is an omnibus 2nd edition, generation III (GaAS) device. It has a turn-on/turn-off (10-90%) time of less than 10 ns and its photo-cathode has a quantum efficiency (QE) of up to 30% in the red end of the spectrum and an overall effective quantum efficiency [7] ($EQE = QE/NF^2$) of $\sim 6\%$, where NF is the noise factor. The phosphor is a high-efficiency P43 and has an approximate decay time (90 – 10%) of 1.2 ms. The light emitted from the phosphor is primarily at 540 nm, which matches the CCD response well. A 40 ns gate around the laser pulse is provided for the image intensifier in order to minimise the recording of background light.

The CCD camera is a Peltier cooled, back-illuminated, frame-transfer type, scientific grade CCD chip with 576×384 pixels. Half of these pixels are used for storage giving 288×384 usable pixels. Each pixel is $22 \mu\text{m}$ square giving an active area of $6.3 \text{ mm} \times 8.4 \text{ mm}$. The vertical transfer rate per row is $0.65 \mu\text{s}$, hence to clock down all 288 rows takes $188 \mu\text{s}$. The total readout time of the chip is $\sim 1.15 \text{ s}$ in the fast mode and 7.5 s in the slow (lower ADC noise) mode. The dark noise on the chip is less than 1 electron per second per pixel and the readout noise is 4.8 electrons RMS where the camera reciprocal gain is 2.5 electrons/count. The CCD chip has a quantum efficiency of $\sim 71\%$ in the green, which provides a good match to the wavelength at which the image intensifier mainly emits.

PC & network

The CCD camera is coupled to a PC from which the camera is controlled. From the PC the CCD image is transferred onto the main Linux network where it is analysed to produce the profiles.

6.2.2 Triggering system

The Thomson scattering system is operated completely automatically for every MAST plasma discharge. A schematic overview of the triggering system is shown in figure 6.7. In order for the system to run, a total of 7 triggers are required. The triggers are mainly provided using fibre-optics in order to prevent any magnetic pick-up that could cause a ghost trigger during a plasma discharge. The central MAST computer system provides 7 optical triggers, 3 for the ruby laser, 3 for the CCD camera and 1 for the image intensifier.

The three laser triggers (*charge*, *fire* and *dump*) charge the banks, fire the laser and dump the power after the plasma discharge. The power dump facility is included as a safety procedure to protect the laser by preventing the banks from remaining charged for long times whenever a plasma discharge is aborted.

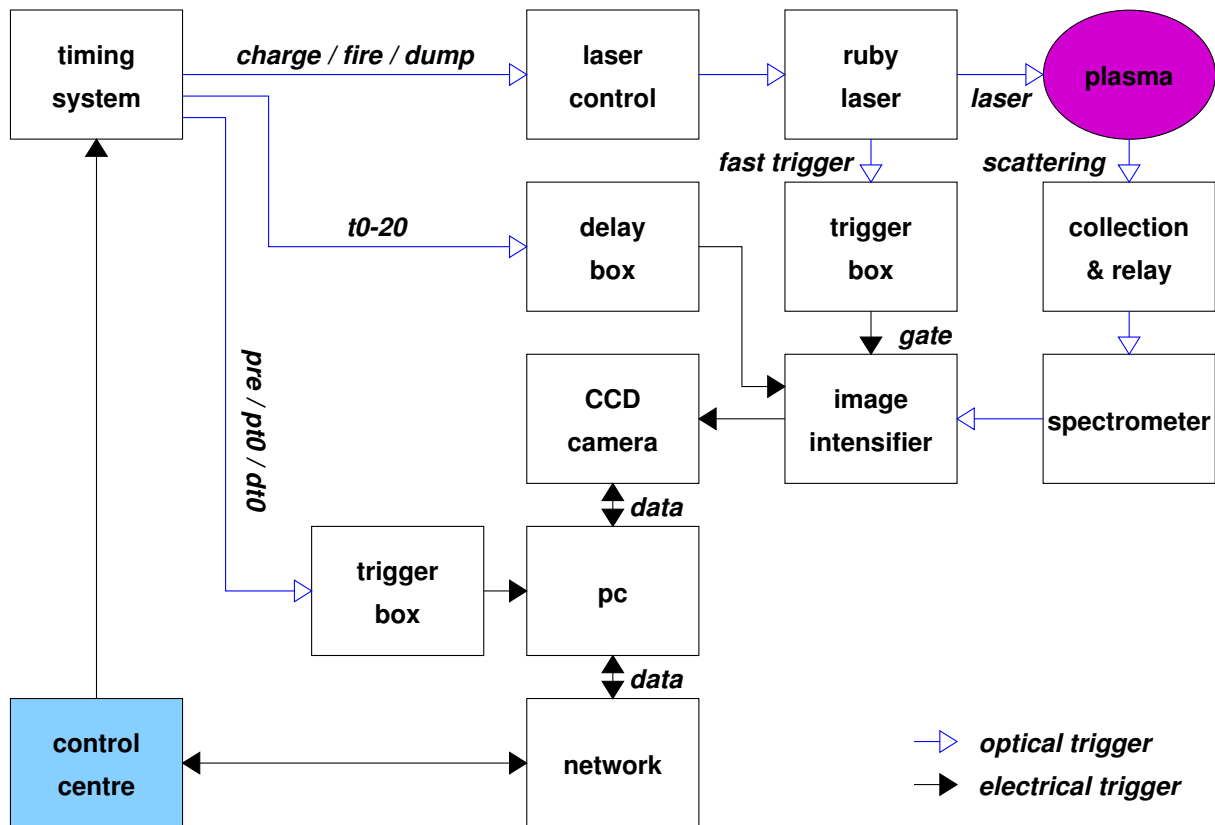


Figure 6.7: Automated triggering system for the Thomson scattering diagnostic on MAST.

The three CCD camera triggers (*pre*, *pt0* and *dt0*) start the charge cleaning of the CCD camera before the plasma discharge, stop the charge cleaning and open the shutter, and start the readout of the camera. The trigger (*t0-20*) leading to the image intensifier solely activates the image intensifier power supply for a short period around the plasma discharge in order to minimise any accidental over-illumination of the intensifier.

The 7th trigger is used to trigger the 40 ns gate for the image intensifier. This optical trigger is picked up at the oscillator of the ruby laser. The total path length of this pulse is ~ 10 m shorter than the path length of the scattered photons (measured from oscillator to collection lens). This translates in a time advantage of ~ 33 ns, which is sufficient to trigger the gate before the scattered light reaches the image intensifier.

From the PC, the CCD camera image is transferred to the main network where the spectra are analysed and the profiles produced automatically after every plasma discharge. An automatic email warning is passed on to the diagnostics group members in case of a system failure. The data is stored in the IDA3 format [8] and is generally available within minutes after the plasma discharge.

6.2.3 Operation

The Thomson scattering system is a turn-key system and requires practically no monitoring on a day of tokamak operation. The alignment is checked using the HeNe laser prior to an operational day and in general requires no adjustment throughout the day.

6.3 Calibration

Several calibrations have to be carried out in order to determine the electron temperature and density profiles from the CCD camera image. These calibrations apply to both the spatial and the spectral direction as will be discussed below. Corrections for plasma light, stray light and the calibration of the CCD camera image are also discussed in this section.

Calibration of radial positions

The spatial positions of the scattering volumes inside the MAST vessel are calibrated by back-illuminating the fibre-bundles from the spectrometer end using a bright light source. The fibre-bundles are thus imaged onto a bar held at the position of the laser beam inside the MAST vessel. These positions are marked and provide the adequate radial positions and the scattering angles for the spatial channels related to the fibre-bundles. The spatial positions and scattering angles of the sections in a fibre-bundle are determined by division and linear interpolation.

Relative intensity calibration

A relative intensity calibration of the spatial channels at the ruby laser wavelength is obtained using Rayleigh scattering on N_2 . In order to increase the scattered light level with respect to the stray light level, but avoiding saturation of the CCD camera the tank is filled with 100 mbar N_2 (measured with a baratron) while the gain of the image intensifier is reduced. The calibrations for an inboard (low R , high field) and a central spatial channel are shown in figure 6.8. The slope of the line represents the relative calibration of n_e . The position where the line crosses the pressure-axis provides the equivalent stray light pressure, which is a system-independent variable. Figure 6.9 shows these two quantities as function of radius. The relative calibration clearly shows the boundary between two fibre-bundle, by a local reduction in transmission. The stray light level is less than 0.2 mbar for most of the detection range and is only higher towards the outer limits of the detection range.

The stray light recorded on the outboard side (high R , low field) originates from reflections off the apertures in the flight line. On the inboard side the stray light originates from reflections off the central column, which is approached by the laser at ~ 45 mm. The light reflected off the central column originates from reflections off the apertures in the flight line. Since the collection lens has no view on the beam dump, direct reflections from the beam dump can therefore not contribute to the stray light. Furthermore, none of the active fibre-bundles faces the side of the centre column that faces the beam dump, reflections of central column origination from reflections of the beam dump can therefore also be neglected. Moreover, the optical path from the centre column to the beam dump and back is ~ 5.4 m, which corresponds to an additional flight time of ~ 18 ns. After this time, the shutter of the image intensifier is closed and no light is transferred to the CCD camera. In a similar way, contributions from secondary reflections off the vessel wall or poloidal field coils, can be neglected because of the dimensions of the MAST vessel.

Absolute intensity calibration

An absolute intensity calibration for n_e is obtained from the line-integrated n_e measurement, made by the CO_2 interferometer, and the laser energy, from a series of plasma discharges. The laser energy is monitored by sampling the signal from the ruby laser just after the last amplifier.

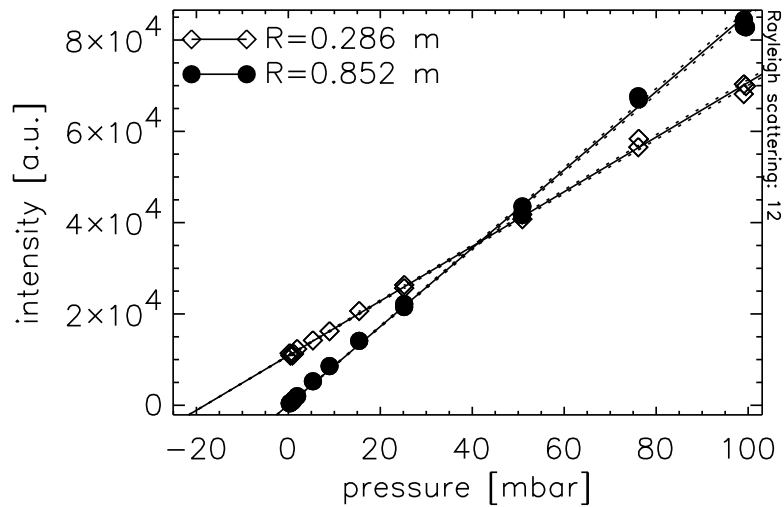


Figure 6.8: The intensities of the Rayleigh scattered light for an inboard ($R = 0.286$ m) and a central ($R = 0.852$ m) channel are linear with the pressure in the vessel. The slope of the calibration curve of the central channel is steepest, this channel therefore shows the highest sensitivity. The offset on the horizontal axis produces the equivalent stray light pressure. This is highest for the inboard channel due to reflections of the centre column. The solid lines show the best fit to the data, from which the relative density calibration and equivalent stray light pressure are obtained. The dashed lines show the excursion of one standard deviation around the best fit.

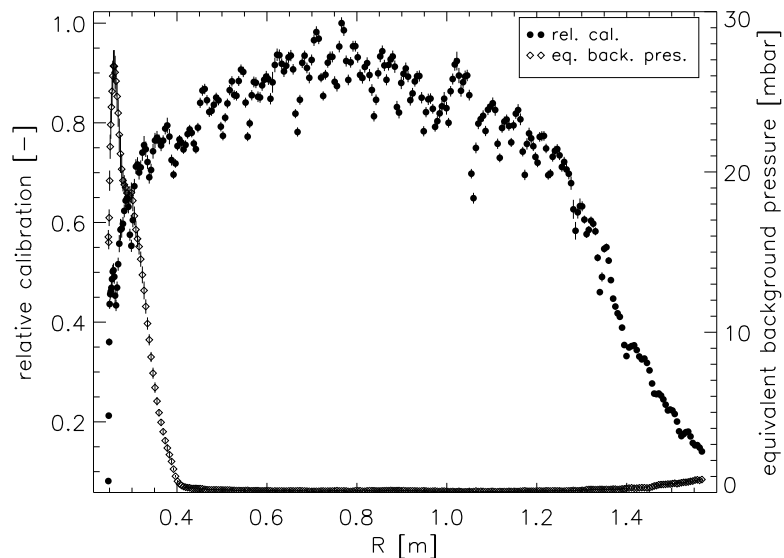


Figure 6.9: Relative spatial calibration and equivalent stray light pressure measured using Rayleigh scattering on N_2 .

In order to minimise the dependence of the beam energy on the beam profiles the sample is reflected off a white (Lambertian type) surface. The reflected light is optically transmitted and recorded using an ADC. This has provided an absolute calibration factor that is used, together with the laser energy, for all the other plasma discharges. Then each n_e profile is corrected against the line-integrated n_e measurement by calculating the line-integral of n_e along the path of the CO_2 laser. This produces a correction factor. This is done for two reasons:

1. to provide an accurate n_e measurement, independent from system changes (discharge-to-discharge fluctuations or long term)
2. to measure the long-term stability of the system by monitoring the value of the correction factor

Figure 6.10 shows the distribution of the correction factor for ~ 250 plasma discharges. The mean of the correction factor is 1.03 with an standard deviation of 0.18. Discharge-to-discharge fluctuations in the correction factor are thought to arise from:

- vibrations of the vessel causing misalignment of the laser beam with respect to the collection optics
- fluctuations in the shape and height of the laser beam pulse, which provides the trigger for the shutter of the image intensifier, thus causing small variations in the timing of the gate with respect to the laser pulse
- statistical errors on the raw data leading to errors on the fitted spectra
- profile distortion due to plasma light
- uncertainties in the line-integral calculation
- errors on the CO₂ \bar{n}_e measurements, which in general produce an error on n_e of $\leq 0.15 \times 10^{19} \text{ m}^{-3}$

Since n_e is calibrated against the CO₂ interferometer for each single discharge, the systematic error on n_e is only determined by the error on the integral and on \bar{n}_e . Long term changes in the correction factor have not been recorded yet, but they could arise from the changing conditions of the many surfaces the scattered light passes. Among these surfaces are the vessel window, which is slowly contaminated due to the process of depositing plasma particles, and the diffraction grating, which reduces performance due to the exposure to light and dust on the long term. Such changes were recorded in the diffraction grating of the lower resolution TS system described in Chapter 5.

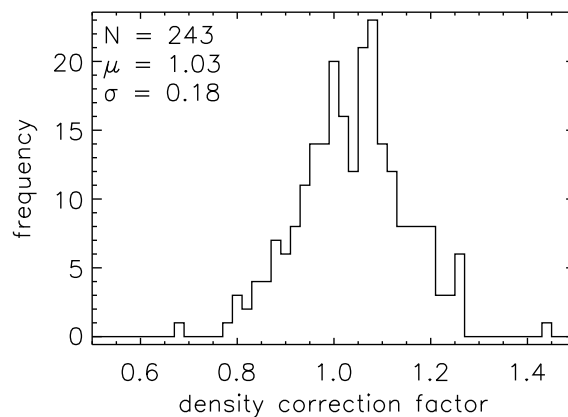


Figure 6.10: The density correction factor, which is the ratio of the CO₂ interferometer and TS densities, for 243 plasma discharges. The correction factor has a mean of 1.03 and a standard deviation of 0.18.

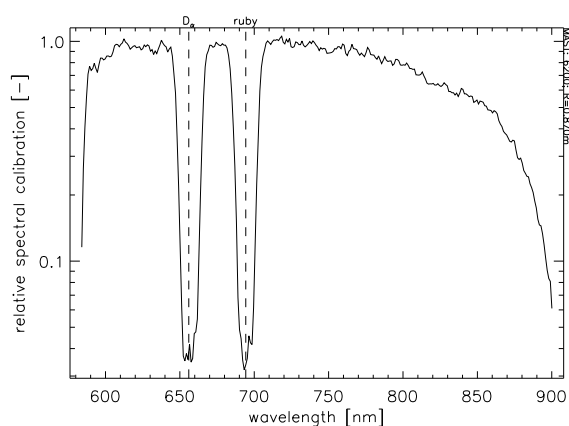


Figure 6.11: Relative wavelength calibration for a central channel. The signal has been corrected for the wavelength characteristics of the white paper, opal plaque, tungsten lamp and polariser sheet. The signal has been normalised to its value at the ruby laser wavelength using a similar measurement without spectral filters on the field mirror.

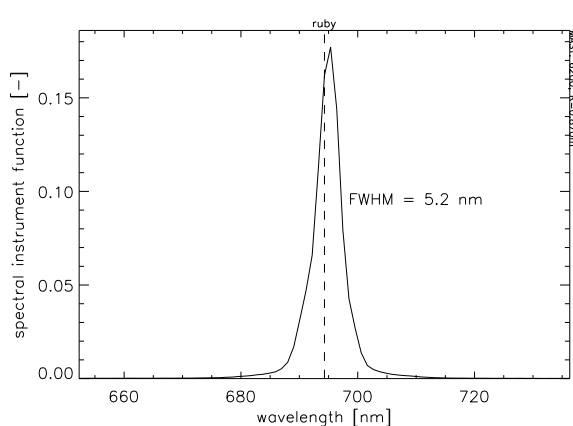


Figure 6.12: Spectral instrument function determined using Rayleigh scattering on high and zero pressure.

Spectral calibration

A spectral calibration of the spatial channels is obtained by illuminating white paper that is calibrated against an opal plaque in the line of sight of the collection lens with a calibrated tungsten lamp. Since the light source under consideration is not polarised, the polariser sheet has been removed during this calibration and its transmission values have been determined separately. The calibration has also been carried out without the spectral filters on the field mirror in order to provide a normalisation factor at the ruby laser wavelength. Figure 6.11 shows the wavelength characteristic for a central channel corrected for the polariser sheet. The spectral range extends from 580 nm to 900 nm which accommodates temperatures of up to ~ 6 keV. The lower limit of the temperature range is determined by the width of the cut-out in the spectrum around the ruby laser wavelength. This width is governed by the slit width and results in a lower temperature limit ranging from ~ 18 eV on the inboard side to ~ 44 eV on the outboard side, the difference occurring because of the different scattering angle (see section 6.7).

Spectral instrument function

Due to the width of the laser beam in the vessel and the width of the entrance slit, a single wavelength is imaged over a narrow wavelength region on the CCD camera image. This spectral instrument function has been determined by taking a Rayleigh scattering spectrum at high pressure and subtracting a stray light spectrum (0 pressure) from it. Both of these spectra have been corrected for the laser energy. The instrument function for a central channel is shown in figure 6.12. The instrument function consists of a central peak with a full width at half maximum (FWHM) of 5.2 nm and a broader tail. This tail will be discussed in more detail later on in section 6.5.

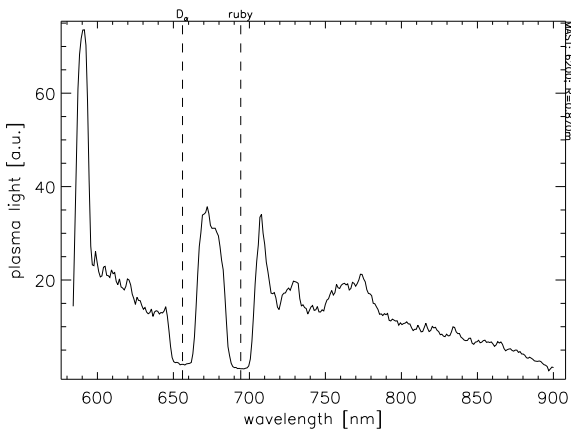


Figure 6.13: Plasma light calibration spectrum. The spectrum has been recorded using a 100 ns gate length and is an average of all spectra in the spatial direction.

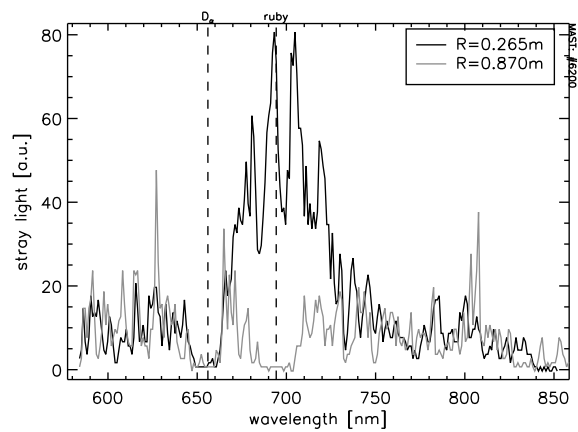


Figure 6.14: Stray light calibration spectra for a spatial channel facing the central column and for a central spatial channel. The first shows an increase of signal around the ruby laser wavelength. In the latter the stray light is virtually non existing. In either case this signal is very low compared to the scattered spectrum.

Plasma light and stray light calibration

The signal recorded during a plasma discharge will, apart from Thomson scattered light, also contain plasma light and stray light. These contributions must be accounted for in the spectral analysis. The plasma light originates mainly from impurity line radiation and *bremstrahlung* and it can contribute significantly to the signal in the low temperature and density regions of the plasma. The plasma light is recorded using an image intensifier gate length of 100 ns. The plasma light has been averaged over the full spatial range in order to provide a calibration spectrum (see figure 6.13). This spectrum can be re-recorded for plasma conditions with expected strong line radiation, *e.g.* He-puff experiments for charge-exchange diagnostic purposes.

As seen previously, the stray light predominately originates from reflections of the ruby laser light, originating from reflections off the apertures in the flight line, on the central column. However, for the majority of the spatial range the stray light level is significantly lower than the scattered light and plasma light levels. During plasma operation the spectral filter at ruby laser wavelength on the field mirror cuts out most of the stray light. The remainder of the stray light spectrum is recorded by firing the ruby laser during a vacuum test on MAST. Figure 6.14 shows examples of stray light spectra for channels with high and low stray light levels. Because of exceedingly high stray light levels, that saturate the CCD image, the innermost fibre-bundle has been deactivated.

Calibration of CCD camera image pixel positions

Before the analysis of all the spectra described above can take place, the spatial and spectral positions on the CCD camera image have to be determined. Also, the image is corrected for background and perspective effects introducing a trapezoidal distortion.

The spatial positions of the fibre-bundles on the image have been determined using the spectral calibration images obtained using the white light source. The fibre-bundles can be distinguished on the CCD camera image due to a non-perfectly tight fit to the adjacent fibre-

bundle at the spectrometer input which results in a local reduction of the signal between two fibre-bundles. Each of the 25 active fibre-bundles covers 11 or 12 pixels in spatial direction. Each pixel row corresponds to one spatial channel, thus adding up to a total of 284 spatial channels.

The wavelength positions on the CCD camera have been determined using the positions of the ruby laser wavelength (694.3 nm) and the D_α emissivity line (656.3 nm) obtained in a scattering experiment in which the spectral filters have been removed. The dispersion is assumed to be uniform and has a value of 1.05 nm/pixel.

The detector offset (~ 1000 counts) and dark current (a few counts) are determined by averaging over a dark area on the CCD chip, yielding the correction for the background effect. The variations on the chip of this correction are small (< 1 count) and are therefore neglected.

The perspective effect is due to the tilt of the mirror with respect to the optical axis of the Littrow spectrometer [9]. The entrance slit is imaged with different magnifications for each wavelength. As a result, the spectrum of each spatial position is slightly (max $\sim 5\%$) tilted with respect to the grid of the CCD camera resulting in a trapezoidal distortion of the image. This could be corrected for by optics, but a simple correction by software is sufficient. The tilt has been determined by using the spectral calibration image in which the individual positions of the fibre-bundles are distinguished. From these the tilt for each spatial position is determined, yielding an algorithm which is then used to correct the image for the trapezoidal distortion. This correction was included in the determination of the spatial and spectral positions as described above.

6.4 Data processing

The processing of the data is fully automated after every MAST plasma discharge. Since a large amount of data is required and only part of this data changes on a discharge-to-discharge basis, the data are divided into two sets: the experimental (raw) data and the calibration data. Both sets are collected after the plasma discharge and processed by an engine that produces an analysed data set:

$$\text{raw data} + \text{calibration data} \implies \text{analysed data}$$

The analysed data set is then stored into the standard IDA3 data format [8] and is generally available.

Inside the engine the raw and calibration spectra are determined from the data for each spatial channel. Then a theoretical Thomson scattering spectrum corrected for the calibration data is fitted to the raw spectrum. Each CCD image is analysed in high resolution producing 284 spatial points. Furthermore, the data is also analysed in low resolution, where the signal corresponding to one fibre-bundle is analysed to produce 25 spatial points in order to provide accurate profile measurements, also at low density.

Determination of the spectra

An example of the CCD camera image is shown in figure 6.15. From this image the background, which is obtained as described above, is subtracted and the spectrum in each spatial channel is determined using the pixel positions on the image. In the low resolution case, the spectra of 11 or 12 spatial channels, corresponding to one fibre-bundle, are averaged to provide one spectrum. No binning in the spectral direction is applied in either case. The calibration spectra are obtained

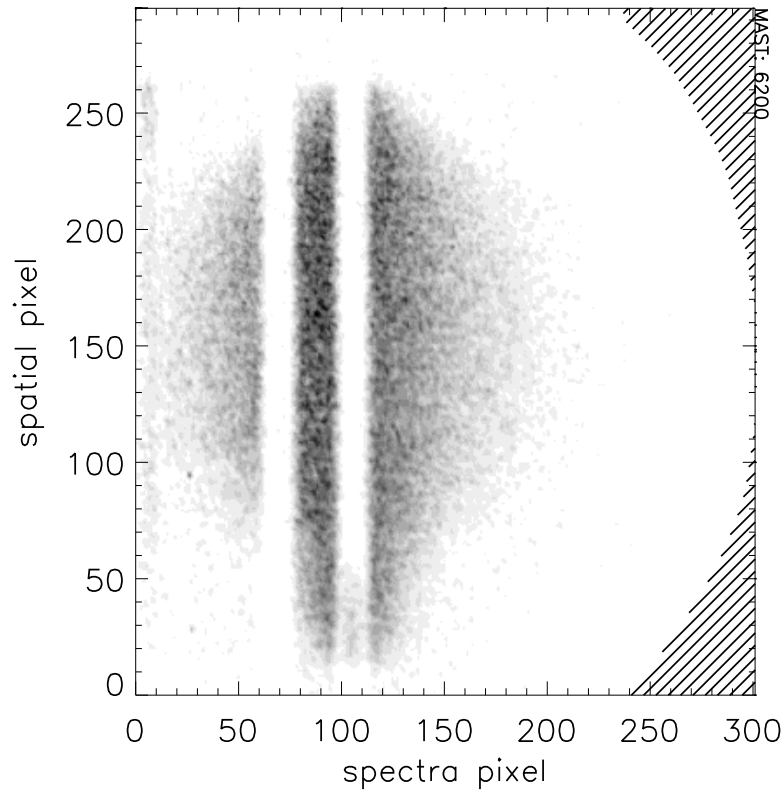


Figure 6.15: Example of a CCD camera image. The darkness in the figure reflects the intensity in the channels. The filters for the reduction of ruby light and D_{α} light are clearly visible. The shaded area indicates the area on chip that is not used for the recording of the spectra.

in a similar way, although the plasma light spectrum is determined by averaging over all spatial channels.

Fitting the spectra

An expected spectrum F will be fitted to the scattered spectrum S for each spatial channel using four free parameters $\vec{a} = [a_0, a_1, a_2, a_3]$. The theoretical Thomson scattering spectrum for a relativistic Maxwellian velocity distribution is used as given by Nielsen [10] (see also Chapter 4). The spectrum given by (4.24) depends on T_e and n_e , which will produce the first two fitting parameters, a_0 and a_1 . Examples of the theoretical spectrum are given in figure 4.2. The theoretical spectrum is then convolved with the spectral instrument function (see figure 6.12) and corrected for spectral calibration, figure 6.11. Then the plasma light and stray light are added using two additional scaling parameters, which are the third and fourth free parameter, a_2 and a_3 respectively, to produce the expected spectrum F .

The obtained expected spectrum $F(\vec{a})$ is fitted to the raw spectrum S using a non-linear least square fitting routine [11]. This routine minimises χ^2 by optimising the fitting parameters \vec{a} . χ^2 is defined as:

$$\chi_i^2 = \sum_j W_{i,j} [S_{i,j} - F_{i,j}(\vec{a})]^2 \quad (6.1)$$

The equation is expressed for channel i in the spatial direction and for j in the spectral direction. In the case of low resolution analysis, $S_{i,j}$ is the average of 11 or 12 pixels in the spatial direction. In the high-resolution analysis, $S_{i,j}$ is the signal in one pixel. In the spectral direction, index j

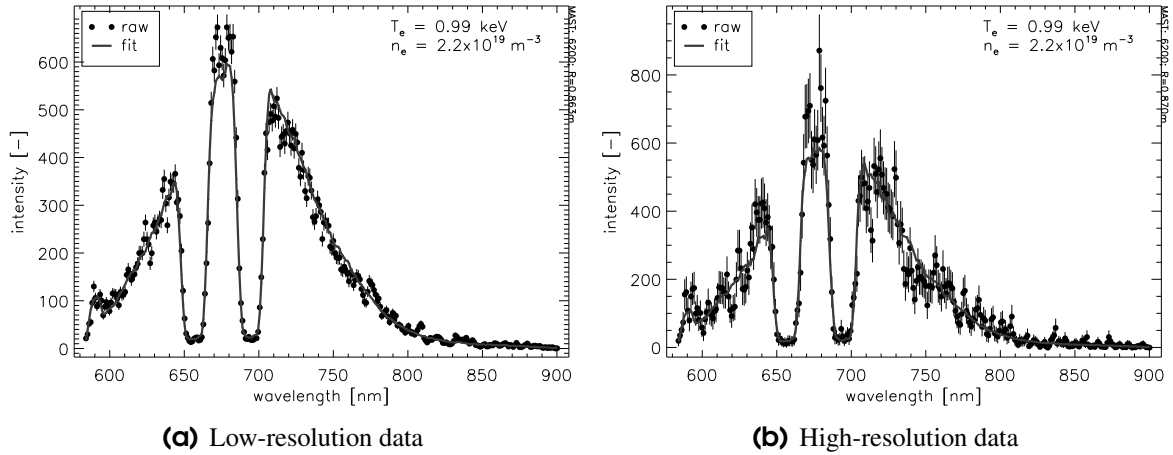


Figure 6.16: Fits to raw spectra in low- and high-resolution analyses.

corresponds to a single pixel. In both cases the weight function $W_{i,j}$ contains an estimate of the error on the measured spectra, $\sigma_{S,i,j}$:

$$W_{i,j} = \frac{1}{\sigma_{S,i,j}^2} \quad (6.2)$$

The error in the measurement, $\sigma_{S,i,j}$, is governed by the photon statistics in the system. An extensive study of the contributions of noise at various stages in the system is presented in [12] and in section 6.5. The raw spectra are fitted in two or more steps. In each step information of the previous step is used in order to improve the estimate of the error and therefore the estimate of the fitting parameters. In the first step the weight is determined from the error on $S_{i,j}$. In the second and subsequent steps the weight is determined from $F_{i,j}$, which is returned in the previous step. Figure 6.16 shows an example of fits to raw spectra in low- and high-resolution analyses.

Determining the profiles

T_e follows directly from a_0 and the error in T_e follows from the fitting error in a_0 . In order to obtain n_e , a_1 is corrected for the relative and absolute calibrations (see above). The error on n_e is based on the fitting error on a_1 and the error on the calibration data. Finally, the electron pressure p_e can be calculated using the ideal gas law ($p_e = k_B T_e n_e$ where k_B is Boltzman's constant). For the determination of the error on p_e the covariance between the errors on T_e and n_e has been taken into account. More on the determination of the errors follows in section 6.5.

Figure 6.17 shows an example of the measured profiles analysed in both high and low resolution. The profiles are in good agreement. Fitting parameter a_2 provides a line-integrated plasma light profile. This shows a well-defined plasma edge on the outboard side. On the inboard side the edge is less well defined, which is due to the shorter path of the line of sight through the radiative cold edge of the plasma (see also section 7.2).

Check for laser alignment

The pixel position of the ruby laser wavelength is fixed for a stable laser alignment. However, during a plasma discharge, the laser might get misaligned minimally due to movement of the

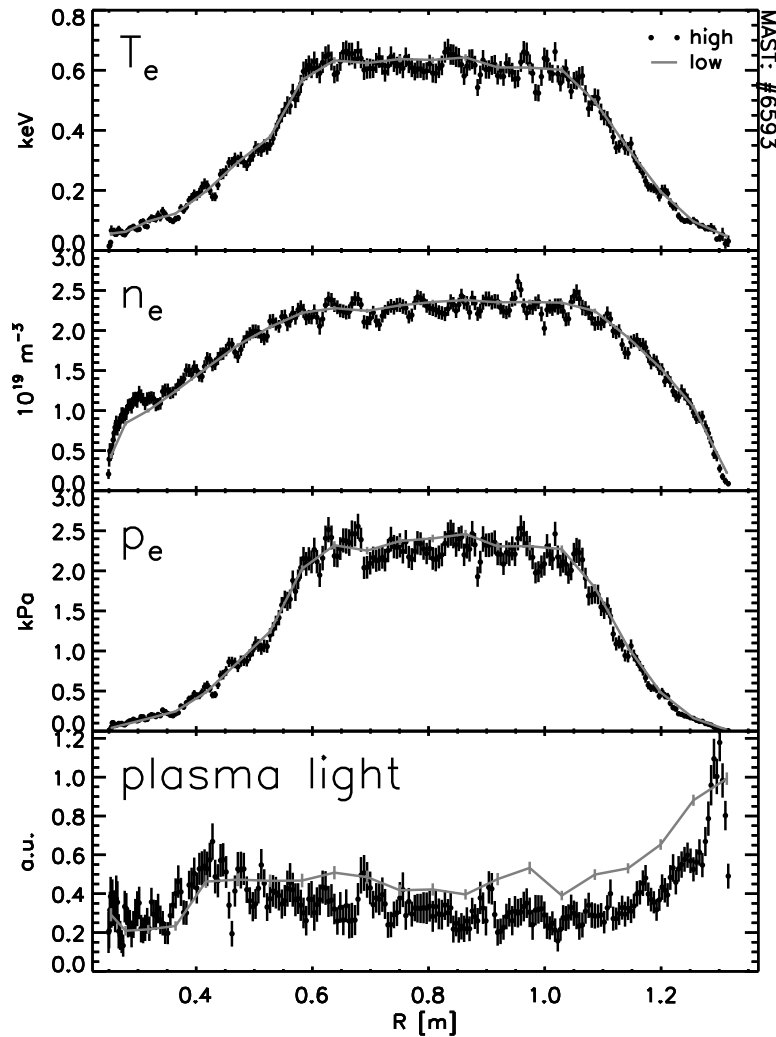


Figure 6.17: Example of TS profiles of T_e , n_e , p_e and plasma light in MAST analysed in high (symbol) and low (line) resolution.

vessel, which could cause the ruby laser wavelength to be assigned to a neighbouring pixel instead. To remedy for this, a scan is made along the neighbouring pixels and for each position a new fit is made, from which the best fit is selected: in fact, this provides a 5th free fitting parameter. The shift from the central pixel provides a measurement alignment.

The image of the fibre-bundle at the collection volume has a height of ~ 6 mm. The fibre-bundle is built up of four fibres in the vertical direction, which is the direction of misalignment. Figure 6.4 shows the packing of the fibres in the bundles. A displacement of the laser beam from the row containing the fibre marked 'b', to the row containing the fibre marked 'h'. This is a displacement of half the height of the fibre-bundle, *i.e.* of ~ 3 mm. At the spectrometer end the displacement from the fibre marked 'b' to the fibre marked 'h' corresponds to a shift of six fibres. Since one fibre matches one pixel on the CCD camera image, the laser beam displacement of ~ 3 mm results in a shift of six pixels. A shift of the position of ruby laser wavelength over one pixels therefore corresponds to a misalignment in vertical direction of ~ 0.5 mm. Figure 6.18 shows an example of the laser alignment, which, in general, is zero pixels, *i.e.* < 0.5 mm. Only beyond the plasma edges, where the density is low, there is a spread in the alignment because of the weak signal.

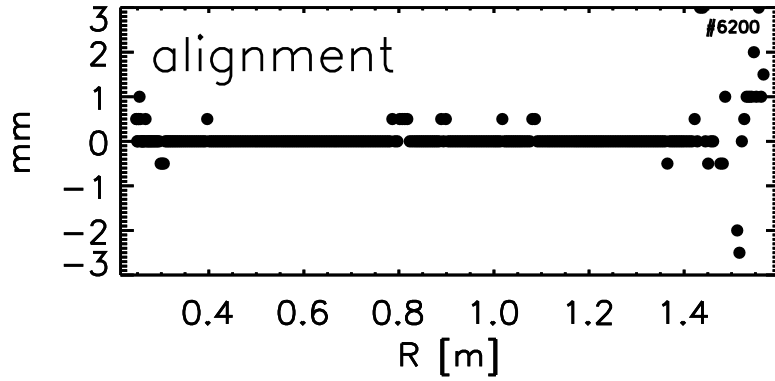


Figure 6.18: Vertical laser alignment.

A shift of the central wavelength can also be caused by the plasma current. A technique is therefore at hand to measure the current density using a TS diagnostic [13, 14]. However, the wavelength shift introduced by the drift velocity $v_{d,e}$ of the electrons is small compared to the spectral resolution of the system. In MAST the typical plasma current is $I_p \approx 1$ MA. Assuming a parabolic current density profile $j(r)$, a minor radius of $a = 0.55$ m and edge elongation of $\kappa = 2$, this produces a central current density of $j \approx 2$ MA m⁻². Since the mass of the electrons is much lower than the mass of the ions, the current density is mainly carried by the electrons: $j = -n_e e v_{d,e}$, where e is the elementary charge. In a plasma with a central density of $n_e = 4 \times 10^{19}$ m⁻³, this produces an electron drift velocity $v_{d,e} \approx 0.3 \times 10^6$ ms⁻¹. The drift velocity of the electrons causes a spectral shift:

$$\Delta\lambda_d = -\frac{2v_{d,e}}{c}\lambda_0 \sin\left(\frac{\theta}{2}\right) \sin\left(\phi - \frac{\theta}{2}\right) \cos\gamma \quad (6.3)$$

where c is the speed of light and λ_0 is the wavelength of the incident beam. The geometrical factor contains the scattering angle θ , the angle γ between the scattering plane and $v_{d,e}$ and the angle ϕ between the incident vector k_0 and the projection of $v_{d,e}$ onto the scattering plane. In the plasma centre the angles are $\gamma \approx 0$, $\theta \approx \frac{\pi}{2}$ and $\phi \approx \frac{\pi}{2}$, such that $\Delta\lambda_d \approx -\frac{v_{d,e}}{c}\lambda_0$. For the given density this produces $\Delta\lambda_d = 0.7$ nm, which is less than the resolution of one pixel (1.05 nm). This wavelength shift is of the same order or less than the shift in the spectrum due to a misalignment, which implicates that the use of the TS diagnostic as a tool to determine the current density profile in MAST requires extremely good laser alignment.

6.5 Error estimates

The significance of a measurement is determined by its error, therefore a good estimate of the error is essential. T_e and n_e result from a fit to the raw spectra, the errors on this raw data therefore contribute to the errors on T_e and n_e . These errors also play a role in determining the best fit to the spectra (see section 6.4). In addition, relative and absolute calibrations contribute to the error on n_e . This section presents an estimate of the error on T_e and n_e .

First, the determination of the errors on the raw data is described by analysing the detection branch of the system in detail. Secondly, these errors on the data are used in Monte-Carlo simulations of fits to spectra in order to estimate the error on T_e and n_e . It will be shown that the error is built up of a statistical and systematical part.

Error on the raw data

In order to obtain an estimate for the error on the raw data a good understanding of the error on the raw data is required [15]. The raw signal is measured in units counts in the pixels on the CCD camera. The signal is subject to read-out noise, but since the read-out noise has a mean of zero, the signal $S_{i,j}$ is equal to the signal C on the CCD camera. However, the uncertainty in both values is not the same. In the error on $S_{i,j}$ the error on the read-out noise ($\sigma_{readout}$) is included:

$$\sigma_{S,i,j}^2 = \sigma_{C,i,j}^2 + \sigma_{readout}^2 \quad (6.4)$$

The read-out noise is determined from a dark region on the CCD image and produces $\sigma_{readout} \approx 1$ count. For the error on the signal $C_{i,j}$ it is not possible to simply use the error that would be found if the data on the CCD were Poisson distributed. This would cause an underestimate of the error due to the magnification of the image intensifier and due to the smoothing of the signal in the various optical elements of the system. However, the redistribution of light does not change the error on the measurement as is shown in [12].

The error on the data is determined in the image intensifier. The scattered photons entering the image intensifier are converted to photo-electrons in the photo-cathode. These photo-electrons are accelerated by an electric field onto the micro channel plate (MCP). Due to collisions of the electrons with the walls of the channels of the MCP, secondary electrons are released. In this way the signal is amplified. In order to protect the photo-cathode from the ions that are released in the MCP, the photo-cathode is protected by the so-called ‘reverse ion bombardment coating’. This coating introduces a loss factor. A second electric field accelerates the secondary photo-electrons onto a phosphor screen where the light is emitted that is transmitted onto the CCD camera chip.

The error is determined by Poisson statistics at the stage in the system where the signal is smallest, that is, at the entrance of the MCP. This signal will be called M . These photo-electrons are multiplied in the MCP and accelerated to the phosphor screen where the secondary photons are released that are finally recorded on the CCD camera. Since the multiplication process in the MCP is non-linear, care has to be taken in deriving the effect on the error. This non-linearity can easily be verified by introducing ‘probability generating functions’ [16, 17]. The probability generating functions for this TS system have been set up as presented in [12], the outcome of this analysis is presented here.

The signal measured on the CCD camera can be related to M as:

$$C_{i,j} = F_{eff} G M_{i,j} \quad (6.5)$$

where G is the average gain of the MCP and F_{eff} is the effective noise factor of the MCP. It is assumed that the gain of the MCP is uniform ($G = 12.6$). F_{eff} is introduced by the photo-electron loss processes in the MCP and also includes effects of the reverse ion bombardment coating and packing factor of the MCP. The effective noise factor increases the uncertainty in the signal ($F_{eff} = 5$). It can now be shown [12, 15] that the error on C is related to the error on M as:

$$\sigma_{C,i,j}^2 = \frac{F_{eff}^2 G^2}{\Gamma} \sigma_{M,i,j}^2 \quad (6.6)$$

Here Γ is a smoothing factor [15]. The smoothing factor Γ reflects the smoothing of the signal after the MCP. This smoothing is related to the imaging between the phosphor screen and the CCD camera and by the trapezoidal correction of the CCD image. The quantity of all these effects depends on the position of the pixel on the CCD camera, *i.e.* the trapezoidal effect is

negligible in the centre of the CCD image, but increases towards the edges. However, for simplicity in the modelling of the error a uniform smoothing function is assumed.

In the case of a perfect focuss of the image onto the CCD camera, the signal recorded on one pixel originates from a certain area on the phosphor screen. But, because of defocussing, the signal from this area is imaged onto more than one pixel. *Visa versa*, one pixel receives information from a larger area. Therefore, the error related to a Poisson distribution can be taken from a larger signal ($> M_{i,j}$) than would have been expected if there was not any smoothing, this consequently produces a smaller error on the measured data, hence $\Gamma > 1$.

The smoothing factor Γ has been calculated from a 2-D function that describes the smoothing effect after the phosphor screen. An estimate for this has been obtained from a measurement of the 1-D smoothing profile in radial direction. This 1-D smoothing profile has been measured at the ruby laser wavelength during a Rayleigh scattering calibration. For this calibration, the field mirror has been blackened but for a narrow slit that has been cleared. The slit covers a width of less than one pixel in the spectral direction. The calibration has been carried out at different radial positions, an example of such a measurement is shown in figure 6.19(a). The thus measured profile can be fitted with a Gaussian of width σ . The width σ depends on the number of channels in the MCP that the light coming from the slit illuminates. The minimum recorded width of the 1-D smoothing profile, out of all measurements at the various spatial positions, is ~ 0.64 . It is assumed that this corresponds to the illumination of an area corresponding to one single pixel on the CCD camera.

Because of the low intensity of the measured signal it is not possible to measure the 2-D smoothing function directly. Therefore, an estimate of the 2-D function is obtained using the 1-D smoothing function. For the derivation of the 2-D smoothing function the system is assumed to be rotationally symmetric at the stage beyond the image intensifier. This assumption can be validated by the fact that all wavelength information is lost after the photo-cathode, the 1-D smoothing profile can thus be taken as a radial cross-section of the 2-D smoothing function. The latter function therefore consist of a Gaussian of $\sigma \sim 0.64$. Due to the lack of intensity in the measurement of the 1-D smoothing profile only the central peak is observed. However, the halo of the phosphor screen will also introduce a much broader smoothing profile, of low intensity compared with the sharp peak, as will be seen in section 6.6. The best estimate of this tail is a Gaussian with a σ 15 times wider than the sharp peak but with an intensity 1.5×10^{-5} times the intensity of the central peak. The thus obtained 2-D smoothing function is shown in figure 6.19(b)

The value for Γ is now obtained by calculating the error on the signal on the phosphor screen for a single spatial channel by summing up all the contributions of the neighbouring channels according to the 2-D smoothing function. In this summation is included the fact that the smoothing in the wavelength direction does not alter the error. The summation has been described in detail in [15]. In this, the assumption is made that the signal is uniform in order to obtain a value for Γ . This exercise yields $\Gamma = 4.85$ for the high-resolution measurement. A similar exercise can be performed for the low-resolution analyses of the data, this produces $\Gamma = 2.37$ and $\Gamma = 2.36$ for integration over 11 and 12 pixels respectively. It is assumed that Γ is uniform for all channels $[i, j]$.

Having obtained the value for Γ , the error on the raw data ($\sigma_{C,i,j}$) can now be estimated using (6.6). It can be shown that the signal before the MCP, $M_{i,j}$, is Poisson distributed, for which $\sigma_{M,i,j} = \sqrt{M_{i,j}}$, where $M_{i,j}$ is obtained using (6.5). Finally, the error on the signal on the CCD camera ($\sigma_{S,i,j}$) can be calculated using (6.4). This provides the weight $W_{i,j}$ for the measurement used in the minimised χ^2 fit, (6.1).

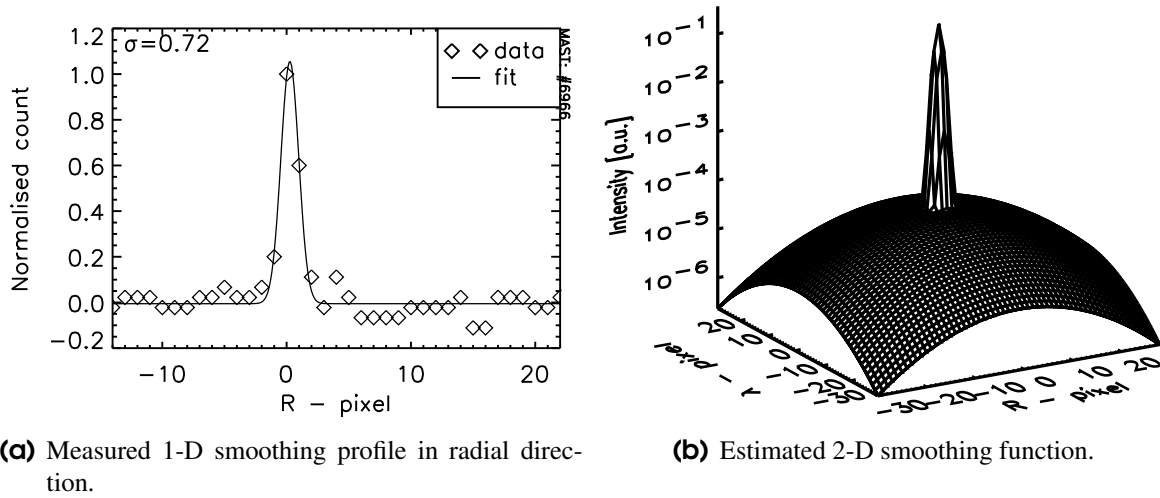


Figure 6.19: Smoothing functions of the high-resolution TS system.

Error on the measurement

A Monte-Carlo simulation will be used to estimate the error on T_e and n_e for a central channel, but any channel can be simulated in a similar way. In order to be able to use the same fitting engine as used in the profile analyses, test CCD images are made from uniform T_e and n_e profiles. Noise has been added at the stage of the MCP and the signal has been convolved with the 2-D smoothing function. A more detailed description of the setup of this test image is presented in appendix 6.A. The thus generated CCD image is provided to the fitting engine which return profiles for T_e and n_e . The returned values of T_e and n_e , using an input of $T_e = 1000$ eV and $n_e = 4.00 \times 10^{19} \text{ m}^{-3}$, are distributed as shown in figure 6.20.

The output of the Monte-Carlo simulations shows that the distributions of T_e and n_e resemble Gaussian distributions. The widths of the distributions are introduced by the noise on the raw data: $\sigma_{T_e} = 39$ eV and $\sigma_{n_e} = 0.10 \times 10^{19} \text{ m}^{-3}$. This produces the relative statistical errors: $\sigma_{T_e}/T_e = 3.9\%$ and $\sigma_{n_e}/n_e = 2.5\%$. The mean of the T_e distribution is $\mu_{T_e} = 1000$ eV and the mean of the n_e distribution is $\mu_{n_e} = 4.01 \times 10^{19} \text{ m}^{-3}$. The data is therefore subject to small relative systematical errors: $\sigma_{T_e}/T_e = 0.0\%$ and $\sigma_{n_e}/n_e = 0.2\%$. These are well below the statistical errors. As yet, the T_e and n_e data have not been corrected for this small systematical error.

The Monte-Carlo simulation has been performed for a range of temperatures and densities, the results are shown in figure 6.21. These show that the relative errors decrease for increasing density as would be expected from a statistical point of view. Due to the limited spectral range the relative error also increases towards lower and higher temperatures. The measurement typically has a statistical error of $< 5\%$ of T_e and $< 4\%$ of n_e in the range 40 eV – 2 keV for $n_e \sim 4 \times 10^{19} \text{ m}^{-3}$. This error is important when analysing small fluctuations on the profiles. The absolute systematic error is typically $< 1\%$ of T_e and $< 1\%$ of n_e in the same temperature range and for the same density.

Not included in the error on n_e is the systematic error in each channel which is introduced by the relative and absolute calibrations. This error is typically 1.5% for most of the radial range, but rises to $\sim 2.5\%$ for the channels facing the central column due to the increased stray light level in this region (see section 6.3). The statistical error on the n_e profile (see section 6.3) is neither included, because this error does not come into play when analysing the details in the

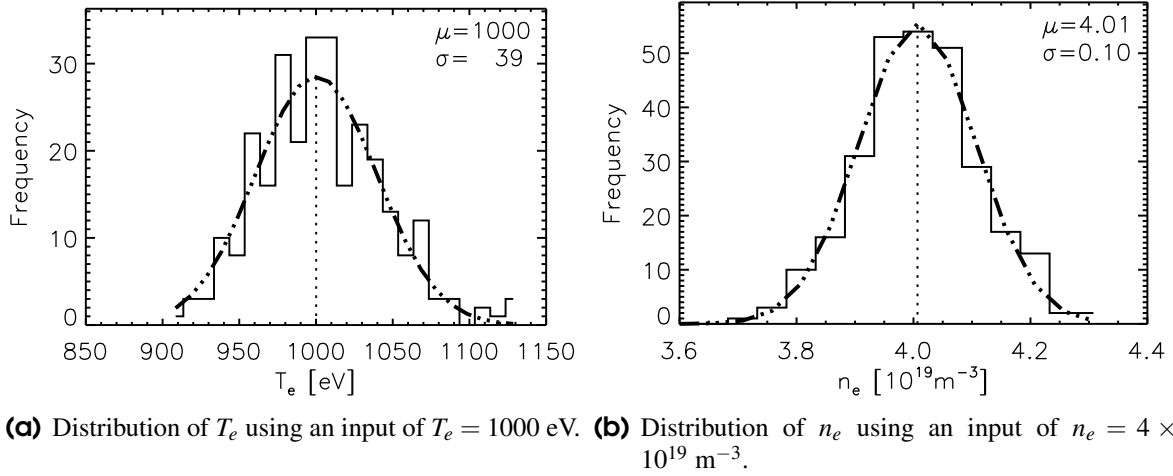


Figure 6.20: Distribution of T_e and n_e resulting from a Monte-Carlo simulation of uniform profiles with added noise. The dashed-dotted lines show fitted normal distributions of mean μ and variance σ^2 .

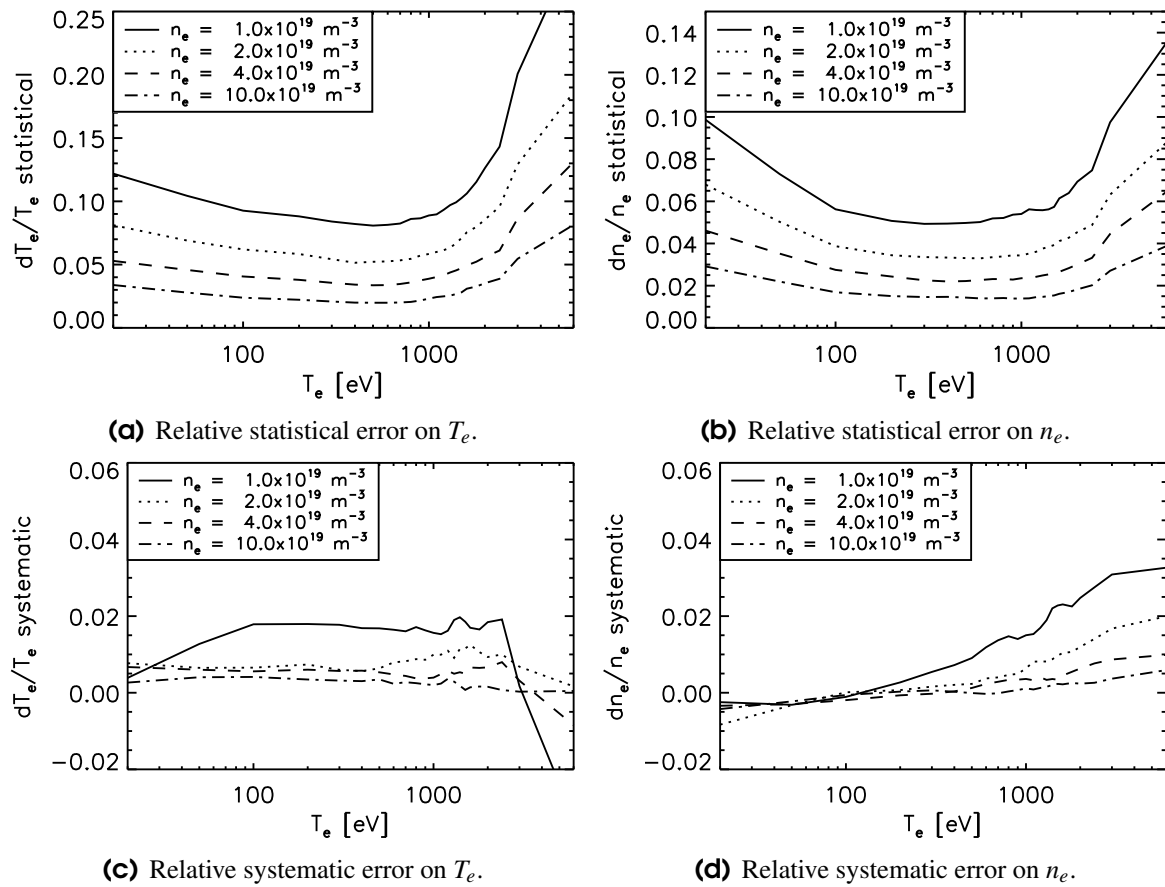


Figure 6.21: Relative statistical and systematic errors on T_e and n_e following from Monte-Carlo simulations.

n_e profile.

Van Milligen *et al.* [18] have studied Thomson-scattered spectra from a high-resolution TS diagnostic similar to the one used on MAST. Their work indicates that some improvements can be made in the analyses. Currently the MAST TS spectra are fitted by minimising χ^2 , but the publication claims that this technique can lead to a bias in T_e and n_e . A small bias has also been observed on the MAST data, especially in the more extreme parameter range (see figure 6.21). The publication recommends the use of the maximum likelihood method to avoid the systematic error due to the fitting technique. Preliminary results of fits to TS data using this technique indeed show a reduction of the bias. The maximum likelihood technique, as well as other fitting techniques, have yet to be explored in detail and proved productive on the MAST TS data.

6.6 Normalised-flux resolution

The highest possible spatial resolution is one pixel, corresponding to ~ 5.3 mm in the plasma. However, the instrument profile of the system is wider, as shown in figure 6.22. The graph is produced by illuminating a ~ 1.5 mm wide slit (smaller than the maximum resolution) at the position of the scattering volume of a central channel with a white light source. The profile is averaged over 60 pixels. The profile shows a sharp peak of ~ 3.3 pixels FWHM plus a broad low tail. The averaging makes the tail visible. The broadening is caused by the resolution of the different optical and electro-optical components of the system. The halo of the phosphor of the image intensifier is the cause of the broad tail. This also accounts for the tail observed in the spectral instrument function of figure 6.12. The broad tail is so low that it does not affect the resolution, but it is important for the final data interpretation as it produces an offset to the signal and affects the error on the measured spectrum as seen in section 6.5.

The profiles are normally plotted versus R , the distance of the centre of the sample volume to the centre of the rod. Where the laser approaches the rod at close range (45 mm) this R only changes minimally from one spatial point to the next, this as shown in figure 6.24(a). Moreover the laser beam is parallel to the flux surfaces on the inboard side as shown in figure 6.23. A very high resolution in flux coordinates is therefore achieved on the inboard side (see figure 6.24(b)). This normalised-flux resolution is further enhanced by the fact that the flux surfaces are more widely spaced on the inboard side due to the Shafranov shift.

The normalised-flux resolution is introduced as a machine-independent measure for the resolution of a TS system. In addition it provides a measure for the resolution of the system independent of the location of the measurement. It is defined as:

$$\Delta\psi_N = \Delta R \frac{\partial\psi_N}{\partial R} \quad (6.7)$$

where ΔR is the radial resolution for which the definition will be given later on. In addition to the above definition, the root-normalised-flux resolution is defined:

$$\Delta\sqrt{\psi_N} = \Delta R \frac{\partial\sqrt{\psi_N}}{\partial R} \quad (6.8)$$

Since $\sqrt{\psi_N}$ is roughly proportional to the minor radius, the latter definition can be seen as the resolution of the normalised radius. In these definitions a low value means a high resolution.

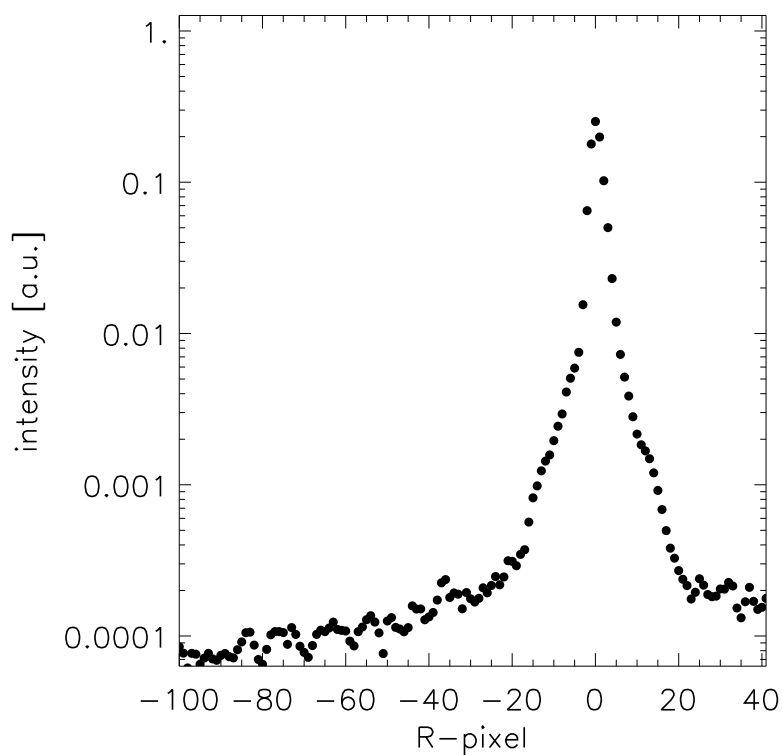


Figure 6.22: Logarithmic plot of the radial instrument function.

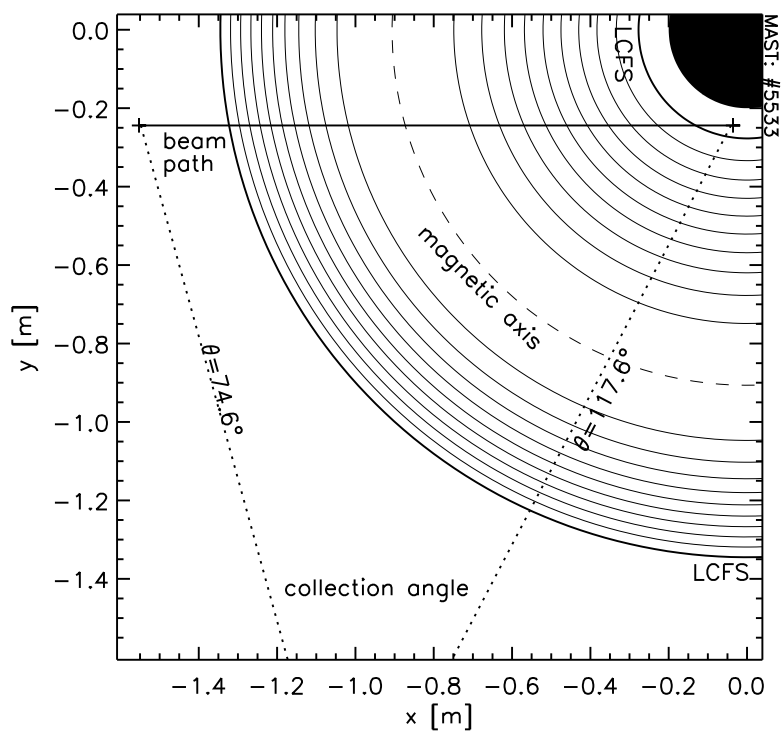
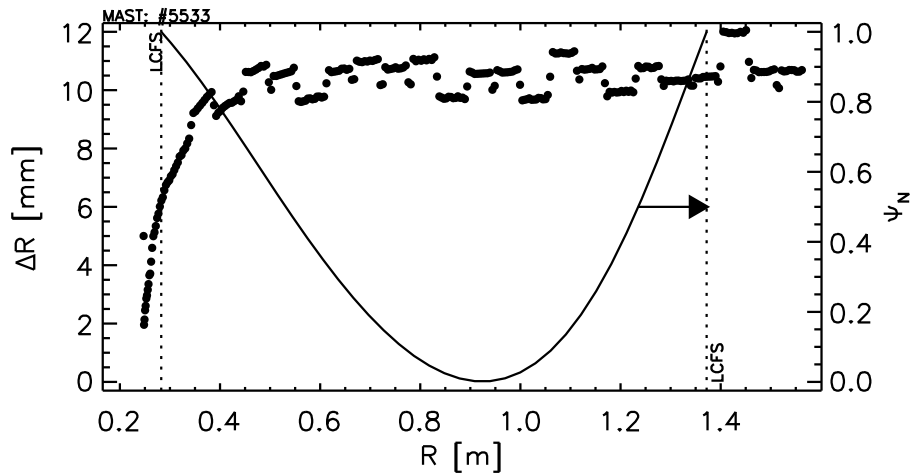
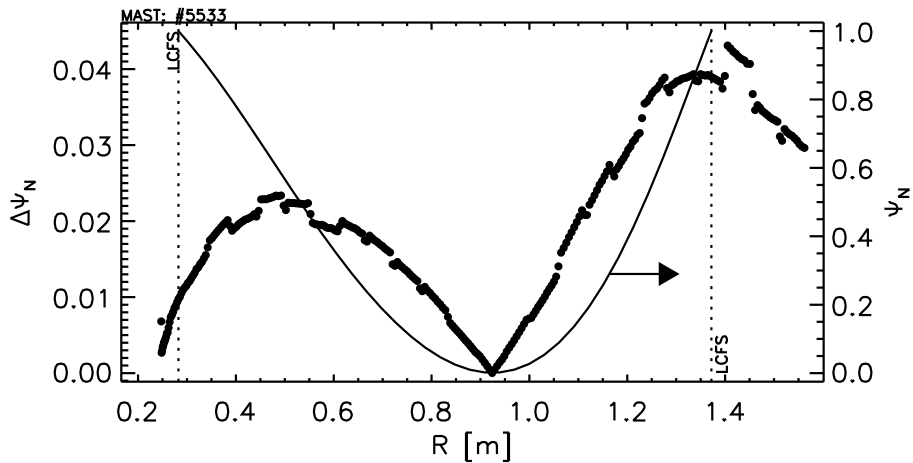


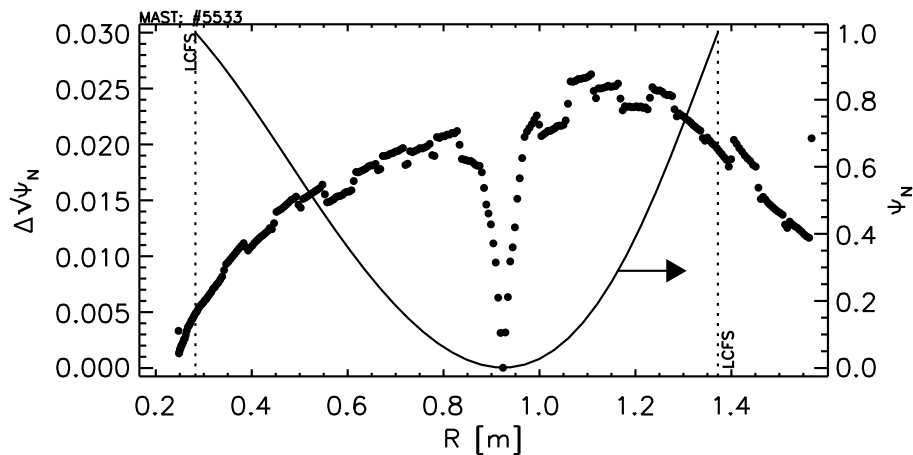
Figure 6.23: Top view of the MAST vessel showing the laser beam path with respect to the magnetic flux surfaces.



(a) Radial resolution on R .



(b) Normalised-flux resolution on R .



(c) Root-normalised-flux resolution on R .

Figure 6.24: Resolution of the TS diagnostic in three definitions. The resolution is high when the function, *e.g.* $\Delta\psi_N$, is low and viceversa. The resolution is highest at the inboard edge. The improved resolution at the magnetic axis is due to the small gradient in the magnetic flux. The apparent ‘steps’ in the profiles are introduced due to the limited accuracy of the measurement of dR and the separation of dR in either 11 or 12 pixels on the CCD camera image.

The radial resolution (ΔR) is a scale length for the maximum gradient that can be measured at a given radius:

$$\Delta R = Y \left(\frac{\partial Y}{\partial R} \right)_{\max}^{-1} \quad (6.9)$$

where Y is the measured quantity, *e.g.* n_e . The maximum gradient $\partial Y / \partial R$ as measured by the TS diagnostic at a given radius R' is derived from a top-hat profile convolved with the instrument function. The top-hat function y is defined as:

$$y(r) = \begin{cases} 1 & : r \leq R' \\ 0 & : r > R' \end{cases} \quad (6.10)$$

where r is the coordinate in radial direction. Measurement of this function $y(r)$ by the TS diagnostic yields the profile $Y(R)$. A mathematical expression for $Y(R)$ is obtained in two steps. First, the sampling volumes are considered. All information within the limit $R - dR/2 < r < R + dR/2$ is summed in one data point at R (in one pixel column on the CCD camera image), where dR is the full width of the sampling volume in radial coordinates. The data point thus produces the average value within the limit of the sampling range. A value for dR is determined from the length of the scattering volumes along the beam path and considering the radial extent of the laser beam. The extent of the collection volumes is determined by back-illuminating the fibre-bundles and projecting the images onto a sheet positioned in the laser beam path.

Secondly, this averaged function is convolved with the instrument function $I(R)$ shown in figure 6.22. This produces the following expression for $Y(R)$:

$$Y(R) = \frac{1}{dR} \int_{R-dR/2}^{R+dR/2} y(r) dr \otimes I(R) \quad (6.11)$$

From this the gradient $\partial Y / \partial R$ at $R = R'$ is determined in order to obtain the radial resolution ΔR . Using (6.7) and (6.8) now produces $\Delta \psi_N$ and $\Delta \sqrt{\psi_N}$ shown in figure 6.24. The resolution as expressed in $\Delta \sqrt{\psi_N}$ is highest at the inboard edge ($\Delta \sqrt{\psi_N} \approx 1/200$) and reaches a minimum of ($\Delta \sqrt{\psi_N} \approx 1/50$) towards the outer edge. The improvement of the resolution at the magnetic axis is a result of the small gradient in the magnetic flux.

Figure 6.25 shows the result of (6.11) on a step function n_e on the inboard side plotted on ψ_N . This is then compared with to relatively steep inboard edge n_e profile measurement from MAST. This example shows that the measurement of the n_e gradient is not limited by the resolution of the system. The TS system is therefore a powerful tool in edge gradient studies. More on edge gradient studies is presented in Chapter 7.

6.7 Known issues

Fluctuations on the profiles

The high-resolution profiles shown in figure 6.17 are not smooth and appear to show fluctuation. However, these could well be due to statistical noise. The fluctuations in the centre of the profiles, in the region $0.6 \text{ m} < R < 1.1 \text{ m}$ are therefore compared with the error on the data. The low-resolution profile is subtracted from the high-resolution profile. The result is divided by the error. The distribution functions of the such obtained signals are shown in figure 6.26 compared to a normal distribution of standard deviation 1. The fluctuations in this particular example can not be distinguished from the error and are therefore not statistically significant.

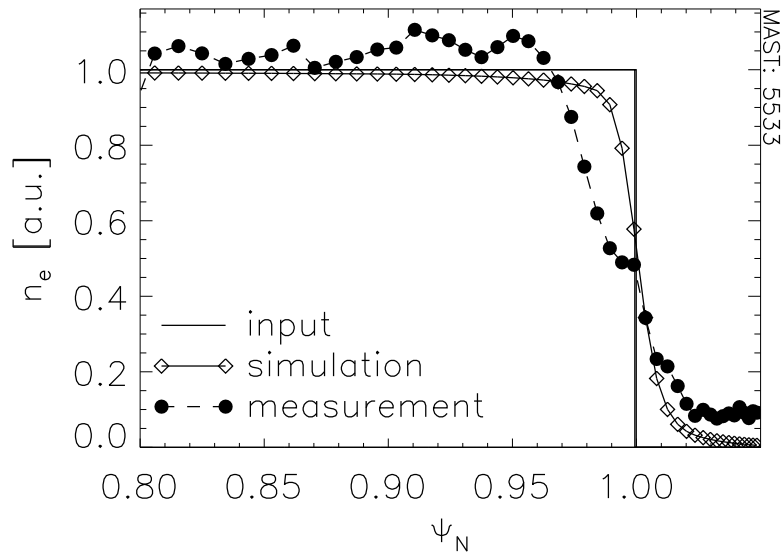


Figure 6.25: Result of (6.11) on a top-hat function and comparison with a measured inboard edge density profile from MAST.

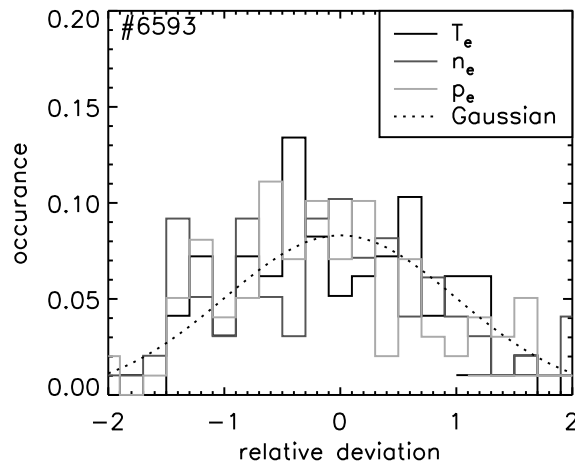
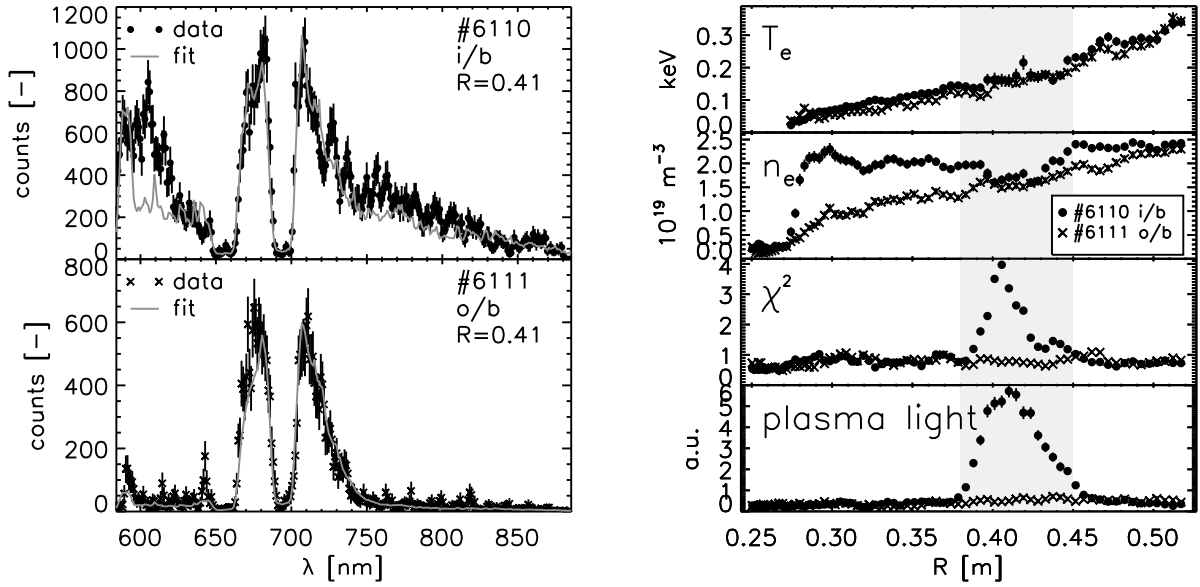


Figure 6.26: Distribution of the deviation of the high-resolution data from the low-resolution data relative to the error for the data in central region of the T_e , n_e and p_e profiles shown in figure 6.17. The distributions are compared with a normalised distribution of standard deviation 1. The fluctuations in the profiles can not be distinguished from the error.

Inboard gas fuelling

MAST is equipped with an inboard gas fuelling system positioned in the midplane in the centre column. This system facilitates the access to H-mode [19]. However, due to the position of the nozzle, the gas-puff crosses the line of sight of some of the spatial channels of the TS system around $R = 0.41$ m. The plasma light resulting from the influx of particles from the inboard gas-puff forms a significant part of the recorded spectrum in the region. This complicates the performance of the fit to the spectrum. Figure 6.27(a) compares the spectra of plasma discharges with inboard and outboard gas fuelling and shows the fits to the spectra. In general, T_e will be overestimated in the region, while n_e is underestimated. This is shown in figure 6.27(b). The figure also shows the increase in plasma light (fitting parameter a_2 , see section 6.4) and the rise in χ^2 in this region. To date no adequate remedies have been found to overcome this issue.



(a) Spectra and fit of spatial point in the region most affected by the inboard gas fuelling ($R = 0.41$ m) for a discharge with inboard and one with outboard gas fuelling. The inboard gas fuelling contributes to the spectrum and complicates the fit and therefore the determination of T_e and n_e .

(b) Detail of the TS profiles in the region most affected by the inboard gas fuelling system. The profiles show T_e , n_e , plasma light (fitting parameter a_2) and χ^2 of the fit.

Figure 6.27: The effect of the inboard gas fuelling system on the TS measurement.

However, the nozzle will be removed from the midplane in the centre column and two nozzles on either side of, but at sufficient distance from the midplane will be installed for the 2003 campaign. This will solve the issue of the inboard gas fuelling system for the TS diagnostic.

Limits to the temperature measurements

The lower temperature limit is, amongst other things, determined by the slit width and the corresponding width of the laser wavelength filter on the field mirror. The filter cuts out most of the light at low temperatures, due to the limited width of the Thomson scattered spectrum. Since this width depends on the scattering angle as $\sim \sin(\theta/2)$ (using (4.26)), the minimum detectable temperature varies with radius. The maximum T_e depends on the total width of the detection range, which in turn depends on the grating and the transmission values of the various elements in the detection branch.

Figure 6.28 shows the fraction of the total scattered light detected as function of the temperature for an inboard, central and outboard channel. The fraction drops for high T_e because of the limited wavelength range (584 nm to 900 nm for a central channel). The following example serves to illustrate the effect of the scattering angle on the lower end of the detection range. Supposing that 20% of the scattered spectrum is sufficient and necessary to perform a fit, then the minimum T_e is 18 eV on the inboard side, 23 eV in the centre and 44 eV on the outboard side. Because of contributions to the spectrum of plasma light and stray light, these lower limits increase.

The lower limits can be reduced by narrowing the slit width and the strip width on the field mirror. However, narrowing the slit reduces the total amount of scattered light and therefore

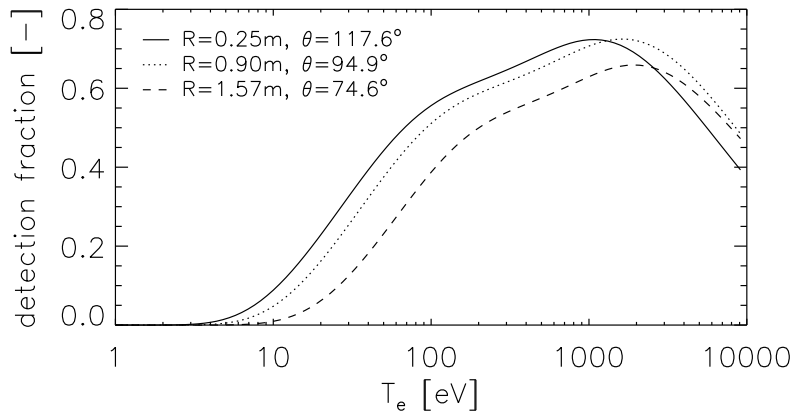


Figure 6.28: Theoretical fraction of the total scattered spectrum detected by the TS system for an inboard ($R=0.25$ m), central ($R=0.90$ m) and outboard ($R=1.57$ m) channel.

reduce the measurement accuracy. But in the regions of low temperature the scattered spectrum is narrow and even though the total amount of scattered light reduces, the ratio of detected light and scattered light increases by narrowing the slit width, implying that lower temperatures can be measured in this manner. The narrowing of the slit, however, is only desired in the low T_e regions, hence only at the plasma edges. Therefore, the width of the slit and strips ought to be R dependent.

Some improvement on the high temperature end can be made by turning the grating over a small angle such that more of the blue side of the scattered spectrum is observed instead of the red side. The blue side of the spectrum is preferred due to the relativistic shift of the Thomson scattered light to lower wavelengths. However, the lower limit of the wavelength range is set by the transmission of the image intensifier which has a cutoff below ~ 560 nm, while the detection range currently extends to ~ 580 nm. A shift of 24 nm can therefore be achieved, increasing the maximum T_e in the plasma centre only by a small fraction. This shift has no effect on the low temperature limit.

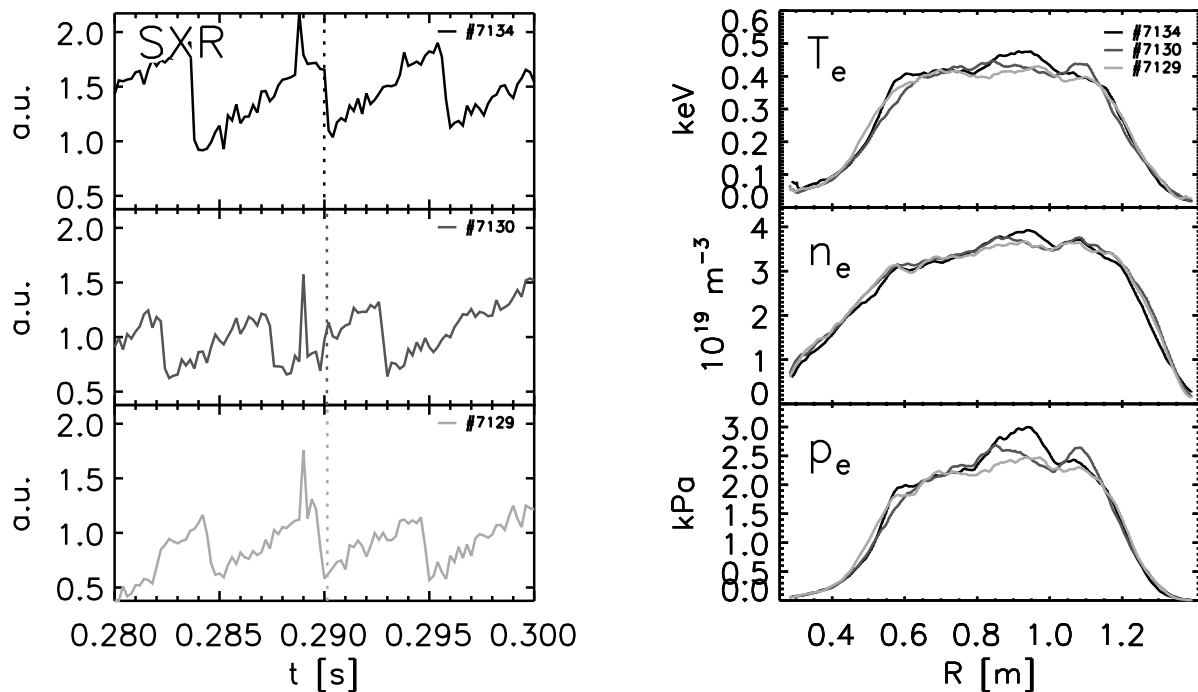
6.8 Profile examples

To illustrate the merits of the high-resolution Thomson scattering system on MAST, some examples of profile measurements are presented showing the capabilities of the diagnostic over the full range of the plasma: in the core the profiles are subject to changes due to sawtooth activity, off-axis magnetic islands have been observed, and clear pedestals are observed in high confinement.

Sawtooth activity

The first example shows the behaviour of the profiles during a sawtooth cycle. Two cases are presented: first Ohmic discharges, and secondly NBI heated discharges. In both cases the sawtooth period is ~ 5 ms.

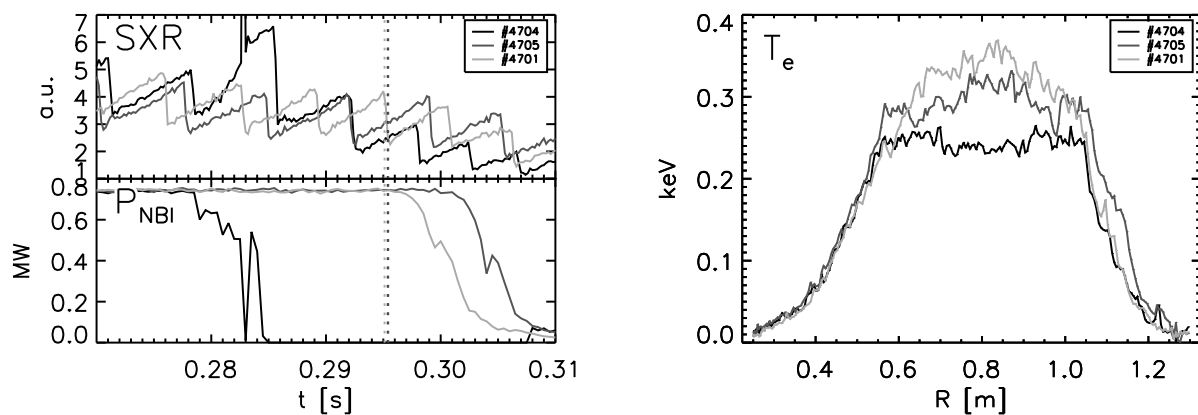
Figure 6.29 shows three similar Ohmic heated discharges for which the TS measurement is performed at different phases in the sawtooth cycle. A flattening occurs on both the T_e and n_e profile, which is believed to be within the $q=1$ region. Outside this region the profiles are very similar, but within the region small changes appear, seen clearest on the p_e profile. During the



(a) Soft X-ray traces at the midplane. The detectors show some pickup of the TS equipment at 1 ms before the laser pulse.

(b) Smoothed TS profiles of T_e , n_e and p_e .

Figure 6.29: Effect of sawtooth crash on TS profiles during Ohmic discharges. The TS measurement is taken at different phases during the sawtooth cycle; in #7129 just after the crash, in #7130 at midpoint in the cycle, in #7134 just before the crash.



(a) Soft X-ray traces at the midplane and NBI power.

(b) TS T_e profiles during the sawtooth cycle.

Figure 6.30: Effect of sawtooth crash on TS profiles during NBI heated plasma discharges.

sawtooth cycle a small rise in the central p_e is observed, which is lost at the sawtooth crash. The peak on the central p_e also shows some asymmetry. Although the changes are small, they can still be detected with the TS diagnostic.

The effects on the profiles of a sawtooth cycle are more obvious when NBI heating is applied. Figure 6.30 again shows three similar plasma discharges for which the TS measurement takes place at different phases in a sawtooth cycle of ~ 5 ms. For one of the plasma discharges (#4704) the NBI has been switched off ~ 12 ms before the TS measurement. The TS measurement took place ~ 3 ms after a sawtooth crash and shows a flat (possibly hollow) T_e profile. The T_e profile for #4705 is taken at approximately the same time compared to the sawtooth crash as for #4704. But, #4704 has ~ 0.87 MW NBI applied and it can be seen that the plasma centre is heated. Finally, the TS measurement for #4701 is taken just before the sawtooth crash and shows a peaked T_e profile.

Magnetic islands

The evolution of magnetic islands at medium to high β_N ($\beta_N \geq 1$) in MAST is well described by the neoclassical tearing mode (NTM) physics model [3]. 3-D field modelling is used to calibrate magnetically estimated island size measurements. Such island sizes can be compared to those measured by the TS diagnostic as shown in figure 6.31 for a tearing mode. This particular one is not definitely identified as an NTM, but still serves to test magnetic estimates, as the mode has the same structure and location. The width of the $m/n = 2/1$ island in this plasma discharge is estimated using the physics model at ~ 12 cm on the inboard side. The thus calculated dimension of the island is indicated by the horizontal bar in the figure. An estimate of the width of the island on the outboard side is also indicated in the figure. The p_e profile shows a clear flattening around the position of the $q = 2$ surface provided by EFIT.

Pedestals in high confinement

Due to the wide radial extend, the high resolution, the many spatial points and the high accuracy, the TS diagnostic makes it possible to measure the inboard and outboard T_e , n_e and p_e pedestals in a single plasma discharge. Examples of such measurements during the inter-ELM period of H-mode plasma discharges are shown in figure 6.32. These pedestal measurements make it possible to study in detail the behaviour of the pedestal during ELMs and to calculate the pedestal energy accurately, which ultimately could lead to improved pedestal scaling law predictions. More on these topics is presented in Chapter 8.

6.9 Summary

A single-pulse high-resolution Thomson scattering system has been installed on MAST. It measures the radial profile of T_e and n_e along a horizontal chord through the midplane of the MAST vessel. The chord covers the full plasma width and is continuous. The measurement also returns the line-integrated plasma light profile. The system is fully automated and requires little daily maintenance.

The data can be analysed in low- and high-resolution. Extensive error analyses have been carried out on the raw data and on the fitted data. The measurement accuracy is typically $< 5\%$ of T_e and $< 4\%$ of n_e in the range 40 eV - 2 keV for a density of $n_e \sim 4 \times 10^{19} \text{ m}^{-3}$ in high resolution.

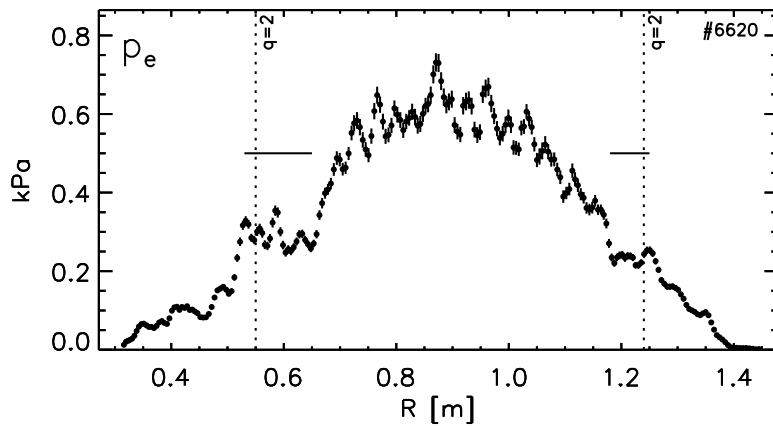


Figure 6.31: TS p_e profile clearly showing an $m/n = 2/1$ island positioned at the $q = 2$ surface as produced by EFIT. The prediction of the width of the island following from 3-D field modelling is indicated by the horizontal bars.

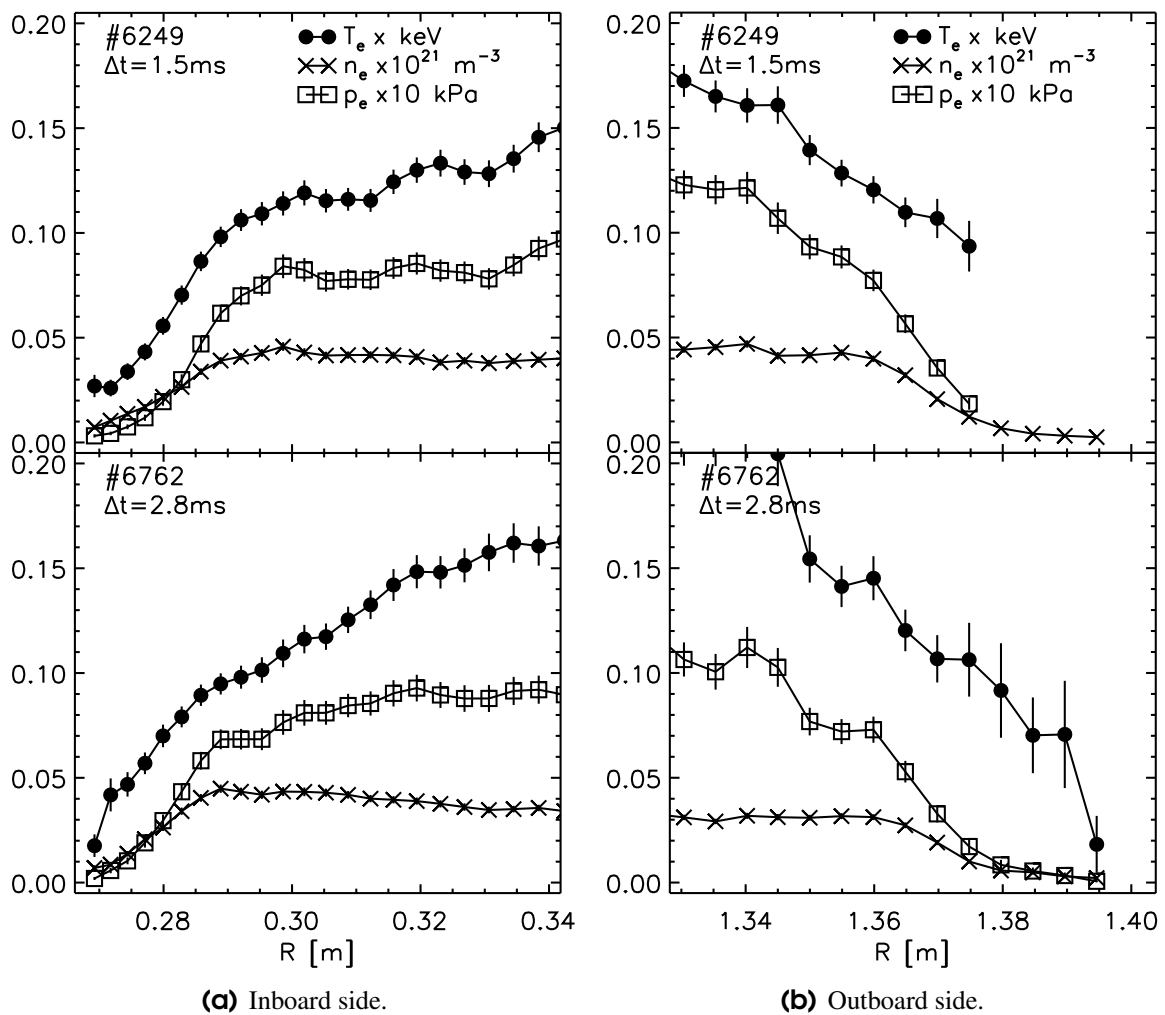


Figure 6.32: Pedestal measurements during the inter-ELM time of an H-mode plasma discharge. Δt indicates the time since the last ELM.

Due to the orientation of the laser beam path and of the collection optics, good scattering geometry and high normalised-flux resolution are achieved, especially at the inboard edge and in the magnetic centre. The root-normalised-flux resolution is introduced to express the resolution of the system by a machine-independent variable. The resolution is best at the inboard edge ($\Delta\sqrt{\psi}_N \approx 1/200$) and rises to $\Delta\sqrt{\psi}_N \approx 1/50$ towards the outboard edge. The high-resolution TS system is therefore a powerful tool in edge gradient studies.

Bibliography

- [1] P.C. Liewer. *Nuclear Fusion*, 25:543, 1985.
- [2] B.B. Kadomtsev. *Tokamak plasma: a complex physical system*. Bristol and New York, 1992.
- [3] R.J. Buttery et al. Neoclassical tearing physics in the spherical tokamak mast. *Physical Review Letters*, 88(12):125001–1:125005–4.
- [4] E.R. Arends et al. Measurement and modelling of H-mode density profiles with edge density ‘ears’ on the MAST spherical tokamak. Submitted for publication in *Plasma Physics and Controlled Fusion*, March 2003.
- [5] M.J. Walsh et al. Interactive Optical Design and Realisation of an Optimised CCD Thomson Scattering System for the Spherical Tokamak START. *Review of Scientific Instruments*, 70(1):742–746, January 1999.
- [6] M.J. Walsh et al. Combined visible and infrared Thomson scattering on the MAST experiment. *Review of Scientific Instruments*, 74(3), March 2003.
- [7] R.J. Hertel. Signal and noise properties of proximity focused image tubes. *SPIE*, 1155:332–343, 1989.
- [8] J. Waterhouse. On IDA3. Technical report, UKAEA/Fusion.
- [9] C.J. Barth, C.C. Chu, M.N.A. Beurskens, and H.J. v.d. Meiden. Calibration procedure and data processing for a TV Thomson scattering system. *Review of Scientific Instruments*, 72(9):3514–3527, September 2001.
- [10] P. Nielsen. Thomson scattering in high temperature devices. In *Diagnostics for fusion reactor conditions*, volume 1, pages 225–259, Varenna, Italy, September 1982. Commission of the European communities.
- [11] N.J. Conway. *The non-linear least square fitting routine LMBEVFIT*. UKAEA Fusion, Culham Science Centre, Abindon, Oxfordshire, OX14 3DB, UK.
- [12] S.K. Nielsen. Investigation of electron particle behaviour in the MAST spherical tokamak from Thomson scattering using Ruby laser and Nd:YAG laser systems. Master’s thesis, Aarhus University, Institute for Physics and Astronomy, Ny Munkegade, 8000 Aarhus, Denmark, 2002.
- [13] I.H. Hutchinson. *Journal of Physics D: Applied Physics*, 10(L11), 1977.

- [14] K.A. Karelse. Measurements of the current density profile with tangential Thomson scattering in RTP. *Plasma Physics and Controlled Fusion*, 43(4):443–468, April 2001.
- [15] M.N.A. Beurskens et al. Error analyses of RTP Thomson scattering data. *Review of Scientific Instruments*, 70(4):1999–2011, April 1999.
- [16] W. Feller. *An introduction to probability theory and its applications*, volume 1. Wiley, 1968.
- [17] T. Jorgensen. On Probability Generating Function. *American Journal of Physics*, 16:285–289.
- [18] B.P. van Milligen, I.G.J. Classen, and C.J. Barth. Revision of TV Thomson scattering data analyses and detection of profile structure. Submitted for publication in *Review of Scientific Instruments*, December 2002.
- [19] A.R. Field et al. Improved H-mode access with inboard gas puffing. In *Proceedings of the 29th EPS Conference on Controlled Fusion and Plasma Physics*, volume 26B, June 2002.

6.A Setup of test CCD image used for Monte-Carlo simulation of errors

The Monte-Carlo simulation will be used to estimate the error on T_e and n_e for a central channel, but any channel can be simulated in a similar way. In order to be able to use the same fitting engine as used in the profile analyses, test CCD images are made from uniform T_e and n_e profiles. All channels have also been given equal values for scattering angle (here 90°) and spectral region. From these parameters, the theoretical scattered spectra are determined. These spectra were convolved with the spectral instrument function and multiplied with the wavelength response of the system. The radial instrument function (see section 6.6) has no effect on a uniform profile, and is therefore not included. Finally, plasma light and stray light spectra are added in proportions similar to measured values. At this stage, the spectra for all radial channels on the CCD image are the same.

Now Poisson noise is added to the signal at the stage before the multiplication process in the MCP, *i.e.* noise is added to $M_{i,j}$. For the calculation of the mean of the Poisson distribution, the smoothing factor Γ must not be taken into account, since the smoothing only happens after the noise is added. Thus, the mean of the Poisson distribution is $M_{i,j}$.

The CCD image is finalised by convolving the data with the 2-D instrument function. It has to be noted, that the instrument function in the spectral direction includes the radial component of the 2-D smoothing function. Therefore, the smoothing is applied twice in the spectral direction, this results in broadening of the spectra. However, this broadening can be neglected since the width of the smoothing function is much smaller than the width of the spectrum. From (4.26) follows for this ruby system ($\lambda_i = 694.3$ nm) that the 1/e width can be approximated by $\Delta\lambda \approx 2\sqrt{T_e}$ nm, where T_e is expressed in eV. For $T_e > 22$ eV this width is at least 10 times bigger than the 1/e width of the 2-D smoothing function ($\Delta = \sqrt{2} \times 0.64 \text{ pixel} \times 1.05 \text{ nm/pixel} = 0.95$ nm). The 1/e width of the convolution of the two function is $\sqrt{\Delta\lambda^2 + \Delta^2}$, as a result the broadening of the spectrum is less than 1% for $T_e > 22$ eV. Therefore, the effect of the 2-D smoothing function on the broadening of the spectra can be neglected for the whole detectable temperature range.

Chapter 7

Edge density gradient measurements

The edge electron density gradient in MAST is determined in two ways. First, by using the high-resolution Thomson scattering system. This method provides both inboard and outboard edge gradients, the former having the highest resolution. Secondly, by extracting it from the narrowing of the radial D_α emissivity profile at the plasma edge. A method is presented to extract the ‘real’ edge gradient and pedestal values in the plasma from the data in a consistent way by fitting the profiles to a mathematical function describing the shape of the pedestal in the plasma.

7.1 Introduction

One of the signatures of the high-confinement regime (H-mode) of a tokamak plasma is the development of steep edge density gradients. During H-mode the edge gradient can be affected by the presence of edge localised modes (ELMs) or other edge localised instabilities. The changes induced by the instabilities can be marginal and happen on fast time scales (< 100 ms). In order to study these changes, high precision spacial and temporal measurements of the edge density gradient are necessary. Also for other reasons it is desirable to have a good measurement of the edge density gradient: *e.g.* it is associated with a high edge density, which largely determines losses of neutral beam particle injection (NBI) and plays a basic role in the understanding of the fuelling efficiency of the plasma. Furthermore, the edge gradient plays a role in the determination of pedestal values, *e.g.* pedestal width and stored energy, which are input to transport studies and scaling laws. The edge electron density gradient is therefore a key factor in understanding many edge dominated phenomena. On MAST, two diagnostics are employed to measure the edge electron density gradient ($\partial n_e / \partial r$) at high accuracy and time resolution.

The first of these is the high-resolution Thomson scattering (TS) system described in Chapter 6. It measures the actual gradients on both the high and low field sides of the plasma at high accuracy. However, on MAST the measurement of the edge density profiles using the high-resolution TS system is limited to once per plasma discharge.¹ In order to measure the edge density gradient with high time resolution a diagnostic based on the atomic physics interpretation of the radial D_α emissivity is implemented. The latter is reconstructed from the linear CCD camera data which monitors the plasma edge emission. The system, as presented in [1], takes advantage of the simple atomic physics of hydrogen ionisation and excitation, and provides a robust and inexpensive method for extracting the edge density gradients. For the calibration of this diagnostic the n_e measurement from TS are indispensable.

¹Technically it is possible to upgrade the system to give two measurements per discharge, with the consequence of losing accuracy.

This chapter gives an analysis of the measurements of the edge density gradients using the high-resolution Thomson scattering system (see also Chapter 6) and describes the measurements of the edge density gradients using the linear D_α camera.

7.2 Edge density gradients from Thomson scattering

The high-resolution Thomson scattering system on MAST measures the electron temperature (T_e) and density (n_e) profiles at ~ 300 spatial points along a horizontal chord through the mid-plane of the plasma. An extensive description of this TS system is given in Chapter 6.

An important aspect of this system for edge gradient measurements is the spatial resolution of the system. For the determination of the edge pedestal one has the choice between the high field (inboard) and low field (outboard) side of the plasma. The difference between the two will be highlighted here. Secondly, a method will be described to standardise the determination of the edge pedestal and edge gradient by fitting the profiles to a mathematical function that includes the finite size of the collection volumes and the instrument function.

7.2.1 Comparison of inboard and outboard density gradient measurements

The detection range of the TS diagnostic covers the full plasma, such that both inboard and outboard density gradients are measured. If the parallel particle transport along the field lines is sufficiently faster than the perpendicular transport these gradients are expected to be equal as function of the flux coordinate. Instabilities at the edge of the plasma or enhanced radial transport can create differences. In order to be able to study the discrepancies between the two gradients, it is necessary to understand the differences in the measurements between the two sides. These are caused by the diagnostic, by the magnetic configuration and by the orientation of the optics with respect to the plasma. The following list presents an overview of, the differences between between and the pros and cons of the inboard and outboard gradient measurements.

- Orientation of the laser beam with respect to the vessel.
Where the laser beam approaches the centre column at close range (~ 45 mm, see figure 6.23), the change in radial position from one collection volume to the next decreases (see section 6.6). The radial extent of the collection volumes is therefore smallest close to the centre column.
- Orientation of the laser beam with respect to the flux surfaces.
The laser beam is parallel to the flux surfaces close to the centre column on the inboard side, while it is perpendicular on the outboard side. Therefore, the flux coordinate changes less from one spatial point to the next on the inboard side than on the outboard side. As a result the resolution is highest on the inboard side. This is illustrated in figure 7.1.
- Shafranov shift.
The former effect is enhanced by the wider spread of the flux surfaces on the outboard side due to the Shafranov shift.

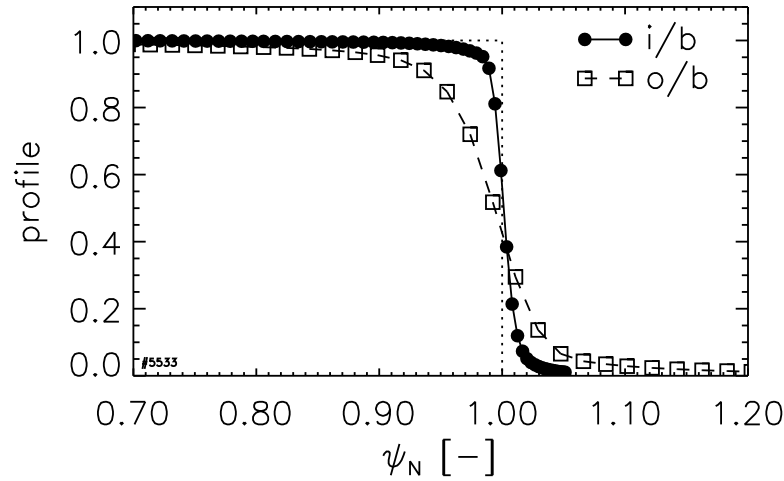


Figure 7.1: Comparison of the maximum theoretical gradients to be measured by the TS diagnostic on inboard and outboard side as function of the normalised flux coordinate ψ_N . The figure is obtained by folding in the finite size of the collection volumes and the radial instrument function into a step function profile on inboard and outboard side. This method is described in section 6.6. The dashed curved shows the ‘real’ input step function profile.

- Orientation of the collection optics with respect to the plasma edge.
On the inboard side the orientation of the lines of sight of the individual spatial channels of the TS diagnostic with respect to the flux surfaces is close to perpendicular, again as illustrated in figure 6.23. These lines of sight cross the cold edge of the plasma, from where most plasma light originates due to the ionisation of neutral particles and other processes, over a minimal distance. On the outboard side this line of sight is almost parallel to the last closed flux surface (LCFS) and a maximum amount of plasma light is therefore collected. The contribution of plasma light to the total collected spectrum complicates the fit, this would therefore be a disadvantage for the outboard side. However, the level of plasma light is generally very small compared to the scattered spectrum.
- Orientation of the collection optics with respect to the laser beam path.
The scattering angle (θ) is largest on the inboard side at $\theta = 117.6^\circ$ and reduces to $\theta = 74.6^\circ$ on the outboard side. Since the width of the Thomson scattered spectrum ($\Delta\lambda$) in approximation scales with $\sin(\theta/2)$ (see Chapter 4) the spectrum will be broader on the inboard side for equal temperatures. This is of importance for the low temperature range where the scattered spectrum is narrow ($\Delta\lambda \sim \sqrt{T_e}$). A narrow wavelength region around the laser wavelength is filtered out to avoid saturation of the detection unit by stray light (see Chapter 6). The filter therefore sets limits to the minimum T_e that can be measured, which will be lowest on the inboard side due to the higher scattering angle ($\Delta\lambda \sim \sin(\theta/2)$).
- Plasma approaching the centre column.
Since the LCFS can, in some circumstances, approach the centre column at close distance, the inboard gradient can sometimes (partially) fall outside the TS range of observation and be missed.
- Stray light reflected of the centre column.
The centre column forms a source for stray light on the measured TS spectrum (see figure

6.9), which decreases the accuracy of the measurement slightly.

- Edge localised modes.

The outboard edge gradient is flattened during ELM events while the inboard edge gradient is not as will be shown in section 8.5.

To conclude: the measurement of the edge density gradient on the inboard side is more accurate than on the outboard side, but the inboard gradient can be missed when the plasma approaches the central column at close range.

In the next section a method will be presented by which the ‘real’ edge gradient can be recovered from the TS data on both radial and normalised flux coordinates, so that a comparison can be made between the inboard and outboard edge data.

7.2.2 Fitting edge gradient and pedestal

In order to standardise the determination of the edge gradient and pedestal on the n_e (and T_e and p_e) profiles the profiles are fitted to a standard edge profile function. This function is based on the modified tangent hyperbolicus (*mtanh*) function [2] and will be defined as:

$$\text{edge}(x, \vec{a}) = \frac{a_2 - a_4}{2} \left[\text{mtanh} \left(\frac{a_0 - x}{2a_1}, a_3 \right) + 1 \right] + a_4 \quad (7.1)$$

where the *mtanh* function is defined as:

$$\text{mtanh}(x, b) = \frac{(1 + bx) \exp(x) - \exp(-x)}{\exp(x) + \exp(-x)} \quad (7.2)$$

The *mtanh* function is a modification of the *tanh* function, which is the natural shape of the edge density profile resulting from a simplification of the particle transport model presented in Chapter 5. In this simplification the diffusion profile D is uniform, the electron transport is diffusive ($\vec{V} = 0$) and the equations are solved in steady state and in a slab rather than a cylindrical coordinate system. The fit parameters $\vec{a} = [a_0, a_1, a_2, a_3, a_4]$ have the following meaning:

a_0 : position of transport barrier

a_1 : width of transport barrier

a_2 : height of pedestal

a_3 : linear core slope

a_4 : scrape off layer (SOL) value

An example of the function illustrating the meaning of the fit parameters is shown in figure 7.2.

The edge profiles in the plasma are assumed to have the shape of the *edge* function. The TS diagnostic measures slightly different profiles due to the finite size of the collection volumes and to the radial instrument function, as explained in section 6.6. These determine the resolution as described in section 6.6. In order to compare (7.1) with the TS measurement, the collection volumes and the instrument function have to be taken into account. This is done as in (6.11) as regards the determination of the spatial resolution, but instead of a top-hat function, the *edge* function is used:

$$\text{TS}(\text{edge})(x) = \frac{1}{dx} \int_{x-dx/2}^{x+dx/2} \text{edge}(x') dx' \otimes I(x) \quad (7.3)$$

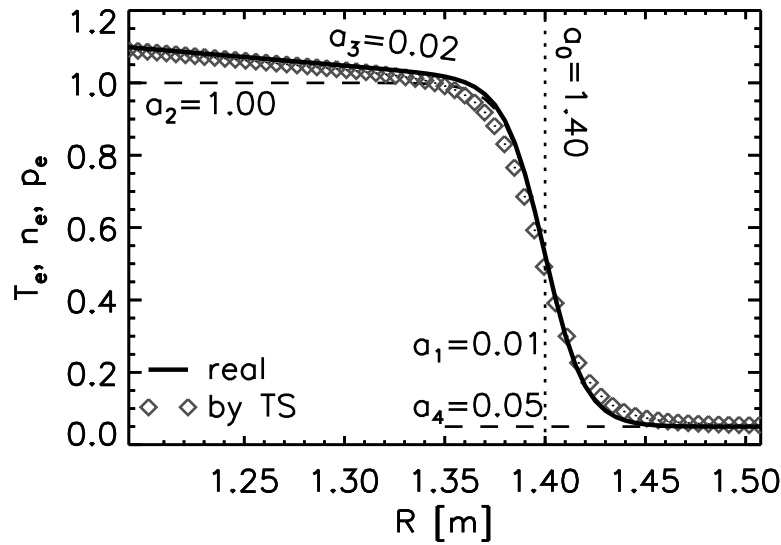


Figure 7.2: Schematic of the *edge* function as it appears in the plasma ('real') and as it is measured by TS.

This function is also shown in figure 7.2 and it shows a clear change in the region of the steep gradient, while outside the region the profile is less affected. The simulated measurement is lower inside the gradient (and higher outside the gradient) due to the long tail of the instrument function (see figure 6.22).

The function is fitted to the TS measurements on either base R or ψ_N using a least-square fitting routine, where ψ_N is provided by the equilibrium reconstruction code EFIT [3]. Initially, the fitting requires some guess work as to the fitting parameters. The initial guess for the position of the transport barrier on the outboard side (a_0) is taken from the position of the D_α peak as measured by the linear camera (see section 7.3). As to the width of the transport barrier (a_1) the distance between a_0 and the position of the outboard LCFS provided by EFIT is taken. As to fittings on the inboard side the initial value for a_0 is given by the position of the inboard LCFS plus the width derived for the outboard side. The start value for the pedestal height (a_2) is simply taken as twice the measured value at initial guess for a_0 . The slope (a_3) and SOL value (a_4) start off at 0. An example of a $TS(edge)$ fit to both inboard and outboard n_e profiles is shown in figure 7.3. The figure also shows the 'real' pedestal obtained from the *edge* function.

The fitting provides the parameters \vec{a} from which the pedestal height and edge gradient are determined. The shape of the pedestal is given by the *edge* function using (7.1), using the parameters \vec{a} for which the linear core slope is suppressed ($a_3 = 0$). The gradient is calculated at the position of the barrier ($R = a_0$) which normally gives the maximum gradient. The pedestal width is for simplicity defined (for n_e but similar for T_e and p_e) as:

$$\Delta n_{e,ped} \equiv 4a_1 \quad (7.4)$$

In this definition, the pedestal covers 76% of the pedestal height over the extent of the pedestal width. This width is indicated in figure 7.3 by the shaded area. The advantage of this method of fitting is that, when fitting using normalised flux coordinates, the inboard and outboard pedestal parameters can be compared.

The fitting routine has been used to fit a test set of inboard (i/b) and outboard (o/b) n_e gradients. The data set contains both L-mode and H-mode plasma discharges and therefore a wide range of density gradients is covered. The discharges that have been selected show a clear

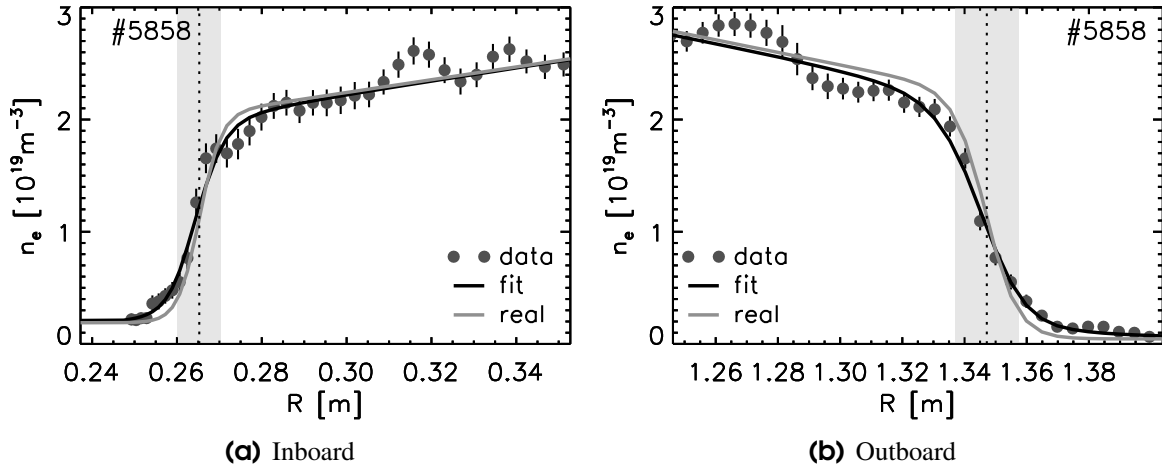


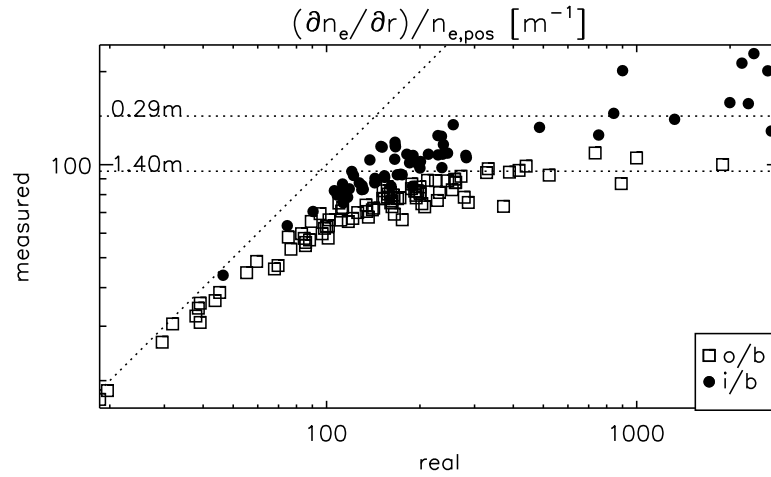
Figure 7.3: Example of a $TS(edge)$ function fit to an inboard and outboard n_e profile. Also shown is the ‘real’ n_e pedestal in the plasma described by the $edge$ function. The vertical dashed line locates the position of the transport barrier. The shaded area marks the pedestal width $\Delta n_{e,ped}$.

edge density gradient and pedestal and have data points up into the SOL. Since many discharges have a geometry that is very close to the central column, which favours the access to H-mode in combination with the application of the inboard gas-feeding system (see section 8.3) TS data are often missing for the SOL and therefore an accurate fit cannot be made.² The data have been fitted both on axes of radius and normalised flux. The pedestals have been fitted to both the $edge$ function (7.1) and the $TS(edge)$ function (7.3) to show the effect of including the finite size of the collection volumes and instrument function on the determination of the pedestal values.

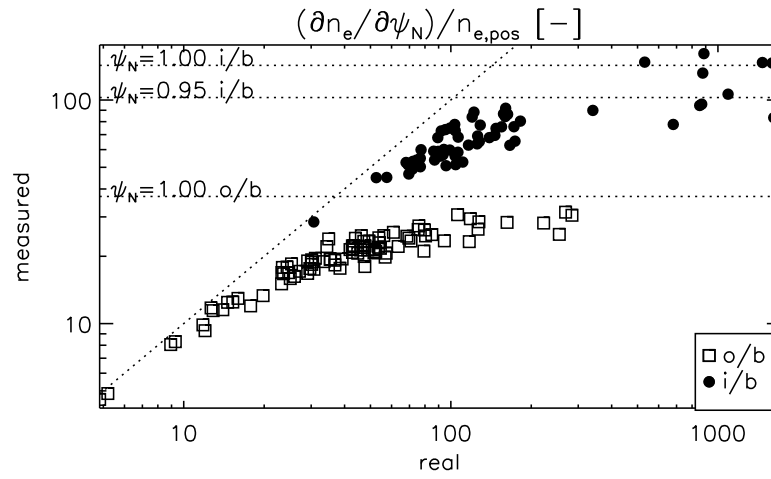
A comparison of the inverse gradient length as measured by the diagnostic with the ‘real’ gradient is shown in figure 7.4. For fitting on the radial axis the inverse gradient length is defined as in (6.9) by $(\partial n_e / \partial R) n_{e,pos}^{-1}$, for fitting on the normalised flux as in (6.7) by $(\partial n_e / \partial \psi_N) n_{e,pos}^{-1}$. Here the gradient and density values are taken at the position of the barrier (a_0). For small gradients the measured inverse gradient length approaches the ‘real’ values: in the limit of $\partial n_e / \partial R \rightarrow 0$ the instrument has no effect on the measurement of the gradient. For steep gradients the inverse gradient length approaches the resolution of the system as indicated in the figures by the horizontal lines. These limits, ΔR and $\Delta \psi_N$ respectively, have been determined from a step function ($a_1 \rightarrow 0$) in section 6.6 and are shown in figure 6.24. The data for higher gradients on the inboard side are scattered due to the rapidly changing resolution in this region (see figure 6.24) and the spread in the position of the transport barrier.

Figure 7.5 shows a comparison of the pedestal height with the barrier position determined a) using the $TS(edge)$ function and b) using the $edge$ function. This shows that the limited size of the collection volumes and instrument function have little effect on both the height of the pedestal (a_2) and the position (a_0). Determination of the pedestal height without taking the collection volumes and instrument function into account produces an underestimation between 0% and 5% of both inboard and outboard data. In this way, the position is underestimated by $\sim 0.1\%$ on the outboard side, and $\sim 0.4\%$ on the inboard side. The latter number is higher mainly due to the lower value of the denominator of the plotted ratio on the inboard side ($a_0 \sim 0.27$ m) compared to the outboard side ($a_0 \sim 1.4$ m).

²For some profiles, not affected by ELMs, the outboard SOL data can be mapped to the inboard side in order to provide enough data to perform an accurate fit.



(a) Radial inverse density gradient scale length.



(b) Normalised flux inverse density gradient scale length.

Figure 7.4: Limits to the density gradient lengths in radial and normalised flux coordinates on the inboard (i/b) and outboard (o/b) sides. The measured gradients are similar to the ‘real’ gradients for small gradients, but are limited by the resolution of the system for steeper gradients. The resolutions ΔR and $\Delta\psi_N$ at various positions of R and ψ_N respectively are indicated by the horizontal dashed lines.

Figure 7.6 shows the position of the barrier (a_0) compared to the LCFS for the inboard and outboard data. Not included in the graph is the uncertainty in the determination of the LCFS using EFIT. To minimise these uncertainties, the plasma size as returned by EFIT has been minimally corrected by stretching the radial axis to give the best mapping of the profiles of the inboard side onto the outboard side. In general, the position of the barrier is, as expected, just inside the LCFS, though this applies more to the inboard data than the outboard data. For some of the outboard data, the barrier is positioned outside the LCFS. It is assumed that this is, in addition to the uncertainty in the determination of the position of the LCFS, due to the presence of ELMs (see section 8.5). No correlation is observed between the position of the barrier and the steepness of the gradient.

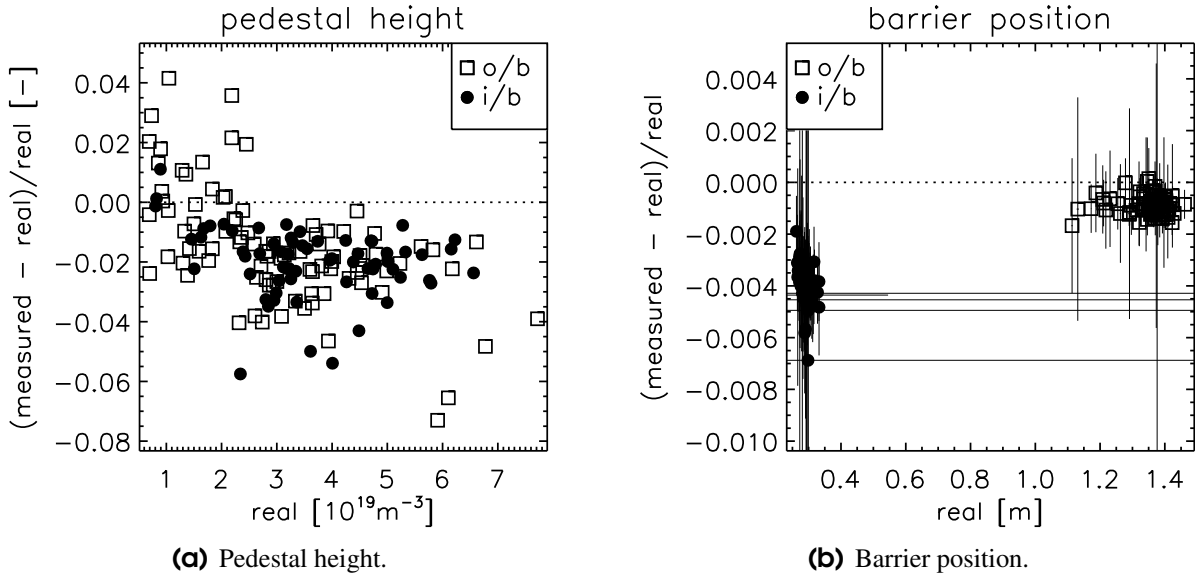


Figure 7.5: Comparison of the fitting parameters for fits to the n_e pedestal using the $TS(\text{edge})$ function ('real') and using the edge function ('measured').

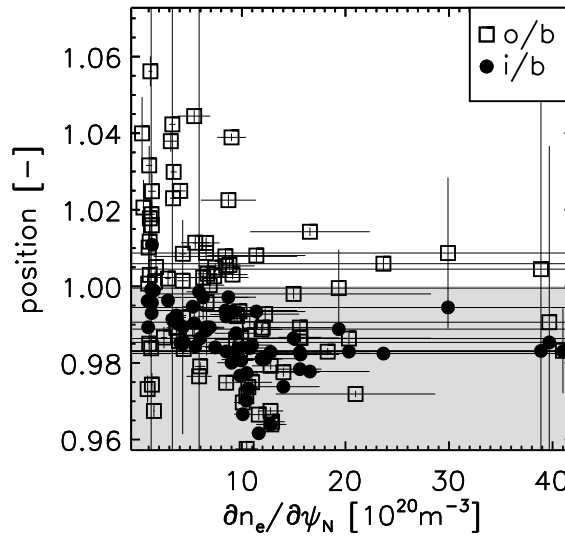


Figure 7.6: Position of barrier, as determined by a edge function fit to the data, in normalised flux coordinates as function of the density gradient. The shaded area indicates the region within the LCFS.

7.3 Edge density gradients from linear D_α camera

On MAST a linear D_α camera monitors the outboard edge emission of deuterium discharges with high time resolution (≥ 1 kHz). From this the average edge electron density gradient can be determined after calibration the data using the high-resolution TS edge density gradient measurements.

The edge electron density can be derived, by making some assumptions, from the Balmer- α spectral line emission. This is generally the dominant source of visible emission at the plasma edge. From the linear D_α camera data, the radial D_α emission profile can be determined using inversion algorithms [1]. During the transition from L- to H-mode plasmas in MAST it is

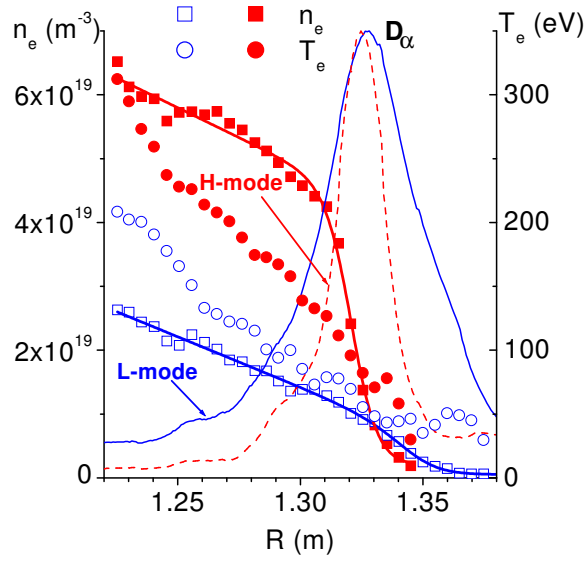


Figure 7.7: Normalised radially unfolded D_α emissivity profiles for two MAST plasma discharges, one during L-mode (#5980) and one during H-mode (#6012), with contrasting edge n_e gradients. The T_e profiles are also presented and show less change [1].

observed that there is a strong correlation between the narrowing of the radial width of the D_α radiation and the steepening of the edge n_e gradient, measured by the high-resolution Thomson scattering system (see Chapter 6) as illustrated in figure 7.7. The narrowing the electron source function during this transition was previously presented in Chapter 5.

The radial D_α emissivity profile can be presented as the product of the neutral and electron densities and of the effective rate coefficient $\langle\sigma_{ex}v_e\rangle$ for populating the $n = 3$ principal quantum level:

$$\varepsilon = \langle\sigma_{ex}v_e\rangle n_e n_n \quad (7.5)$$

The observed D_α emissivity profile is primarily determined by the n_e gradient at the edge and is much less sensitive to changes in T_e at the edge. Typically, T_e ranges between 40 eV and 200 eV for most of the D_α emissivity in MAST plasmas, where ion and impurity impact ionisation are negligible, and is well in excess of the hydrogen ionisation potential (13.6 eV), thus making the rate coefficients almost temperature independent. Both the effective ionisation rate ($\langle\sigma_{ion}v_e\rangle$) responsible for n_n attenuation in the plasma edge and the excitation rate ($\langle\sigma_{ex}v_e\rangle$) responsible for populating the $n = 3$ principal quantum level, vary only by $\pm 15\%$ in the typical radial scale length of D_α emissivity [4]. For example, at typical edge densities around $\sim 10^{19} \text{ m}^{-3}$ the effective rate will only rise from $\sim 2.1 \times 10^{-15} \text{ m}^3\text{s}^{-1}$ to $\sim 2.5 \times 10^{-15} \text{ m}^3\text{s}^{-1}$ as regards excitation and from $\sim 2.5 \times 10^{-14} \text{ m}^3\text{s}^{-1}$ to $\sim 3.2 \times 10^{-14} \text{ m}^3\text{s}^{-1}$ as regards electron impact ionisation in the temperature range between 40 eV and 200 eV (see figure 5.9).

Taking advantage of these atomic physics effects, the edge D_α emissivity profile can be readily estimated from densities alone. For the sake of simplicity and as a preliminary estimate a simple one-dimensional analytical model has been developed relating the behaviour of the full width at half maximum (FWHM) of the radial D_α emissivity profile (Δ_α) to the plasma edge parameters.

In Chapter 5, a model for the transport of neutral particles was presented based on the conservation of neutral particles (5.8). A simplified version of the model is used here; this time

the equation is solved in steady state in a slab coordinate system, the results of which is:

$$n_n = n_n(0) \exp\left(-\frac{\langle\sigma_{ion}\nu_e\rangle}{|\vec{V}_n|} \int_0^r n_e(r') dr'\right) \quad (7.6)$$

where r is the distance from the plasma edge and $n_n(0)$ is the edge neutral density.

The edge n_e profile is now represented by a simple linear approximation:

$$n_e = \frac{\partial n_e}{\partial r} r \quad (7.7)$$

where the density gradient, $\partial n_e/\partial r$, is assumed constant in the edge region. An expression for the edge neutral density profile is thus found:

$$n_n = n_n(0) \exp\left(-\frac{\langle\sigma_{ion}\nu_e\rangle}{2|\vec{V}_n|} \frac{\partial n_e}{\partial r} r^2\right) \quad (7.8)$$

In this assumption the radial D_α emissivity profile can be approximated by:

$$\varepsilon(r) = \langle\sigma_{ex}\nu_e\rangle \frac{\partial n_e}{\partial r} r n_n(0) \exp\left(-\frac{\langle\sigma_{ion}\nu_e\rangle}{2|\vec{V}_n|} \frac{\partial n_e}{\partial r} r^2\right) \quad (7.9)$$

Taking $\langle\sigma_{ion}\nu_e\rangle$ and $\langle\sigma_{ex}\nu_e\rangle$ to be constant in the D_α emissivity range, *i.e.* neglecting the weak temperature dependence, the position of the maximum of the radial D_α emissivity, r_α , can be found by differentiating (7.9):

$$r_\alpha = \sqrt{\frac{|\vec{V}_n|}{\langle\sigma_{ion}\nu_e\rangle \partial n_e / \partial r}} \quad (7.10)$$

Using (7.10), (7.9) can be written as:

$$\varepsilon(r) = \langle\sigma_{ex}\nu_e\rangle \frac{\partial n_e}{\partial r} r n_n(0) \exp\left(-\frac{1}{2} \left(\frac{r}{r_\alpha}\right)^2\right) \quad (7.11)$$

Expressing the D_α emissivity at a position of half maximum, r_Δ ($\varepsilon(r_\Delta) = \varepsilon(r_\alpha)/2$), (7.11) can be rewritten as:

$$\xi \exp\left(-\frac{\xi^2}{2}\right) = \frac{1}{2} \exp\left(-\frac{1}{2}\right) \quad (7.12)$$

where ξ is a dimensionless variable given by:

$$\xi = \frac{r_\Delta}{r_\alpha} = \sqrt{\frac{\langle\sigma_{ion}\nu_e\rangle}{|\vec{V}_n|} \frac{dn_e}{dr} r_\Delta} \quad (7.13)$$

There are two unique solutions of (7.12) ($\xi = 0.319$ and $\xi = 1.369$) corresponding to each side of the D_α emissivity at the position of half maximum. Therefore, the FWHM of D_α emissivity (Δ_α) can be approximated by:

$$\Delta_\alpha = 1.688 \sqrt{\frac{|\vec{V}_n|}{\langle\sigma_{ion}\nu_e\rangle \partial n_e / \partial r}} \quad (7.14)$$

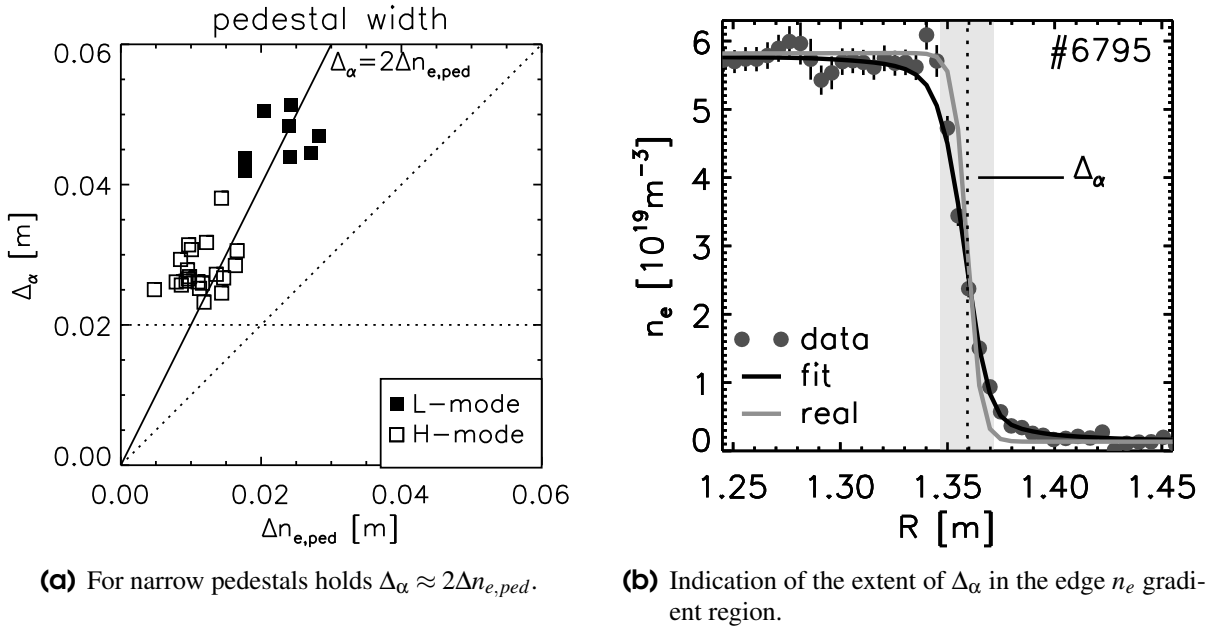


Figure 7.8: Width of the radial D_α emissivity profile peak compared with the pedestal width obtained from fits to the TS data. The former is linear with the latter and the ‘real’ edge gradient is approximately linear in region of width Δ_α .

Thus:

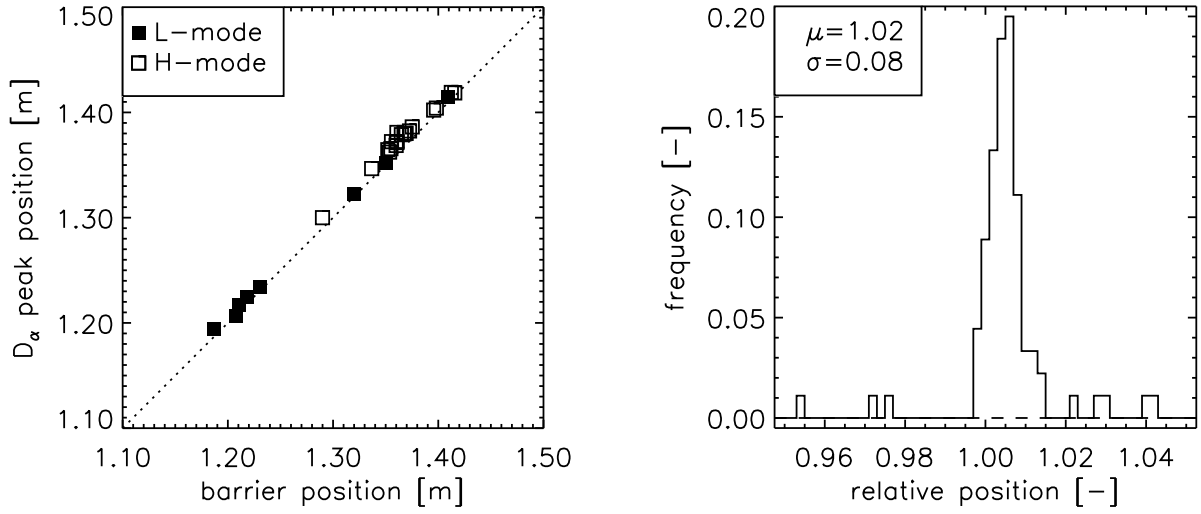
$$\frac{\partial n_e}{\partial r} = \frac{|\vec{V}_n|}{\langle \sigma_{ion} \nu_e \rangle} \left(\frac{1.688}{\Delta_\alpha} \right)^2 \quad (7.15)$$

Thus a simple linear relationship between edge n_e gradient ($\partial n_e / \partial r$) and $1/\Delta_\alpha^2$ as well as neutral influx velocity (\vec{V}_n) is found.

The analytical approximations of Δ_α are compared with computer simulations of the radial D_α emissivity based on the ADAS database [5]. The edge neutral density was modelled using the one-dimensional Monte-Carlo neutral particle transport code DOUBLE [6] using a range of plasma edge conditions ($T_e \sim 40 - 200$ eV) to test the T_e sensitivity. These modelling results [1] show an almost linear dependence of $\partial n_e / \partial r$ on $1/\Delta_\alpha^2$ and neutral on influx velocity, in accordance with (7.15).

A test set of the edge n_e measurements in MAST deuterium discharges was combined using the high-resolution TS diagnostic at the time of the TS measurement. These measurements are taken during L-mode and ELM-free periods of H-mode to guarantee minimal changes in the gradient. The edge gradients from the TS data have been estimated using the $TS(edge)$ fit (see section 7.2). Figure 7.8(a) shows a comparison of Δ_α with the density pedestal width $\Delta n_{e,ped}$ ($\equiv 4a_1$, where a_1 is the fitting parameter determining the width of the pedestal described by the $edge$ function). This shows that the FWHM of the radial D_α profiles scales as $\Delta_\alpha \approx 2\Delta n_{e,ped}$. The lower limit for Δ_α is ~ 0.02 m and is set by the smearing of the optics of the linear D_α camera system.

Δ_α has been compared with gradients obtained from $TS(edge)$ fits to the TS data. The gradients are taken at the barrier position, which normally produces the maximum gradient. The gradient is taken at the position of the barrier, which is close to the D_α peak position as shown in (see figure 7.9). A comparison of the gradient data is shown in figure 7.10. This shows the limits in the resolution of resolving Δ_α for high gradients ($> 7 \times 10^{20} \text{ m}^{-4}$). If however the



(a) The D_α peak position and barrier position show a linear relationship.

(b) Histogram of the ratio of the D_α peak position and the barrier position. The distribution has a mean of 1.02.

Figure 7.9: Comparison of barrier position following from the $TS(edge)$ fit to the n_e profile with the D_α peak position. The two positions show a good agreement.

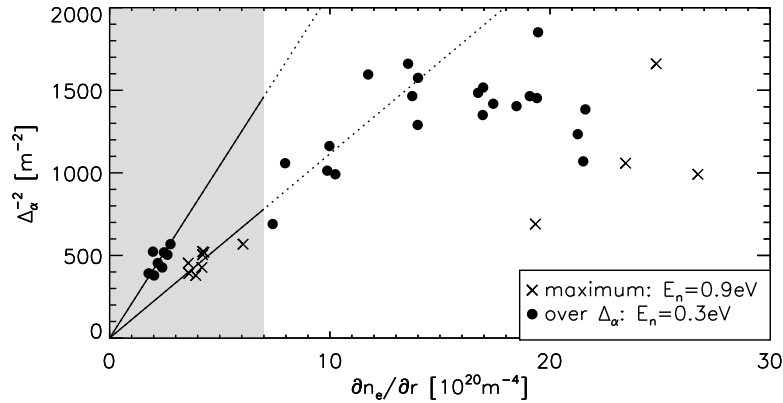


Figure 7.10: Comparison of the width of the radial D_α emissivity profile with the maximum and average 'real' n_e gradient from the TS diagnostic of a test set of L-mode and ELM-free H-mode deuterium discharges. The data are linear in the shaded region, which produces calibration factor for obtaining the edge density gradient from the linear D_α camera data for small gradients.

gradient is calculated as the average gradient over a region, then a better comparison with Δ_α can be made. The average gradient is preferred since an average gradient is assumed in the model using (7.7) and since Δ_α is obtained by observing a region of finite width over which the n_e gradient varies.

For the width of the region over which the average n_e is calculated, the value Δ_α has been chosen. This region covers most of the 'real' n_e gradient as is shown in figure 7.8(b). When obtaining the $\partial n_e / \partial r$ from the radial D_α emissivity profiles, the neutral influx velocity, \vec{V}_n , has been used as a free parameter in order to achieve the best linear fit to the TS data in the low gradient region, indicated by the shaded area in figure 7.10. This results in an influx energy of $E_n \sim 0.3$ eV. Using this value the average edge density gradient can be extracted from the linear D_α camera data and compared with the average gradient provided by the TS diagnostic,

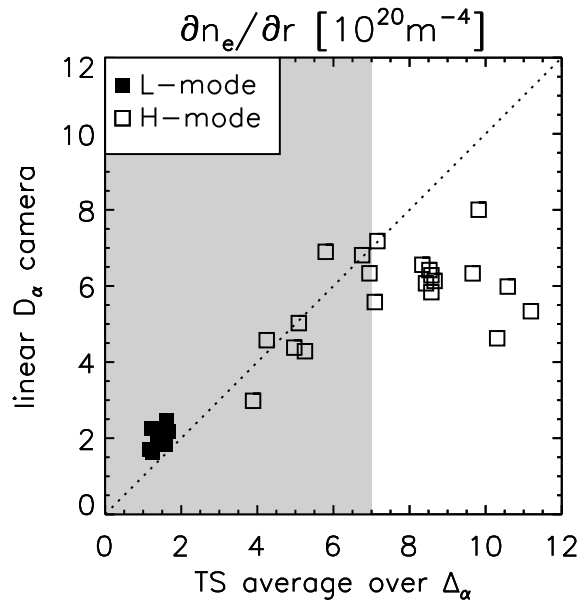


Figure 7.11: Experimentally obtained $\partial n_e/\partial r$ from D_α emissivity and TS measurements for a number of MAST deuterium discharges. Gradient measurements using the linear D_α camera are limited by the resolution of the D_α system to average gradients of up to $\sim 8 \times 10^{20} \text{ m}^{-4}$, as indicated by the shaded area.

as shown in figure 7.11. Lower gradient results are found to be in good agreement, whereas the measurement of higher gradients is limited by the resolution of the linear D_α camera measurements.

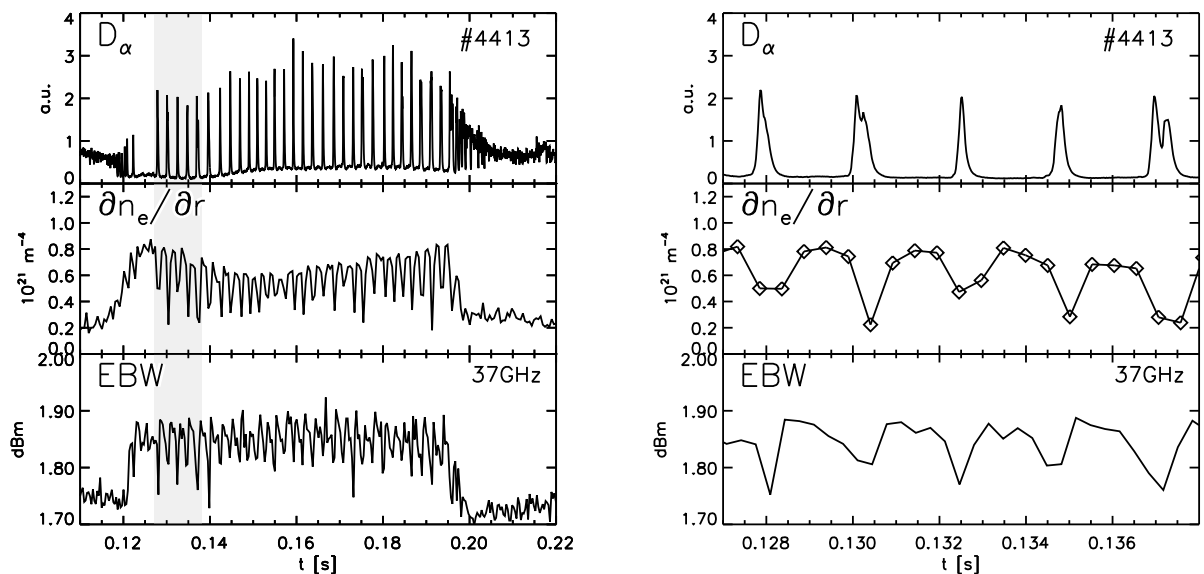
To demonstrate the merits of this diagnostic an example is given of $\partial n_e/\partial r$ measurements during an H-mode plasma discharge with regular ELMs. Figure 7.12(b) shows the D_α emissivity and the $\partial n_e/\partial r$ gradient obtained from the linear D_α camera. A clear spontaneous increase of the edge density is observed at the L-H transition. The gradients are flattened at an ELM event and increase during the inter-ELM period. Figure 7.12(b) shows a more detailed view of the inter-ELM period.

The graphs also show the radiation power of the Electron Bernstein Wave (EBW) radiometer [7] installed on MAST. Strong overdense plasma emission was observed during H-mode operation, indicating a rise in the edge density gradient. A strong correlation between the EBW emission and $\partial n_e/\partial r$ is observed, showing a buildup of the density gradient during the H-mode phase of the discharge with a subsequent decrease in $\partial n_e/\partial r$ when the plasma returns to L-mode. The change in n_e gradient is also clearly observed during the inter-ELM periods.

7.4 Summary and discussion

The TS system on MAST measures the edge density profiles on both inboard and outboard sides with high resolution once during a plasma discharge in MAST. The resolution on the inboard side is higher than on the outboard side due to the orientation of the laser beam path and of the collection optics with respect to the magnetic topology of the plasmas.

A method has been developed to determine the edge pedestal values using a fit of an analytical function describing the pedestal in the plasma, to the edge profiles taking into account the finite size of the collection volumes and the instrument function of the diagnostic. In this



(a) Full ELMy H-mode period. The shaded area is shown in detail in (b).

(b) Time enhancement showing the increase in $\partial n_e / \partial r$ during inter-ELM periods with a subsequent reduction in $\partial n_e / \partial r$ at an ELM event.

Figure 7.12: Evolution of $\partial n_e / \partial r$, D_α emission and EBW radiation power observed in an ELMy H-mode MAST plasma.

way a higher resolution can be achieved than from the measurements alone. The edge pedestals are well described by this *edge* function. When fitting the pedestals on ψ_N a comparison can be made between the inboard and outboard pedestal parameters.

The edge n_e gradient can be derived, by making some assumptions, from the Balmer- α spectral line emission. The linear D_α camera installed on MAST provides an accurate estimate of the average outboard edge density gradient over a region $\Delta_\alpha = 2\Delta n_{e,ped}$ at high time resolution (≥ 1 kHz) during the full discharge duration. These gradient measurements have been calibrated using results from the TS diagnostic. From these measurements a neutral influx energy of ~ 0.3 eV was derived.

The obtained value on the neutral influx energy is in agreement with simulations of the development of the edge density ‘ear’ ($E_n = 0.33$ eV) (see Chapter 5). This indicates the presence of a cold bath of neutrals outside the MAST plasma, which could be accounted for by the large vessel volume surrounding the plasma. These values are low compared to the expectations of energies around 2 eV of Franck-Condon neutrals as a result of molecular dissociation in the SOL, but similar low energies have also been obtained on other fusion devices [8].

During ELMy H-mode the D_α camera diagnostic can be used as a tool to record the changes of the edge n_e gradient during the ELM event and during inter-ELM periods.

Bibliography

- [1] M.R. Tournianski, P.G. Carolan, N.J. Conway, E.R. Arends, and M.J. Walsh. Use of 1D D_α camera to measure edge electron density gradients. *Review of Scientific Instruments*, 73(3), March 2003.

- [2] R.J. Groebner and T.N. Carlstrom. Critical edge parameters for H-mode in DIII-D. *Plasma Physics & Controlled Fusion*, 40:673–677, 1998.
- [3] L.L. Lao, H. St. John, R.D. Stambaugh, A.G. Kellman, and W.W. Pfeiffer. *Nuclear Fusion*, 25:1611, 1985.
- [4] D.E. Post et al. Steady-state radiative cooling rates for low-density high-temperature plasmas. *Atomic data and nuclear data tables*, 20:397–439, 1977.
- [5] H.P. Summer. Atomic Data and Analysis Structure. *JET Report, JET-IR(94)*, 06, 1994.
- [6] M.R. Tournianski, P.G. Carolan, N.J. Conway, G.F. Counsell, A.R. Field, and M.J. Walsh. Poloidal rotation and associated edge behaviour in START plasmas. *Nuclear Fusion*, 41(1):77–89, January 2001.
- [7] V. Shevchenko et al. EBW observations on COMPASS-D and MAST. In *Proceedings of the 28th EPS Conference on Controlled Fusion and Plasma Physics*, volume 25A, pages 1285–1288, June 2001.
- [8] Ph. Mertens et al. Hydrogen release from plasma-facing components into fusion plasmas - recent results from a spectroscopic approach. *Plasma Physics and Controlled Fusion*, 43:A349–A373, 2001.

Chapter 8

High confinement in MAST

The potentials of the high-confinement regime (H-mode) on a spherical tokamak as a regime of operation in a nuclear power plant have been explored on the Mega-Ampere Spherical Tokamak. H-mode is regularly accessible in MAST and shows all the characteristics of an H-mode as shown on other conventional tokamaks, including a significant drop in D_α emission, the occurrence of edge localised modes (ELMs), the development of pedestals on the T_e and n_e profiles and an increase in the energy confinement time. MAST H-mode confinement data compares well with the IPB98(y,2) scaling for conventional tokamaks: $H_H = 1.0 \pm 0.2$. H-mode is readily accessible in the connected double null divertor configuration. Inboard-refuelling helps the L-H transition. The n_e profiles develop a pronounced pedestal, often with so-called edge density 'ears', while the T_e pedestal seems to be limited in growth. During an ELM event particles are expelled from the outboard side of the plasma in a convective manner. The inboard edge is not affected during the ELM. Therefore, the power exhaust is strongly biased to the outboard side during ELM events, with $< 10\%$ leaving on the inboard side. MAST data would introduce an approximately linear dependence on the aspect ratio in the pedestal energy scaling law.

8.1 Introduction

The high-confinement regime, or H-mode, offers interesting potentials as an operating regime for the nuclear fusion power plant in that it spontaneously increases the stored energy in the plasma compared to the low confinement regime (L-mode). First H-mode was observed by Wagner *et al.* [1] on ASDEX and since then the H-mode has frequently been observed on other tokamaks including the spherical tokamak (ST) variant. The access to H-mode appears to be limited to specific plasma configurations and requires a heating power above a certain threshold.

In conventional tokamaks H-mode is characterised by a spontaneous steepening of the edge density gradient resulting in a narrowing of the D_α profile. Other signatures are an increase of the average density and the subsequent rise in the stored energy and confinement of energy and particles. Particles are released from the plasma by edge instabilities, the so-called edge localised modes (ELMs). All these characteristics are also observed on the Mega-Ampere Spherical Tokamak (MAST).

The steepening of the edge density gradient is generally explained as a result of locally reduced transport at the edge of the plasma, which is called the edge transport barrier (ETB). When this barrier appears it produces an increase in average density on the time scale of the particle confinement time, with some further improvement of confinement in the bulk plasma.

The rise in average density during H-mode is limited by the occurrence of ELMs. These ELMs have the advantage that they control the increase in density and therefore prevent a den-

sity limit from being reached. Also, they limit the buildup of impurities in the plasma. On the other hand, ELMs are associated with loss of confinement and pulsed heat loads. The latter could potentially cause problems when the ST is extrapolated to the scale of a power plant. Due to the compact geometry of the ST the target area for the lost power on the high field side is small. This can cause material wear and potential reduction of the machine lifetime. In order to prevent this, demands are put on the materials used in the target area. However, MAST (and also START) shows pronounced inboard-outboard power exhaust asymmetry during the L- and H-mode, due to which the power load onto the target plates on the high field side is limited. A natural asymmetry arises due to the fact that the outer plasma surface is greater than the inner plasma surface, in MAST the surfaces differ a factor ~ 4 in size. The asymmetry is observed to be enhanced during ELM events.

The increase in average density leads to an increase in the stored energy and, since the transition to H-mode is spontaneous, to an increase in the energy confinement time (τ_E). Most scaling laws for τ_E for ITER are based on data taken during high confinement. These data are obtained from machines with a range of operational parameters. The extreme geometry of the ST leads to a broadening of the operational space of these data, mainly due to the low aspect ratio, and the addition of the ST data is therefore likely to improve predictions.

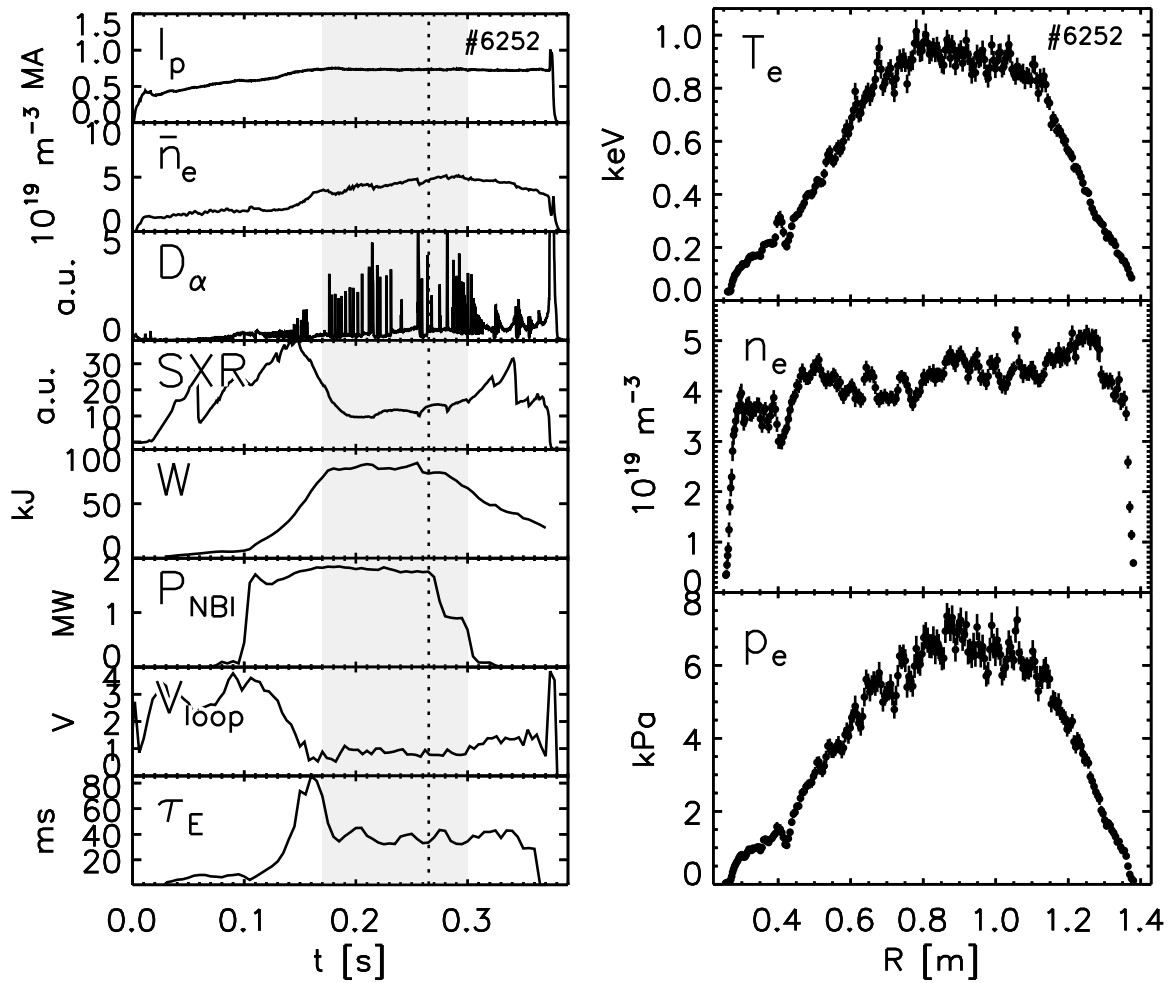
While most scaling laws look at the total energy contained in the plasma, some of the scaling laws are based on the energy stored in the pedestal. The pedestal is the result of the ETB and has an effect on, *e.g.* the edge losses and heating efficiency and therefore affect the global confinement. The existing pedestal scaling laws only include data from conventional aspect ratio tokamaks and do not include a dependence on aspect ratio. Addition of the MAST pedestal data will introduce the aspect ratio dependence in the scaling law.

On MAST, the high-resolution Thomson scattering system plays an important role in the study of many H-mode phenomena that characterise the performance of the machine and therefore determine the potential of the ST as a fusion power plant. Throughout this chapter the results from the TS diagnostic will be used to study the access to H-mode and the behaviour of the profiles and pedestals during H-mode. Measurements of the edge gradients will play a role in characterising the asymmetric power exhaust during ELMs. Accurate measurements of pedestal data, that are recorded with the diagnostic, will be used to include an aspect ratio dependence in the existing pedestal scaling law. In addition, the data from the linear D_α camera will be used to study the behaviour of the outboard edge density gradient during ELMy H-mode. But firstly, this chapter presents the characteristics of H-mode in MAST and compares the performance of MAST with other tokamaks.

8.2 Characteristics of H-mode in MAST

H-mode access is routinely observed in MAST in both Ohmic and neutral beam (NBI) heated plasmas [2–7]. The resulting plasmas demonstrate all of the established H-mode signatures, including ELMs, increase in particle and energy confinement, steepening of the edge gradients and narrowing of the D_α profile at the plasma edge. In addition, a dramatic increase in the Electron Bernstein Wave (EBW) emission [8] is detected as a result of the steepening of the density gradients.

An example of a quasi-steady state H-mode plasma discharge in MAST is shown in figure 8.1(a). The discharge maintained $\tau_E \sim 40$ ms for over 120 ms as indicated by the shaded area. The discharge is of the connected double-null type (see section 8.3) and is started us-



(a) Time traces of plasma current (I_p), line-average density (\bar{n}_e), D_α emission, midplane soft X-ray emission (SXR), stored energy (W), neutral beam power (P_{NBI}), loop voltage (V_{loop}) and energy confinement time (τ_E). The vertical dashed line indicates the TS time.

(b) High-resolution TS profiles taken during H-mode at 265 ms.

Figure 8.1: Example of a quasi-steady state MAST plasma with $\tau_E \approx 40$ ms maintained for over 120 ms as indicated by the shaded area in (a).

ing the direct induction technique (see Chapter 3). The plasma current maintains a flat-top of $I_p \sim 0.73$ MA from 150 ms in the discharge to termination. Two neutral particle beams are available, being able to deliver a maximum power of $P_{NBI} \sim 1.8$ MW for ~ 180 ms. From the switch-on of the NBI the stored energy in the plasma (W) rises from 6 kJ to 82 kJ at which value it stabilises for ~ 120 ms. The L-H transition is triggered by the ramping down of V_{loop} at ~ 120 ms. The H-mode initially shows ‘grassy’ ELMs followed by ELM-free periods and regular ELMs. The line-average density (\bar{n}_e) more than doubles during the H-mode period. The discharge furthermore obtains high β .

The TS measurement taken at 265 ms during the quasi-steady state of the discharge is shown in figure 8.1(b). The profiles show pedestals on both the T_e and n_e profiles, which are typical characteristics of H-mode ($T_{e,ped} \sim 100$ eV, $n_{e,ped} \sim 3.8 \times 10^{19} \text{ m}^{-3}$). Whereas the n_e pedestal reaches a value close to the central density, which is high compared to conventional tokamaks,

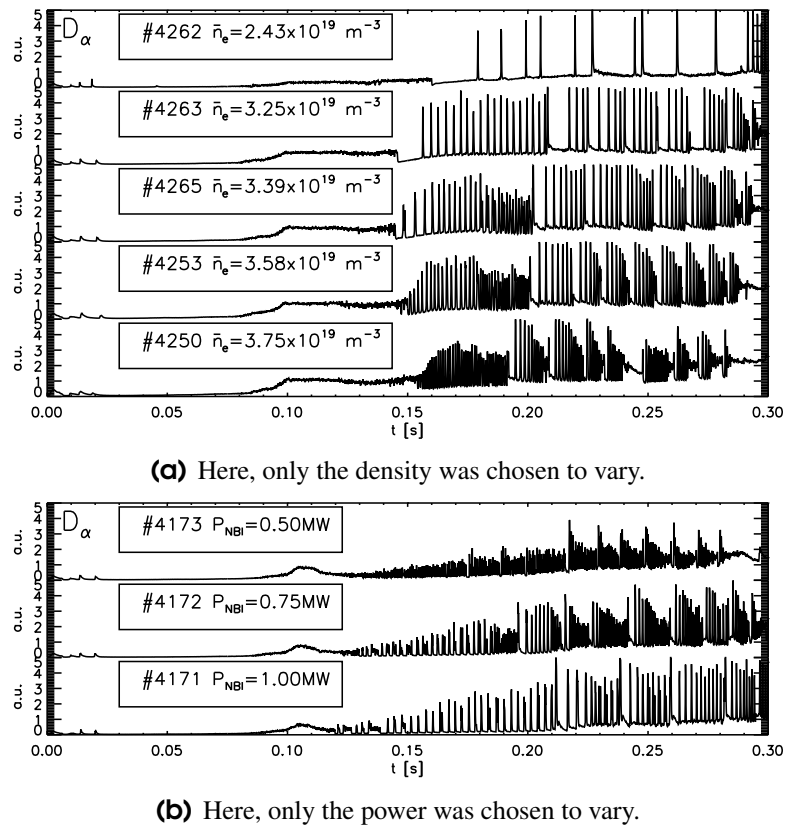


Figure 8.2: D_α emission for series of typical H-mode plasma discharges for which density and auxiliary heating power scans are made. The ELM frequency changes positively with line-average density and negatively with heating power. This behaviour is typical for ELMs classified as type-III on conventional tokamak.

the T_e pedestal only reaches to about 10 – 15% of the central temperature, which is low compared to conventional tokamaks. The cold edge can possibly be related to increased radiative and convective losses because of the high n_e , or to the earlier observations of a cold neutral bath surrounding the plasma and high recycling rate. The low aspect ratio can also be pinpointed as a cause for the cold edge as will be discussed in section 8.6.

The achievement of routine H-mode access with regular ELMs provides a valuable comparison with the conventional tokamak ELMy H-mode. For instance, it makes it possible to study the correlation of the ELM-frequency and various bulk plasma parameters. Two examples of such a study are shown in figure 8.2 [4]. Figure 8.2(a) shows the D_α emission traces for ELMy H-mode plasma discharges for which a density scan is performed. The discharges have nominal parameters $I_p \sim 750$ kA, $B_\phi \sim 0.45$ T, $A \sim 1.5$ and $P_{NBI} \sim 1$ MW. The temporal evolution of the D_α emission in the L-mode phase is highly reproducible. Following the L-H transition the plasmas cease to be similar and a correlation between ELM frequency and onset line-average density is observed. Based on this data, the L-H transition power threshold on MAST exceeds international scaling that does not include an aspect ratio dependence, as was presented in [9]. A similar experiment has been performed where the input auxiliary heating power (rather than density) is scanned (see figure 8.2(b)). In this case, a reduction of the ELM frequency is observed for an increase of auxiliary power. This behaviour with density and auxiliary heating is typical for ELMs classified as type-III on conventional aspect ratio tokamaks [10].

Owing to its low aspect ratio, MAST can make an important contribution to conventional

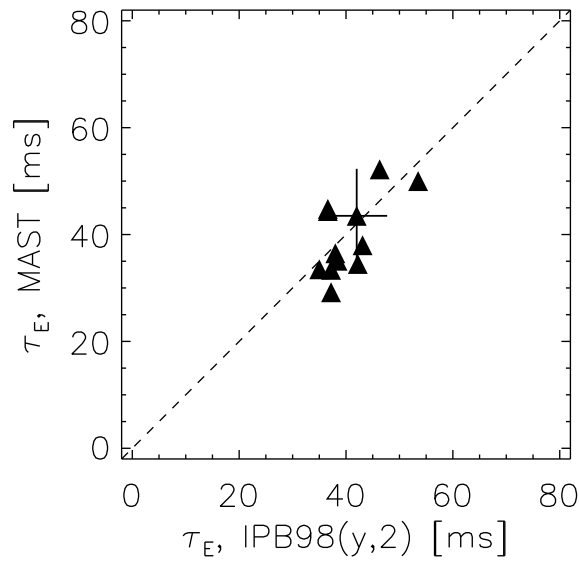


Figure 8.3: The energy confinement time for quasi-steady state MAST plasmas scales well with the prediction of the IPB98(y,2) scaling [12]. A description of the scaling law is presented in appendix 8.A.

tokamak H-mode confinement and pedestal scalings. The importance of the data of MAST, combined with those of other STs, is that it extends the range of inverse aspect ratio ϵ of the international tokamak databases from medium sized devices by a factor of two: the international database features the range $0.2 < \epsilon < 0.37$, while MAST has $\epsilon \approx 0.68$. These data can potentially impose powerful constraints on dependencies of heat transport on dimensionless parameters. In addition, MAST data are making the databases more symmetric around the ITER point along the aspect ratio axis ($\epsilon_{ITER} \approx 0.34$) and thus this should improve the predictive capability of scalings towards ITER.

Most of the scaling laws in the international database are based on data taken during quasi-stationary H-mode plasma discharges. Since MAST achieves reliable H-mode access (as will be shown in section 8.3) in the connected double null divertor configuration with the application of inboard refuelling, plasma discharges can be performed that meet the criteria of the international database, *i.e.* $\dot{W}/P < 0.35$. The MAST confinement data is compared to the IPB98(y,2) scaling law [11]. Descriptions of the determination of the energy confinement time in MAST and the IPB98(y,2) scaling can be found in appendix 8.A. To satisfy the criteria of the international database the MAST data have been critically extracted from dedicated plasma discharges. The data consist of plasmas in the double null divertor configuration (see section 8.3), low ELM frequency and have deuterium as a working gas: an example of such a discharge is shown in figure 8.1. Figure 8.3 shows a comparison of the MAST data with the scaling law. The H_H -factor is the ratio of the measurement and the prediction of the confinement time τ_E . The quasi-steady state discharges in MAST typically have $H_H(y,2) = 1.0 \pm 0.2$. The data is therefore close to the scaling prediction and thus, to a first order approximation, the MAST data confirm the aspect ratio dependence in the IPB98(y,2) scaling. Since this scaling law is derived using data mainly originating from tokamaks of medium aspect ratio, this shows that the global confinement in MAST scales as that on conventional tokamaks.

8.3 H-mode access in MAST

Magnetic configuration

The magnetic configuration has an impact on the accessibility of H-mode in MAST [13]. MAST usually operates in double null divertor (DND) configuration with upper and lower X-points which do not necessarily lie on the same flux surface. By varying the vertical position of the magnetic axis three distinctions are made between lower DND (LDND), connected DND (CDND) and upper DND (UDND) where lower and upper indicate the position of the active X-point (see figure 8.4).

The three configuration types can be distinguished by the separatrix separation at the outboard midplane δ_{sep} , derived from EFIT equilibrium reconstructions [14]. A configuration is considered ‘connected’ if $|\delta_{sep}|$ is less than half the outboard midplane ion Larmor radius ρ_i for deuterium (≈ 6 mm). The outboard midplane is chosen since the cross-field transport is determined by at least ρ_i : the magnetic field is lowest, and the transport highest on the outboard midplane.

The quality of H-mode is indicated by the edge n_e gradient measurements of the high-resolution TS diagnostic (maximum outboard gradient) and the D_α emissivity profiles obtained from the linear D_α camera (average gradient) (see Chapter 7). Figure 8.5 shows that higher quality Ohmic H-mode can most readily be accessed in CDND plasma discharges, and similar conclusions apply to NBI heated discharges. Within the limits $|\delta_{sep}/\rho_i| < 0.5$ of CDNDs, discharges biased towards the lower X-point show H-modes with more separated and deeper ELMs [13].

Inboard gas-feeding

In MAST the access to H-mode also depends on the position of the refuelling system with respect to the plasma. On the inboard side the plasma approaches the centre column at close range, on the outboard side the vessel wall is far (~ 1 m) from the plasma. In addition, the gradient and curvature of the magnetic field causes particle drifts which result in a particle drift in the direction of the major radius R . This drift brings particles at the inboard side to the core and at the outboard side from the core to the edge.

During the first campaign¹ on MAST H-mode transitions [15] relied on recycling of deuterium from inner graphite tiles on the centre column and outboard gas-feeding. The plasma-facing surfaces were first loaded with deuterium by generating a density-limited discharge. In order to provide greater flexibility, control and reproducibility an inboard gas-feeding system was installed [5]. The feeding tube has a 3 mm bore and runs under the centre column armour from the top of the vessel to an outlet in the midplane. D_2 gas is supplied at ≤ 10 bar via a pneumatic valve, constant flow being achieved after ~ 50 ms at typically 60 mbl/s (3×10^{21} atoms/s) for 2 bar inlet pressure. This alone is sufficient to sustain the plasma density. As a result, H-mode plasmas can be generated more reliably for DND discharges without prior wall loading.

The evolution of two otherwise similar Ohmic discharges with outboard and inboard gas-feeding is shown in figure 8.6(a). These discharges, with ~ 0.65 MA plasma current and CDND figuration, exhibit a similar behaviour until ≈ 0.14 s when the inboard-refuelled discharge begins a gradual transition to H-mode with the onset of ‘dithering’ ELMs and increases in density,

¹January-June 2000

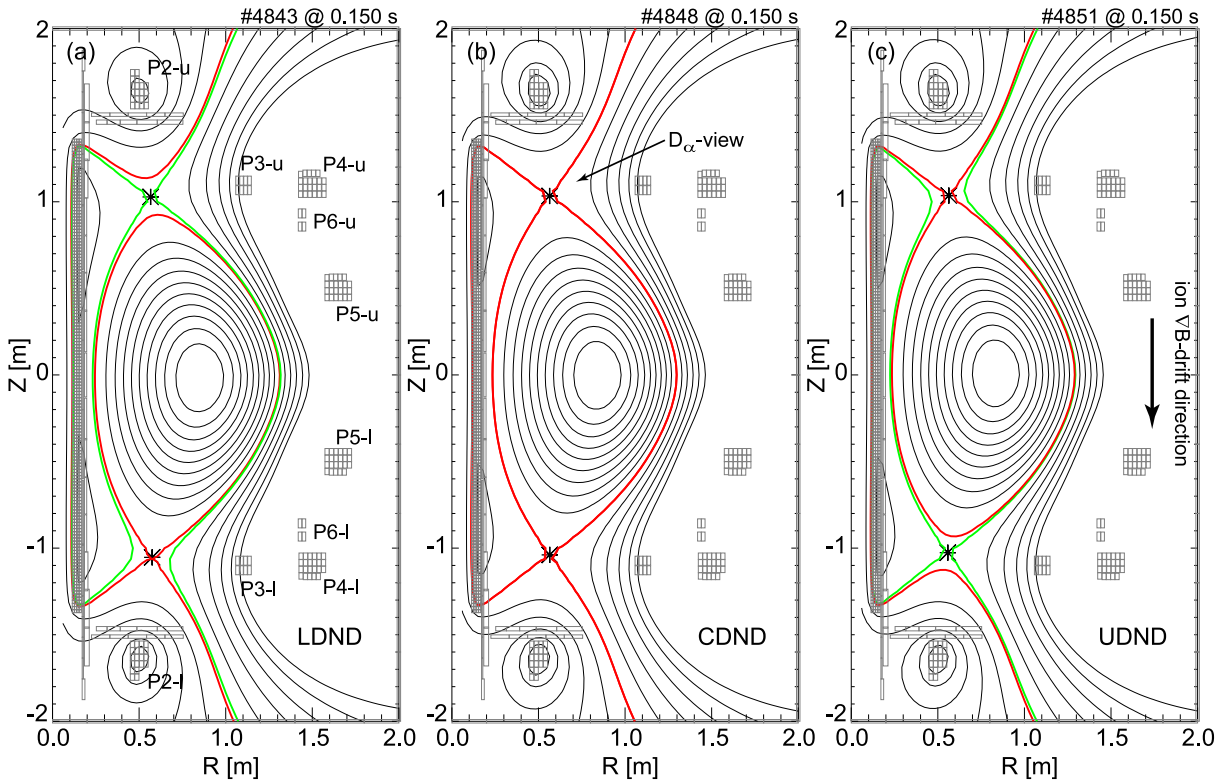


Figure 8.4: EFIT reconstructions of the DND configurations in MAST: from left to right lower DND, connected DND and upper DND. The positions of the poloidal field coils are also indicated (P2 - P6).

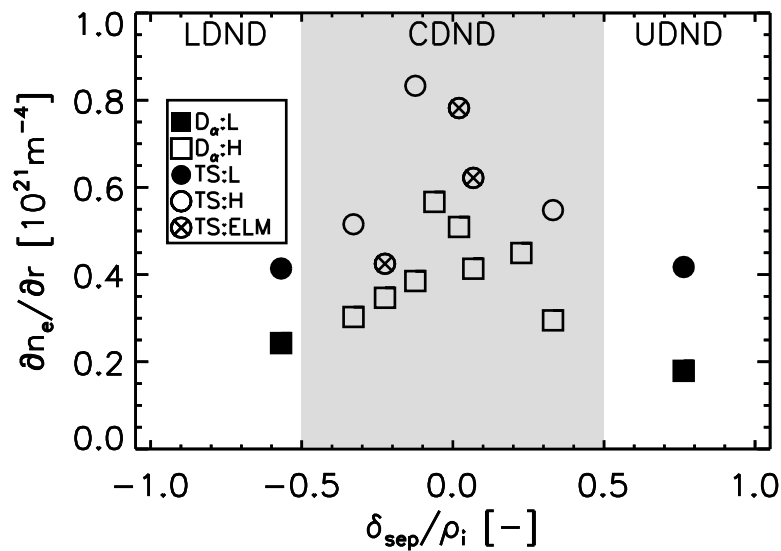
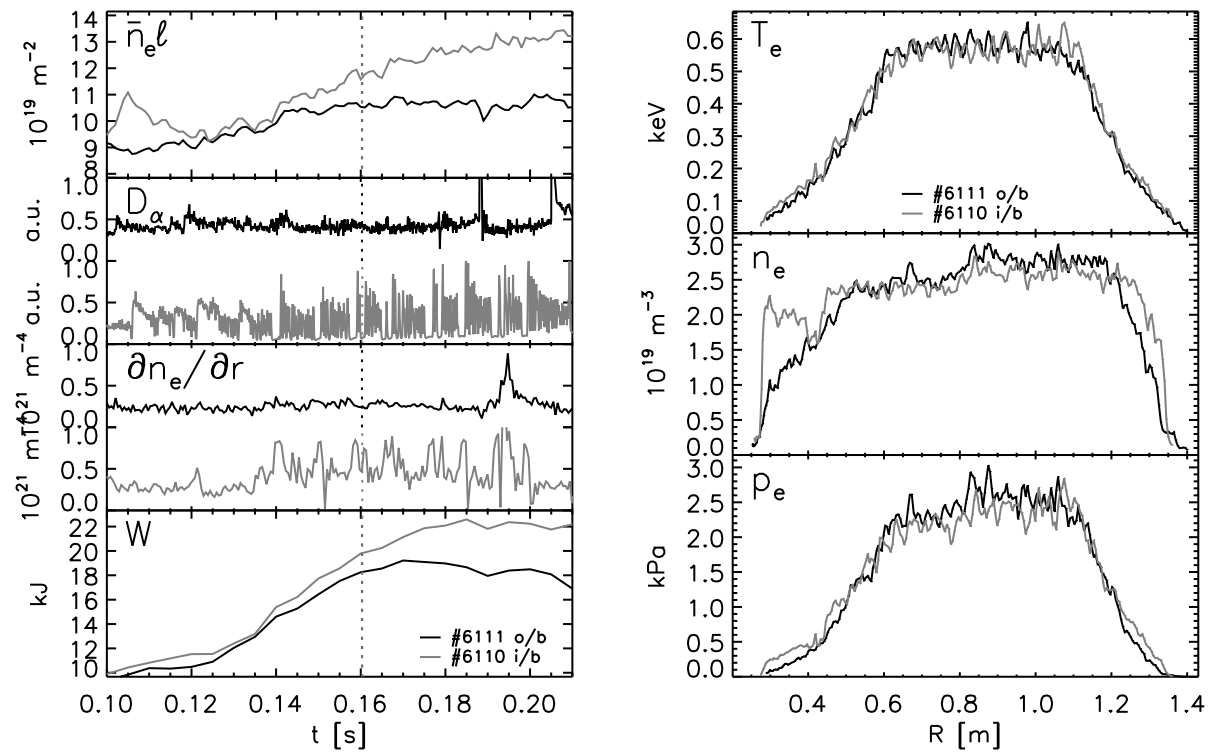


Figure 8.5: Pedestal density gradient variation with normalised separatrix separation for a series of Ohmic discharges. Higher quality Ohmic H-mode, *i.e.* a higher density gradient, was obtained for CDND configurations $\delta_{sep} / \rho_i < 0.5$.



(a) Line-average electron density ($\bar{n}_e \ell$), D_α emission, average outboard edge density gradient ($\partial n_e / \partial r$) and stored energy W . The vertical dashed lines indicate the time of the TS measurements.

(b) TS profiles taken at 160 ms in the discharges shown in a.

Figure 8.6: Comparison of similar Ohmic discharges refuelled by outboard (#6111) and inboard (#6110) gas-feeding. The time traces show that only the inboard-refuelled discharge enters H-mode. The profiles show the steepening of the edge density gradient in H-mode and the difference in the pedestal heights between the inboard-refuelled H-mode plasma discharge and the outboard-refuelled L-mode discharge.

average outboard edge density gradient and stored energy compared to the outboard-refuelled discharge.

The TS profiles measured at 0.16 s in both discharges (see figure 8.6(b)) show a difference at the edge of the plasma, while the core shows similar profiles. The pedestals on n_e and p_e are doubled and also a $\sim 15\%$ increase in the T_e pedestal is observed during H-mode of the inboard-refuelled discharge compared to the outboard-refuelled discharge. The core n_e and p_e are $\sim 4\%$ lower in the inboard case than the outboard, while the core T_e is similar.

The TS profiles provide the electron contribution to the stored energy in the plasma (W_e) (see appendix 8.A). For the inboard-refuelled discharge this produces $W_e = 11.7$ kJ at 160 ms, an increase of 8% compared to the $W_e = 10.9$ kJ measured for the outboard-refuelled discharge. This increase is in keeping with the total increase in W produced by EFIT and shown in figure 8.6(a), which increases by 8% from $W = 18.3$ kJ to $W = 19.8$ kJ. Since these are Ohmic discharges, there is no contribution of fast particles to W , therefore the electrons contribute for 59% of the stored energy and the ions for 41%. Measurements from the neutral particle analyser [16] (NPA) indicate that $T_i = T_e$, therefore the energy distribution produces a dilution factor of $n_i/n_e = 0.7$. Assuming the plasma only contains carbon impurities this produces $Z_{eff} = 2.5$.

8.4 H-mode profiles

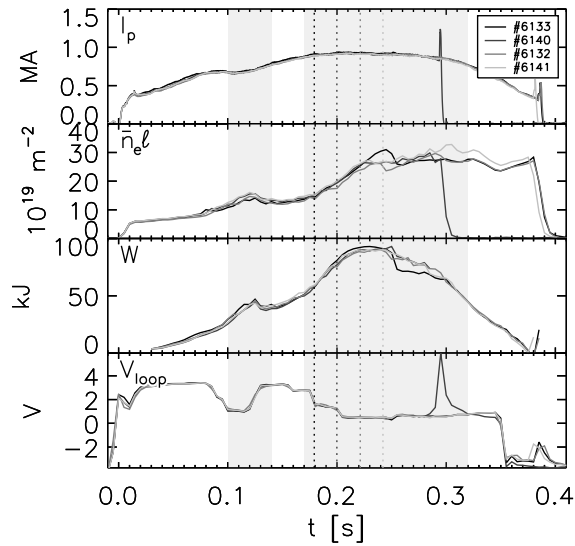
Long ELM-free H-modes in MAST are characterised by the formation of edge density ‘ears’ (EDEs): the edge density rises above the central density. These EDEs have previously been observed on START [17], on DIII-D [18] and have also been observed on NSTX [19]. The behaviour of the EDE was first explained in [20]. In Chapter 5 a more detailed explanation of the EDE was presented: the EDEs can be formed by a reduction of the edge diffusion coefficient in H-mode compared to L-mode. The steepening of the n_e edge gradient causes a steepening of the n_n gradient just inside the separatrix. This results in a peaking of the electron source at the edge due to electron-impact ionisation of the neutrals. Inward convection is required to drive the electrons into the plasma. Contrary to the n_e profiles, the T_e profiles develop only a small pedestal ($T_{e,ped} \sim 100$ eV) compared to the central temperature ($T_{e,core} \sim 1$ keV) and compared to tokamaks at conventional aspect ratio (*e.g.* on JET $T_{e,ped}/T_{e,core} \gtrsim 25\%$).

This section presents these phenomena as well as, more briefly, another phenomenon that was observed on the profile measurements in H-mode on MAST. The latter is introduced here to illustrate the complexity of profile behaviour during H-mode, and also to provide a basis for further investigation.

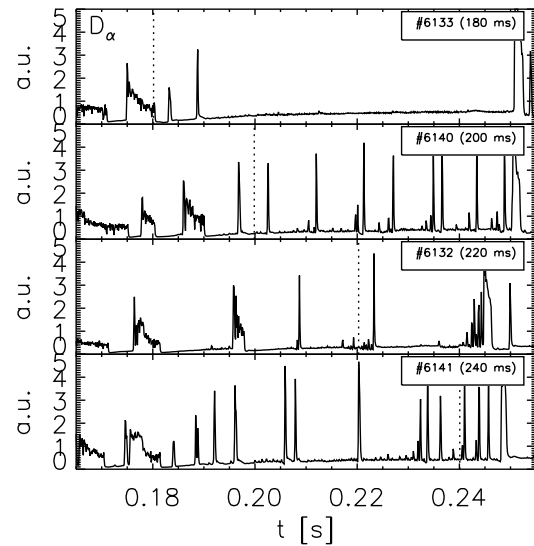
Temperature and density pedestal development

The data used in the transport analyses of the EDEs in Chapter 5 were measured using the 30 point TS system which showed limits in resolving the edge gradients. Improved measurements of the H-mode profiles are made using the high-resolution TS system (see Chapter 6). Figure 8.7 shows four similar inboard-refuelled, NBI-heated ($P_{NBI} \sim 1$ MW) H-mode plasma discharges. The time traces of the discharges are shown in figure 8.7(a), in which the shaded areas mark the H-mode periods. A rise of the line-integrated density $\bar{n}_e \ell$ and associated stored energy W is recorded during the initial phases of the H-mode periods. The measurement of the profiles is scanned through H-mode as indicated in the traces of the D_α emission (see figure 8.7(b)).

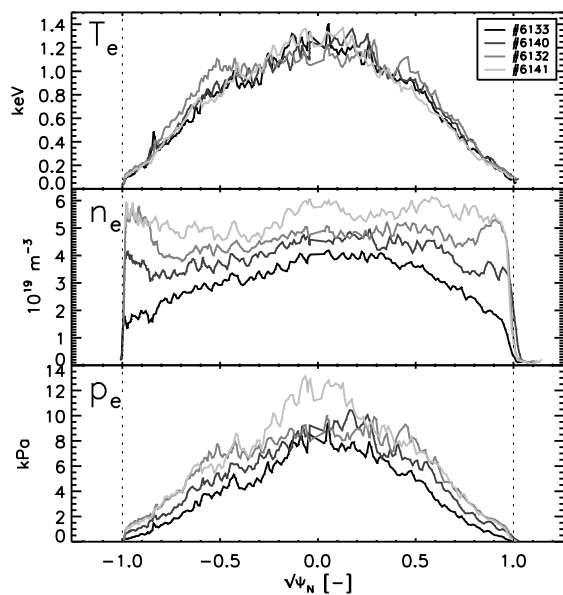
The TS profiles measured in the time scan through H-mode are shown in figure 8.7(c). The details of the inboard edge are displayed in figure 8.7(d). The most dramatic change is observed on the n_e profile, showing the development of a pedestal. The increase in n_e is most obvious on the edge, where EDEs are formed (see Chapter 5). EDEs are observed on both the inboard and outboard edges and the n_e pedestal continues to rise throughout the H-mode period. No obvious changes on the T_e profiles are recorded; the edge shows a rise in the pedestal from ~ 100 eV (#6133) to ~ 140 eV (#6132) during the ELM-free period. This pedestal has dropped to ~ 120 eV (#6141) when recorded ~ 5 ms after an ELM and is very similar to the pedestal measured ~ 5 ms after an ELM much earlier in H-mode (#6140). It can therefore be concluded that for these discharges the height of the T_e pedestal depends mainly on the time elapsed since the last ELM, while the height of the n_e pedestal depends on the total duration of the H-mode period (including ELMs) prior to the measurement. More detail on the behaviour of the pedestal during ELMy H-mode can be found in section 8.5.



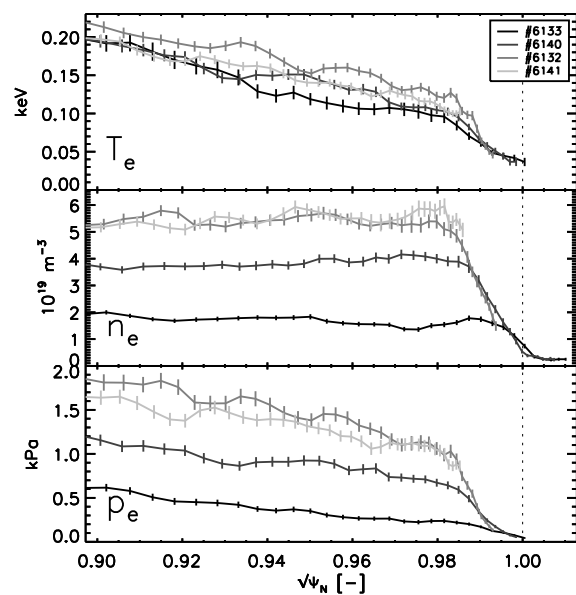
(a) Time traces of plasma current (I_p), line-integrated density ($\bar{n}_e \ell$), stored energy (W) and loop voltage (V_{loop}). The shaded areas mark the H-mode periods.



(b) Time traces of D_α emission at the upper X-point. The vertical lines indicate the times of the TS profile measurements. These times are also indicated in the legends.



(c) TS profiles during four different stages of H-mode. The profiles are presented as function of $\sqrt{\psi_N}$, where the inboard side gets a negative sign. The dashed lines indicate the position of the separatrix.



(d) Detail of the inboard TS profiles showing the development of the T_e , n_e and p_e pedestals during H-mode. The dashed lines indicate the position of the separatrix.

Figure 8.7: Four similar H-mode plasma discharges through which a time scan of the high-resolution TS profiles is made.

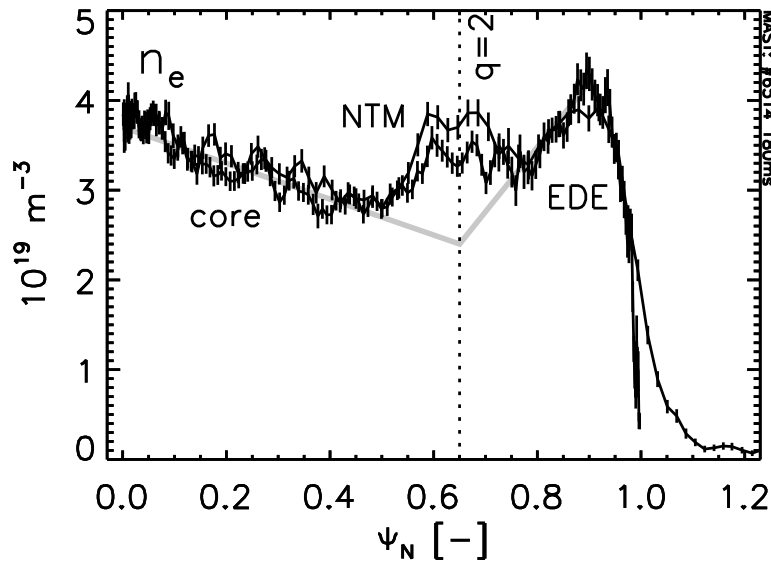


Figure 8.8: H-mode profile of n_e showing a tearing mode with $m = 2$ characteristics at the position where core and EDE meet as indicated by the straight lines. The dashed line shows the position of the $q = 2$ surface as produced by EFIT.

Transition between EDE and core density profile

The EDE measured during ELM-free periods of H-mode show a steep gradient at the edge of the plasma and a less steep gradient towards the core. There is often a sharp transition between the gradient on the inside of the EDE and the core profile. In Chapter 5 it has already been mentioned that there might be a relation with the presence of a rational $q = 2$ surface at the position of the transition. Rational q -surfaces are known to affect local confinement [21]. The sharp transition is more clearly observed on the high-resolution TS data, however q -profile reconstructions from EFIT are not yet reliable enough to establish the link between the gradient transition and the presence of the $q = 2$ surface, therefore measurements of other phenomena related to $q = 2$ must be used to identify the position of the surface.

Some plasma discharges show the presence of a tearing mode with $m = 2$ characteristics on the Mirnov coils [22]. The confinement in the island differs from that of the surrounding plasma. When the TS laser crosses the island through the O-point (or crosses the island at a position close to the O-point), it is clearly visible on the TS profiles. Figure 8.8 shows an example of such an island on the n_e profile of an H-mode plasma discharge. This island can be seen both on the inboard and the outboard profiles, which confirms the even m characteristic of the mode. Inside the island, the density builds up, this indicates an enhancement of the local confinement island the magnetic island. The temperature inside the island is uniform. Similar observations have been made on TEXTOR [23].

The position of the island coincides with that of the inside of the EDE. This position has been indicated in figure 8.8 by extrapolation of the n_e slope in the core and at the inside of the EDE, regions in which the slope appears to be almost linear when presented as function of ψ_N .² This observation therefore supports a possible relation between the gradient transition and the presence of the $q = 2$ surface, this however requires further investigation.

² $\psi_N = (\psi_0 - \psi)/(\psi_0 - \psi_a)$ where ψ_0 and ψ_a are the magnetic flux ψ at the magnetic centre and at the last closed flux surface, respectively.

8.5 Asymmetric power exhaust during ELMs

The power loading onto plasma-facing surfaces is an important issue in tight aspect ratio tokamaks, because the power exhausted from the plasma may be distributed over a smaller area. This puts high demands on the quality of the material used for the target plates. The power load on small areas might lead to material wear and potential shortening of the machine lifetime.

A detailed study of the power deposition to the four strike points of a DND configuration has revealed a strong inboard-outboard asymmetry [24, 25]. During L-mode and H-mode discharges, at least 4 times more power leaves the plasma on the outboard side than on the inboard side. This reduces the problems for the ST related to the power exhaust. The asymmetry in the power exhaust is even enhanced during ELMs. This section presents detailed analyses of the asymmetric power exhaust during ELMs by comparing the behaviour of the inboard and outboard edge gradients.

Power loss during ELMs

Langmuir probes in the upper and lower divertor target plates, both on the inboard and outboard side, measure the power and particle flux going out of the plasma [26]. Integration of the power flux over the inboard and outboard target areas results in the power going to the inboard side (P_{in}) and the power going to the outboard side (P_{out}), respectively.

It is observed that the power flux is strongly biased to the outboard side during L-mode phase and even more during the H-mode phase [24, 25]. During an ELM event, the ratio of power going to the outboard side over power going to the inboard side is increased even more as shown in figure 8.9(a). For plasma discharges with ELMs, the outboard-inboard target ratio P_{out}/P_{in} exceeds 30 during ELM events. This implies that $> 96\%$ of the power flowing to the targets flows to the outboard side. In between ELMs this ratio drops to ~ 10 for high frequency ELMs ($> 90\%$ to outboard side). Thus, in typical ELMy H-mode plasma discharges in MAST, more than 90% of the energy released during an ELM and observed at the target plates is released to the outboard side. For long inter-ELM periods, however, the ratio decreases to ~ 4 , which is comparable with the ratio of surface areas of the outboard and inboard separatrices (indicated by the dashed line in figure 8.9(a)).

These data are consistent with the hypothesis that the transport into the SOL is being driven predominantly by poloidally symmetric processes during inter-ELM periods. In L-mode plasma discharges, P_{out}/P_{in} reaches values comparable with those during ELM events. Therefore, presumably, in L-mode and during ELMs, transport is enhanced by poloidally asymmetric processes more prominent on the outboard side.

On the inboard side the power efflux from the plasma during the ELM is equal to the power efflux from the plasma in between ELMs, this is shown in figure 8.9(b). The ratio of the two quantities (ELM/inter-ELM) is independent of the ELM frequency. This shows that very little of the power released during the ELMs reaches the inboard targets. On the outboard side the power loss during the ELM can be up to ~ 5 times bigger than in between ELMs, for low ELM frequencies. Since this ratio decreases for higher ELM frequencies, it is likely that the period of time necessary for the pedestals to recover after the ELM is greater than the inter-ELM period, *i.e.* the T_e and n_e pedestals cannot recover in between high frequency ELMs.

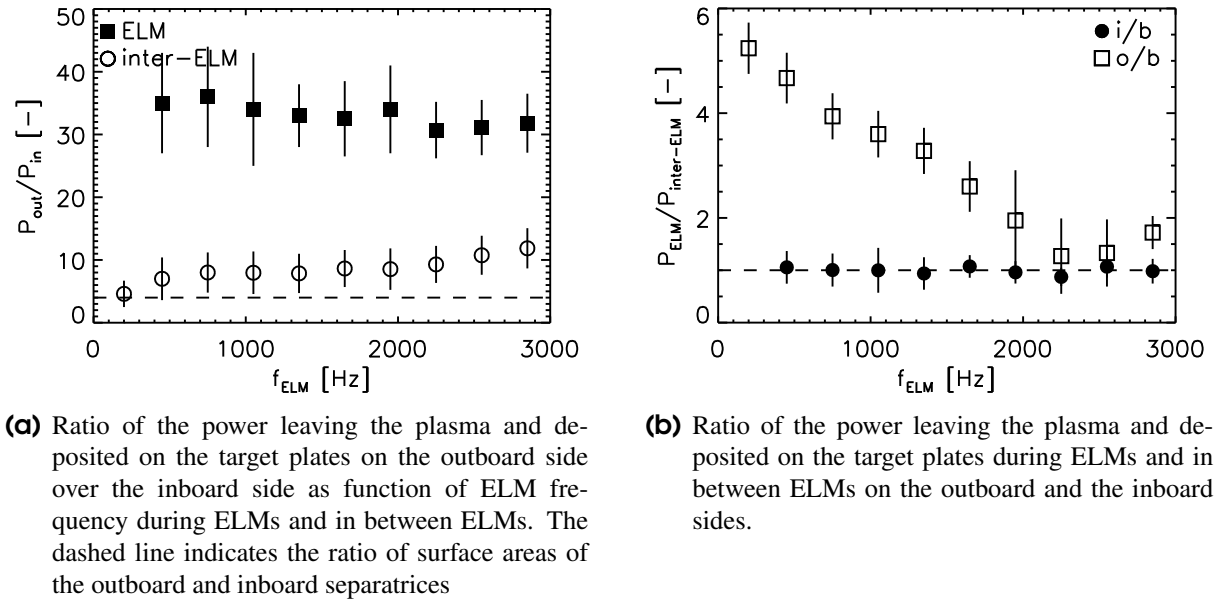


Figure 8.9: Power efflux from the plasma during ELMy H-mode.

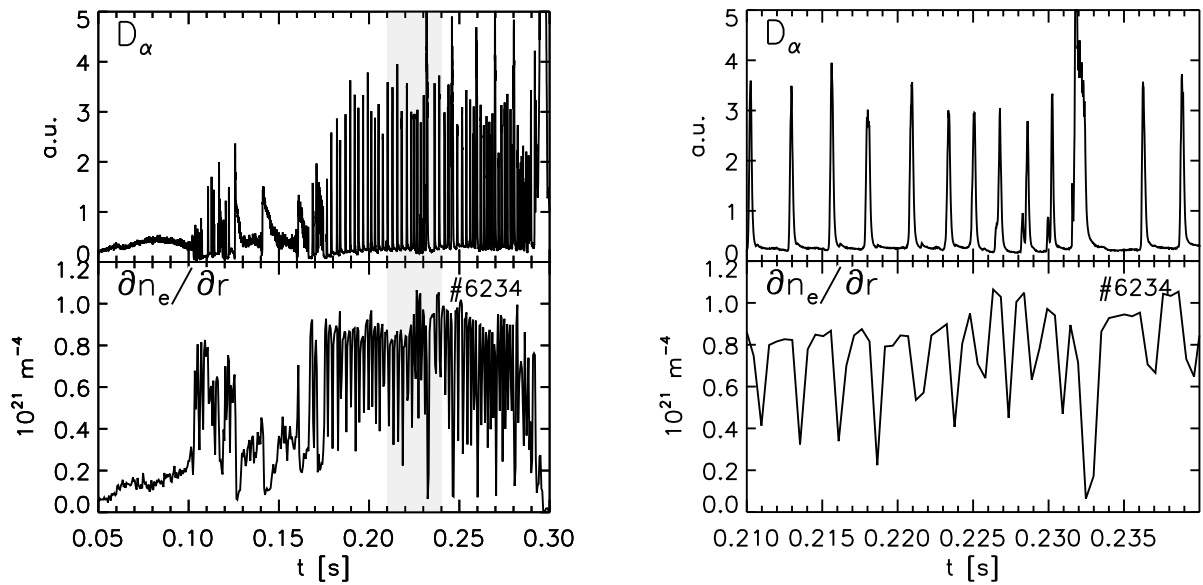
Effect of ELM on edge gradients

ELM losses originate from the edge of the plasma. In order to understand the power losses from the plasma during ELM events and during inter-ELM periods it is therefore essential to study the behaviour of the edge parameters in detail. Since the heat loss from the plasma during ELMs is associated with particle losses, the edge density gradients will be studied here. The edge density gradient is one of the signatures of H-mode, this is illustrated in figure 8.10(a). The figure shows a clear increase of the average outboard n_e gradient, as measured by the linear D_α camera (see Chapter 7), after the L-H transition, which is recognised by the reduction of the D_α emission. A clear correlation is observed between the presence of ELMs and the reduction of the outboard edge gradient. This is shown in more detail in figure 8.10(b). The size of the ELM determines the loss in the gradient. During the inter-ELM periods the gradient recovers.

In order to examine the pedestal during an ELM event, three similar plasma discharges are compared. The TS measurements are taken during a period of regular ELMs, but at different times compared to the ELM preceding the measurement (see figure 8.11). The discharge had a flat top plasma current of $I_p \sim 0.66$ MA, and $P_{\text{NBI}} \sim 0.8$ MW. Table 8.1 shows the time with respect to the peak of the last ELM and the T_e and n_e pedestal values taken at $\psi_N = 0.95$.

The full T_e and n_e profiles are shown in figure 8.12. Since the measurements are taken at different time intervals to a sawtooth crash, the central T_e (within $q = 1$) is different in each discharge. The crash has little effect on the central n_e . The n_e profiles are similar except at the edge regions. On the inboard edge an EDE is observed which is largest for the measurement taken furthest away from the ELM. On the outboard edge no peaked EDE is observed, and for the discharge taken during the ELM (#5756) a density of up to $\sim 10^{19} \text{ m}^{-3}$ is observed in the scrape-off layer (SOL). The effect on T_e is less obvious on this scale.

The effect of the ELM on the T_e and n_e pedestals are shown in more detail in figure 8.13. The measurement taken furthest away from the ELM (#5752) now shows the EDE with a peaked edge on the inboard side. The temperature shows a ~ 100 eV pedestal. During the ELM (#5756) T_e reduces to 70 eV and the EDE appears partly truncated. Just after the ELM (#5757)



(a) Full plasma discharge showing the steepening of the outboard edge gradient from L to H-mode. The shaded area is shown in detail in figure 8.10(b).

(b) Time enhancement showing the steepening of the outboard edge gradient during ELM events.

Figure 8.10: Variation of upper X-point D_α emission and outboard edge gradient as measured by the linear D_α camera from L to H-mode and during ELMs.

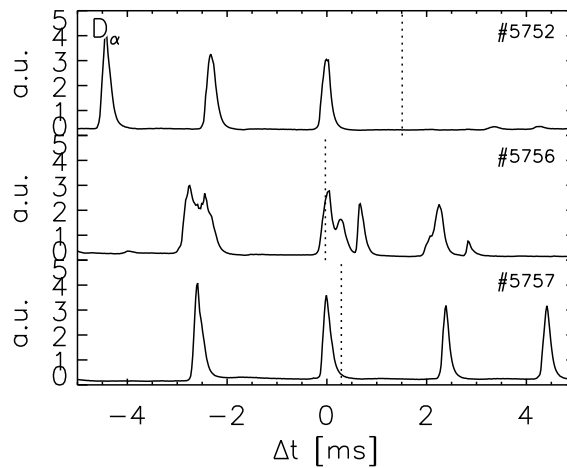


Figure 8.11: D_α emission showing the TS times relative to the ELM for the profiles shown in figure 8.13.

Table 8.1: Pedestal parameters of the profiles used in figure 8.13.

discharge	Δt ms	$T_{e,95}^{in}$ eV	$T_{e,95}^{out}$ eV	$n_{e,95}^{in}$ 10^{19} m^{-3}	$n_{e,95}^{out}$ 10^{19} m^{-3}
#5752	1.5	100	135	2.9	2.6
#5756	0	70	100	2.9	2.2
#5757	0.3	100	135	2.3	2.0

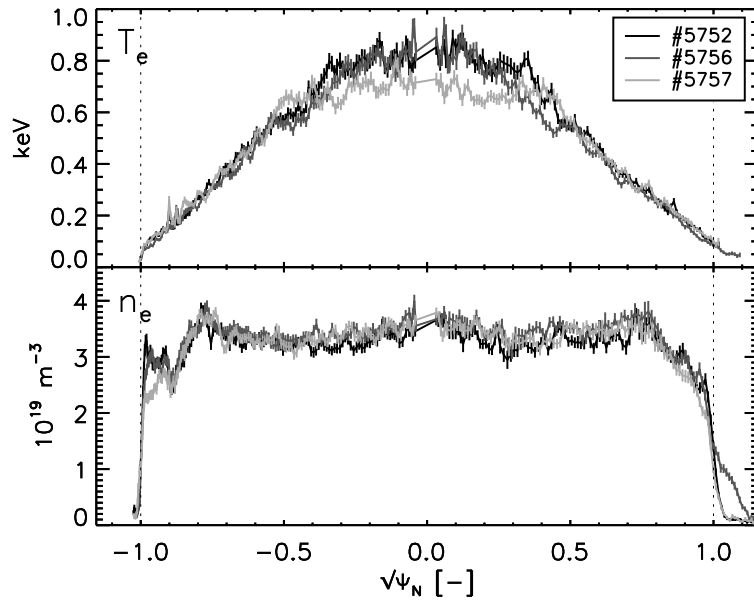
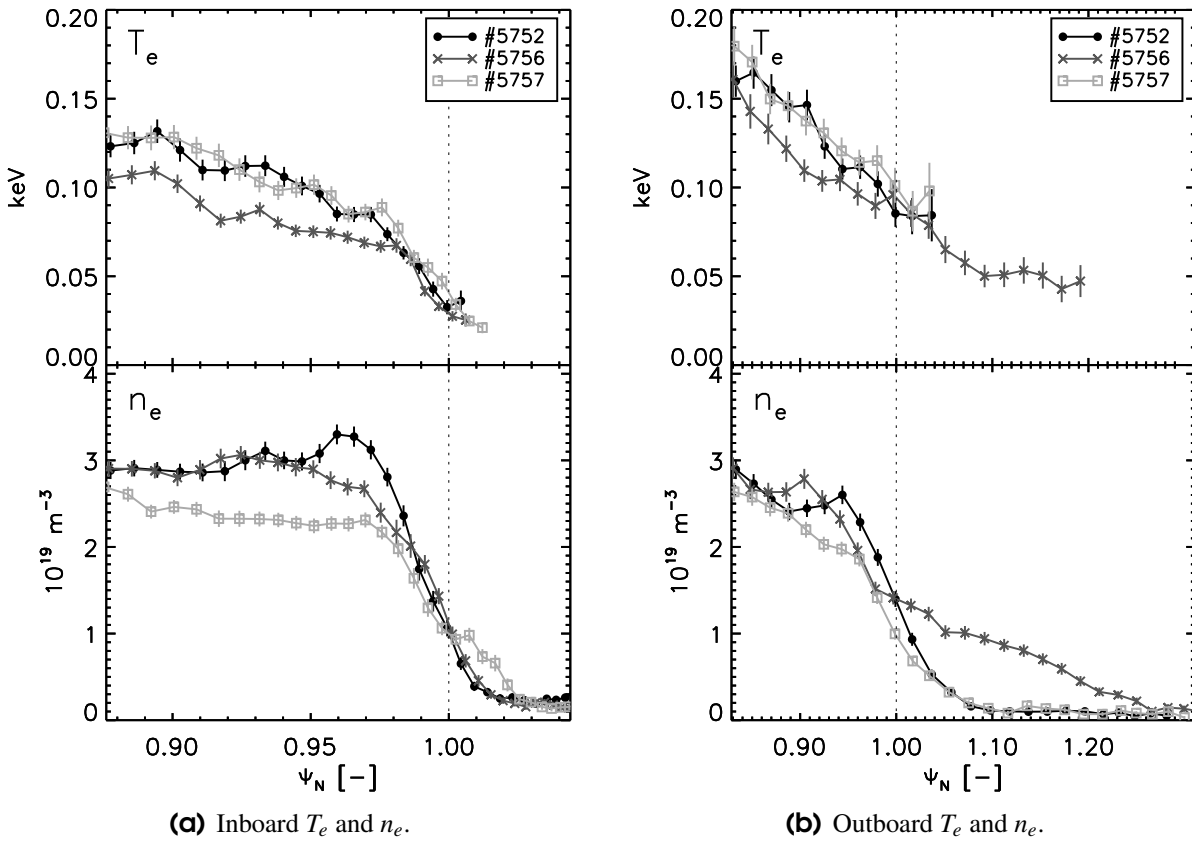


Figure 8.12: T_e and n_e profiles of comparable ELMy H-mode plasma discharges, but taken at different time intervals to an ELM.



(a) Inboard T_e and n_e .

(b) Outboard T_e and n_e .

Figure 8.13: Effect of an ELM on the edge gradients. The profiles are taken before (#5752), during (#5756) and after (#5757) an ELM as indicated in figure 8.11. The T_e pedestal collapses during the ELM event but recovers soon after. The n_e pedestal also collapses during the ELM event, but does not recover on the same time scale. During the ELM event a flow of particles is observed in the SOL on the outboard side forming a tail on the n_e profile. This is not observed on the inboard side. Some data for T_e is missing in the SOL, because T_e or n_e lies outside the detection range.

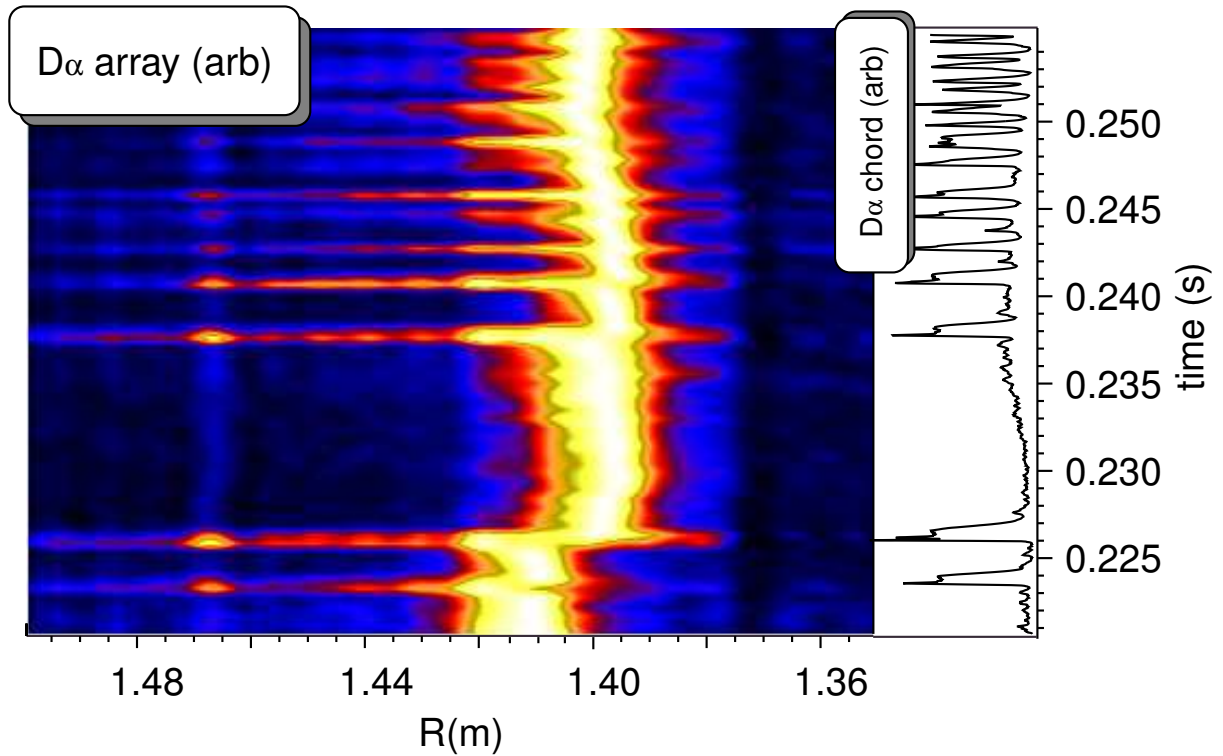


Figure 8.14: Formation of outboard tail as detected by the D_α camera. Each time slice has been normalised at the maximum intensity to enhance the tail [24].

a substantial loss of the EDE is observed. However, T_e has recovered to the value prior to the ELM (~ 100 eV) and is therefore expected not to rise any higher during the inter-ELM period. No differences in the edge n_e gradients are observed between the measurements before and during the ELM; however, the measurement directly after the ELM shows a small kink in the gradient indicating a flow of particles going into SOL.

On the outboard side the losses in the T_e and n_e pedestals are also observed. But in addition, a change in edge gradient during the ELM is detected compared to the edge gradient before the ELM; the gradient flattens during the ELM. Also, during the ELM an increase in n_e is observed outside the separatrix in the SOL leading to the formation of a tail on the outboard edge n_e profile. This broadening of the pedestal width was already observed in less detail on the data from the linear D_α camera (see figure 8.10). The behaviour of T_e is less obvious from the present measurements since T_e and n_e in the SOL are outside the detectable range.

In general, the event-related plasma heat loss can be described by a conductive $\langle n_e \rangle \Delta T_e$ term and a non-conductive (convective and/or diffusive) $\langle T_e \rangle \Delta n_e$ term. Here $\langle \rangle$ denotes the average value of T_e and n_e before and after the event and Δ denotes the change in the value of T_e and n_e . Since figure 8.13 shows that T_e has recovered after the ELM event to the value before the event, while a loss in n_e is observed, the heat loss during the ELM is predominantly non-conductive:

$$\langle T_e \rangle \Delta n_e \gg \langle n_e \rangle \Delta T_e \quad (8.1)$$

The burst of particles out of the plasma due to the ELM event is associated with an increase in plasma light (Balmer- α and *bremstrahlung*) due the interaction of the expelled particles with the neutrals outside the plasma. The linear D_α camera shows the formation of an outboard tail of D_α emission coincident with the appearance of the ELMs (see figure 8.14).

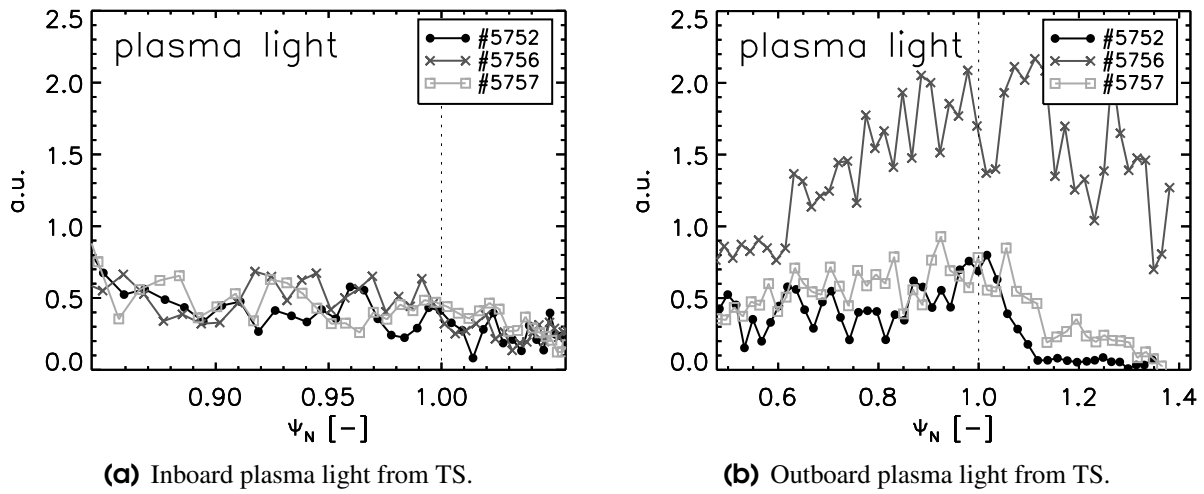


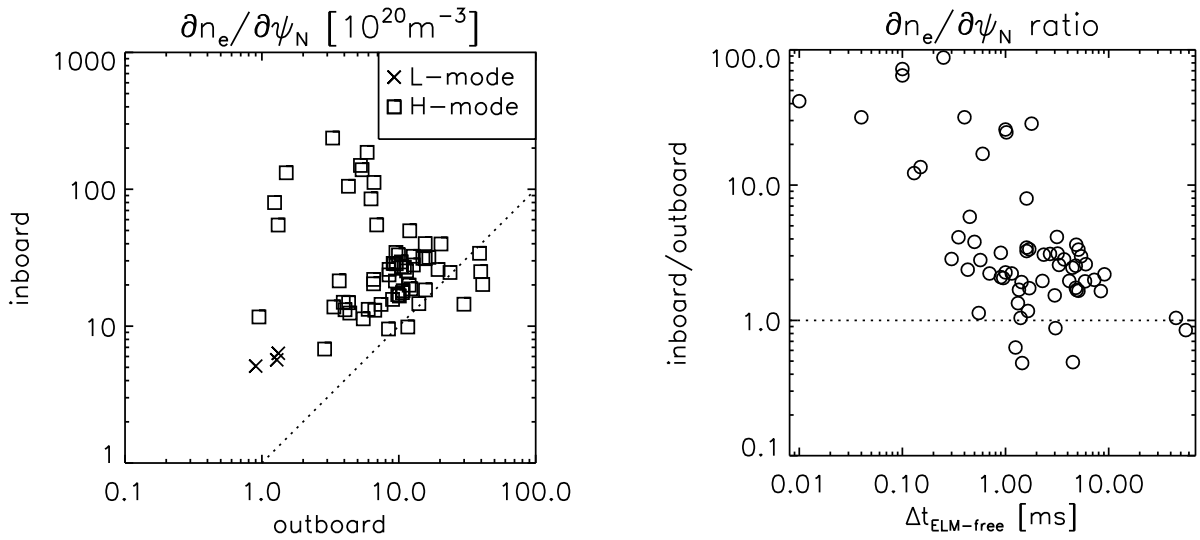
Figure 8.15: Plasma light as measured by the Thomson scattering diagnostic before (#5752), during (#5756) and after (#5757) an ELM on inboard and outboard edges. The plasma light profiles correspond to the T_e and n_e profiles shown in figure 8.13. During the ELM a substantial increase of plasma light is observed on the outboard side only.

The formation of an outboard tail of emission is also observed on the TS data. The TS diagnostic measures the plasma light spectrum recorded along the viewing chord of each spatial channel in addition to the scattered spectrum (see figure 6.23 and section 6.7). The outboard side shows an increase in plasma light during the ELM (see figure 8.15(b)) while no change is observed on the inboard side with viewing chords on the central column (see figure 8.15(a)).

To show that mainly the outboard n_e gradient is effected by ELMS, the n_e pedestal values of a large set of plasma discharges are determined by fitting the inboard and outboard n_e pedestals to the $TS(edge)$ function on normalised flux coordinates as outlined in section 7.2. Figure 8.16(a) shows that in general the inboard gradient is steeper than the outboard gradient by a factor of ~ 2 , but this ratio can also be much higher. Assuming that the particle transport parallel to the field lines is much greater than that perpendicular to the field lines, the inboard and outboard gradients should have similar gradients on normalised flux coordinates. The factor ~ 2 is the result of the unfolding of the gradients using the technique presented in section 7.2: the unfolded gradients are limited by the spatial resolution, which is highest on the inboard side, therefore the steepest gradients can be resolved on the inboard side (see also figure 7.4(b)).

Nonetheless, the inboard density gradient can be much greater than the outboard density gradient. Figure 8.16(b) shows that the ratio of the inboard and outboard gradient increases to values close to ~ 100 for n_e profiles recorded just after the ELM. However, for longer ELM-free periods ($\Delta t_{ELM-free} > 1$ ms) the inboard and outboard gradients reach similar values. This shows that, in general, the ELM has an effect on the outboard edge gradient mainly: the ELM expels particles out of the plasma and a flattening of the outboard gradient is observed. This causes the outboard n_e pedestal to drop. The particle transport during ELMS is presumably enhanced by poloidally asymmetric processes more prominent on the low field outboard side.³ Subsequently, the inboard n_e pedestal can drop and the inboard n_e gradient flatten due to transport along the field lines. Such a change of the inboard density profile after an ELM has been shown in Chapter 5.

³The low field side is also referred to as the ‘bad curvature’ side; this is where the pressure gradient and the gradient in the magnetic field work in the same direction away from the plasma core [27].



(a) Gradients are generally steeper on the inboard side. (b) The ratio of inboard over outboard n_e gradients as function of the time elapsed since the last ELM. The ratio is highest after the ELM and goes to 1 for long ELM-free periods.

Figure 8.16: Comparison of inboard and outboard n_e gradients in L and H-mode plasma discharges.

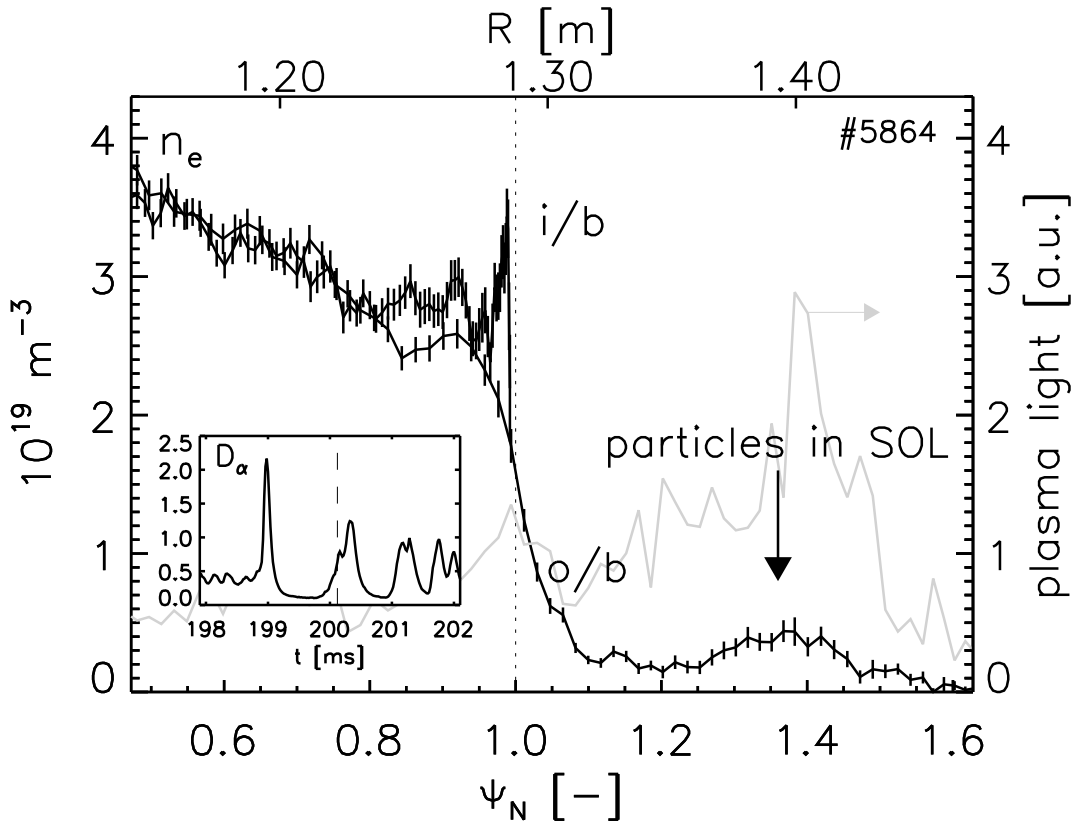


Figure 8.17: TS n_e profile showing a reduction of n_e inside the outboard edge and an increase of n_e in the SOL. The inboard edge is still unaffected at the time of the TS measurement and shows a small EDE with a very steep edge gradient. The inset shows the time of TS measurement relative to the ELM. The graph also shows the plasma light as measured by the TS system on the outboard side, which is shown to increase in the SOL.

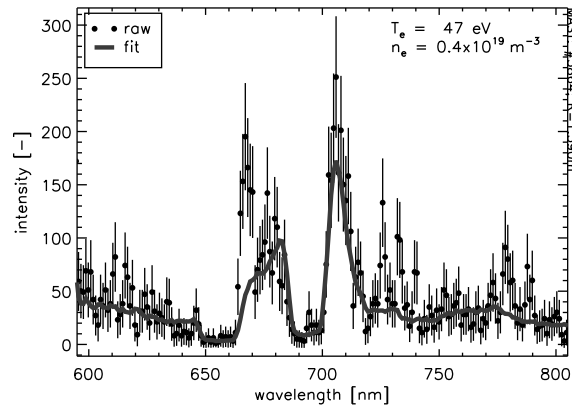


Figure 8.18: Thomson scattered spectrum at the spatial point positioned at $R = 1.39$ m of the profiles shown in figure 8.17. Although the scattered spectrum is distorted by what appears to be atom line-radiation, still a good fit the spectrum is made producing $T_e \approx 47$ eV and $n_e \approx 4 \times 10^{19} \text{ m}^{-3}$.

The difference in effect of the ELM on the inboard and on the outboard sides is summarised in figure 8.17. On the inboard edge an EDE with a steep gradient is observed just inside $\psi_N = 1$ (indicated by the dashed line). The outboard edge is degraded by the ELM and electrons are observed in the far SOL. The peak temperature and density of these particles are $T_e \approx 50$ eV and $n_e \approx 4 \times 10^{19} \text{ m}^{-3}$. Figure 8.18 shows the TS spectrum for the spatial channel at $R = 1.39$ m to support the observation. It is assumed that the presence of the particles in the SOL is the result of an extension of the density tail (see figure 8.13(b)). At this stage the edge gradient returns to its pre-ELM level. To illustrate this, figure 8.19 shows a cartoon of the behaviour of the outboard edge n_e gradient during the ELM. After the ELM the gradient returns to the situation prior to the ELM. This shows that the loss is of a convective rather than diffusive manner.

From figure 8.17 the radial velocity of the expelled electrons can be estimated. The distance from the outboard separatrix to the front of the heap of particles in the SOL is ~ 0.14 m. The time of the start of the increase of D_α emission, shown in the inset in the figure, is regarded as the time at which the ELM occurs. The time elapsed between the ELM and the TS measurement (as indicated in the figure) is ~ 0.1 ms. This produces a radial velocity of $\sim 1.4 \text{ km s}^{-1}$ at which the electrons are expelled from the plasma. This appears to be consistent with the radial expansion of a poloidally localised structure at $1 - 2 \text{ km s}^{-1}$ as measured by the reciprocating probe at close distance to the plasma edge [24].

Figure 8.17 also shows the plasma light as measured by the TS diagnostic. While the intensity of the plasma light normally decreases from the edge of the plasma towards the SOL (see figure 8.15(b)), during the ELM an increase is observed around the particle heap in the SOL. The increase in plasma light would be the result of the interaction of hot particles originating from the plasma with cold particles outside the plasma, which gives rise to *e.g.* *bremstrahlung* and charge-exchange recombination radiation. This hypothesis supports the presence of the flow of particles from the bulk plasma into the far SOL. The tail in the linear D_α camera signal during the ELM is again shown in figure 8.20. During the ELM at 243 ms into the discharge the tail is recorded disconnected from the plasma edge, as was seen on the plasma light profile. This feature is not recorded for all ELM events as can be seen from the figure. This might be due to: the sampling function and so-called ‘dead-time’ of the camera; the possible toroidal and poloidal structure of the ELM due to which the ELM is not in view of the camera at all times; or a combination of both. A detailed examination of this event in high time resolution is planned on MAST [28].

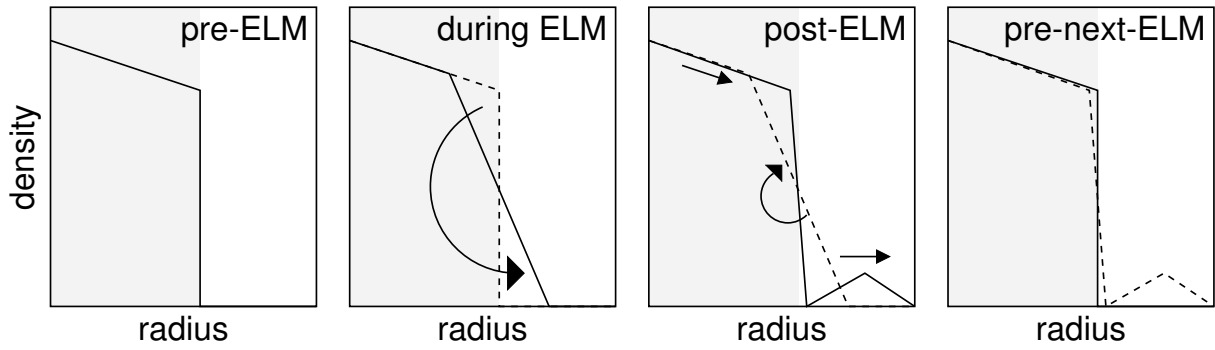


Figure 8.19: A cartoon showing the behaviour of the outboard edge n_e gradient during an ELM event. The shaded area indicates the region of the bulk plasma. The arrows indicate the direction of the movement of the gradient and particles. Before the ELM ('pre-ELM') the gradient is steep. During the ELM ('during ELM') the gradient is flattened and a tail is observed in the SOL. Just after the ELM ('post-ELM') the particles drift further into the SOL while the gradient steepens. Long after the ELM parallel transport in the SOL has removed the particles from the SOL and the gradient has returned to the 'pre-ELM' situation.

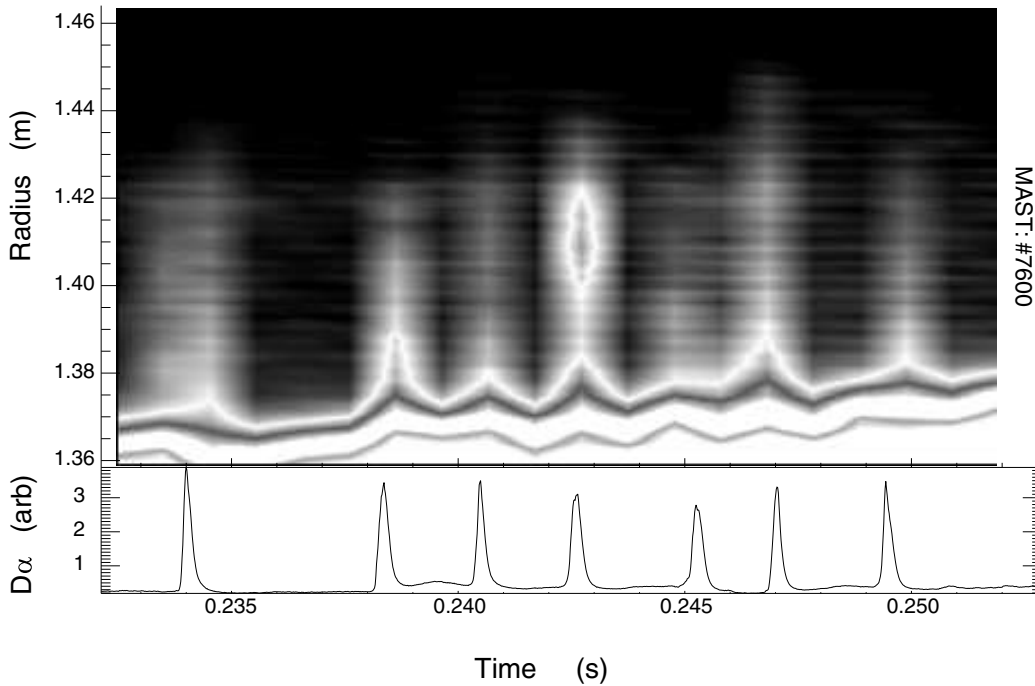


Figure 8.20: D_α emission is recorded far into the SOL during ELMs. Occasionally this tail is recorded disconnected from the edge of the plasma, such as at 243 ms.

The TS system is designed to measure T_e and n_e in the core plasma and operates at the limits of its performance by measuring the scattered light from the particles in the SOL (see Chapter 6). For more detailed studies of this phenomenon, the implementation of a TS diagnostic focussed on the edge could be considered on MAST [28]. Such a diagnostic can use the same ruby laser system and have the collection optics positioned closer to the scattering volumes. This will increase the intensity of the scattered signal and therefore reduce the lower limit of the detectable density range. Furthermore, the lower limit for T_e will reduce compared to the present setup, because of the reduction in scattering angle (see Chapter 7).

Summary of asymmetric power exhaust during ELMs

Before the addition of the aspect ratio to the pedestal scaling law is presented in the next section, this section is finalised with a brief summary of the observations made on the asymmetric power exhaust during ELMs.

It has been shown that the power exhaust during ELMs is preferentially released on the outboard side. On the inboard side the power exhaust during ELMs is equal to the power exhaust during inter-ELM periods. The outboard edge density gradient is flattened during an ELM and steepens during the inter-ELM periods. The inboard edge density gradient is not affected during the ELM. Associated with the ELM is the convective loss of particles from the plasma on the outboard edge, as seen on both the linear D_α camera as the TS diagnostic. No additional losses are detected during the ELM on the inboard edge compared to the inter-ELM period.

8.6 Addition of aspect ratio to pedestal scaling law

In section 8.4, and before that in Chapter 5, it has been shown that the density profile develops a pedestal with a height in the order of the central density, while the temperature pedestal only reaches 10 – 15% of the core value. The behaviour of the pedestal in MAST is therefore different than on most conventional tokamaks. However, in section 8.2 it has been shown that the global confinement during H-mode in MAST scales with that of conventional tokamaks. The behaviour of the pedestal and core in MAST is therefore fundamentally different from other machines. A possible explanation for this difference is the aspect ratio of the plasma, which is much lower than in conventional tokamaks. The leading scaling law for the stored energy in the pedestal [29] has been derived from data from conventional tokamaks, and includes no aspect ratio dependence. MAST data will be compared to this database and the aspect ratio dependence will be added.

Pedestal scaling

A description of the determination of the global confinement time and the calculation of the stored energy in the plasma is found in appendix 8.A. As an alternative to the global confinement scaling, a two-term energy confinement scaling is used, which based on the core (W_{core}) and pedestal energy content (W_{ped}):

$$\tau_E = \frac{W_{core} + W_{ped}}{P} \quad (8.2)$$

The pedestal scaling can be determined as function of the global variables: plasma current (I_p) in MA, major radius (R) in m, loss power (P) in MW, effective mass (M) in AMU and the shaping factor $q_{sh} = \frac{q_{95}}{q_{cyl}}$ with $q_{cyl} = 5\kappa_a a^2 B / R I_p$ and elongation $\kappa_a = V / 2\pi^2 R a^2$ (where V is the plasma volume). The leading scaling of W_{ped} has a dependence of the form [29]:

$$W_{ped,scal} = e^{-3.74 \pm 0.10} I_p^{1.71 \pm 0.04} R^{1.16 \pm 0.01} P^{0.31 \pm 0.02} M^{0.30 \pm 0.11} q_{sh}^{1.20 \pm 0.15} \quad (8.3)$$

This form has been derived using the Kadomtsev high β constraint. The dependence on density ($\sim n_e^{0.004 \pm 0.07}$) and magnetic field ($\sim B^{0.06 \pm 0.07}$) is very weak and the used data set is not extensive enough to determine the scaling taking into account the parameters κ_a or ϵ . This

scaling is derived from the subset of ‘medium aspect ratio’ tokamaks with a small range of $\epsilon = 0.24 - 0.37$ [30]. Since MAST has an inverse aspect ratio of ~ 0.68 , addition of the MAST data will double the parameter space and is therefore expected to provide a useful constraint on the scaling law. However, addition of the MAST data requires accurate determination of the energy in the pedestal.

Methods of determining the pedestal energy

The energy in the pedestal can be calculated from kinetic measurements or from magnetic measurements. In general, the reconstructed pressure profiles using EFIT do not show clear pedestals, therefore the pedestal value must be taken at a specific value of ψ , *e.g.* at ψ_{95} . This choice is quite arbitrary. Contrary to that, the kinetic data result from direct measurements and can show pedestals on the profiles. Calculating the stored energy from kinetic measurements is, therefore, the preferred method.

The energy in the pedestal separates into an electron ($W_{e,ped}$) and an ion ($W_{i,ped}$) contribution $W_{ped} = W_{e,ped} + W_{i,ped}$. These individual terms are calculated using the $p_{e,ped}$ and $p_{i,ped}$ profiles and the plasma volume. Profile diagnostics with high resolution are therefore required. On MAST the high-resolution Thomson scattering diagnostic (see Chapter 6 and Chapter 7) provides the means of measuring $p_{e,ped}$. The p_i profile is determined from T_i measured by charge-exchange radiation spectroscopy [31] (CXR) and n_i calculated from n_e assuming a dilution factor of 0.6-0.8. The determination of the electron pedestal will be discussed in more detail.

In order to determine the p_e pedestal, several methods are available, each possibly resulting in different values for $W_{e,ped}$. So far, no consistency exists in the determination of the p_e pedestal on the different machines providing data to the pedestal database. This raises questions about the usefulness of the scaling law, which is derived from these data.

The following list shows an overview of the different methods of calculating $W_{e,ped}$. A reference is provided for those methods which have been researched.

1. $\frac{3}{2}p_{e,ped}V$, where $p_{e,ped}$ is determined at ψ_{95}
2. $\frac{3}{2}p_{e,ped}V$, where $p_{e,ped}$ is determined at the D_α peak radius -2 cm at outboard midplane [24] (see figure 7.7)
3. $\frac{3}{2}eT_{e,ped}n_{e,ped}V'$ where the volume has been reduced by 8% to take account of the trapezoidal nature of the pedestal [29]
4. $\frac{3}{2}p_{e,ped}V$, where a fit of a function based on \tanh or $m\tanh$ to p_e on R , z or ψ_N is made from which $p_{e,ped}$ is derived [12, 13, 32]
5. new method developed for MAST data

Most of these methods can be applied to the profile at any crossing of the separatrix, *e.g.* at inboard or outboard midplane as, for example, in MAST, and more methods can easily be defined.

The first two methods in the list take the $p_{e,ped}$ value at quite arbitrary positions in the plasma and do not take the trapezoidal shape of the pedestal into account. In addition, the second method is machine size dependent. The third method, like the first two, locates the pedestal at an arbitrary position and assumes pedestal stiffness. The fourth method does not

take the trapezoidal shape of the pedestal into account, and therefore overestimates the energy in the pedestal.

In the fourth method analytical functions describing the shape of the pedestal in the plasma are fitted to the measured pedestal data. These functions are directly fitted to the pedestal data, without taken the instrument function of the used diagnostic into account. This instrument function can have an important smoothing effect on the measured pedestal data (see *e.g.* section 7.2). In this case, the measured data therefore differs from the ‘real’ pedestal in the plasma.

Since different machines use different diagnostics to determine the pedestals, the data obtained from each of these machines needs to be unfolded to remove effects due to the instrument function of the used diagnostic. In other words, the determination of the pedestal must be diagnostic independent. For low-resolution diagnostics, the instrument function can have a strong smoothing effect on the edge gradient and therefore on the determination of $p_{e,ped}$ and $W_{e,ped}$. In section 7.2 it has been shown that the smoothing does not affect the determination of the pedestal height on the high-resolution TS data measured on MAST significantly, but nonetheless, for sake of correctness, the instrument function will be taken into account in a fifth method developed for the determination of $W_{e,ped}$ in MAST. This method can easily be adopted for other machines as well.

Determining the pedestal energy in MAST: method 5

A description of the TS diagnostic used on MAST and the instrument function of this diagnostic is presented in Chapter 6. The effect of the instrument function on the profile measurements is presented in section 7.2. This section presents a method for determining the pedestal and edge gradient. This method assumes that the ‘real’ edge profile has the shape of the *edge* function, (7.1), based on the *mtanh* function [32], which is a good approximation.

The finite size of the collection volumes and the instrument function are folded into the *edge* function to take account of the diagnostic and so the $TS(edge)$ function (7.3) is obtained. This new function is fitted to the edge p_e profile. The fit returns five fitting parameters (\vec{a}) determining the shape, size and position of the ‘real’ edge profile. The shape of the pedestal is determined by the *edge* function using \vec{a} for which the parameter determining the linear core slope is suppressed ($a_3 = 0$). This results in $p_{e,ped}$. The energy in the pedestal is now calculated by [29]:

$$W_{e,ped} = \frac{3}{2} \int_0^1 p_{e,ped}(\psi_N) \frac{\partial V}{\partial \psi_N} d\psi_N \quad (8.4)$$

where $\partial V / \partial \psi_N$ is the partial volume produced by EFIT.

The pedestal energy can be calculated both from the inboard and outboard data. The error on the pedestal measurement consists of contributions of the error on the integral and of the systematic error on p_e . The error on the integral is determined from the error on the fitting parameters and the error on the plasma volume produced by EFIT ($\approx 6\%$). The error on p_e is governed by the error on \bar{n}_e (see section 6.3). For these particular discharges this produces an error on p_e of $\sim 5\%$.

An example of a fit to the inboard and outboard p_e profiles on ψ_N is shown in figure 8.21. The figure shows the difference in resolution between the inboard data and outboard data as explained in section 7.2. Due to the higher resolution, more data points are available in the pedestal region for which reason the fit is better on the inboard side (see section 7.2). The shaded area in the figure marks $p_{e,ped}$. The pedestal electron energy is $W_{e,ped} = 6.9 \pm 0.5$ kJ

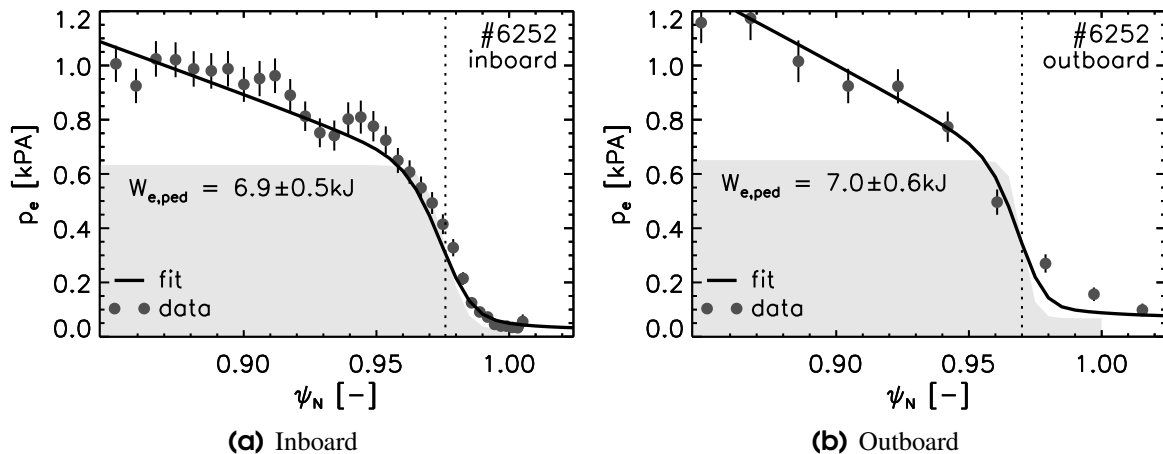


Figure 8.21: Fit of the $TS(edge)$ function to the edge p_e profile on ψ_N . The shaded area represents the ‘real’ pedestal as defined by the $edge$ function in the plasma.

resulting from the inboard data and $W_{e,ped} = 7.0 \pm 0.6$ kJ from the outboard data. The average value of the inboard data and outboard data is taken to be the pedestal energy $W_{e,ped}$.

To illustrate the difference with the other methods of determining $W_{e,ped}$, table 8.2 presents the values calculated using the various methods. This shows that method 5 guarantees the smallest error in the calculation and the best agreement between inboard and outboard measurements. This method is therefore the preferred method for calculating $W_{e,ped}$ in MAST and is the advised method for pedestal energy calculations on other machines providing data to the pedestal scaling database.

Table 8.2: Calculation of the pedestal energy of plasma discharge #6252 using 5 different methods.

method	$W_{e,ped}$ [kJ]	
	inboard	outboard
1	8.6 ± 0.8	7.4 ± 0.7
2 ^a		10.2 ± 0.9
3 ^b	6.3 ± 0.5	6.4 ± 125
4 ^c	7.1 ± 0.6	6.5 ± 0.7
5	6.9 ± 0.5	7.0 ± 0.6

^aThe inboard D_{α} peak is not recorded on MAST.

^b $T_{e,ped}$ and $n_{e,ped}$ have been determined using the $edge$ function.

^c $p_{e,ped}$ is determined by applying a $mtanh$ fit on ψ_N to the data.

Effect of an ELM on the pedestal energy determination

In section 8.5 it has been shown that an ELM event degrades the pedestal, therefore the time-averaged pedestal energy can be calculated during the ELMy H-mode. However, on MAST, the high-resolution TS diagnostic only measures one profile per plasma discharge. The measurement can have any time separation to the appearance of the ELM. A time-average pedestal energy can therefore not be provided on MAST. An alternative would be to repeat the plasma discharge so that the average of more than one discharge, and thus of more than one TS measurement, taken at different time interval to the ELM event, can be calculated.

To illustrate the effect of the ELM on the electron contribution to pedestal energy, $W_{e,ped}$ has been calculated using the inboard edge for the plasma discharges shown in figure 8.13. The results are shown in table 8.3. This shows that $W_{e,ped}$ substantially varies (by almost a factor of 2) whether it is measured during or after the ELM event.

Table 8.3: Electron contribution to the pedestal energies of the profiles used in figure 8.13.

discharge	Δt ms	$W_{e,ped}$ kJ
#5752	1.5	3.5
#5756	0	2.0
#5757	0.3	2.1

In section 8.5 it has been shown that the inboard side is least affected by the ELM, which makes the inboard side the preferred side for determining the pedestal energy. The T_e pedestal has been shown to drop during the ELM event, but also to recover soon afterwards and to stabilise. The n_e pedestal also collapses during the ELM, recovers afterwards and increases until the next ELM event appears (see figure 8.16(b)). Therefore the validity of the pedestal energy calculation has to be questioned whenever the measurement is close to the ELM. The most reliable measurements are made half way in between two ELMs, when the T_e pedestal is expected to have been established and the n_e pedestal has approximately reached its average value between the ELMs.

Only for high frequency ELMs ($f_{ELM} > 2.2$ kHz) is the power flux from the plasma during the ELM equal to that in between the ELMs (see figure 8.9(b)), and which shows that the T_e and n_e pedestals do not recover from one ELM to the next. For this type of ELMs the pedestal energy can be determined at any time during the ELM phase.

Addition of MAST data to the pedestal scaling

A data set of quasi-steady state H-mode plasma discharges, used for global confinement scaling (see section 8.2), provides a basis for comparison with the international database for pedestal scaling (8.3) [29]. From the data set a subset of data is taken for which accurate TS data taken during the quasi-steady state of the discharge are available. The selected TS data result from TS measurements performed reasonably far from an ELM event (> 1 ms), so that the pedestal energy values obtained are the most reliable.

To determine the ion contribution to the pedestal energy the ion density (n_i) and ion temperature (T_i) pedestals are compared with the electron equivalents. As regards density, a dilution of 0.8 is assumed: $n_{i,ped} \approx 0.8n_{e,ped}$. Estimates of the T_i pedestal follow from CXR measurements. These values are not routinely available on MAST, however CXR data indicate that $T_i \approx T_e$. Together with the assumption concerning the ion density pedestal this yields $W_{i,ped} \approx 0.8W_{e,ped}$, which results in $W_{ped} = 1.8W_{e,ped}$.

A comparison of the MAST pedestal energy with the scaling law is shown in figure 8.22. The measured values are, on average, a factor of ~ 5.1 lower than predicted. It is believed that this is related to the low aspect ratio of the plasma. The latter alters the plasma surface geometry in STs strongly compared to that of conventional tokamaks. The plasma surface determines the heat fluxes in and out of the plasma, and therefore the pedestal. The geometrical dependency on aspect ratio is not included in the existing scaling law (8.3). The inverse aspect ratio (ϵ) in MAST is on average ~ 2.3 times higher than in the data used to derive the scaling law (8.3).

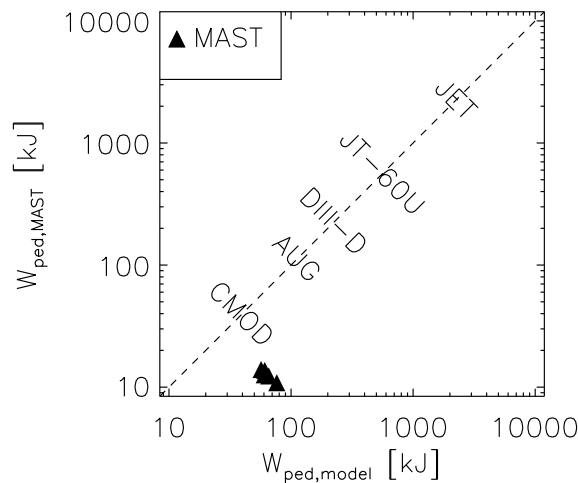


Figure 8.22: Pedestal energies in MAST compared to the International Pedestal confinement scaling [29].

Assuming that this difference is due to the geometry dependence, MAST would introduce about a quadratic aspect ratio dependence in the pedestal scaling $W_{ped} \propto \epsilon^{-2}$, as was presented in [12]. The exponent has a strong dependence on the value of the T_i pedestal, which is not known with high accuracy on MAST because of difficulties in determining T_i at the edge using CXR (see Chapter 3). For example, a doubling of T_i will relax the inverse aspect ratio dependence to $W_{ped} \propto \epsilon^{-1.5}$.

8.7 Conclusions

The ST could have the potential to be extrapolated to the scale of a nuclear power plant. This requires, *i.e.* reliable access to H-mode and good confinement. Also, the power exhaust from the plasma should not lead to material wear and therefore limit the lifetime of the machine. The measurements of the high-resolution TS diagnostic have been used to study these topics on MAST.

H-mode can regularly be accessed in MAST in both Ohmic and NBI heated plasma discharges primarily in CDND configuration with the use of inboard refuelling. The resulting discharges demonstrate all of the established H-mode signatures, including ELMs, increase in particle and energy confinement, steepening of the edge gradients, and narrowing of the D_α profile at the plasma edge. The energy confinement time recorded during the quasi-steady state H-mode in MAST scales well with IPB98(y,2) scaling which is mainly based on data from tokamaks at conventional aspect ratio ($H_H = 1.0 \pm 0.2$).

The profiles recorded with the high-resolution Thomson scattering system (see Chapter 6) during H-mode show the development of pedestals on both T_e and n_e . The T_e pedestal only reaches values up to 10 – 15% of the central value (~ 140 eV), while the n_e pedestal can reach values close to the central value. The cold edge is likely to be related to increased radiative and conductive losses due to the high n_e at the edge, but also due to the compact geometry of the plasma.

The T_e pedestal degrades during an ELM event, but recovers soon after the ELM, indicating that ELM-related losses are predominately non-conductive. The edge density is partially degraded by the ELM, but rises continuously during inter-ELM periods.

The power exhaust during ELM events shows a significant inboard-outboard asymmetry: $> 90\%$ of the power is released on the outboard side. For the ST in the concept of a fusion power plant this is an advantage, because of the limited space on the high field side and therefore small surface of the divertor target areas.

The ratio of the power lost during the ELM event and in between ELMs is 1 on the inboard side, indicating that no power is lost by the ELM on the inboard side. On the outboard side this ratio is ~ 5 for an ELM frequency ~ 250 Hz, but decreases for higher ELM frequencies. It indicates that the pedestal is not completely re-established during the inter-ELM periods of high frequency ELMs.

During the ELM event particles and heat are released from the plasma on the outboard side only, no changes are observed during the ELM on the inboard side. The particle transport during ELMs is presumably enhanced by asymmetric processes more prominent on the outboard side. The ratio of inboard over outboard n_e gradient reaches values of ~ 100 just after the ELM event and decreases to 1 for long ELM-free periods.

Particles are detected far into the SOL at an ELM event. This indicates that the loss of the particles out of the plasma is of a convective nature. The radial velocity of the particles is determined at $\sim 1.4 \text{ km s}^{-1}$, this is consistent with observations of the radial expansion of a poloidally localised structure at $1 - 2 \text{ km s}^{-1}$ as measured by the reciprocating probe at close distance to the plasma edge [24].

The pedestal behaviour in MAST is different from that on other machines, which could be due to the extreme aspect ratio. MAST pedestals during quasi-steady state have been compared to an existing scaling law for the energy stored in the pedestal. A method has been developed to accurately and consistently determine the electron component of the pedestal energy in MAST. The MAST data fall short of the scaling by a factor of ~ 2.3 . Inclusion of MAST data in the database would introduce about a quadratic aspect ratio dependence in the pedestal scaling.

Bibliography

- [1] F. Wagner et al. Regime of improved confinement and high beta in neutral beam heated divertor discharges of the ASDEX tokamak. *Physical Review Letters*, 49, 1982.
- [2] A. Sykes et al. First physics results from the MAST Mega-Amp Spherical Tokamak. 8(5):2101–2106, May 2001.
- [3] R.J. Akers et al. On the neutral beam heating of spherical tokamak plasmas. page To be published Nuclear Fusion, Sorrento, Italy, 4-10 October 2000.
- [4] R. Akers et al. H-mode access and performance in the Mega-Amp Spherical Tokamak. *Physics of Plasmas*, 9(9):3919–3929, September 2002. Special Topics Section:Papers from a Special Session on Modes of Transport in Geospace, American Geophysical Union 2001 Fall Meeting, San Francisco. [This paper is based on an invited talk at the 2001 APS DPP Meeting, Long Beach, CA.].
- [5] A.R. Field et al. H-mode plasmas in the mast spherical tokamak. *Plasma Physics and Controlled Fusion*, 44, Supplement 5A:A113–A121, May 2002. Special Issue:Papers from the 8th IAEA Technical Committee Meeting on H-Mode Physics and Transport Barriers, Toki, Japan 5-7 September 2001.

- [6] A. Sykes et al. Results from the mast spherical tokamak. Accepted for publication in *Fusion Engineering & Design*, January 2002.
- [7] P.G. Carolan et al. H-mode access physics in MAST. *19th IAEA Fusion Energy Conference, Lyon, France, 14-19 October 2002*.
- [8] V. Shevchenko et al. EBW observations on COMPASS-D and MAST. In *Proceedings of the 28th EPS Conference on Controlled Fusion and Plasma Physics*, volume 25A, pages 1285–1288, June 2001.
- [9] B. Lloyd et al. Overview of recent experimental results on MAST. 2002.
- [10] J.W. Connor. Edge-localized modes-physics and theory. *Plasma Physics and Controlled Fusion*, 40:531–542, 1998.
- [11] ITER Physics Expert Groups on Confinement and Transport and Confinement Modelling and Database, ITER Physics Basis Editors, ITER EDA, and Naka Joint Work Site. Plasma confinement and transport. *Nuclear Fusion*, 39(12):2175–2249, 1999.
- [12] M. Valovič and other. Energy confinement in ELMy H-mode on MAST. In *Proceedings of the 29th EPS Conference on Controlled Fusion and Plasma Physics*, volume 26B, June 2002.
- [13] H. Meyer et al. The effect of magnetic configurations on h-mode in mast. In *Proceedings of the 29th EPS Conference on Controlled Fusion and Plasma Physics*, volume 26B, June 2002.
- [14] L.L. Lao, H. St. John, R.D. Stambaugh, A.G. Kellman, and W.W. Pfeiffer. *Nuclear Fusion*, 25:1611, 1985.
- [15] R. Akers et al. L-H transition in the Mega-Amp Spherical Tokamak. *Physical Review Letters*, 88(3):035002–1–035002–4, 21 January 2002.
- [16] C. Byrom. *Thermal & Fast Ion Behaviour in the MAST Experiment*. PhD thesis, Department of Physics, University of Manchester Institute of Science and Technology, Manchester, 2002.
- [17] P.G. Carolan et al. Enhanced performance in the START tokamak. 40:615–620, 1998.
- [18] E.A. Lazarus et al. The role of shaping in achieving high performance in DIII-D. In *Proceedings of the 15th International Conference on Plasma Physics and Controlled Nuclear Fusion Research*, volume 1, page 609, 1995. IAEA-CN-60/A5-1.
- [19] R.E. Bell et al. Kinetic profile in NSTX plasmas. In *Proceedings of the 28th EPS Conference on Controlled Fusion and Plasma Physics*, volume 25A, pages 1021–1024, 2001.
- [20] E.R. Arends, M.J. Walsh, N.J. Lopes Cardozo, and the MAST and NBI teams. Electron transport during H-mode on mast. In *Proceedings of the 28th EPS Conference on Controlled Fusion and Plasma Physics*, volume 25A, pages 589–592, 18-22 June 2001.
- [21] N.J. Lopes Cardozo et al. Electron thermal transport in rtp; filaments, barriers and bifurcations. *Plasma Physics and Controlled Fusion*, 39:B303–B316, 1997.

- [22] R.J. Buttery et al. Neoclassical tearing physics in the spherical tokamak MAST. *Physical Review Letters*, 88(12):125001–1:125005–4.
- [23] P. de Vries. Density profile peaking inside the $m/n = 2/1$ magnetic islands in TEXTOR. *Nuclear Fusion*, 37:1641–1646, 1997.
- [24] G.F. Counsell et al. A review of plasma boundary phenomena in the Mega Ampere Spherical Tokamak. In *Proceedings of the 15th Conference on Plasma Surface Interaction, Gifu, Tokyo, For publication Journal of Nuclear Materials*, May 2002.
- [25] A. Kirk et al. In *Proceedings of the 15th Conference on Plasma Surface Interactions*, pages P3–74, 2002.
- [26] J-w. Ahn. *Investigations of the Boundary Plasma in the MAST tokamak*. PhD thesis, Imperial College of Science, Technology and Medicine, United Kingdom, 2002.
- [27] J. Wesson. *Tokamaks*. Clarendon Press, Oxford, 1987.
- [28] MAST Diagnostics Review Meeting. Culham Science Centre, February 2003.
- [29] K. Thomsen, J.G. Cordey, et al. *Plasma Physics and Controlled Fusion*, 44(5A):A429, 2002.
- [30] L. Horton et al. *Plasma Physics and Controlled Fusion*, 44(5A):A274, 2002.
- [31] M. McGrath. *Charge-exchange spectroscopy on the MAST tokamak*. PhD thesis, National University of Ireland, University College, Dublin, March 2003.
- [32] R.J. Groebner and T.N. Carlstrom. Critical edge parameters for H-mode in DIII-D. *Plasma Physics & Controlled Fusion*, 40:673–677, 1998.
- [33] P. Helander. The confinement time in an evolving tokamak discharge. Internal Report, EURATOM/UKAEA Fusion.
- [34] R. Akers. Results on beam driven plasma current experiments. Internal presentation, 2002.
- [35] J.P. Christiansen. *Nuclear Fusion*, 32(2):291, 1992.

8.A Determination of the global energy confinement

Establishing scaling laws for the global energy confinement time requires accurate calculations of the stored energy and heat flux in the plasma. These values can be obtained on MAST due to the extensive range of precise diagnostics.

Global energy confinement time

The global energy confinement time (τ_E) is evaluated using the definition:

$$\tau_E = \frac{W}{P} \quad (8.5)$$

where W is the stored energy in the plasma and P is the integral of the total heat flux consisting of convective, conductive and radiative terms and includes the rate of change of thermal energy (\dot{W}):

$$P = \int_S \vec{Q} \cdot d\vec{S} \quad (8.6)$$

Although some MAST plasmas can be regarded as being in a steady-state regime, the confinement time in MAST is usually long compared with the flat-top plasma duration available so far. As a result, non-steady state effects have to be taken into account in deriving τ_E and considerable care has to be taken in the evaluation of P [33]. This was assumed to be equal to the net power input to the plasma, itself derived from the sum of the absorbed auxiliary power (P_{aux}) input from neutral beam and the flux of electromagnetic energy from the induced toroidal electric field ($V_{loop}I_p$) (allowing for changes in the plasma boundary), less the rate of change of the plasma ($\dot{W} - (3p_a/2)\dot{V}$, where p_a is a constant edge pressure and V the plasma volume), and magnetic field (X) energies. Low aspect ratio effects were also taken into account, such as the rate of change of both poloidal and toroidal field energy components [33]. Inclusion of all these terms yields the energy confinement time:

$$\tau_E = \frac{W}{P_{aux} + V_{loop}I_p - \dot{W} + (3p_a/2)\dot{V} - X} \quad (8.7)$$

Stored energy

The energy stored in the plasma, W , is evaluated from equilibrium reconstructions using the EFIT code [14]. This can be compared to the kinetic determination of W along with any contributions of fast particles. The kinetic energy content (W_{kin}) of the plasma is the sum of the electron and ion contributions. The electron contribution ($W_{kin,e}$) is calculated from electron temperature and density profiles and from plasma volume (V) reconstructions from EFIT according to:

$$W_{kin,e} = \frac{3}{2} \oint_V n_e T_e dV \quad (8.8)$$

where T_e is expressed in eV. The ion contribution is calculated in a similar way from the T_i and n_i profiles. T_i is measured by CXR or, alternatively, the central value is taken from the NPA and the shape of the profile is taken to be equal to the T_e profile. In order to get an estimate for n_i from n_e an ion dilution of $0.7 < n_i/n_e < 0.9$ is assumed. In general there is little difference between the values of W and W_{kin} , which indicates the relatively small role played by the neutral beam fast ion component in W . However, during specially designed beam-driven plasma current experiments, the contribution of the fast ions to the total energy has reached values of up to 85% [34].

Global confinement scaling

The scaling of the global confinement can be determined as a function of the global variables: plasma current (I_p) in MA, magnetic field (B) in T, loss power (P) in MW, density (n_{19}) in 10^{19}m^{-3} , effective mass (M) in AMU, major radius (R) in m, minor radius (a) in m, inverse aspect ratio (ϵ) and elongation ($\kappa_a = S/\pi a^2$ where S is the poloidal plasma cross-section). MAST confinement data are compared to the IPB98(y,2) international database given by [11]:

$$\tau_{E,IPB98(y,2)} = 0.0562 I_p^{0.93} B^{0.15} P^{-0.69} n_{19}^{0.41} M^{0.19} R^{1.97} \epsilon^{0.58} \kappa_a^{0.78} \quad (8.9)$$

In order to compare MAST data with ELMy H-mode energy confinement time scalings in a meaningful way, the plasma should be quasi-stationary. In particular, acceptance to the international ELMy dataset requires that the time derivative of energy content (\dot{W}) should be small [35]:

$$-0.05 \leq \frac{\dot{W}}{P} \leq 0.35 \quad (8.10)$$

Moreover, the duration of such a regime should be sufficiently long in comparison with the energy confinement time.

Chapter 9

Evaluation and discussion

The present work compares the high-confinement regime (H-mode) in a spherical tokamak (ST) to that in a conventional aspect ratio tokamak (CT). The ST is an extension of the conventional tokamak design to a more compact geometry (see Chapter 2). The STs intrinsically have the potential to indicate the way to achieving efficient compact fusion facilities. Furthermore, due to the extreme geometry of the plasma, STs increase the parameter range of energy confinement scaling laws and can therefore verify predictions for future large scale fusion devices.

Promising results obtained on the first spherical tokamak in which high temperature plasmas were achieved, START, have led to the development of the large machine MAST (Mega-Ampere Spherical Tokamak). This machine achieved its first plasma in December 1999 and has since demonstrated plasma currents of $I_p \sim 1.35$ MA, pulse lengths of ~ 0.7 s and quasi-steady state H-mode.

The interest of H-mode lies in the fact that during that regime the confinement is spontaneously increased. H-mode is the result of reduced transport at the edge of the plasma, the so-called edge transport barrier. In conventional tokamaks the barrier leads to the development of steep edge density and temperature gradients and therefore to a pedestal on the density and temperature profiles.

Associated with H-mode are edge instabilities, the so-called edge localised modes (ELMs). These ELMs control the increase of the density, but are also associated with pulsed heat loads on the divertor target plates. The latter could potentially lead to problems for the ST in a full-scale fusion reactor because of the compact geometry and therefore small target areas on the high field side of the plasma: the heat pulses might lead to material wear and thus reduce the lifetime of the machine. The effect of ELMs in tight aspect ratio plasmas has been investigated on MAST.

H-mode on the ST is an under-explored regime because of the small number of ST experiments. MAST therefore provides vital information on the effect of aspect ratio on H-mode. In order to do so, MAST is equipped with a wide range of diagnostics (see Chapter 3). Because of the geometry of the MAST machine, the plasma has good accessibility for diagnostics.

9.1 Summary of diagnostics development

The questions that were addressed in the Introduction of this dissertation (see Chapter 1) were mainly related to the development of the electron density pedestal and edge gradients in H-mode and during ELMs. In order to be able to study these, a multi-point Thomson scattering (TS) system was developed on MAST. This system is based on the scattering of electromagnetic waves on the free electrons in the plasma (see Chapter 4). From the spectrum of the scattered waves

the electron temperature (T_e) and electron density (n_e) can be determined. Initially the system on MAST measured the profiles of T_e and n_e at 30 – 40 spatial positions along a horizontal chord in the midplane of the plasma (see Chapter 5). This system proved to be inadequate for resolving the steepest edge gradients and to produce continuous profiles over the full plasma diameter. Therefore, the system was upgraded to produce close to 300 spatial measurements at high resolution (see Chapter 6). The latter system also produces profiles of line-integrated plasma light, which has proven to be of use for the study of ELMs.

Extensive error analyses were carried out on the raw data recorded by the high-resolution TS diagnostic (see Chapter 6). Smoothing effects in the detection branch of the diagnostic have been included and Monte-Carlo simulations have been carried out to determine the statistical error in the T_e and n_e measurements. The measurement accuracy is typically $< 5\%$ of T_e and $< 4\%$ of n_e in the range 30 eV – 2 keV for a density of $n_e \sim 4 \times 10^{19} \text{ m}^{-3}$. The density is absolutely calibrated using the line-integrated density measured obtained using the CO₂ interferometer.

The high-resolution TS system covers the full plasma diameter and measures both plasma edges. The root-normalised-flux resolution is introduced to express the resolution of the system as a machine-independent variable (see Chapter 6). The resolution is best at the inboard edge ($\Delta\sqrt{\Psi_N} \approx 1/200$) and rises to $\Delta\sqrt{\Psi_N} \approx 1/50$ towards the outboard edge. The high-resolution TS system is therefore a powerful tool in edge gradient studies. Because of a combination of a high-resolution system that measures the temperature and density profiles over the full plasma diameter and a large scale device that produces H-modes, MAST has put itself in a unique position to study H-mode profile phenomena.

A technique has been developed to deconvolve the measurements for the limited size of the collection volumes of each spatial point and for the instrument function of the diagnostic (see Chapter 7). This enhances the resolution and provides a means of comparing the inboard and outboard gradients.

The high-resolution TS system performs one measurement during a plasma discharge. In order to measure the temporal behaviour of the edge electron density gradient during H-mode, a diagnostic based on the Balmer- α emission is implemented on MAST (see Chapter 7). A linear D $_{\alpha}$ camera with an average sampling rate of 1 kHz measures the narrowing of the D $_{\alpha}$ peak at the outboard plasma edge, which yields, by making some reasonable assumptions, the average electron density gradient. This gradient is calibrated using the results from the high-resolution TS system. This calibration has resulted in a measurement of the neutral influx energy: $E_n \approx 0.3 \text{ eV}$. This value indicates that the plasma is surrounded by a bath of low-energetic neutrals.

9.2 Results of H-mode studies

The large range of diagnostics and in particular the Thomson scattering and linear D $_{\alpha}$ camera systems on MAST have been used to study the H-mode regime. This section gives an evaluation of the observations that have been made in relation to the questions raised in Chapter 1.

H-mode in MAST

H-mode in MAST is readily accessible in the so-called ‘connected double null’ configuration and by application of inboard-refuelling (see Chapter 8). The L-H transition power threshold in MAST exceed international scalings that do not include an aspect ratio dependence. The energy confinement during H-mode in MAST is in keeping with the IPB98(y,2) scaling law

($H_H(y, 2) = 1.0 \pm 0.2$) and is therefore comparable to that of the conventional tokamak. MAST shows the same characteristics during H-mode as conventional tokamaks; among those are a steepening of the edge density gradient and an increase of the average density and the energy confinement. ELMs have also been observed during H-mode in MAST and have been classified as type-III. H-mode on STs is therefore very similar to H-modes on CTs. Long ELM-free H-modes in MAST have a peculiarity in that the density profile develops the edge density ‘ear’ (EDE), which refers to the edge densities rising above the central value (see Chapter 5 and Chapter 8). The EDE is depleted with the appearance of ELMs.

Edge density ‘ears’

A simple one-dimensional phenomenological transport model was set up to simulate the development of EDEs by introducing a reduced diffusion coefficient at the edge of the plasma during H-mode (see Chapter 5). This model is based on conservation of electrons and makes an heuristic approach for the description of the neutrals using simple analytic methods and results obtained from the transport code DOUBLE. The source of electrons arises from direct ionisation of the neutrals penetrating the plasma from the edge and from ionisation of neutrals that are spatially redistributed by charge-exchange processes. The simulations yield a reduction of the edge diffusion coefficient from $D \approx 5.5 \text{ m}^2\text{s}^{-1}$ in L-mode to $D \approx 0.44 \text{ m}^2\text{s}^{-1}$ in H-mode. The profile of the diffusion coefficient during H-mode is almost uniform. An inward pinch term is required to drive the electrons into the plasma and thus to shape the EDE.

The simulation assumes a neutral bath of constant density outside the plasma, which is justified due to the large vessel volume to plasma volume ratio and distance to the vessel walls. Estimates produce an edge neutral density of $n_n(a) \approx 4.4 \times 10^{16} \text{ m}^{-3}$. The simulations yield a neutral influx energy of $E_n \approx 0.33 \text{ eV}$, which is in good agreement with the neutral influx energy derived from calibration of the linear D_α camera (see Chapter 7). This image of the recycling is different from that on CTs that generally show a reduction of neutral density at the L-H transition outside the plasma and where the energy of the neutrals is generally reported to be much higher.

The transport model is also used to predict the development of the n_e profile for long ELM-free periods and to simulate the depletion of the EDE by an ELM (see Chapter 5). First, the simulation over long ELM-free periods ($> 3\tau_E$) shows that the n_e profile fills up towards the centre and thus a pedestal is formed. Secondly, the loss in density due to the ELM is modelled successfully by increasing the diffusion coefficient D at the edge during a short time Δt , the product of the two quantities produces $D\Delta t \sim 11 \times 10^{-3} \text{ m}^2$. Although the correct drop in line-average density can be simulated in this way, the details in the n_e profile cannot be reproduced. This indicates that ELM losses presumably do not have a purely diffusive character. In Chapter 8 it was indeed shown that ELM losses are of a convective nature.

The results of the model provide a simple understanding of the EDE phenomenon. This knowledge can be used during the implementation of more advanced transport codes that attempt to describe the low aspect ratio plasma of an ST.

ELMs and edge density gradients

The behaviour of the edge n_e gradients is studied in more detail during ELMs using the high-resolution TS and linear D_α camera diagnostics (see Chapter 8). These show that the outboard edge n_e gradient flattens during the ELM while the inboard edge n_e gradient is not affected

during the ELM. The outboard n_e gradient steepens during the inter-ELM periods. For inter-ELM periods longer than 1 ms the inboard and outboard gradients reach similar values on normalised flux. The particle transport during ELMs is presumably enhanced by poloidally asymmetric processes more prominent on the low field side.

High-resolution TS measurements of n_e have revealed a flow of particles into the scrape-off layer due to the ELM (see Chapter 8). This ELM related loss of particles was shown to have a convective character. The radial velocity of these particles is estimated at $\sim 1 - 2 \text{ km s}^{-1}$. These measurements are supported by observations from the linear D_α camera and a reciprocating probe at close range to the separatrix.

The pulsed heat loads that are associated with ELMs are highly asymmetric in MAST: $> 90\%$ leave the plasma through the outboard separatrix (see Chapter 8). Since the ELM event only appears on the outboard side, the power exhaust during the ELM is equal to the exhaust during the inter-ELM periods on the high field side. Therefore, no additional heat is deposited on the target plates on the high field side due to ELMs. Thus, the pulsed heat loads due to ELMs are likely not to cause any additional wear to the target plates in a tight aspect ratio fusion reactor.

Pedestals

Contrary to the high n_e pedestal, the T_e pedestal is low in MAST: it only reaches up to 10 – 15% of the central value, while values of $\gtrsim 25\%$ are common on *e.g.* JET. Possible explanations for the cold edge are found in the large, relatively cold bath of neutrals outside the plasma - typically 10 times colder than on conventional tokamaks - and high recycling rate in H-mode due to the high n_e . Since NSTX plasmas have similar dimensions but a tight fitting vessel wall, it will be interesting to compare its recycling with that in MAST. Increased radiative and conductive losses due to the high n_e and low magnetic field, because of the compact geometry, are also expected to reduce T_e at the edge. The T_e pedestal is degraded by the ELM, but recovers soon after the ELM. Losses in n_e are not compensated directly after the ELM. Therefore, there is evidence that ELM heat losses are predominantly non-conductive (see Chapter 8).

The stored energy in the pedestal has been determined using a reliable technique which was developed for MAST (see Chapter 8). The pedestal data is deconvolved for the instrument function of the diagnostic. The obtained values of stored energy in the pedestal in MAST fall short of the leading pedestal scaling law, mainly due to the low T_e pedestal. This scaling law, which is based on conventional tokamaks, has no aspect ratio dependence. Inclusion of the MAST data would introduce a nearly quadratic aspect ratio dependence: $W_{e,ped} \sim \epsilon^{-2}$, which helps to predict pedestal energy levels in a reactor.

9.3 In conclusion

The high-confinement regime in MAST behaves and performs very similar to that observed in conventional aspect ratio tokamaks, however the edge electron density and temperature, and neutral recycling generally differ. This difference is likely introduced by the large volume of neutral gas surrounding the plasma. The question remains to what degree the difference in plasma shape plays an important role in this. The particle and power exhaust during edge localised modes is strongly asymmetric and biased to the low field side. This means that heat pulses due to these instabilities are not likely to cause any additional material wear on the compact high field side target areas of a low aspect ratio fusion reactor.

List of abbreviations

abbreviation	full name	description
ADC	Analog to digital converter	appliance
CCD	Charge coupled device	appliance
CT	Conventional aspect ratio tokamak	tokamak type
CXR	Charge-exchange radiation	diagnostic
DIII-D	Doublet III D	tokamak device
DND	Double null divertor	tokamak terminology
EBW	Electron Bernstein waves	electromagnetic waves
ECRH	Electron cyclotron radiation heating	auxiliary heating
EDE	Edge density 'ear'	plasma phenomenon
EFIT	Equilibrium fitting	diagnostic
ELM	Edge localised mode	plasma phenomenon
ETB	Edge transport barrier	plasma phenomenon
FOM	Stichting voor Fundamenteel Onderzoek der Materie	organisation
FWHM	Full width at half maximum	mathematic term
H-mode	High-confinement regime	tokamak terminology
HFS	High field side	tokamak terminology
IRE	Internal reconnection event	plasma phenomenon
ITB	Internal transport barrier	plasma phenomenon
JET	Joint European Torus	tokamak device
L-mode	Low-confinement regime	tokamak terminology
LCFS	Last closed flux surface	tokamak terminology
LFS	Low field side	tokamak terminology
MAST	Mega-Ampere Spherical Tokamak	tokamak device
MCP	Micro channel plate	part of appliance
MHD	magnetohydrodynamics	plasma model
NBI	Neutral particle beam injector	auxiliary heating
NPA	Neutral particle analyser	diagnostic
NSTX	National Spherical Tokamak eXperiment	tokamak device
NTM	Neoclassical tearing mode	plasma phenomenon
ORNL	Oak Ridge National Laboratory	organisation
RMS	Root-mean-square	mathematical term
RTP	Rijnhuizen Tokamak Project	tokamak device
SOL	Scrape-off layer	tokamak terminology
ST	Spherical tokamak	tokamak type
START	Small Tight Aspect Ratio Tokamak	tokamak device
SXR	Soft x-ray camera	diagnostic
TM	Tearing mode	plasma phenomenon

abbreviation	full name	description
TS	Thomson scattering	diagnostic
UKAEA	United Kingdom Atomic Energy Authority	organisation
VDE	Vertical displacement event	plasma phenomenon
Ω	Ohmic	tokamak terminology

List of symbols and constants

symbol	description	definition	value	unit
a	minor radius			m
A	aspect ratio	R_0/a		-
B	magnetic field strength			T
B_θ	poloidal magnetic field			T
B_ϕ	toroidal magnetic field			T
c	speed of light in vacuum		2.998×10^8	ms^{-1}
D	diffusion coefficient			m^2s^{-1}
e	elementary charge		1.602×10^{-19}	C
E_n	neutral influx energy			J/eV
I_p	plasma current			A
k_B	Boltzmann constant		1.38×10^{-23}	JK^{-1}
m_0	electron rest mass		9.11×10^{-31}	kg
m_i	ion mass			kg
n_e	electron density			m^{-3}
n_n	neutral density			m^{-3}
\bar{n}_e	line-average electron density			m^{-3}
$\bar{n}_e \ell$	line-integrated electron density			m^{-2}
p_e	electron pressure			Pa
q	safety factor			-
r	minor radius			m
r_0	classical electron radius	$e^2/4\pi\epsilon_0 m_0 c^2$	2.818×10^{-15}	m
R_0	major radius			m
t	time			s
T_e	electron temperature			K/eV
T_n	neutral temperature			K/eV
v_{th}	electron thermal velocity	$(2k_B T_e/m_0)^{1/2}$		ms^{-1}
$v_{th,i}$	ion thermal velocity	$(2k_B T_i/m_i)^{1/2}$		ms^{-1}
\vec{V}	pinch velocity			ms^{-1}
\vec{V}_n	neutral influx velocity			ms^{-1}
W	stored energy			J
Z	ion charge			-
Z_{eff}	effective ion charge			-
β	confinement efficiency			-
β_{th}	relative electron thermal velocity	v_{th}/c		-
$\vec{\Gamma}_e$	electron flux			$\text{m}^{-2}\text{s}^{-1}$
$\vec{\Gamma}_n$	neutral flux			$\text{m}^{-2}\text{s}^{-1}$
δ	triangularity			-

symbol	description	definition	value	unit
δ_{sep}	separatrix separation			m
ΔR	radial resolution			m
$\Delta\Psi_N$	normalised-flux resolution	$\Delta R \partial\Psi_N / \partial R$		-
$\Delta\sqrt{\bar{\Psi}_N}$	root-normalised-flux resolution	$\Delta R \partial\sqrt{\bar{\Psi}_N} / \partial R$		-
$\Delta\alpha$	D_α profile width			m
ε	inverse aspect ratio	a/R_0		-
ε_0	permittivity of free space		8.854×10^{-12}	Fm^{-1}
θ	scattering angle			rad
κ	elongation			-
λ	wavelength			m
λ_0	ruby laser wavelength		694.3	nm
λ_D	Debye length	$(k_B T_e / 4\pi n_e e^2)^{1/2}$		m
ρ_i	ion Larmor radius	$v_{th,i} / \omega_{ci}$		m
τ_E	energy confinement time			s
τ_p	particle confinement time			s
Ψ	magnetic flux			Tm^2
Ψ_0	magnetic flux at magnetic centre			Tm^2
Ψ_a	magnetic flux at separatrix			Tm^2
Ψ_N	normalise magnetic flux	$(\Psi_0 - \Psi) / (\Psi_0 - \Psi_a)$		-
ω_{ci}	ion gyrofrequency	$ZeB / m_i c$		rad s^{-1}
$\langle \sigma_{ex} \nu_e \rangle$	excitation rate			$\text{m}^3 \text{s}^{-1}$
$\langle \sigma_{ion} \nu_e \rangle$	effective ionisation rate			$\text{m}^3 \text{s}^{-1}$

Acknowledgements

Since this is the part of the dissertation that most people read, searching for their own name, I have to make sure I do not miss anyone out that has contributed to my dissertation in one way or another. This, I am afraid, will be an impossible task. During the years of my Ph.D. I have worked with many people both at FOM institute 'Rijnhuizen' and UKAEA Fusion and there is not enough space to mention all of those. I will concentrate on a few important people only. First of all, I would like to thank Michael Walsh for the continuous support that I received from him throughout my Ph.D., for sharing his knowledge, for his positive attitude, for the valuable input towards my dissertation, for his immense patience and for his great character. It has always been a pleasure working with him. Secondly, I would like to thank Niek Lopes Cardozo for his critical but justified views on my dissertation and for making my studies at Culham possible. Patrick Carolan I would like to thank for hosting me in the diagnostics group at Culham. Not to be missed out are all the people of the MAST team that have contributed in providing the experimental data used in this dissertation, in particular the ones I have worked in close cooperation with to discuss physics, data and other topics. Also many thanks to the people in the reading committee.

Then there are many others that have, above all, contributed to making my stay at Culham enjoyable. First of all these are the many fellow students from the 'Ghetto': Setthivoine You and Joon-wook 'Enoma' Ahn were always ready for a chat and their company made the many long evenings bearable; Ian Lehane taught me the art of hurling and has been a pleasant friend and colleague; I had many walks around the car park with 'Big' John Rainnie; Stefan Nielsen brought some Northern European flavour into the 'Ghetto'; with Mark McGrath and Phillip Jones I could share the ups and downs of writing up towards the end of our Ph.D.s; Roger O'Gorman is the ever friendly and helpful Irishman; I wish the new generation students Michaela Nelson and Fraser Lott the best of luck. One floor below the 'Ghetto' I also found a good friend in Calum Byrom. Secondly, there are the more 'permanent' staff: family man Martin Dunstan - one of the few true Oxfordians - has always been extremely helpful and good for nice conversations as well; Celso 'Mr. Rivers' Ribeiro provided me with litres of coffee and endless anecdotes in return for *stroopwafels*.

Outside work I was fortunate enough to make many friends with whom I had many nice dinners (especially on Sunday's), drinks in the pubs, nights out in cinemas and theatres, weekend trips in Britain, etc. Some of whom I could meet in their native countries, which gave me a great opportunity to explore Europe. A special mentioning is for Emma Kerrigan and Bess Bradfield, whom provided a warm home for me at #20, and for my parents who did the same 'back home'. Finally, *un bon merci* to Noëlle Cuny for checking every single letter and character in this dissertation, *super!* Groet.

Curriculum vitae

I was born on the 14th of March 1973 in Hillegom in the Netherlands. In May 1991 I have completed the VWO exam at Leeuwenhorst College in Noordwijkerhout. From August 1991 to May 1997 I read Applied Physics for an M.Sc. at the University of Technology in Delft. For my master's project, I conducted experimental work on two-phase flows in a natural-circulation boiling-water fission reactor at the Interfaculty Reactor Institute in Delft. After a period of travelling and temporary employment as a data analyst, I began a Ph.D. at the FOM Institute for Plasma Physics 'Rijnhuizen' in March 1998. The experimental research for my doctorate was undertaken at the UKAEA Fusion laboratory at the Culham Science Centre in Oxfordshire in the United Kingdom. This dissertation is the record and culmination of that work.